Geochemical and mineralogical investigations of fine growth structures of ferromanganese nodules from the Clarion and Clipperton Zone, Pacific Ocean

Von der Naturwissenschaftlichen Fakultät der

Gottfried Wilhelm Leibniz Universität Hannover

zur Erlangung des Grades

Doktorin der Naturwissenschaften (Dr. rer. nat.)

genehmigte Dissertation

von

Dipl.-Geow. Anna Viktoria Wegorzewski

geboren am 24.06.1983, in Schweidnitz (Polen)

[2015]

Table of contents

Zusammenfassung

Marine Manganknollen und Fe-Mn Krusten sind aus nm-µm dicken konzentrischen Lagen aufgebaute Präzipitate. Aufgrund ihrer hohen Gehalte an wirtschaftlich bedeutenden Metallen (Ni, Cu, Co, Zn, Mo, Li, Seltene Erden) sind diese eine wichtige potentielle Rohstoffquelle für die Zukunft. In dieser Arbeit wurden Gesamtknollen, sowie deren nm-µm großen Wachstumsstrukturen, aus dem „Manganknollengürtel" in der Clarion und Clipperton Bruchzone (CCZ) im zentralen Pazifik detailliert auf ihre chemische und mineralogische Zusammensetzung untersucht.

Die Erforschung der Genese und der Anreicherungsprozesse der Metalle in die Mn-Mineralphasen ist im Hinblick auf eine spätere metallurgische Aufbereitung von hoher Wichtigkeit.

Gesamtknollen zeigen Mn/Fe Verhältnisse zwischen 4 und 6 mit einem maximalen Ni+Cu Gehalt von ~3 Gew.%. Dies wurde bisher als oxisch-diagenetische Bildung interpretiert. Im Gegensatz dazu, weisen die nm-µm dicken Einzellagen eine weitaus höhere chemische Heterogenität auf. Zwei genetisch unterschiedliche Lagentypen konnten bestimmt werden.

Lagentyp 1: Mn/Fe Verhältnisse <3, Ni+Cu Gehalte ~1 Gew.%, Co Gehalte <0,6 Gew.%. Dies ist charakteristisch für oxisch-hydrogenetisches Wachstum. Mineralogisch bestehen diese Lagen aus Fe-Vernadit (δ-MnO_2), welcher epitaktisch mit einer amorphen δ-FeOOH Phase verwachsen ist. Sie weisen 67 - 82% Mn^{4+} und 18 - 33% $Mn^{2+}+Mn^{3+}$ auf.

Lagentyp 2: Mn/Fe Verhältnisse 9 - 826, Ni+Cu-Gehalte von 0,8 bis 6,5 Gew.%, Co Gehalte <0,06 Gew.%. Dieser Lagentyp ist auf eine suboxisch-diagenetische Entstehung, ähnlich wie bei den Knollen aus dem Peru Becken, zurückzuführen. Mineralogisch besteht der *Lagentyp 2* aus thermisch unterschiedlich stabilen, fehlgeordneten Phyllomanganaten (10 Å/7 Å Vernaditen) mit durchschnittlichen Mn-Oxidationsstufen von ~3,6±0.2. Ältere Lagen zeigen eine Stabilisierung des Vernaditkristallgitters durch einen erhöhten Einbau von Mg^{2+} in die Zwischenschichten. Es konnte keine eindeutige Korrelation der thermisch unterschiedlich stabilen Vernadite mit unterschiedlichen Ni+Cu Gehalten nachgewiesen werden.

Todorokit wurde in den hier analysiert Knollen nicht detektiert.

Die Ergebnisse der Einzellagen zeigen, dass die Geochemie der Gesamtknollen nicht die einzelnen Wachstumsprozesse wiederspiegelt und somit für eine genetische Interpretation ungeeignet ist.

Die individuellen Lagen der Knollen aus der CCZ zeigen, dass diese in ihrer Entstehungsgeschichte unterschiedlichen Umgebungsbedingungen ausgesetzt waren. Die Änderung des Umgebungsmillieus ist vermutlich auf klimatische Veränderungen (Glazial-Interglazial Wechsel) zurückzuführen. Unter den heutigen oxischen Bedingungen im bodennahen Wasser sowie im Sedimentporenwasser können sich ausschließlich oxisch-hydrogenetische Lagen bilden. Die Metallanreicherung ist unabhängig von der Anreicherungsquelle (bodennahes Meerwasser oder Porenwasser).

Typisch oxisch diagenetische Lagen wurden in den Knollen nicht als eigenständige Lagen charakterisiert.

Computertomographische Analysen der Knollen haben ergeben, dass die Porenräume durchgängig miteinander verbunden sind. Dadurch haben Fluide die Möglichkeit die Knollen nachträglich zu durchströmen und die Porenräume auszufüllen, sowie bereits auspräzipitierte Mn-Phasen sekundär umzubilden.

Schlagwörter: Mn-Knollen, suboxisch-diagenetisch, Vernadit

Abstract

Marine ferromanganese nodules and crusts are encrustations of nm-µm thick layers, which incorporate high amounts of economically interesting metals (Ni, Cu, Co, Zn, Mo, Li, rare earth elements). Due to that, nodules and crusts become a valuable ore deposit.

In this study manganese nodules and in detail, their nm-µm thick growth structures, from the so called "Manganese nodule belt" from the Clarion Clipperton Zone (CCZ) of the central Pacific Ocean, were analyzed for their chemical and mineralogical composition. The investigations of the genesis and the enrichment processes of metals into Mn-minerals are very important for future metallurgical treatment.

Bulk nodules show Mn/Fe ratios between 4 and 6 and Ni+Cu contents of ~3 wt.%, which is interpreted up to now as oxic-diagenetic growth. In contrast to that, detail investigations of nm to µm-thick nodule layers reveal a much higher chemical heterogeneity. Two genetically different layers were detected.

Layer type 1: Mn/Fe ratios <3, Ni+Cu contents ~1 wt.%, Co content <0.6 wt.%, which is characteristic for an oxic-hydrogenetic growth. Mineralogically, these layers consist of Fe-vernadite (δ-MnO_2), which is epitaxially intergrown with an amorphous δ-FeOOH phase. These layers consist of 67 - 82% Mn^{4+} and 18 - 33% Mn^{2+}+Mn^{3+}.

Layer type 2: Mn/Fe ratios 9 - 826, Ni+Cu contents 0.8 - 6.5 wt.%, Co contents <0.06 wt.%, which is typical for suboxic-diagenetic growth similar to nodules from the Peru Basin. Mineralogically, those layers consist of different, thermally stabile turbostratic phyllomanganates (10 Å/7 Å vernadites) with a Mn-oxidation state of ~3.6 $\pm$ 0.2. Older nodule layers show a thermal stabilization of the vernadite structure due to the incorporation of Mg^{2+} into the interlayers. No distinct relationship between different vernadites and the metal content was found.

Todorokite was not detected within the nodules of this study.

The results of individual layers show, that the bulk geochemistry of entire nodules do not show individual growing processes and is therefore not suitable for genetic interpretation.

The genetically different nm-µm thick layers of nodules from the CCZ show that they were grown under different environment conditions, which are caused probably by changes of the glacial and interglacial periods.

Under recent oxic conditions of the near-bottom water and the sediment pore water, exclusively oxic-hydrogenetic layers can be formed.

The incorporation of metals is independent of the enrichment source (near bottom water or sediment pore water).

Typical oxic-diagenetic layers were not detected as individual layers.

Computer tomography analyses of the nodules show, that the pores are interconnected to a pore system, which enable fluids from the surrounding environment to penetrate the nodules and alter the primary Mn-phases.

Keywords: Mn-nodules, suboxic-diagenetic, vernadite

Chapter I

1.1 Introduction

Ferromanganese encrustations (nodules and crusts) on the deep-sea floor were first discovered during research cruises of H.M.S. Challenger between 1872 and 1876 (Murray 1876; Murray and Renard 1891). Detailed German exploration on nodules began in the early 1970`s with the vessels "Valdivia II" (1972 - 1978) and "SONNE" (up to 1982), since nodules and crusts were of high economic interest due to their chemical composition. Nodules are enriched in economically important metals such as Ni, Cu, Co, Mn, Li, and Mo as well as rare earth elements and Y (REY; Fig. 1.1), and are also called polymetallic nodules. In contrast, ferromanganese crusts are more enriched in Co, Mn, Ni, Te, Pt, Bi, Ti, Mo, W and the high field strength elements (Hein et al.,2013).
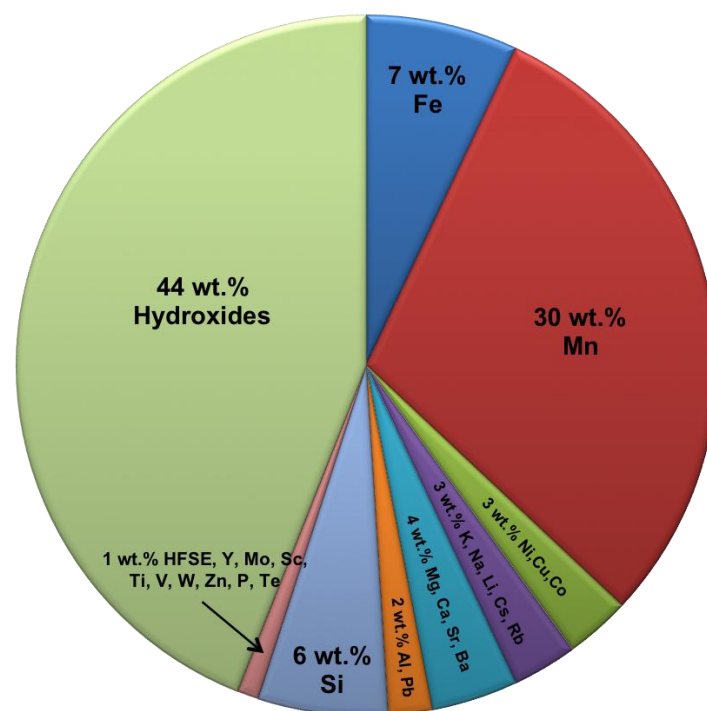
Figure 1.1 Average concentration of major, minor and trace elements of ferromanganese nodules from the eastern German license area between the Clarion and Clipperton Zone (CCZ) in the central Pacific Ocean.

Ferromanganese nodules were recovered from the sea floor of the Pacific, Atlantic, and Indian Oceans (Halbach et al., 1981; von Stackelberg, 1997; De Lange et al., 1992; Jauhari and Pattan, 2000). However, the high nodule abundance (>10 kg/m^2) and the high concentration of Ni+Cu+Co (up to 3 wt.%) (Mero, 1965; Rühlemann et al., 2011) in nodules from the

central Pacific Ocean within the Clarion and Clipperton Zone (CCZ) makes up the so called "Manganese nodule belt" to an economically valuable area for manganese nodule exploration (Halbach et al., 1981; Morgan, 2000).

Since the beginning of the discovery of ferromanganese nodules, extensive research studies were carried out on the chemical and mineralogical composition of nodules and crusts for obtaining a better understanding of their origin and the accumulation processes of the metals (e.g., Mero, 1965; Burns and Burns, 1975; Burns, 1976; Burns et al., 1977; Glasby, 1973; Glasby et al., 1982; Halbach et al., 1988; Hein et al., 1997; von Stackelberg and Beiersdorf, 1991).

The interest for ferromanganese nodules persisted to the mid 1980`s but with dropping metal prices on the global markets, the interest on ferromanganese nodules decreased until the 2000s.

However, because of the increasing demand and consumption of economically important metals, the economic interest in polymetallic nodules has increased again after the millennium turn. Germany needs to import valuable metals (Ni, Cu, Mn, Mo, REEs) for high technology applications, green-tech industry, electronic industry, steel industry etc. (Hein et al., 2013)

Due to Germany's large dependency on the import of resources it is essential to discover new and own potential ore resources/deposits such as polymetallic nodules from the central Pacific Ocean since economic and political problems in the supplying countries (e.g., Africa, South America, China) may cause supply risks of certain commodities.

In July 2006, Germany signed a contract with the International Seabed Authority (ISA) on the exploration of polymetallic nodules in the northeast equatorial Pacific Ocean within the "Manganese nodule belt" in the Clarion and Clipperton Zone (CCZ). The license area (75.000 km^2) is divided into two exploration areas: a Western area (W1) of ~17.000 km^2 and an Eastern area (E1) of ~58.000 km^2 (Fig. 1.2; Wiedecke-Hombach et al., 2009; 2010; Rühlemann et al., 2010). The Federal Institute for Geosciences and Natural Resources (BGR) in Hannover, Germany is authorized to investigate the license areas for nodule abundances and metal contents as well as to study the environmental parameters and the biological diversity within these two areas for 15 years (2006-2021; Rühlemann et al., 2010). Next to Germany, several private and state-owned contractors hold licenses for the exploration of Mn-nodules in the CCZ (Fig. 1.2) indicating the economic interest in this potential resource.
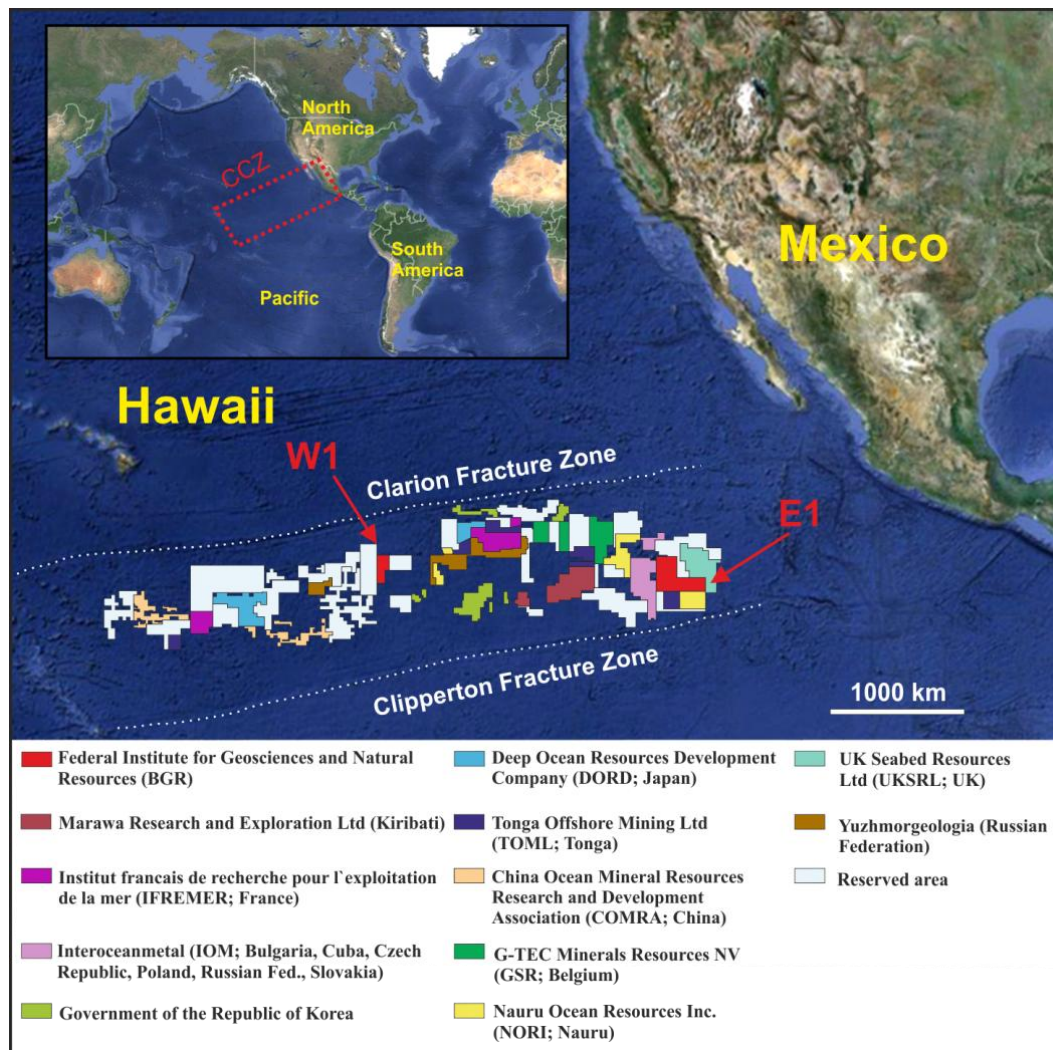
FIGURE 1.2 Clarion and Clipperton Zone (CCZ) with all contractors. The two German license areas (W1 and E1) are marked in red; (modified after the International Seabed Authority (ISA, 2013)).

Since 2008, five cruises were conducted to study the German license areas. The PhD thesis was prepared within the Project "MANGAN" of the department B1.4 "Marine Resource Exploration" at the BGR in cooperation with the Gottfried Wilhelm Leibniz University of Hannover, Germany.

The analyzed samples (nodules/crust) of this PhD derived from the eastern German license area (E1, for a detailed description see Chapter II). The manganese nodules were sampled by using box corers in five study areas (SA1, 2, 3, 5, 6) and a ferromanganese crust was collected with a chain-bag dredge from a seamount in the SA4 (Chapter II; Fig. 2.2; Fig. 3.1) during two cruses (SO205 with R/V Sonne in 2010 and BIONOD12, R/V L`Àtalante in 2013).

1.2 Aim of this study

The aim of this study was to investigate the geochemical and mineralogical composition of bulk Mn-nodules and their nm-µm thick growth structures from the CCZ. The knowledge about the accretion processes of nodules and in particular of the mineralogical nodule composition and the incorporation mechanism of metals (e.g., Ni+Cu) into these Mn-minerals will provide useful information for a tailored metallurgical extraction of those metals.

The main objectives of this study are:

- Geochemical characterization of bulk nodules and high resolution analyses of their individual nm-µm thick growth structures: How does the chemistry of bulk Mn-nodules reflect the individual layers.

- Geochemical characterization of the outermost nodule layers in context with the recent environmental conditions.

- Determination of Mn-oxidation state of genetically different layers.

- Characterization of different Mn-minerals: todorokite and/or phyllomanganates and their distribution within nodules.

- Is the chemical composition of the nodules dependent on their mineralogy, especially with respect to metals such as Ni and Cu?

- Do internal growth structures show any post depositional transformation of the chemical and mineralogical composition during their growth history?

1.3 Origin of ferromanganese nodules and crusts

Ferromanganese nodules and crusts are Mn-Fe oxyhydroxides which are formed in different marine areas under specific environment conditions (e.g., Eh, pH, sedimentation rates, sediment type; seawater chemistry; Halbach et al., 1988; Hein et al., 1997).

Ferromanganese crusts grow as encrustations on exposed, sediment free rock surfaces on seamounts due to slow metal precipitation (few mm per million of years) exclusively out of oxic sea water by hydrogenetic growth processes (Halbach et al., 1988). During the hydrogenetic growth, Mn-Fe oxyhydroxide colloids form within the water column. According to their different surface charge, metals dissolved in sea water will be adsorbed and complexed on oxide surfaces (Koschinsky and Halbach, 1995). The surface charge of the Mn-Fe oxyhydroxides depends on the pH_{zpc} (zpc: zero point of charge). In sea water dissolved hydrated cations or chloro-complexes are adsorbed preferentially on the negatively charged Mn-oxide (MnO_2^-) surface (pH_{zpc} 2.8; Stumm and Morgen, 1981). In contrast, negatively and neutrally charged complexes are adsorbed on the surface of Fe-oxyhydroxide colloids ($FeOOH^+$) which have a slightly positively charged surface (pH_{zpc} 8.5; Stumm and Morgan, 1981; Koschinsky and Halbach, 1995; Fig. 1.3). At the beginning of crust growth, the mixed colloids are precipitated as amorphous oxides and oxyhydroxides on sediment-free, hard substrate at seamounts and subsequently are subject to re-crystallization processes to solid phases. The metals are re-arranged within the crystal structure or remain adsorbed on the mineral surface (Koschinsky and Halbach, 1995).
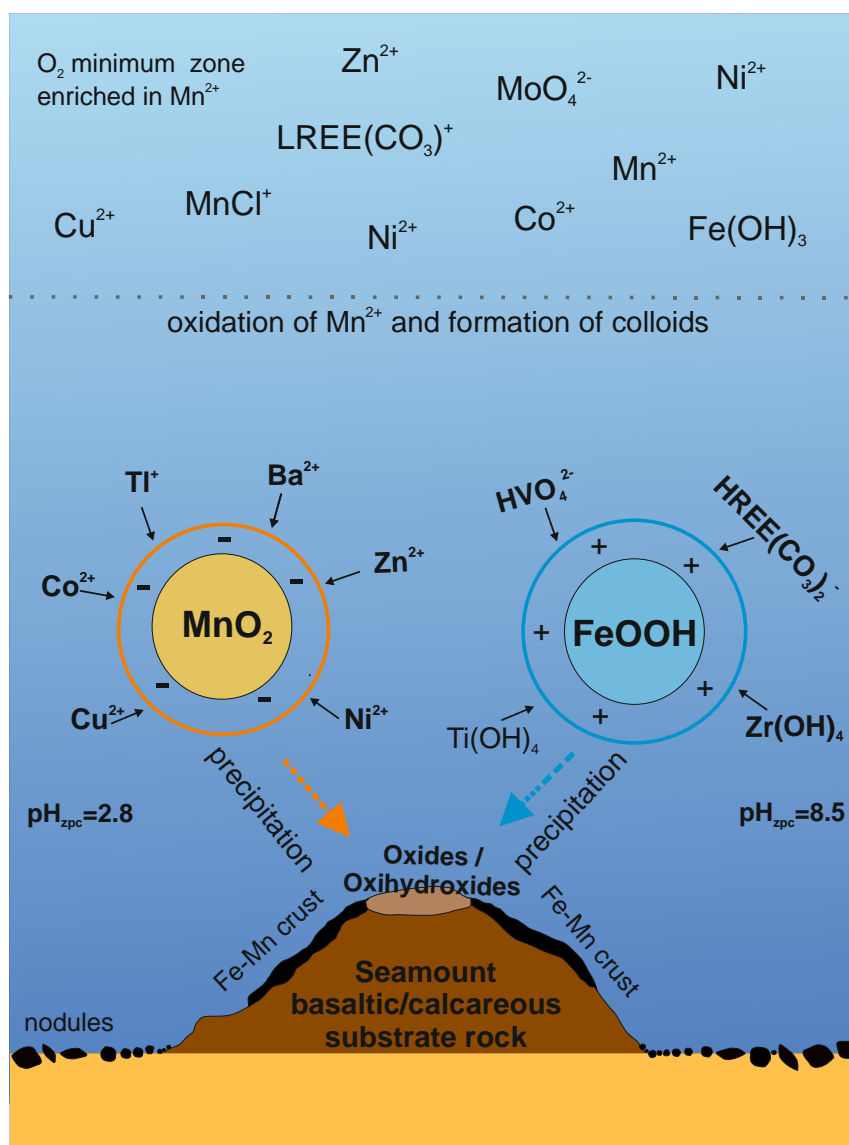
FIGURE 1.3 Simplified illustration of hydrogenetic metal precipitation and formation of ferromanganese crusts on seamounts and hydrogenetic nodules. Dissolved hydrated cation and anion complexes within the water column will be adsorbed on the negatively charged MnO_2^--surface or at the slightly positively charged Fe oxyhydroxide surface and precipitate as mixed colloids on hard substrate (modified after Koschinsky and Halbach, 1995).

Ferromanganese crusts show a low Mn/Fe ratio (≤ 3) (Halbach et al., 1981). Mineralogically, Mn-Fe crusts consist of crypto-crystalline Fe-bearing vernadite (δ-MnO_2), which is epitaxially intergrown with an amorphous Fe-oxyhydroxide phase (Koschinsky et al., 2010a). Due to the high content of positively charged FeOOH phases, crusts are enriched in REYs relative to nodules (Fig. 1.4). Furthermore, redox sensitive elements such as Co and Te are enriched in crusts because of their slow growth rates of some mm per million of years (1-5 mm/Ma; Halbach et al., 1988) during which those elements can be adsorbed and oxidized on the surface of the δ-MnO_2 phase (vernadite).
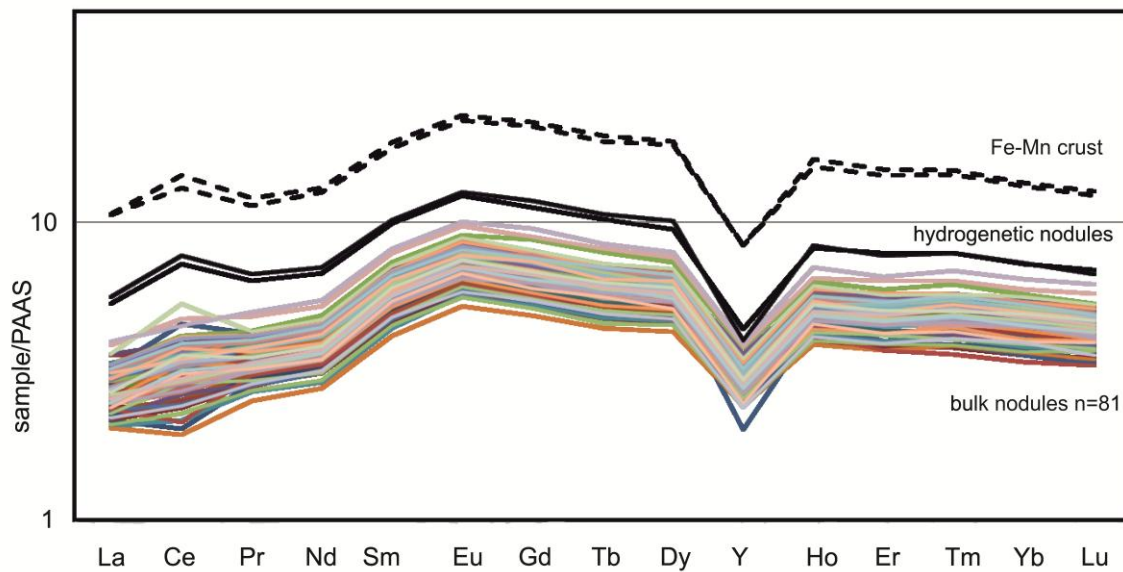
FIGURE 1.4 Shale-normalized REY patterns for bulk nodules from the CCZ compared to two ferromanganese crust samples (BGR data). The crust samples show the much higher concentrations of REYs compared to the nodules. Some of the nodules have a positive Ce anomaly and contain higher amounts of hydrogenetic material than other nodules with a negative Ce anomaly and lower REYs. All samples (crust and nodules) show a negative Y anomaly.

In contrast to Fe-Mn crusts (Fig. 1.5A), ferromanganese nodules consist of individual, genetically different nm-μm thick layers which are concentrically arranged around a nucleus (Fig. 1.5B). The latter can either be micro-nodules, rock pieces, biogenetic fragments or sediment, which are laying on the sediment surface (Halbach et al., 1988). Ferromanganese nodules occur on the slopes of seamounts and in their vicinity as well as in abyssal plains in depth between 3500 and 6500 m (Hein et al., 2013). Their size varies between 1 and 16 cm in their maximum dimension (Fig. 1.5B-D). Smaller spherical nodules occur near seamounts and will be formed on the sediment surface, whereas bigger, ellipsoid-shaped nodules are found in abyssal plains and can be partly (bottom side of the nodules) or even completely be buried in the upper few cm of the peneliquid layer of the sediment (Fig. 1.6; Halbach et al., 1988).
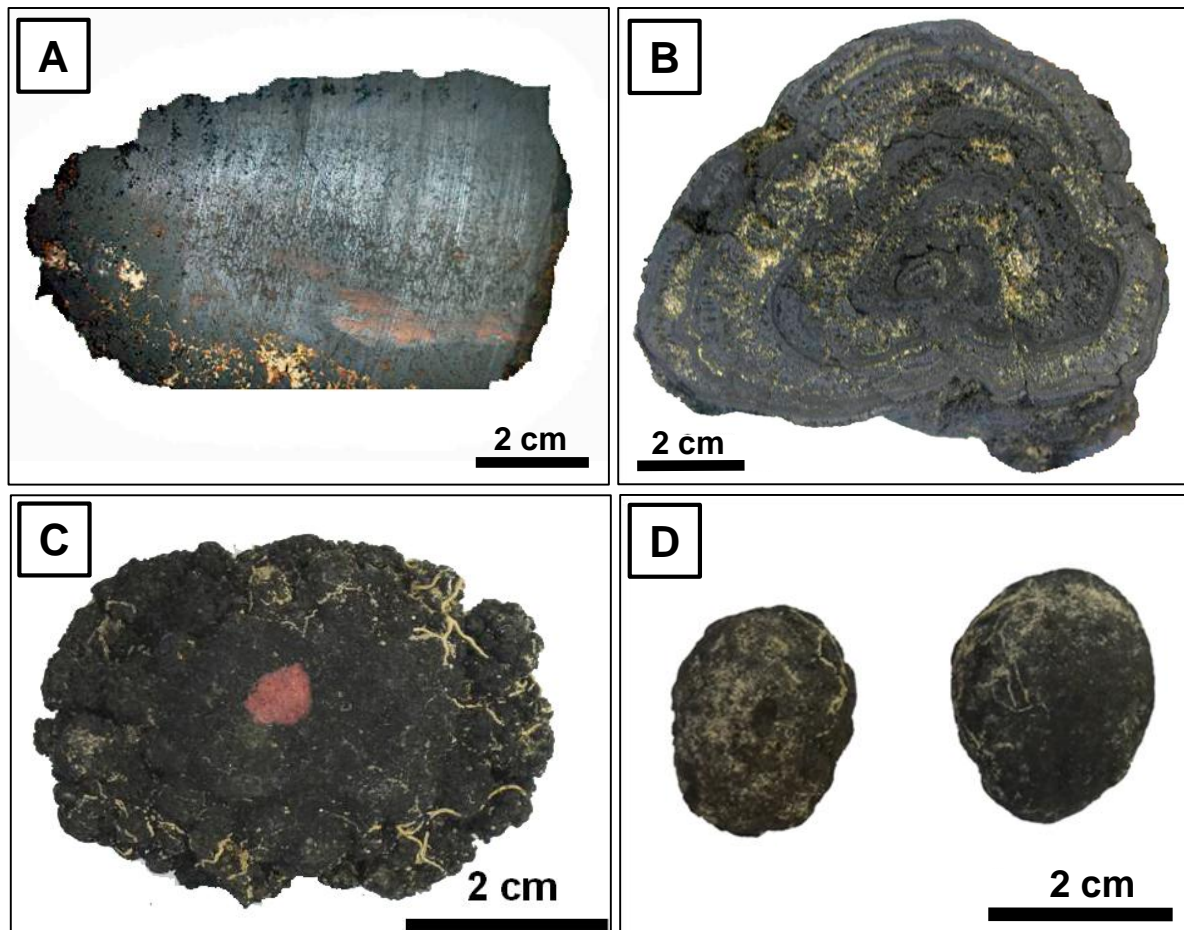
FIGURE 1.5 A: Representative specimen of a ferromanganese crust from a seamount of the eastern German license area (SA4; Fig. 2.2). **B:** Cross section of a typical big nodule from the eastern German license area. The nodule shows concentrically arranged thin layers of porous dendritic growth structures and dense layers. Cracks and pores spaces are filled with sediment. The surface of the nodule is smooth in contrast to the rough lower side of the nodule, which was embedded in the upper few cm of the sediment. **C:** Medium sized spheroidal to ellipsoidal nodule with a smooth surface (red dot) and a rough bottom side. The rim, which is the interface between the near bottom water and the sediment show a botryoidal growth structure. **D:** Typically small nodules with a slightly botryoidal smooth to rough surface.

The growth of ferromanganese nodules is depending on two different accretion processes: a hydrogenetic and a diagenetic accretion.

Nodules formed on seamounts or on their slopes, which are free of sedimentation, are of hydrogenetic growth, similar to ferromanganese crusts (Halbach et al., 1981; Hein et al., 2000). These nodules grow very slowly by metal precipitation from oxic sea water (Halbach et. al., 1988). Similar to Fe-Mn crusts those nodules consist of vernadite (δ-MnO$_2$) which is epitaxially intergrown with an amorphous δ-FeOOH phase. Low Mn/Fe ratios ($\leq$3), low Ni+Cu contents but an enrichment of Co and REY are characteristic for those nodules (Hein and Koschinsky, 2014).

In contrast to that, nodules which are formed in abyssal areas down to 6500 m water depth (Fig. 1.6) show two different growth processes. The upper surface of the nodules, which is in contact with the near-bottom water, is exclusively formed by metal precipitation out of the water column due to hydrogenetic processes similar to those observed in Fe-Mn crusts and hydrogenetic nodules (Halbach et al., 1981). The bottom side of nodules, which is in contact with the sediment surface or even completely buried in the upper centimeters of the sediment, is of diagenetic growth. This is the case for nodules which can be found in the Peru Basin (von Stackelberg, 1997).
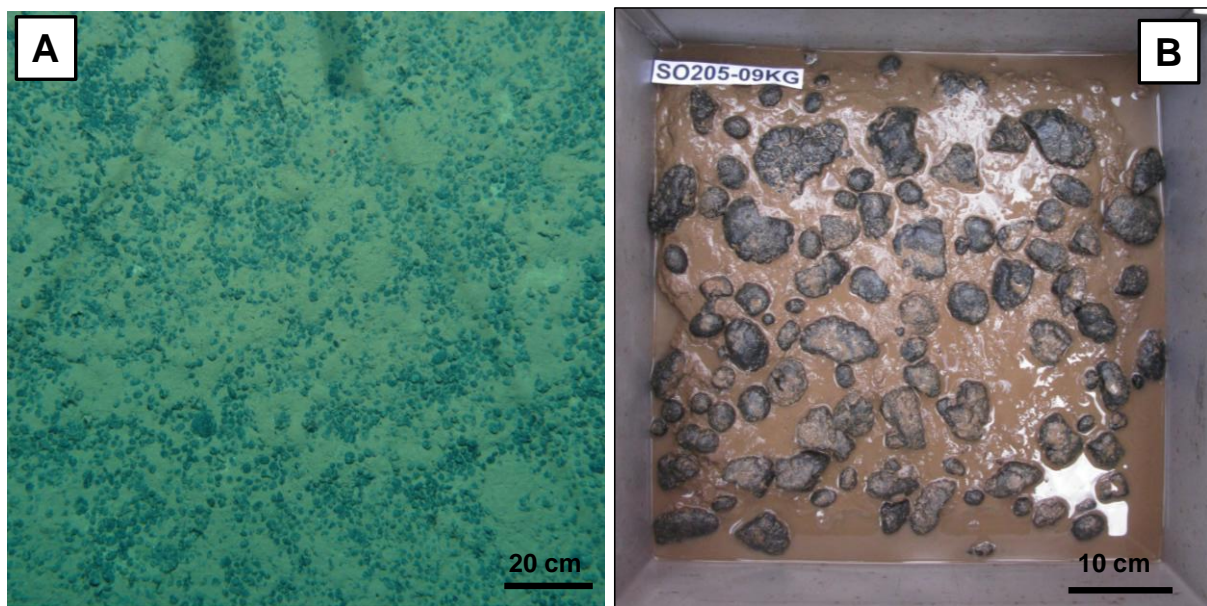
FIGURE 1.6 Photos of **A:** manganese nodules of the seafloor in the German eastern license area (E1) in ~4250 m depth (© BGR). **B:** Box core (SO205-09KG) with manganese nodules. The bottom sides of the nodules are embedded in the upper few cm of the sediment (Rühlemann et al., 2012).

Nodules which are formed by both processes are called mixed-type nodules and are representative for the CCZ (Halbach et al., 1981).

However, diagenetic growth occurs via metal precipitation out of the sediment pore water and can be found in sediment with oxic conditions as it is the case in the CCZ (Halbach et al., 1988; Chester and Jickells, 2012) or under suboxic conditions as it is the case in the Peru Basin (PB) (Halbach et al., 1988; von Stackelberg, 1997).

The oxic diagenesis is driven by the degradation of organic matter by using dissolved O_2 from the pore waters (Koschinsky et al., 2010a). Trace metals are released into the pore fluids upon the decay of organic matter and could be taken up into the Mn-phases. In addition, metals which are adsorbed on the surface of organics and sediment particles are released into the

pore water during oxic diagenesis (Dymond et al., 1984; Chester and Jickells, 2012) and can then be incorporated into the forming Mn-minerals (Lei and Boström, 1995). According to Halbach et al., (1981), oxic-diagenetic nodules show Mn/Fe ratios ranging from 3 to 10 and high metal contents (e.g., Ni+Cu <3 wt.%) in contrast to hydrogenetic or suboxic nodules. According to Chester and Jickells (2012), typical Mn-minerals which are formed under oxic diagenetic processes are Ni-, Cu-, Zn-rich todorokites.

Müller et al. (1988) suggested that oxygen is available in the whole sediment column of the CCZ and therefore, oxic diagenesis is the main process of nodule growth in this area (Halbach et al., 1988).

In contrast to that, suboxic diagenesis can be found in areas with low oxygen concentrations (<5µmol O_2/l, Hein and Koschinsky, 2014). If free oxygen is completely consumed by degradation of organic matter and a secondary oxidant is needed, manganese dioxide can act as electron acceptor. Thus, Mn^{4+} is reduced to Mn^{2+} and as such it is released into the pore water, the metals, which are bound to the Mn-phases like Ni are also released into the pore waters. Because of a concentration gradient dissolved metals (e.g., Mn^{2+}, Ni^{2+}, Cu^{2+}) can migrate upwards through the sediment column. Mn^{2+} will be re-precipitated to $Mn^{4+}O_2$ when it gets into contact with oxygen migrating downwards from the sediment surface (Chester and Jickells, 2012). This so-called redox front mainly is at or close to the sediment surface. During suboxic diagenesis, todorokite as well as phyllomanganates (birnessite) are formed (Koschinsky et al., 2010b). For suboxic diagenetic nodules a high fractionation of Mn and Fe is typical, since Fe^{3+} is not reduced and mobilized under suboxic conditions. Typical suboxic-diagenetic nodules occur in the Peru Basin (von Stackelberg, 1997) and show high Mn/Fe ratios >10 (Halbach et al., 1988).

Chapter II

The influence of suboxic diagenesis on the formation of Manganese nodules in the Clarion Clipperton nodule belt of the Pacific Ocean

The formation of polymetallic nodules from the Clarion and Clipperton Zone is depending on the environmental conditions (e.g., dissolved oxygen, bioproductivity, sediment type, Eh, pH) prevailing in the different nodule areas. Changes of these conditions influence the chemical and mineralogical composition of individual growth layers of nodules. In this study recent, outermost growth structures (<10 nm) were characterized in context with recent conditions prevailing in the near bottom water and the pore water to obtain information about enrichment processes of the different metals (e.g., Ni and Cu). Additionally, analyses of inner lying older layers and their comparison with the currently growing layers should give information about changes in the environment conditions and enrichment processes.

2.1 Abstract

Polymetallic nodules and a single Fe-Mn crust from the Clarion and Clipperton Zone (CCZ) of the equatorial eastern Pacific have been analyzed to determine their chemical and mineralogical compositions. ICP-OES analyses of bulk nodules from the CCZ indicate that the nodules formed under oxic diagenetic conditions with typical Mn/Fe ratios of 4 - 6, Ni+Cu values of 2 - 3 wt.%, Co contents of 0.12 - 0.17 wt.%. However, detail analyses of individual growth layers by electron microprobe analyses (EMPA) reveal much larger chemical heterogeneity of individual layers with Mn/Fe ratios ranging from <1 to >800. Two different genetic types of layers can be distinguished:

Layer type 1: dense layer with average Mn/Fe ratios of 1.80, average Ni+Cu of 0.81 wt.%, Co contents of 0.30 wt.% (hydrogenetic metal precipitation from oxic waters). These layers consist of Fe-vernadite (δ-MnO$_2$) epitaxially intergrown with feroxyhyte (δ-FeOOH) nanoparticles.

Layer type 2: growth structures (dendritic growth structures and dense layers) with average Mn/Fe ratios of 96, Ni+Cu of 3.9 wt.%, Co contents of 0.08 wt.%, and a distinct Ni+Cu maximum of 6.51 wt.% at a Mn/Fe ratio of 56 (suboxic-diagenetic, metal precipitation from suboxic pore waters). Type 2 layers mainly consist of turbostratic phyllomanganates such as 10 Å vernadite, 7 Å vernadite and todorokite are minor compounds.

Mixed layer type 3: These layers can occur as zones of low reflectivity in the transition from layer type 1 to 2 or build up inhomogeneous growth structures of nm-thin layers of low or high reflectivity. The Mn/Fe ratios of this material range between 3 and 11, Ni+Cu of 1 - 4.6 wt.% and Co contents are between 0.02 and 0.77 wt.%. In most cases these growth structures represent a mixture of type 1 and 2 layers.

X-ray photoelectron spectroscopy (XPS) of the recent outermost nm layers of nodules (top, rim and bottom side) indicates hydrogenetic accretion processes under recent oxic conditions both from seawater and pore water. The mixed-type CCZ nodules are interpreted to consist of an oxic-hydrogenetic and a suboxic-diagenetic end member. Calculations of the proportions of the individual layer end members show that suboxic layers make up about 50 - 60% of the chemical inventory of the CCZ nodules whereas oxic-hydrogenetic layers comprise about 35 - 40%. The remaining part (5 - 10%) consists of incorporated sediment particles occurring along cracks and pores.

These results demonstrate that suboxic conditions alternate with oxic conditions during the growth of nodules in the eastern CCZ. This is probably due to fluctuating bioproductivity in the equatorial Pacific surface waters during glacial-interglacial periods which led to changing organic carbon flux to the sediment and changing oxygen consumption in near surface sediments. Furthermore, reduced ventilation of the deep ocean during glacial periods may have led to suboxic conditions in near-surface sediments.

Our investigations prove that bulk chemistry data of whole nodules only provides an average of individual layers that build up the nodules and is inappropriate for genetic interpretation.

2.2 Introduction

Ferromanganese precipitations (polymetallic nodules and ferromanganese crusts) are of high economic interest due to their enrichment of metals such as Ni, Cu, Co, Mo, Li, Te and high field strength elements (rare earth elements, Ti, Hf, Nb, Ta, Zr; Hein et al., 2013). Many studies on the chemical and mineralogical composition were performed to unravel formation processes of manganese nodules (e.g. Glasby, 1973; Burns et al., 1977; Usui, 1979; Halbach et al., 1981; Cronan, 2000; Hein et al., 2000; Koschinsky and Hein, 2003).

Polymetallic nodules have a complex texture that is characterized by irregular, concentrically banded zones of micro-layers around a nucleus. The latter is made up of sediment, rock or biogenetic fragments or micro-nodules (Halbach et al., 1988). The individual layers possess different chemical and mineralogical compositions that are caused by different growth processes: *hydrogenetic* (i.e. precipitation of metals from oxic water column) and *diagenetic* (i.e. metal precipitation from sediment pore water, under oxic or suboxic conditions; Reyss et al., 1985). According to Halbach et al. (1981), manganese nodules are classified into different types in relation to their Mn/Fe ratio and Ni+Cu content. Nodules with a Mn/Fe ratio ≤3 and low Ni+Cu concentrations are typical of hydrogenetic growth process based on precipitation of colloidal particles of hydrated metal oxides from the near-bottom sea water under oxic conditions (Halbach and Özkara, 1979; Koschinsky and Halbach, 1995). These precipitates are called B-type nodules (Halbach and Özkara, 1979) and include crusts, small nodules and polynodules, which occur predominantly on seamounts (crust) or in their vicinity (nodules; Halbach et al., 1988; Hein et al., 2000). Hydrogenetic crusts mineralogically consist of Fe-bearing vernadite (also called δ-MnO_2) which is intergrown with amorphous iron oxyhydroxide (δ-FeOOH) nanoparticles (Koschinsky et al., 2010a).

Nodules with Mn/Fe ratios of 3 to >10 accompanied by an enrichment of trace metals such as Ni and Cu, form during an early stage of diagenesis either under oxic or under suboxic conditions (Halbach et al., 1988). During both diagenetic processes, metal precipitation occurs in the pore water within the "peneliquid layer" (5 to 30 cm of the upper sediment column), where the nodules are formed (Halbach et al., 1988). These nodules are classified as A-type nodules (Halbach and Özkara, 1979) and consist of different manganese minerals, 10 Å manganates, such as the tectomanganate todorokite, and/or turbostratic phyllomanganates (7 Å and 10 Å phyllomanganates; Burns and Burns 1978a,b). Some authors also identify these minerals but used a different nomenclature such as 10 Å vernadite and 7 Å vernadite described by Bodeï et al. (2007). Todorokite as well as the two phyllomanganate types can incorporate different amounts of metals (e.g., Ni^{2+}, Cu^{2+}) in their crystal structure. The average concentration of Ni and Cu in todorokite minerals is about 2 wt.%, 10 Å phyllomanganates can incorporate up to 5 wt.% of Ni and Cu (Bodeï et al., 2007).

Past studies focused on the mineralogy and chemistry of bulk ferromanganese nodules (e.g. Halbach and Özkara, 1979; Elderfield et al., 1981; Calvert and Piper, 1984; Dymond et al., 1984; Lyle, 1978). In this chapter, high resolution chemical analyses of individual nm to μm thick layers in a variety of nodules are presented. By comparing bulk nodule chemistry and mineralogy with those of single growth layers, it can be shown that the formation of nodules in the CCZ is less uniform than previously thought.

2.3 Study areas

The nodules analyzed in this study are from the Clarion and Clipperton Zone (CCZ) in the northeast equatorial Pacific, the so called "Manganese nodule belt" (Halbach et al., 1988; Kuhn et al., 2010) as well as from the Peru Basin (PB) in the southeast Pacific (Fig. 2.1). The CCZ is located north of the equatorial high bioproductivity zone (Antoine et al., 1996). The present-day bioproductivity decreases slightly from east to west in the CCZ (ISA study, 2010). Samples for this study derive from the easternmost part of the CCZ (the German license area E1) and were taken during research cruise SO 205 with the R/V SONNE in 2010 (Wiedicke-Hombach et al., 2009; 2010; Rühlemann et al., 2010; Fig. 2.1; 2.2; area E1). The E1 area is characterized by N-S trending ridges and basins in about 4000 - 4500 m water depth as well as by volcanic seamounts that rise up to 2500 m above their surroundings (Fig. 2.2). About half of the area consists of flat sediment-covered seafloor with high Mn nodule

abundances of up to 30 kg/m^2 (based on wet weight; Rühlemann et al., 2011; Kuhn et al., 2012). The sediments in this area consist of pelagic clay and siliceous ooze (diatoms and radiolarians) and have been deposited with a rate of 0.35 - 0.5 cm/kyr (Mewes et al., 2014). The sediments are almost devoid of carbonates since these sites are slightly below the carbonate compensation depth (CCD; Cronan, 2000). Dissolved oxygen was detectable in sediment pore waters down to 2 - 3 m sediment depth throughout area E1 (Rühlemann et al., 2011). That means that a suboxic front is established in 2 - 3 m sediment depth, which is in marked contrast to previous studies that indicated that the sediments in the CCZ are completely oxic (Müller et al., 1988).
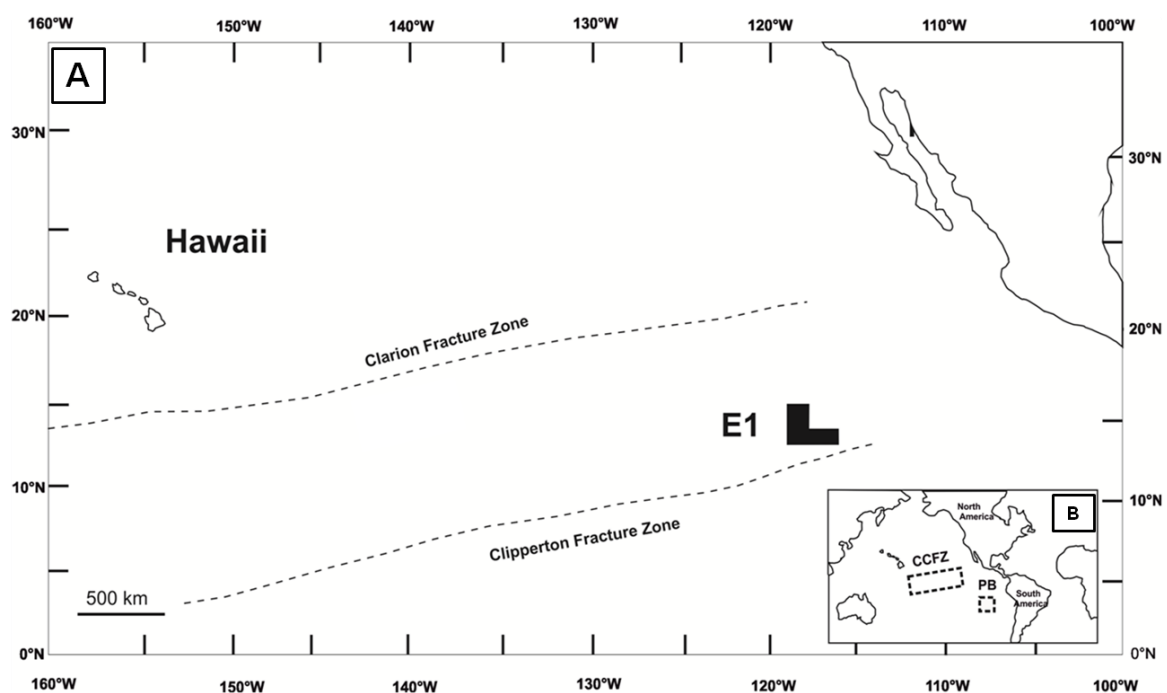
FIGURE 2.1 A: Location of the eastern German license area (E1) for the exploration of polymetallic nodules in the Clarion and the Clipperton Zone (CCZ) in the Pacific Ocean. All samples investigated during this chapter are from E1 (see Fig. 2.2). **B:** Locality of the CCZ and the Peru Basin (PB) in the Pacific Ocean.

The CCZ nodules analyzed here are from six study areas (Fig. 2.2; SA1 - SA6). Whereas SA1, 2, 3, and 6 are located close to seamounts, SA5 is ~150 km away from seamounts (Fig. 2.2; Table 2.1). SA3 is located between two seamounts and is probably influenced by bottom currents. SA4 was chosen for sampling of a Fe-Mn crust from the flank of a seamount.
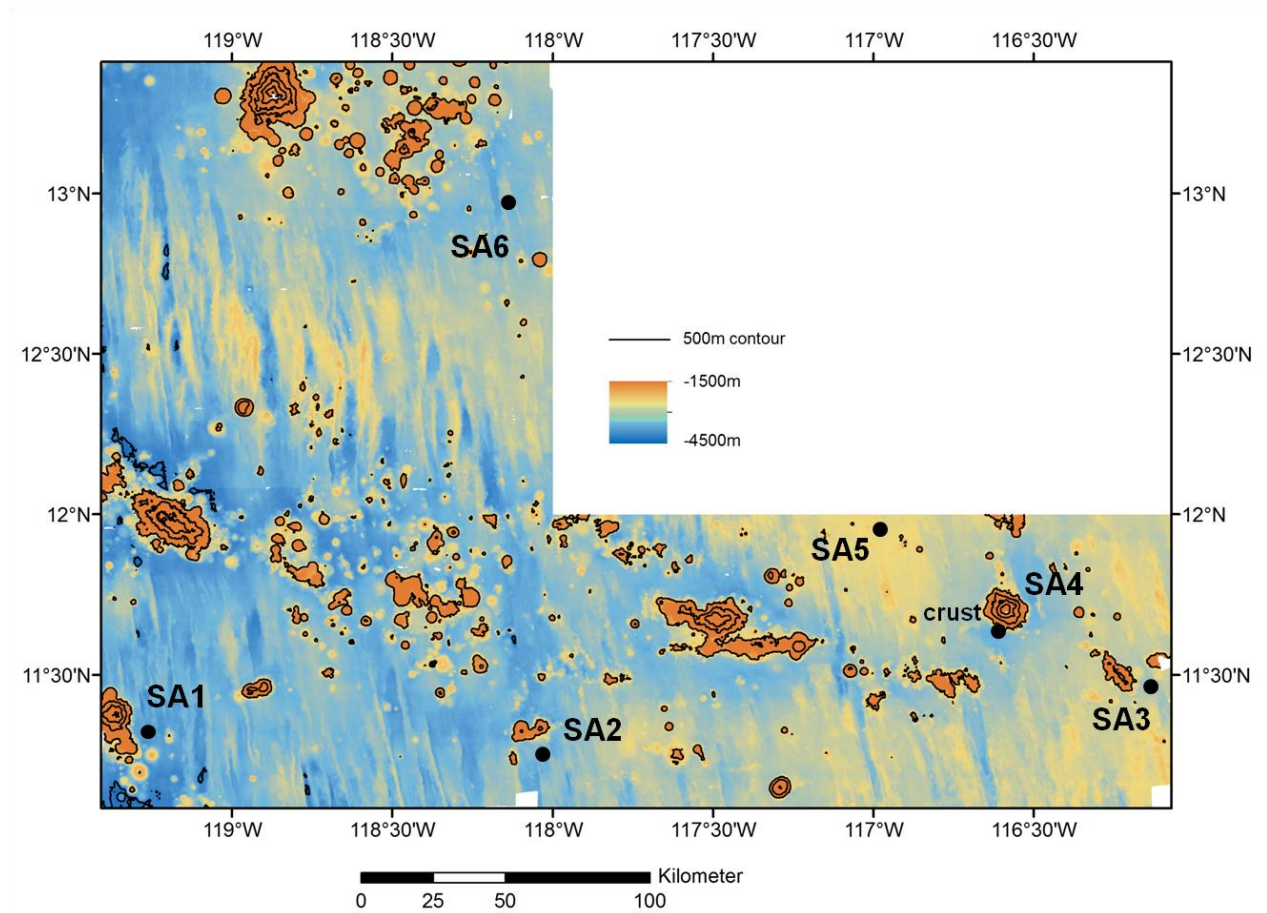
FIGURE 2.2 Bathymetry map of the eastern German license area (E1) with the sites of the study area (SA 1-6; modified after Rühlemann et al., 2010).

TABLE 2.1 Location of nodules and one crust analyzed during this study

Study area (SA)	Sample-ID	Position		Water depth [m]
		Latitude	Longitude	
1	SO205 11KG*[1]-A	11°19.1 N	119°18.4 W	4318
2	SO205 17KG-D	11°09.7 N	117°58.4 W	4393
3	SO205 27KG-1	11°36.4 N	116°9.8 W	4313
	SO205 32KG-5	11°28.6 N	116°9.2 W	4240
4	SO205 37KD-3 (crust)	11°40.6 N	116°38.3 W	4006
5	SO205 44KG-2	11°57.4 N	116°57.2 W	4188
	SO205 49KG-4	11°57.3 N	116°58.6 W	4137
6	SO205 68 KG-C	13°08.6 N	118°6.1 W	4272
Peru Basin „SEDIPERU"	SO79 97KG-1,2	7°05.9 S	90°46.8 W	4148
	SO79 176KL*[2]-3	8°09.7 S	90°49.5 W	4238
Peru Basin „DISCOL"	SO106 204KG	7 °7.8 S	88°34.2 W	4059
	SO106 237KG-1,2	6°34.0 S	90°27.9 W	4127

*[1]KG = Kastengreifer; *[2]Kolbenlot

The Peru Basin (PB) nodules investigated here were recovered during cruises SO 79 in 1992 (von Stackelberg et al., 1993) and SO 106 in 1996 (Schriever et al., 1996) with R/V SONNE. The PB is located in the south-eastern tropical Pacific (Fig. 2.1B). The geographical positions of the samples are given in Table 2.1. In contrast to the CCZ sediments, the PB sediments are characterized by a suboxic front at about 10 cm sediment depth, i.e. dissolved oxygen is consumed in the upper 10 cm (von Stackelberg et al., 1997). This is due to a high bioproductivity in the surface waters leading to high organic carbon flux into the sediments (Halbach et al., 1988). Manganese nodules from the PB currently form by the supply of metals from oxygen-free (suboxic) pore waters at the bottom side of the nodules and by the supply of metals from oxic seawater on top of the nodules (Raab, 1972; Dymond et al., 1984). The sediments of the PB consist of siliceous to calcareous ooze and mud since this area is located slightly above the CCD (Wiedicke-Hombach and Weber, 1996; Stummeyer and Marchig, 2001).

2.4 Samples and analytical methods

2.4.1 Samples

Seven bulk manganese nodules (AB-type nodules) and one ferromanganese hydrogenetic crust from the CCZ and six bulk nodules (AB-type nodules) from the PB were studied for their bulk chemical and mineralogical composition with inductively coupled plasma optical emission spectrometry (ICP-OES) and powder X-ray diffraction (XRD).
Electron microprobe analyses (EMPA) were performed for detailed high resolution chemical analyses of individual layers within the nodules and crust.

2.4.2 Analytical methods

2.4.2.1 Inductively coupled plasma optical emission spectrometry

The chemical composition of the bulk samples were investigated at Jacobs University, Bremen (JUB), Germany. The samples were crushed in an agate disc mill to a powder size of 50 µm and dried at 110°C for 24h. Afterwards the samples were dissolved with HCl/HNO$_3$/HF in a ratio of 3:1:1 ml. The solution was diluted to 50 g in 0.5 M HNO$_3$ and

17

0.05 M HCl. Major and minor elements (Mn, Fe, Ni, Cu, Co, Al, K, Ca etc.) were analyzed with ICP-OES (Spectro Ciros Vision). Analytical precision and accuracy were checked by analyses of certified standard materials such as BGR Fe-Mn standard FeMn-1 (Kriete, 2012), Mn nodule standard NOD-P-1 (United States Geologic Survey) and JMn-1 (Geological Survey of Japan). For a detailed description of the methodology, accuracy, and precision as well as interference refer to Alexander (2008).

2.4.2.2 Electron microprobe analyses

Chemical composition of individual layers within nodule and crust samples was investigated using Electron microprobe analyses (EMPA; CAMECA SX 100) on polish thick sections (~200 µm thickness of the sample) at 15/20 kV accelerating voltage and 40 nA beam current. The bright layers (Mn rich) were measured with a focused (1 - 5 µm) beam and the darker layers (Fe rich) with a defocused (5 - 20 µm) beam.

The counting times for the analyzed elements were 10 s for Mn, Fe, Ni, Cu, Na, Mg, Al, Si, K, Ca, Ti, P, S, Cl, 40 s for V, 45 s for Pb, 50 s for Co, 90 s for Zn 100 s for Ba, Mo and Sr and 110 s for Ce. Rhodochrosite (Mn), haematite (Fe), cobaltite (Co), synthetic Ni_2Si (Ni), cuprite (Cu), albite (Na), kaersutite (Mg, Al, Si), biotite (K), apatite (Ca, P), rutile (Ti), willemite (Zn), barite (S, Ba), monazite (Ce), molybdenite (Mo), krokoite (Pb), celestine (Sr), vanadium metal (V) and tugtupite (Cl) were used as standards (BGR standards). Furthermore, a PAP matrix correction was done according to Pouchou and Pichoir (1991).

The material of individual layers, especially of the darker material, is sensitive to the beam. The oxides contain high amounts of water within their crystal structure (vernadite ~16 - 25 wt.% (Chukhrov et al., 1979); todorokite and phyllomanganates ~10 - 13 wt.%; (Jones and Milne, 1956; Frondel et al., 1960). Furthermore, scanning electron microscope analyses determine a high porosity of the growth structures. Because of these two facts the analytical sums of EMPA often are well below 100% and we decided to accept analytical sums of 70% for layers of low reflectivity (Fe-vernadite) and 80% for bright layers (todorokite or phyllomanganates). Analyses with total sums below 70% were omitted from further consideration and discussion.

2.4.2.3 Scanning electron microscopy

For detail investigations of the growth structures of individual layers within the nodules, scanning electron microscopy (SEM) analyses were realized using a FEI Quanta 600 FEG SEM. The samples were scanned with a focused electron beam produced by a field emission gun (W-crystal) using a 20 kV acceleration under high vacuum conditions (10 - 9 mbar). The scanning beam has a diameter between 1 and 5 µm and a maximum of 250.000 times magnification.

2.4.2.4 X-ray photoelectron spectroscopy

X-ray photoelectron spectroscopy (XPS) was used to study the outer few nm (<10 nm) of two selected nodules (32KG, 49KG) at the Leibniz Institute of Polymer Research in Dresden, Germany (IPFDD). The two nodules were collected from the surface of a box corer together with the surrounding sediment and the near bottom sea water to ensure their natural position. Small pieces (mm sized) of the outermost layer of the nodules were sampled for analyses. These subsamples were from the current surface side, the "equatorial" rim and the bottom side of the nodules.

The XPS spectra were recorded on an AXIS Ultra photoelectron spectrometer (Kratos Analytical, Manchester, UK). The spectrometer was equipped with a monochromatic Al Kα (h·ν = 1486.6 eV) X-ray source of 300 W at 15 kV. The kinetic energy of photoelectrons was determined with a hemispheric analyzer set to pass energy of 160 eV for wide-scan spectra and 20 eV for high-resolution spectra. The pressure in the analysis chamber was not higher than $3 \cdot 10^{-8}$ mbar. For each sample, an area of ca. 1mm² was analyzed. During all measurements, electrostatic charging of the sample was avoided by means of a low-energy electron source working in combination with a magnetic immersion lens. Data analyses were performed with the CASA XPS software package.

2.4.2.5 X-ray diffractometry

The mineralogy of the bulk nodules and the crust were analyzed with a PANalytical X`Pert PRO MPD Θ-Θ diffractometer (Cu-Kα radiation generated at 40 kV and 30 mA), equipped with a variable divergence slit (20 mm irradiated length), primary and secondary soller, Scientific X´Celerator detector (active length 0.59°), and a sample changer (sample diameter

28 mm). The samples were scanned from 2° to 85° 2Θ with a step size of 0.0167° 2Θ and a measuring time of 10 sec per step.

In order to distinguish between the two 10 Å manganese phases such as todorokite and 10 Å phyllomanganate, the nodules were analyzed twice. In a first step, the samples were analyzed after being dried at 40°C/48h and in a second step after heating treatment (100°C/48h; Uspenskaya et al., 1987).

2.5 Results

2.5.1 Sample description and geochemistry of CCZ nodules

2.5.1.1 Bulk nodules

Seven manganese nodules of different sizes and shapes from different study areas (SA1 - SA6; see Fig. 2.2) were analyzed. Nodules long axis range between 3 and 10 cm. The larger nodules (27KG-1 and 44KG-2) have an ellipsoidal to discoidal shape with a botryoidal and coarse rim called "equatorial" rim (Halbach et al., 1981). This rim probably marks the location of the sediment-water interface. The top side of the large nodules is smooth with a subdued botryoidal surface texture. In contrast, the bottom side (within the peneliquid sediment layer) is very coarse with a botryoidal structure.

All the other studied nodules (11KG-A, 17KG-D, 32KG-5, 49KG-4 and 68KG-C) have a long axis of 3 to 5 cm. They have a discoidal to ellipsoidal shape with smooth upper surfaces and coarse bottom sides. The nodules show a more or less symmetric distribution of growth layers around a nucleus.

Furthermore, one ferromanganese crust sample was analyzed in detail from SA4 as a typical hydrogenetic end member.

In general, there are no significant differences between the major and minor element concentrations within the seven bulk nodule samples (Fig. 2.3, Tables 2.2 and 2.3). Manganese concentrations vary between 28 and 34 wt.% in nodules compared to 21 wt.% in the crust sample. In contrast, Fe shows the maximum concentration of 23 wt.% in the crust and much lower concentrations in the nodules (Table 2.2). Bulk Mn/Fe ratios of the nodules range from 4.3 to 6.1; the ferromanganese crust has a low ratio of 0.9. The Ni+Cu

concentrations of the nodules range from 2.1 wt.% to 2.8 wt.%, whereas the Ni+Cu content of the crust is considerably lower (0.5 wt.%). The Co concentration shows the opposite trend, with highest concentration in the crust (0.3 wt.%) and lower ones in the nodules (0.12 - 0.17 wt.%). The smaller nodules (11KG-A, 32KG-5, 49KG-4) have slightly lower Mn/Fe ratios (4.3 - 5.3) as well as lower Ni+Cu concentrations (2.1 - 2.5 wt.%) compared to the bigger ones (Mn/Fe 5.4 - 6.1; Ni+Cu 2.5 - 2.8 wt.%). At a Mn/Fe ratio of 6.06 the highest Ni+Cu content of 2.80 wt.% can be detected (Table 2.2).
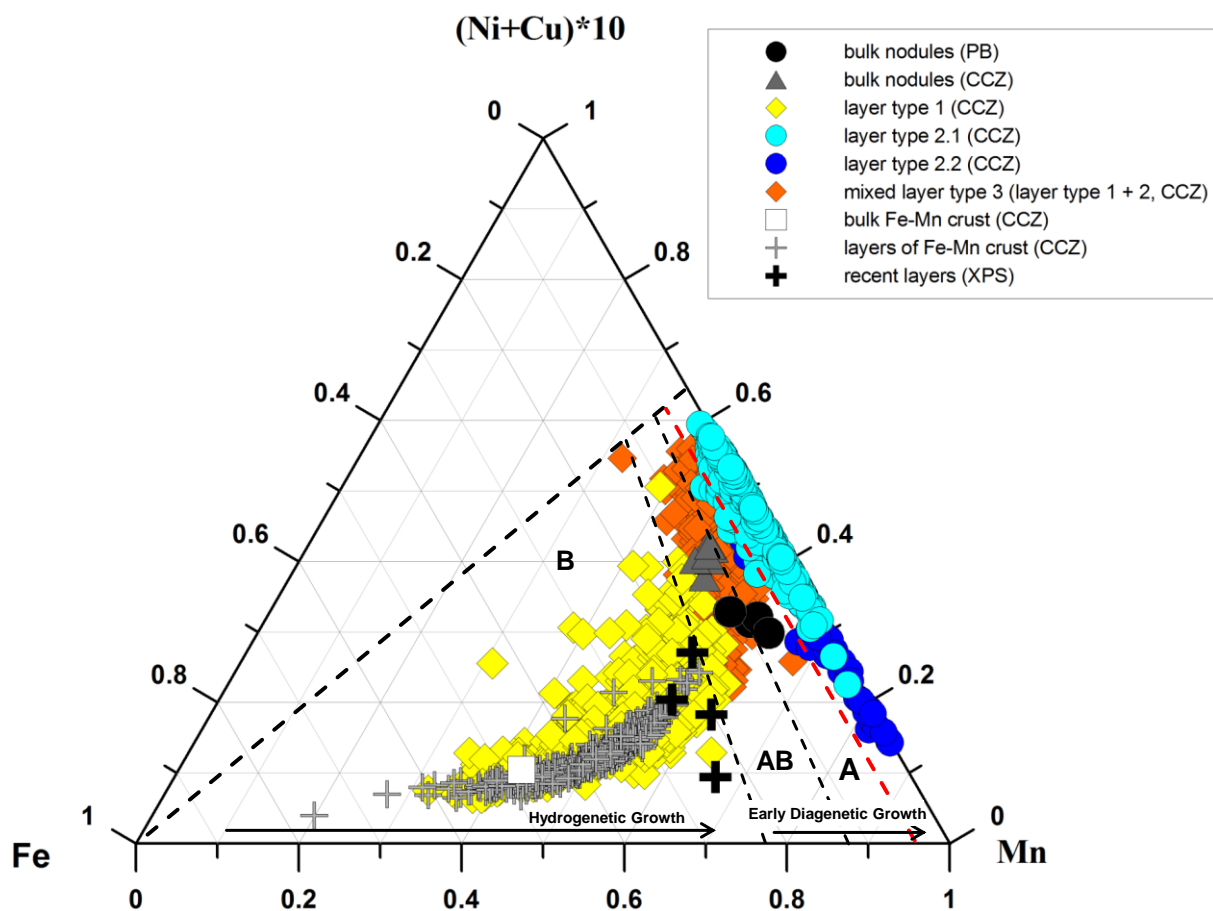
FIGURE 2.3 Three-component diagram of Fe-Mn-(Ni+Cu)*10 according to Bonatti et al. (1972) showing the geochemical relationship between different genetic types of nodules. Dashed black lines border the three nodule type fields A: diagenetic nodules, AB: mixed type nodules and B: hydrogenetic nodules and crusts. Bulk nodule and bulk crust data as well as data of individual growth layers of the same nodules and crust are shown. It is obvious that the individual layers have a much higher scatter than the bulk analyses. Dashed red line border the suboxic-diagenetic field of individual layers (layer type 2). See text for further explanation.

TABLE 2.2 Metal contents, Mn/Fe ratios, and Ni+Cu concentrations of bulk nodules and one ferromanganese crust (37KD-3) from the CCZ and of bulk nodules from the Peru Basin
[*1]SA = study area (Fig.2.2; Table 2.1)

SA[*1] (CCZ)	samples SO205	Mn [wt.%]	Fe [wt.%]	Co [wt.%]	Cu [wt.%]	Ni [wt.%]	Zn [wt.%]	Mn/Fe	Ni+Cu [wt.%]
1	11KG-A	28.1	6.20	0.14	1.16	0.92	0.16	4.53	2.08
2	17KG-D	34.0	6.32	0.17	1.15	1.55	0.17	5.38	2.70
	27KG-1a	29.5	5.16	0.12	1.22	1.33	0.15	5.72	2.55
3	32KG- 4	28.4	6.56	0.14	1.03	1.32	0.15	4.33	2.35
	44KG-2a	33.5	5.53	0.17	1.36	1.44	0.16	6.06	2.80
5	49KG-C	30.3	5.71	0.16	1.26	1.23	0.14	5.31	2.49
6	68KG-C	32.4	5.51	0.17	1.3	1.47	0.17	5.88	2.77
AVERAGE of nodules		30.9	5.86	0.15	1.21	1.32	0.15	5.31	2.53
STD. DEV.		2.42	0.51	0.02	0.11	0.21	0.01	0.66	0.26
MIN		28.1	5.16	0.12	1.03	0.92	0.14	4.33	2.08
MAX		34.0	6.56	0.17	1.36	1.55	0.17	6.06	2.80
4	37KD-3	20.5	23.1	0.31	0.18	0.34	0.06	0.89	0.51
nodules from the Peru Basin		Mn [wt.%]	Fe [wt.%]	Co [wt.%]	Cu [wt.%]	Ni [wt.%]	Zn [wt.%]	Mn/Fe	Ni+Cu [wt.%]
SO79	97KG/1-1	37.8	5.00	0.03	0.62	1.37	0.27	7.55	1.99
	97KG/1-2	37.0	5.53	0.03	0.58	1.37	0.23	6.69	1.94
	176KL-3	38.7	4.51	0.03	0.51	1.33	0.21	8.58	1.84
SO106	204KG	36.9	4.63	0.03	0.65	1.31	0.23	7.97	1.96
	237KG-2	35.3	6.7	0.04	0.59	1.47	0.25	5.27	2.06
	237KG-1	34.9	6.5	0.04	0.57	1.46	0.24	5.37	2.03
AVERAGE of PB nodules		36.8	5.48	0.04	0.59	1.38	0.24	6.91	1.97
STD. DEV.		1.44	0.94	0.01	0.05	0.07	0.02	1.37	0.08
MIN		34.9	4.51	0.03	0.51	1.31	0.21	5.27	1.84
MAX		38.7	6.7	0.04	0.65	1.47	0.27	8.58	2.06

TABLE 2.3 Element content of bulk nodules and one ferromanganese crust (37KD-3) from the CCZ and of bulk nodules from the Peru Basin
[*1]SA = study area (Fig. 2.2; Table 2.1)

SA[*1] (CCZ)	Samples SO205	Na [wt.%]	Al [wt.%]	Ca [wt.%]	K [wt.%]	Mg [wt.%]	Ti [wt.%]	P [wt.%]	Mo [ppm]	Ba [ppm]	Li [ppm]	Sr [ppm]	V [ppm]
1	11KG-A	2.07	2.43	1.53	1.34	1.69	0.16	0.14	649	8660	189	709	540
2	17KG-D	2.25	2.05	1.66	0.88	1.94	0.27	0.14	631	2930	152	703	589
3	27KG-1a	2.02	2.24	1.58	0.88	1.72	0.23	0.14	534	4240	141	617	533
	32KG-4	2.15	2.74	1.51	1.15	2.04	0.29	0.15	605	2910	143	663	595
5	44KG-2a	2.09	2.33	1.69	0.95	1.87	0.27	0.15	687	4820	143	723	609
	49KG-C	1.98	2.36	1.58	0.91	1.85	0.25	0.14	575	6850	178	748	566
6	68KG-C	2.27	2.45	1.60	0.98	1.92	0.27	0.15	719	4720	155	683	626
AVERAGE		2.12	2.37	1.59	1.01	1.86	0.25	0.15	629	5019	157	692	580
STD. DEV.		0.11	0.21	0.06	0.17	0.12	0.04	0.01	64.0	2088	19	4.0	35.0
MIN		1.98	2.05	1.51	0.88	1.69	0.16	0.14	534	2910	141	617	533
MAX		2.27	2.74	1.69	1.34	2.04	0.29	0.15	719	8660	189	748	626
4	37KD-3	1.45	0.97	2.01	0.44	1.09	0.80	0.35	526	1810	2.52	808	707
Nodules from the Peru Basin		Na [wt.%]	Al [wt.%]	Ca [wt.%]	K [wt.%]	Mg [wt.%]	Ti [wt.%]	P [wt.%]	Mo [ppm]	Ba [ppm]	Li [ppm]	Sr [ppm]	V [ppm]
SO79	97KG-1	1.38	1.33	1.79	0.36	1.62	0.14	-	740	2203	-	662	439
	97KG-2	1.54	1.37	1.73	0.35	1.67	0.15	-	667	2247	-	654	412
	176KL-3	3.38	1.33	1.49	0.72	1.49	0.13	-	638	1240	816	535	446
SO106	204KG	1.24	1.53	1.56	0.42	1.78	0.14	-	577	2551	-	617	407
	237KG-2	2.66	1.43	1.98	0.73	1.67	0.15	-	753	1850	346	774	568
	237KG-1	2.57	1.4	1.94	0.7	1.67	0.15	-	751	1840	341	763	573
AVERAGE of PB nodules		2.13	1.4	1.75	0.55	1.65	0.14	-	688	1989	501	668	474
STD. DEV.		0.87	0.08	0.20	0.19	0.09	0.01	-	72.0	454	273	90	76
MIN		1.24	1.33	1.49	0.35	1.49	0.13	-	577	1240	341	535	407
MAX		3.38	1.53	1.98	0.73	1.78	0.15	-	753	2551	816	774	573

2.5.1.2 Individual micro-layers

Individual layers were analyzed to better define accretion processes under different environmental conditions as well as to determine diagenetic changes within nodules. Heterogeneous and complex textures characterize the internal growth structures of manganese nodules. Electron microprobe analyses identified three types of concentrically and irregularly banded nm to μm thick layers of Mn –oxide / Fe –oxyhydroxide material in all studied nodules (Figs. 2.4A - 2.4F). These layers vary in density, continuity, reflectivity and chemistry (Table 2.4).

Layer type 1: low Mn/Fe ratios

Layers of type 1 have a low reflectivity. These layers are dense, some with a columnar growth pattern typical for ferromanganese crusts (Figs. 2.4A and 2.4B). The Mn/Fe ratios of layer type 1 range between 0.53 and 4.24 (Table 2.4). The concentrations of Ni+Cu range from 0.16 to 2.55 wt.% compared to 0.11 - 1.34 wt.% in the crust. Co concentrations are between 0.06 and 0.74 wt.% and 0.09 to 0.86 wt.% in the crust (Table 2.4). The composition of type 1 layers in nodules principally follows the same trend as the individual crust layers but with a slightly larger variability as it is illustrated in Figure 2.3.

The thickness of type 1 layers ranges from 5 μm to ~500 μm and they occur in all nodules in varying amounts. These layers occurs not only on the current top side of the nodules which is in contact with the recent near-bottom water but they also form a few hundreds of nanometer thin layers in the part of the nodule that was buried in the sediment, i.e. in contact with the recent oxic pore water (Fig. 2.4B). XPS measurements of the outermost <10 nm of two nodules (32KG and 49KG: top, rim and bottom side) show similar chemical composition on all sides. The Mn/Fe ratios range from 1.4 - 3.1 and the Co/Mn ratios are between 0.01 - 0.04, respectively (Table 2.5). These results indicate that the outermost nm thick layer is similar to layers of type 1 and ferromanganese crusts (Tables 2.4, Fig. 2.3). Within the nodules, type 1 layers occur at irregular intervals alternating with other structures (layer type 2; Figs. 2.4A - B). The transitions can be sharp or smooth and seamless or chaotic. Furthermore, within type 1 layers small spots or veins of high reflectivity can be distinguished (Fig. 2.4A) indicating higher Mn concentrations with increased Ni+Cu contents (similar to material of layer type 2, see description of layer type 2). Layer type 1 can have higher Mn/Fe ratios (>3) and higher Ni+Cu contents which represent only mixed analyses of the bright inclusions with layer type 1 (see also mixed layer type 3, Table 2.4). Furthermore, layer type 1 material fills pore space in porous parts of the nodules. The chemical composition of the pore space fillings is generally comparable to that of the ferromanganese crust.
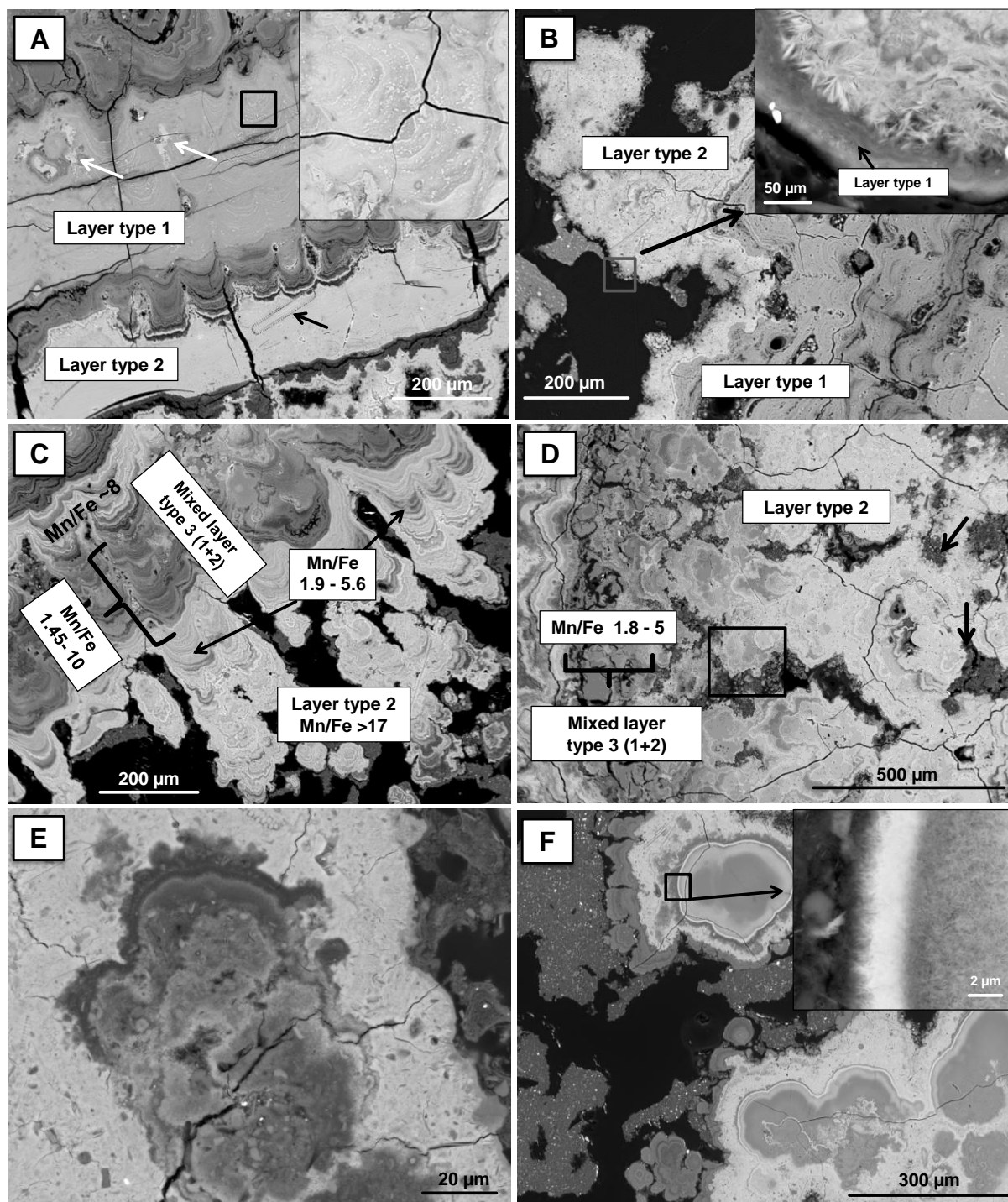
FIGURE 2.4 A: Back scatter electron (BSE) image of typical layer types 1 of nodules from the CCZ. The white arrows mark small spots/veins of high reflectivity within layer type 1. Inserted is an enlarged image of those nm thick veins and spots within layer type 1. Below layer type 1 a dense layer of type 2 can be recognized with inclusion of a microfossil (black arrow) which is completely replaced by Mn oxides. **B:** Typical growth structure of the bottom sides of the nodules, the outermost dendritic structure (layer type 2) is surrounded by layer of type 1 (insert magnification). Below layer type 2, layer type 1 occurs with a columnar growth pattern. **C:** Typical areas of mixed layer type 3. Nanometer thin layers of high and low reflectivity alternate with each other followed by type 2 layers. Single type 3 layers cannot be resolved by EMP analysis. Therefore, these layers are interpreted as a mixture of type 1 and 2 layers. **D:** Dendritic growth structure of layer type 2 which slight changes into areas of low reflectivity. Mn/Fe ratios are very variable and the total sums are in most cases <70% within areas of low reflectivity. The arrows mark darker areas within layer type 2, which are porous and include microfossil fragments and sediment. **E:** Enlargement of dark areas within layer type 2 (rectangle in Fig. 2.4D; SED-image). Sediment particels may be intergrown. **F:** Dendritic growth structures (layer type 2) with typical dark areas. The EMPA total values are partly <70%. Insert: SEM enlargement of an area of high and low reflectivity.

TABLE 2.4 Average element content of individual layers of type 1, 2 and 3 of nodules and a ferromanganese crust from the CCZ (EMPA data; wt.%)

individual layer	layer description		Mn	Fe	Co	Ni	Cu	Zn	Mn/Fe	Ni+Cu	Na	Al	Ca	Mg	K	Si	Ti	Mo	Ba	Ce	Ni/Mn	Cu/Mn	Co/Mn
analyses of crust layers		AVERAGE (n*1=453)	22.8	17.2	0.40	0.44	0.14	0.09	1.38	0.58	1.56	0.52	2.24	1.02	0.38	3.16	0.89	0.04	0.20	0.14	0.019	0.006	0.0170
		STD. DEV.	4.55	2.90	0.15	0.18	0.03	0.02	0.41	0.20	0.43	0.66	0.35	0.18	0.14	2.30	0.17	0.02	0.03	0.04	0.005	0.001	0.0050
		MEDIAN	23.3	17.3	0.37	0.41	0.14	0.09	1.36	0.55	1.54	0.36	2.26	1.04	0.35	2.55	0.87	0.05	0.20	0.13	0.018	0.006	0.0170
		MIN	5.88	5.12	0.09	0.07	b.d.l*2	0.03	0.26	0.11	0.50	0.17	0.72	0.23	0.17	1.15	0.23	b.d.l*2	0.09	0.05	0.010	0.004	0.0080
		MAX	33.1	29.0	0.86	1.15	0.25	0.21	3.05	1.34	2.83	7.67	4.09	1.74	1.72	22.7	1.65	0.09	0.32	0.47	0.037	0.014	0.0350
layer type 1	dense layer of low reflectivity	AVERAGE (n*1=661)	23.1	14.2	0.30	0.46	0.34	0.09	1.80	0.81	1.79	1.06	2.14	1.01	0.46	4.65	0.80	0.04	0.26	0.10	0.020	0.015	0.0135
		STD.DEV.	5.05	3.80	0.12	0.24	0.16	0.03	0.74	0.37	0.70	0.52	0.43	0.29	0.18	1.90	0.29	0.03	0.11	0.04	0.008	0.006	0.0055
		MEDIAN	23.0	14.4	0.27	0.42	0.33	0.08	1.64	0.74	1.73	0.96	2.17	0.95	0.43	4.45	0.75	0.04	0.24	0.09	0.018	0.014	0.0129
		MIN	6.89	3.71	0.06	0.07	0.05	0.03	0.53	0.16	0.22	0.25	0.48	0.27	0.16	1.80	0.07	b.d.l*2	0.08	b.d.l*2	0.007	0.003	0.0035
		MAX	37.0	23.0	0.74	1.55	1.12	0.24	4.24	2.55	4.43	4.34	3.65	2.96	2.26	28.7	1.74	0.15	1.43	0.26	0.065	0.064	0.0289
layer type 2.1	dense and dendritic growth structures of high reflectivity, high Ni+Cu	AVERAGE (n*1=479)	44.0	0.81	0.08	1.97	1.92	0.26	95.9	3.89	2.31	1.18	1.41	2.25	0.96	1.71	0.07	0.06	0.33	0.01	0.046	0.044	0.0022
		STD.DEV.	3.89	0.63	0.08	0.64	0.40	0.12	91.3	0.85	0.71	0.63	0.35	0.59	0.27	1.13	0.06	0.02	0.23	0.01	0.017	0.010	0.0018
		MEDIAN	44.6	0.61	0.06	1.95	1.92	0.22	71.3	3.87	2.13	1.09	1.35	2.16	0.95	1.59	0.05	0.06	0.28	0.01	0.045	0.044	0.0016
		MIN	22.8	0.06	b.d.l*2	0.66	0.80	0.10	8.92	1.46	0.66	0.05	0.80	1.09	0.29	0.03	0.00	0.00	0.05	b.d.l*2	0.013	0.016	0.0002
		MAX	50.9	3.99	0.52	3.92	3.04	0.76	826	6.51	5.39	4.00	2.87	3.87	2.69	11.3	0.55	0.17	1.66	0.06	0.092	0.069	0.0130
layer type 2.2	dense and dendritic growth structures of high reflectivity, low Ni+Cu	AVERAGE (n*1=50)	46.5	0.86	0.06	0.84	0.97	0.49	115	1.81	3.11	0.62	1.88	1.66	0.98	1.87	0.06	0.09	0.23	0.01	0.019	0.021	0.0016
		STD. DEV.	2.75	0.73	0.07	0.37	0.37	0.18	131	0.65	0.56	0.32	0.38	0.37	0.20	1.20	0.05	0.03	0.28	0.01	0.009	0.009	0.0016
		MEDIAN	46.8	0.65	0.04	0.77	0.92	0.46	75.8	1.79	3.23	0.64	1.91	1.59	0.93	1.77	0.05	0.09	0.13	b.d.l*2	0.017	0.020	0.0010
		MIN	39.9	0.07	b.d.l*2	0.27	0.41	0.17	11.9	0.84	1.46	0.02	1.14	1.19	0.71	0.05	0.02	0.04	0.06	b.d.l*2	0.005	0.008	0.0003
		MAX	50.5	3.38	0.34	1.89	1.99	0.88	667	3.32	3.94	1.53	2.46	2.96	1.50	6.73	0.28	0.16	1.56	0.05	0.047	0.044	0.0083
mixed layer type 3	material of low reflectivity, partly inhomogeneous	AVERAGE (n*1=226)	32.0	5.40	0.24	1.51	1.14	0.15	6.54	2.65	1.85	1.56	1.55	2.01	0.71	3.77	0.36	0.07	0.34	0.04	0.048	0.036	0.0077
		STD.DEV.	4.58	1.83	0.14	0.52	0.38	0.06	2.14	0.77	0.78	0.81	0.50	0.62	0.28	2.42	0.24	0.03	0.22	0.03	0.017	0.012	0.0042
		MEDIAN	32.5	4.90	0.22	1.47	1.15	0.14	6.38	2.65	1.75	1.40	1.45	1.97	0.65	3.01	0.28	0.07	0.28	0.04	0.047	0.035	0.0067
		MIN	16.8	2.28	0.02	0.54	0.40	0.06	3.30	1.05	0.37	0.42	0.65	0.73	0.24	0.72	0.03	b.d.l*2	0.10	b.d.l*2	0.013	0.012	0.0006
		MAX	42.1	10.3	0.77	2.74	2.25	0.43	10.9	4.61	5.05	5.17	3.07	4.56	2.35	16.4	1.40	0.23	2.43	0.30	0.097	0.071	0.0231

*1 n = number of analyses; *2 b.d.l = below detection limit

TABLE 2.5 Ratios of different elements (Mn/Fe, Ni/Mn, Cu/Mn, Co/Mn) of the outermost <10 nm thick recent layers of nodule 32KG and 49KG from the CCZ (XPS data)

sample SO205	sample description	Mn/Fe	Ni/Mn	Cu/Mn	Co/Mn
	surface	2.76	0.014	-	0.014
32KG	rim	1.38	-	-	0.027
	bottom side	2.25	-	-	-
	surface	2.33	0.024	0.012	0.036
49KG	rim	3.03	0.035	0.014	0.016
	bottom side	3.06	0.021	0.009	0.035
	AVERAGE	2.47	0.024	0.012	0.026

Layer type 2: high Mn/Fe ratios

Layers of type 2 occur in two different shapes in nodules from the CCZ. They can form dendritic porous growth structures of high reflectivity (Figs. 2.4B - F). This layer type is dominant in the nodules. The larger the nodules are, the thicker the dendritic zones are, which could reach a thickness of up to 10 mm. The dendritic growth structures form cauliflower or irregularly shaped structures (Figs. 2.4B - F) which are responsible for the botryoidal surface and the high porosity of the nodules (26 - 61; Chapter IV). This kind of layers can be observed in all parts of the nodules.

Within the dendritic layers irregular porous dark spots occur containing inclusions of microfossil fragments and sediment components (feldspar, quartz; Figs. 2.4E - F). These dark spots show variable Mn/Fe ratios between 1 and 30. Also the Si content is higher (<12 wt.%) than within the surrounding dendritic growth structure. The total analytical sums of EMPA are in most cases below 70% and were exclude from the interpretation.

The second type of growth structures of layer type 2 are dense and massive layers (0.01 to 0.2 mm thick) of high reflectivity (Fig. 2.4A). This kind of layers is less common and occurs as lamina within layer type 1 or it alternates with type 1 layers and the dendritic growth structures. The boundary between the different layers is sharp. These dense layers of type 2 can occur in different parts of nodules.

In general, layers of type 2 are build up of <5 μm long needles of Mn oxyhydroxides that show a radiating growth (Fig. 2.4B). Furthermore, they contain microfossils which are completely replaced by Mn (Fig. 2.4A; indicating by black arrow).

Chemically this layer type contains high concentrations of Mn (23 - 51 wt.%) relative to Fe (0.06 - 3.99 wt.%). The Mn/Fe ratios range from about 9 to 826. According to the Ni+Cu content, layer type 2 can be divided into two sub-types (Table 2.4; Fig. 2.5). Most of the type 2 layers have average Ni+Cu contents of 3.89 ± 0.85 (layer type 2.1; Fig. 2.5). However, there are a few layers with an average Ni+Cu content of 1.81 ± 0.65 wt.% (layer type 2.2; Table 2.4; Fig. 2.5).
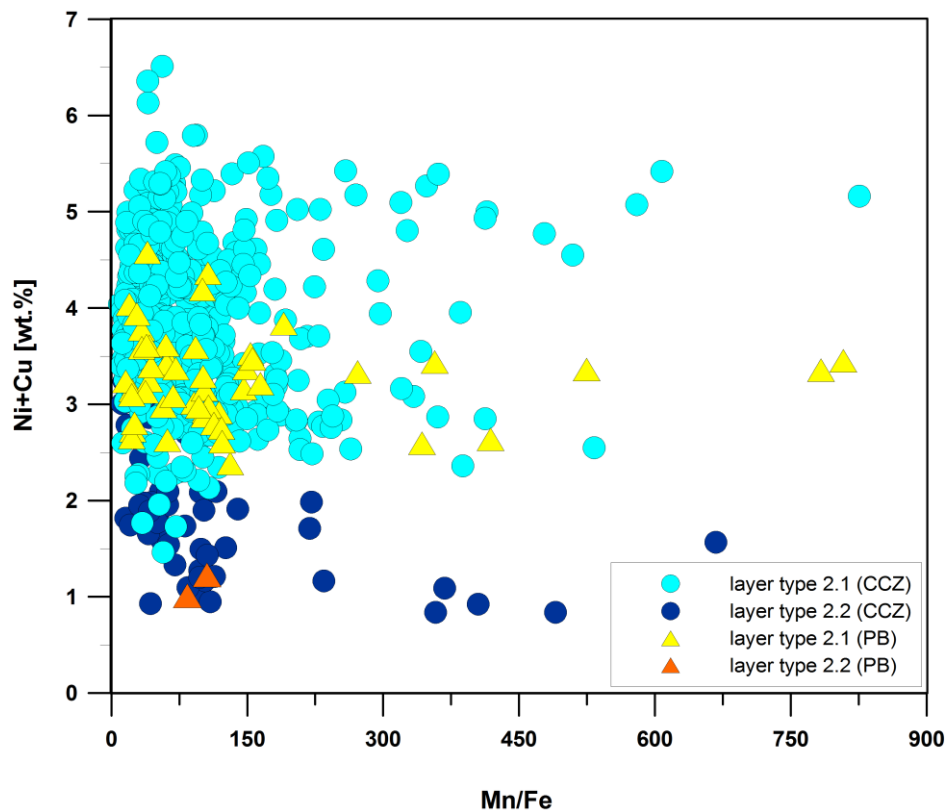
FIGURE 2.5 Ni+Cu vs. Mn/Fe ratios of type 2 layers of nodules from the CCZ compared with those of Peru Basin (PB) nodules. Type 2 layers from both nodule areas are very similar. These structures show high and variable Mn-Fe fractionation and variable Ni+Cu contents. The dense layers with low Ni+Cu of nodules from both localities (type 2.2) are subordinate compared to the other layer type (2.1).

Mixed layer type 3: Mixtures of layers of type 1 with type 2

Additionally to the two distinct layer types, inhomogeneous zones of low reflectivity can be found. Their Mn/Fe ratio is between 3 and 11, the Ni+Cu contents range from 1 to 4.6 wt.% and Co amounts are between 0.02 and 0.8 wt.% (Fig. 2.3, Table 2.4). Zones of this type occur in different characteristics: (1) They can form columnar growth structures of low reflectivity (similar to layer type 1) with a certain chemical variability, especially with respect to the Mn/Fe ratios (e.g., 1.9 - 5.6; Fig. 2.4C). These layers occur at the transition from layer types 1 to 2. In the majority of cases this columnar growth structures consist of very small-sized veins (<1 µm) of material with high reflectivity which are too small to be analyzed with EMP (measuring spot 5 - 20 µm). Therefore, most of the EMP data of this type may be mixtures of layer type 1 with type 2 which results in higher Mn/Fe ratios and Ni+Cu contents (Fig. 2.3). (2) Layer type 3 can also form at the transition from dendritic growth structures to other layers with variable Mn/Fe ratios (1.8 - 5; Fig. 2.4D) but the total analytical sums of EMP analyses often are below 70% indicating either high water content or high porosity or both. In most cases such EMP analyses were removed from further discussion.

2.5.2 Principal component analysis

A principal component analysis (PCA) with varimax rotation was performed with all individual layers of all analyzed CCZ nodules using the following elements: Mn, Fe, Ni, Cu, Co, Zn, Ti, Al, Ca, Si, Ba, and Mo. We did not use Na and K because of a possible contamination with seawater salt (the nodules were not washed with fresh water prior to analysis).

The PCA revealed five factors which account for 48%, 13%, 8%, 6% and 4% of the variance, respectively summing up to 80% of the total data variance (Table 2.6).

The first factor has high loadings for Mn, Ni, Cu, Zn, and Mg representing diagenetic processes. The second factor is rich in Fe, Co, Ti and Ca but show also high negative loadings of Cu and Mn indicating oxic-hydrogenetic phases. The third factor is rich in Al and Si and stands for the siliceous biogenic sediment component. Factors four and five load high on Mo and Ba, respectively. Barite occurs in the nodules in clusters or nests, which were observed under the microprobe explaining the individual Ba factor. The existence of a separate Mo factor indicates that Mo may form a mineral phase on its own and may not or not completely be bound to Mn or Fe oxides.

The remaining 20% of the data variability may be assigned to detritus minerals such as feldspar (Na), clay minerals and other phyllosilicates which could be indentify by XRD and EMPA.

TABLE 2.6 Principal component analysis (PCA) of individual layers of CCZ nodules (number of analyses = 1376) with varimax rotation. Five factors were calculated with different element associations

Elements	Factor 1	Factor 2	Factor 3	Factor 4	Factor 5	Communality
Mg	0.86	-0.29	0.13	0.02	0.16	0.86
Ni	0.84	-0.32	0.04	0.17	-0.06	0.84
Cu	0.72	-0.54	-0.10	0.16	0.07	0.85
Mn	0.58	-0.55	-0.38	0.29	0.12	0.88
Ca	-0.49	0.41	-0.29	0.09	-0.33	0.60
Co	-0.22	0.80	0.01	-0.09	0.04	0.70
Ti	-0.43	0.71	0.07	-0.07	-0.05	0.70
Fe	-0.60	0.68	0.04	-0.27	-0.14	0.92
Zn	0.24	-0.56	-0.33	0.22	-0.22	0.57
Al	0.32	0.01	0.88	0.03	-0.01	0.88
Si	-0.46	0.24	0.65	-0.21	-0.05	0.74
Mo	0.13	-0.19	-0.07	0.94	0.02	0.95
Ba	0.10	0.04	-0.04	0.03	0.93	0.88
Variance [%]	48.36	13.39	8.04	5.97	3.99	Σ79.76

2.5.3 Peru Basin nodules

Nodules from the Peru Basin (PB) are botryoidal and rough on all sides (Fig. 2.6) which are in marked contrast to CCZ nodules. Furthermore, bulk PB nodules show slightly higher Mn/Fe ratios (5.3 - 8.6) compared to bulk nodules from the CCZ (Table 2.2) which is caused by slightly higher Mn concentrations (36.8 ± 1.4 wt.%). The Ni content of PB nodules (1.38 ± 0.07 wt.%) is similar to CCZ nodules (1.32 ± 0.21 wt.%) but the Cu content is significantly lower in PB nodules (0.59 ± 0.05 wt.%) compared to 1.21 ± 0.11 wt.% of CCZ nodules (Fig. 2.7). Other significant differences in the content of main and minor elements are summarized in Tables 2.2 and 2.3.
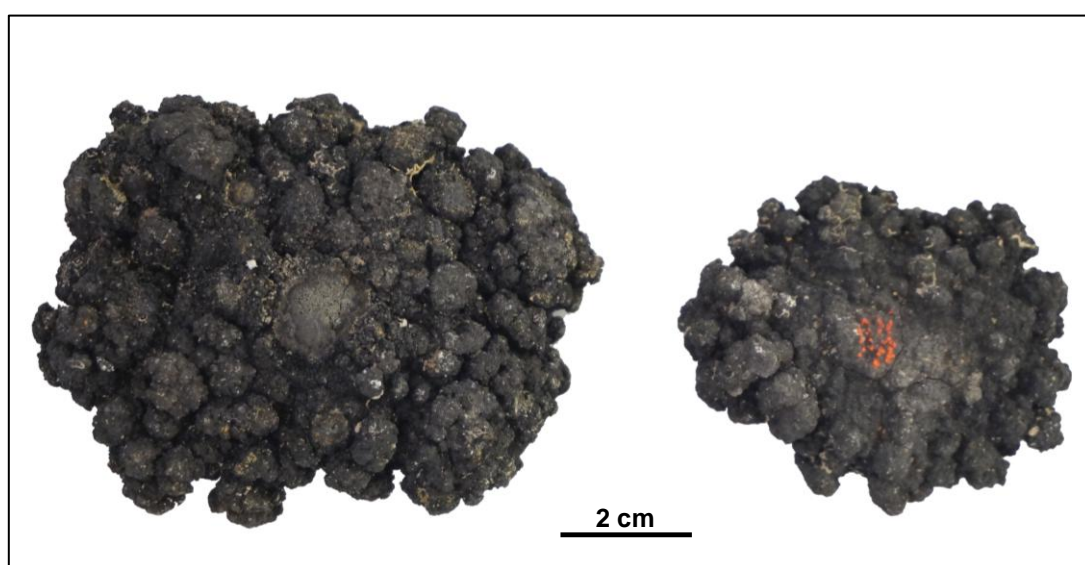
FIGURE 2.6 Two Peru Basin nodules (SO79) with a botryoidal rough growth structure on all sides the nodules. The red dot marks the surface of the nodule, which was in contact with the near-bottom water.
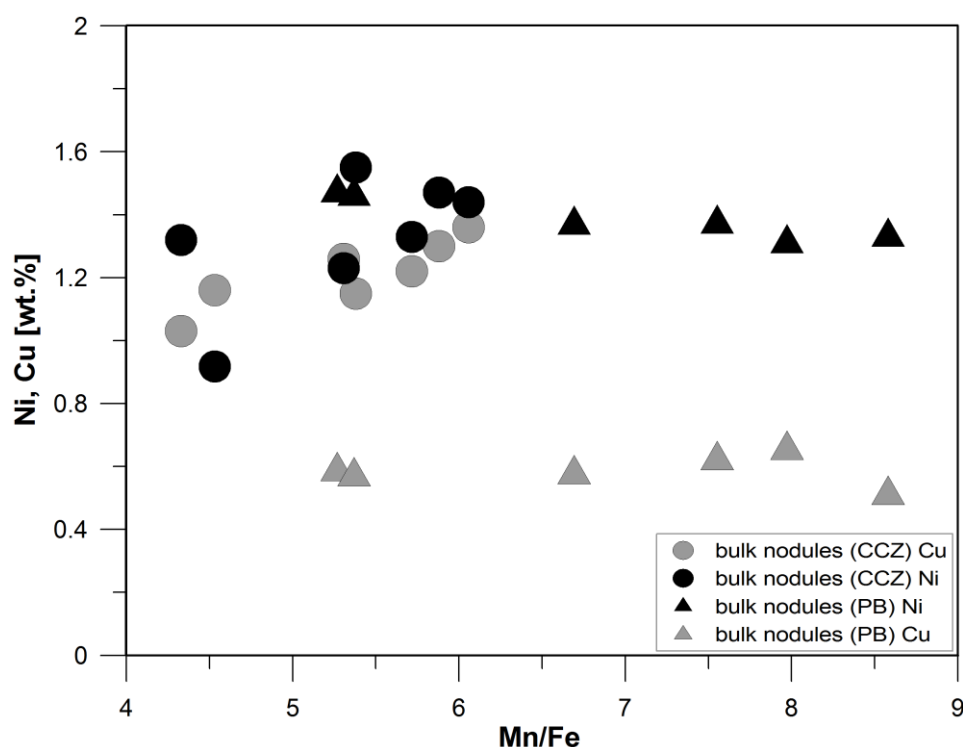
FIGURE 2.7 Mn/Fe vs. Ni and Cu contents of bulk nodules from the CCZ and the PB. Bulk nodules from the PB show slightly higher Mn/Fe ratios. The Ni concentration of both areas is similar whereas Cu is distinctly higher in nodules from the CCZ compared to the nodules from the PB.

Individual layers within the PB nodules reveal two different growth structures (layer type 1 and layer type 2, Fig. 2.8), which are similar to individual layers of nodules from the CCZ. The chemical characteristics of these layers are summarized in Figure 2.5 and Table 2.7.
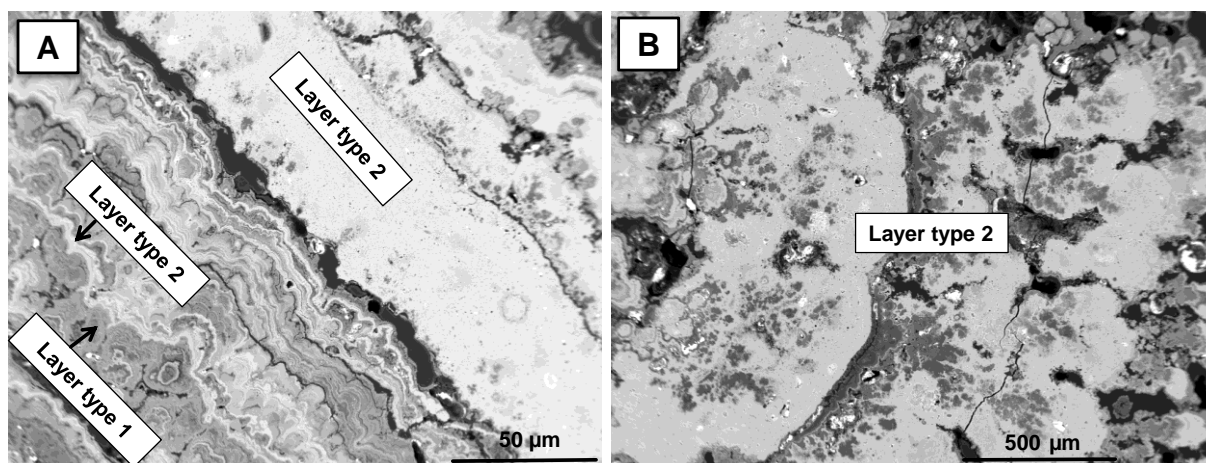
FIGURE 2.8 A-B: Back scatter electron (BSE) images of two characteristic layer types of nodules from the Peru Basin. Layer type 1 and 2 are similar to those of nodules from the CCZ.

TABLE 2.7 Average content of major and minor elements of individual layers of type 1 and 2 of nodule from the Peru Basin (EMPA data; wt.%)

individual layer of PB nodules	layer description		Mn	Fe	Co	Ni	Cu	Zn	Mn/Fe	Ni+Cu	Na	Al	Ca	Mg	K	Si	Ti	Mo	Ba	Ce	Ni/Mn	Cu/Mn	Co/Mn
layer type 1	dense layer of low reflectivity	AVERAGE (n*1=5)	23.3	13.6	0.15	0.40	0.22	0.15	1.81	0.61	0.98	0.52	1.83	0.86	0.22	2.96	0.40	0.06	0.37	0.03	0.017	0.009	0.0064
		STD. DEV.	4.27	2.40	0.06	0.15	0.06	0.02	0.63	0.21	0.33	0.19	0.30	0.30	0.08	0.89	0.05	0.02	0.06	0.01	0.007	0.003	0.0025
		MEDIAN	24.1	13.5	0.13	0.40	0.20	0.14	1.68	0.60	0.99	0.55	1.94	0.67	0.20	2.93	0.43	0.06	0.38	0.03	0.014	0.008	0.0076
		MIN	17.4	10.4	0.06	0.17	0.14	0.12	1.03	0.31	0.56	0.28	1.42	0.61	0.16	1.65	0.31	0.03	0.29	0.01	0.010	0.007	0.0023
		MAX	28.4	17.0	0.20	0.56	0.30	0.17	2.74	0.86	1.31	0.76	2.10	1.28	0.36	4.13	0.44	0.08	0.46	0.04	0.027	0.014	0.0083
layer type 2.1	dense and dendritic growth structures of high reflectivity, high Ni+Cu	AVERAGE (n*1=51)	45.7	0.76	0.03	1.90	1.37	0.39	138	3.27	1.47	1.00	1.17	2.88	0.69	0.60	0.04	0.05	0.29	0.01	0.042	0.030	0.0006
		STD. DEV.	2.56	0.63	0.01	0.44	0.15	0.08	170	0.47	0.29	0.55	0.19	0.46	0.17	0.59	0.08	0.01	0.07	0.01	0.010	0.004	0.0003
		MEDIAN	46.1	0.49	0.02	1.81	1.37	0.37	96.5	3.25	1.45	0.93	1.15	2.89	0.67	0.47	0.02	0.05	0.28	b.d.l*2	0.040	0.030	0.0006
		MIN	37.9	0.06	0.02	0.99	1.08	0.22	15.9	2.38	0.88	0.39	0.81	2.19	0.41	0.04	0.00	0.00	0.13	b.d.l*2	0.021	0.024	0.0003
		MAX	49.6	2.71	0.05	3.17	1.68	0.55	808	4.58	2.07	3.46	2.14	4.23	1.08	3.70	0.57	0.07	0.54	0.02	0.070	0.040	0.0012
layer type 2.2	dense growth structure of high reflectivity, low Ni+Cu	AVERAGE (n*1=2)	48.6	0.52	b.d.l*2	0.50	0.62	0.37	94.6	1.12	0.59	0.35	0.75	3.56	1.26	0.39	0.01	0.06	0.32	b.d.l*2	0.010	0.013	-
		STD. DEV.	0.16	0.09	b.d.l*2	0.01	0.16	0.03	15.2	0.15	0.17	0.14	0.12	0.02	0.13	0.02	0.01	0.00	0.01	b.d.l*2	0.000	0.003	-
		MIN	48.5	0.46	b.d.l*2	0.49	0.50	0.35	83.9	1.01	0.46	0.25	0.66	3.55	1.17	0.37	b.d.l*2	0.06	0.31	b.d.l*2	0.010	0.010	-
		MAX	48.8	0.58	b.d.l*2	0.51	0.73	0.39	105	1.23	0.71	0.45	0.84	3.58	1.36	0.40	0.01	0.07	0.33	b.d.l*2	0.010	0.015	-

*1n = number of analyses; *2b.d.l = below detection limit

2.5.4 Mineralogy

2.5.4.1 Nodules from the CCZ

The diffraction patterns of all analyzed nodules before heating (Fig. 2.9A) show broad and intensive peaks between 9.70 Å and 9.84 Å (001) and a smaller peak between 7.13 Å and 7.23 Å (001) as well as different intensities of the (002) peaks at around 4.81 and 4.92 Å. Furthermore, two asymmetrical $hk0$ reflections (or hk-bands) in the high-angle region of all samples show the same position and intensity at ~2.45Å (100) and ~1.42 Å (110). The calculated d_{100}/d_{110} ratio of every nodule varies between 1.71 and 1.73 (close to $\sqrt{3}$) indicating that all samples may have hexagonal symmetry (Bodeï et al., 2007; Drits et al., 2007; Peacock et al., 2007a).

The XRD patterns after heating at 100°C for 48 hours reveal significant differences in the low angle region, especially around ~9 and ~7 Å (Fig. 2.9B). The intensive, broad ~9 Å (9.02 - 9.44 Å) peak decreased or almost disappeared and the ~7 Å (7.12 - 7.28 Å) peak increased. The location of the $hk0$ diffraction peaks at ~2.45 Å (100) and at ~1.42 Å (110) remained unchanged.

Additionally, quartz (Qz) and minor amounts of feldspar, barite and phillipsite (Ph) are present in all samples.
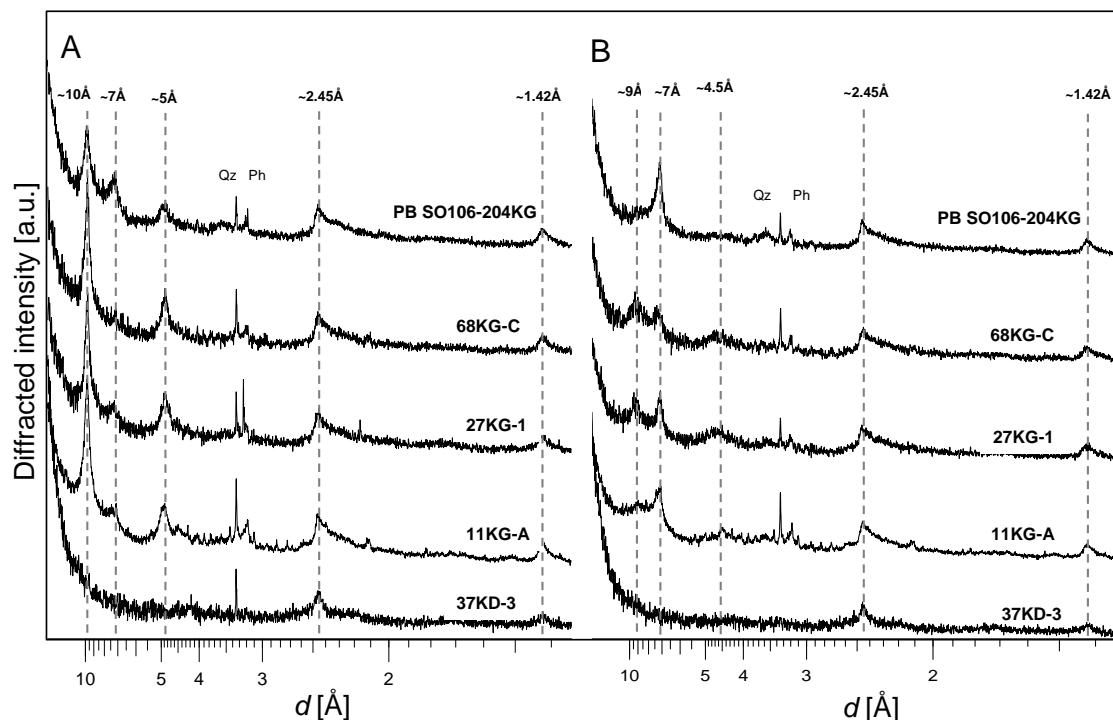
FIGURE 2.9 Comparison of XRD patterns of three typical manganese nodules and one ferromanganese crust (37KG-3) from the CCZ with one typical nodule from the PB. **A:** XRD-pattern before heating (40°C/48h). Broad peaks at ≈10 Å and ≈5 Å are characteristic for 10 Å Mn-phases (todorokite/10 Å phyllomanganate). The peaks around ≈7 Å are corresponding to 7 Å phyllomanganate. XRD-pattern of the crust shows only two *hk*0 reflections at ~2.45 Å and ~1.42 Å which are typical for Fe-rich vernadite. **B:** XRD-pattern after heating treatment (100°C/48h). Broad peaks around ≈9 and ≈4.5 Å which are still present (but with lower intensity) after heating are characteristic for a stable 10 Å Mn –phase. Obviously this phase is present in all analyzed nodules of the CCZ except sample 11KG-A. Increasing peaks at ~7 is indicative for an unstable 10 Å –manganese phase which collapses upon heating to 100°C. This Mn –phase is the major Mn mineral of PB nodules. A stable 10 Å manganate could not be detected in the PB samples. The crust shows no differences after heating (*hk*0 reflections: ~2.45 Å and ~1.42 Å).

2.5.4.2 Nodules from the Peru Basin

All XRD diffractograms of bulk nodules from the PB generally display broad peaks between 9.79 - 9.88 Å (001) and 4.88 - 4.92 Å (002) as well as between 7.18 - 7.26 Å (001) (Fig. 2.9A). After heating (100°C/48h) the reflection peaks around 10 Å almost completely collapsed whereas the ≈7 Å reflections clearly shows increased intensity (Fig. 2.9B). This is in contrast to most of the CCZ nodules which still displayed reflection peaks at ≈10 Å after heating (100°C/48h; samples (Fig. 2.9B). The location of the *hk*0 diffraction peaks at ~2.45 Å (100) and at ~1.42 Å (110) remained unchanged before and after heating the samples.

2.6 Discussion

2.6.1 Bulk nodules vs. individual layers

The chemical compositions, especially the Mn/Fe ratios and Ni+Cu concentrations, of bulk nodules from the CCZ are fairly uniform (Fig. 2.3; Tables 2.2 and 2.3). This result is further confirmed when taking more than 300 bulk nodule analyses from the German license area into account, where the coefficient of variation of the Ni+Cu+Co content is less than 10% (Kuhn et al., 2012). According to the classification of Halbach et al. (1981) these nodules are typical for early diagenetic growth under oxic conditions which is further supported by the ternary diagram Mn-Fe-10*(Ni+Cu) (Bonatti et al., 1972; Fig. 2.3). More precisely, these nodules are mixed type nodules (AB nodules) with variable proportions of hydrogenetic (B) and diagenetic (A) accretion (see individual layers; Halbach and Özkara, 1979; Fig. 2.3).

In contrast to nodules from the CCZ, bulk nodules from the PB show slightly higher Mn/Fe ratios but lower Ni+Cu concentrations (Fig. 2.7) and are of suboxic-diagenetic growth (Halbach et al., 1981).

Bulk nodules from the CCZ of this study have their highest Ni+Cu concentrations of 2.80 wt.% at a Mn/Fe ratio of 6.06 compared with nodules from the PB, which have highest Ni+Cu content of 2.06 wt.% at a Mn/Fe ratio of 5.27. This is consistent with data supplied by Friedrich et al. (1973; 1974) and Halbach et al. (1981) who found the highest Ni+Cu contents of approximately 3 wt.% at a Mn/Fe ratio of 5 in nodules from the CCZ. Halbach et al. (1981) described this as *"point of reversal"*, at *Mn/Fe >5* there is a preferential incorporation of Mn^{2+} into the 10 Å manganate lattice at the expense of Ni^{2+}, Cu^{2+} and other divalent cations under suboxic conditions. The authors argued that strong suboxic conditions led to a steep gradient of dissolved Mn^{2+} in pore water which caused a strong Mn^{2+} flux towards sites of Mn nodule growth. Since the Mn^{2+} cations better fit into the 10 Å manganate lattice, in terms of size and charge, they are preferentially incorporated instead of other divalent ions.

The analyses of a large number of individual layers in CCZ and PB nodules however do not reveal the existence of a significant "*point of reversal*" at Mn/Fe ratio of 5 or even at higher Mn/Fe ratios (Fig. 2.5). Despite the extreme fractionation of Mn and Fe (Mn/Fe ratio >800), high Ni+Cu concentrations in individual nodule layers suggest that Mn^{2+} will not be incorporated into the Mn-oxide lattice at the expense of other divalent metals. The high metal

contents together with the extreme Mn enrichment seem to be rather dependent on the mineralogy of the Mn-oxide phases.

2.6.2 Mineralogy of bulk nodules

Nodules from the CCZ are mainly composed of different 10 Å and 7 Å manganate phases (Fig. 2.9). The collapse of the ~10 Å peak after heating at 100°C and the increase of the ~7 Å peak are interpreted as an unstable 10 Å phyllomanganate. This phenomenon can be seen in all samples from the CCZ and the PB. This unstable 10 Å phyllomanganate probably is the dominant Mn oxide phase in all samples. In most samples from the CCZ a remnant peak at ~10 Å can be detected which is interpreted as a stable 10 Å phyllomanganate. According to the two asymmetrical *hk*-bands (2.45/1.42 Å) the detected Mn-phases are interpreted as turbostratic phyllomanganates (10 Å and 7 Å vernadite; Bodeï et al., 2007). No *hkl* reflections can be distinguished, because the individual [MnO$_6$] octahedral layers are randomly stacked without a translational periodicity in *c**-direction (no 3D ordering as it is the case in birnessite; Giovanoli and Bürki, 1975; Drits et al., 1997; Bodeï et al., 2007). The ~7 Å peak of the original samples (not heated to 100°C) is interpreted as turbostratic 7 Å phyllomanganate. The stable 10 Å Mn-phase and the turbostratic 7 Å phyllomanganate constitute subordinate mineral components in CCZ nodules.

Bodeï et al. (2007) showed that up to 5 wt.% divalent metals (e.g. Ni) can be incorporated into the crystal lattice of 10 Å phyllomanganates in order to balance charge deficits. This is caused by chemical (layer vacancy, mixed valence) and structural (stacking faults, low dimensionality) defects in the crystal structure of the phyllomanganates. In contrast, the ability of todorokite to take up metals for charge balance is limited (≤2 wt.%; Bodeï et al., 2007).

The dense and dendritic type 2 layers with high Cu+Ni contents (>2 wt.%) consist probably of 10 Å phyllomanganates whereas the layers with low Cu+Ni contents (<2 wt.%) may be composed of todorokite. The layers with high Cu+Ni contents form the major component whereas layers with low Cu+Ni are only a minor phase in the nodules.

In contrast to nodules from the CCZ, the PB nodules consist of an unstable turbostratic 10 Å and 7 Å phyllomanganate, exclusively; no stable 10 Å Mn phase such as todorokite was detected. This is in contrast to previous studies which interpret their mineralogical data as

todorokite (e.g., von Stackelberg, 1997). However, some of those studies interpreted the 10 Å peak as todorokite without further mineralogical experiments such as heating the samples to 100°C. However, todorokite cannot unequivocally be distinguished from 10 Å phyllomanganates by ordinary XRD diffraction. Therefore, some of the results previously interpreted as todorokite may simply be a stable 10 Å phyllomanganate.

2.6.3 Individual layers

Layers of type 1 show a chemical and mineralogical composition typical for hydrogenetic processes similar to ferromanganese crusts but with a slightly higher variance (Fig. 2.3). These layers form by precipitation of colloids of hydrated Mn and Fe oxides from ambient oxic sea water and metal enrichment by adsorption, complexation, and oxidation on the oxide surfaces (Koschinsky and Hein, 2003, Hein et al., 2013). Mn/Fe ratios up to ~3, low Ni+Cu and Ba but rather high Co and Ti contents are typical characteristics of such formation. In the analyzed nodules such layers occur on all sides of the nodule, e.g. on the top as well as on the bottom side. XPS data of the outermost nm (<10 nm) of the bottom side of two nodules, which were embedded in the upper few cm of the sediment, as well as SEM investigations of this area, indicate hydrogenetic precipitation from the current oxic sediment pore water. There is a slight enrichment of Mn over Fe (Mn/Fe up to 3, Table 2.5) suggesting a contribution of an oxic diagenesis. But rather high Co/Mn and low Ni/Mn and Cu/Mn ratios of these outermost layers led assumed that this oxic diagenetic contribution is minor (Fig. 2.3, Table 2.5).

The current redox conditions of the near bottom sea water and the pore water (dissolved oxygen content of pore water reaches values of around 150 µmol/l at the sediment surface and dissolved oxygen can be traced down to 2 - 3 m sediment depth**;** Rühlemann et al., 2010) do not allow the overall Mn^{4+} reduction in near-surface sediments and the related mobilization and enrichment of Mn^{2+}. This is confirmed by the absence of dissolved Mn^{2+} in pore waters within the depth of oxygen penetration and the enrichment of leachable Mn in surface sediments (Mewes et al., 2014). It can be suggest that if the conditions within sea water and sediment pore water are similar, the processes of precipitation of hydrated Mn-Fe oxides and the related enrichment of metals by surface adsorption and complexation should also be similar. Layers of hydrogenetic characteristics (up to Mn/Fe ratio of about 3) can, therefore, not only form at the top of nodules which is in contact with seawater but they also form at the bottom side which is in contact with oxic pore water.

Dymond et al. (1984) described three processes which lead to oxic diagenesis within sediments. First, the decomposition and oxidation of organic matter and the dissolution of labile biogenic components releases trace metals such as Ni, Cu, and Zn which can be incorporated in the already existing Mn-oxide phases. Second, amorphous ferromanganese oxyhydroxides and dissolved opal form nontronite within the sediment (Lyle et al., 1977) resulting in the release of Mn and other trace metals, forming Mn-oxide phases. Furthermore, the formation of phillipsite from the alteration of volcanic glass results in an elevation of the pH and therefore leads to an additional oxidation of Mn^{2+} (Bischoff et al., 1981; Hem, 1981). Third, adsorbed metals on sedimentary grains were released due dissolution from the grains and will be enriched in the pore water and further interact with the already existing Mn-oxide phases (Dymond et al., 1984; Lyle et al., 1984).

From these three processes probably only the decomposition of organic matter may play a significant role in the CCZ as indicated by high resolution oxygen pore water profiles and TOC profiles of the bulk sediment (Mewes et al., 2014; Rühlemann et al., 2010). This may be the major process that releases metals into the oxic pore water, probably as organic-metal complexes which may then be adsorbed onto already existing Mn-oxide phases leading to the slight Mn-Fe fractionation of layer type 1 (Lyle et al., 1984). Moreover, phillipsite was only detected in minor amounts in the nodules from the CCZ (Fig. 2.9), nontronite could not be detected, and dissolved Mn concentrations in pore water was below detection limit (Mewes et al., 2014).

In the hydrogenetic layers small-sized veins and spots of significantly higher reflectivity (higher Mn/Fe, high Cu+Ni) than the surrounding type 1 material widely fill up the interstices (Fig. 2.4A). These pore fillings are interpreted as post-depositional overprinting of layer type 1 during suboxic conditions. If hydrogenetic layers which were formed under oxic conditions have been subject to suboxic conditions it may come to re-crystallization processes because of the influx of dissolved Mn^{2+} ions. The higher Mn content has to be accommodated by a re-organization of the crystal structure probably leading to the formation of 7 and 10 Å phyllomanganates. Similarly, the formation of todorokite/birnessite from vernadite is known from ferromanganese crusts when they were subject to post-depositional suboxic conditions (Koschinsky et al., 1997; Halbach et al., 2009).

The small-sized veins and spots often smaller than 1µm and, therefore cannot be measured by EMPA since the measuring spot is much larger than the size of these pore fillings. Regarding to this fact EMP analyses provide always a mixed signal of the spots/veins and the surrounding material often leading to results which were previously interpreted to be oxic-

diagenetic (Mn/Fe of 3 to 10; Cu+Ni up to 3 wt.%; Halbach et al., 1988). The same holds true for transition areas between layer types. These areas are called in this study as mixed layer type 3 but interpret them as analytical mixtures between layer type 1 and 2. Therefore, no significant oxic-diagenetic layers/zones are present in the CCZ nodules. The nodules are interpreted as mixtures between an oxic-hydrogenetic and a suboxic-diagenetic end member. This is confirmed by PCA of the individual layers indicating two principal components consisting of Mn and Fe oxides. One component is made up of Mn oxides with high amounts of Ni, Cu, and Zn representing the suboxic-diagenetic end member, the other component comprises Mn and Fe oxides with Co, Ti and Cu standing for the oxic-hydrogenetic end member. The inclusion of Cu suggests that oxic-diagenetic processes may play a certain role within this end member as discussed above.

The high Mn-Fe fractionation of layer type 2 is characteristic for suboxic-diagenetic growth (Halbach et al., 1981). However, based on thermodynamic calculations, Halbach et al. (1982) assumed that under oxic conditions the dendritic structures of 10 Å manganates with high Mn-Fe contents fractionation can be formed when enough Mn^{2+} ions are available. A suboxic front occurs in about 2 - 3 m sediment depth at some locations of the study areas with dissolved Mn^{2+} concentrations up to about 50 µmol/l below this front. However, Mewes et al. (2014) concluded that this dissolved Mn^{2+} cannot reach the surface sediments and cannot currently influence the nodule formation.

Moreover, the flux of leachable Mn into the sediments (leachable with a hydroxylammonium chloride) is between 285 and 726 $µg/cm^2/10^3$yrs (data from Mewes et al., 2014), whereby only about 22% of this manganese is regenerated under oxic conditions (ca. 60 - 150 $µg/cm^2 * 10^3$yrs; see diffusive Mn flux back into near-bottom water; Halbach et al., 1988). However, the Mn flux into the CCZ nodules is about 2000 $µg/cm^2/10^3$yrs (based on growth rate of 45 mm/Ma, 30% Mn, and 1.396 g/cm^3 (dry bulk density). This flux is considerable higher than the flux of mobilizable Mn.

Therefore, It can be suggest that the environmental conditions on the seafloor must have changed from oxic (as today) to suboxic in order to form layers of type 2 in nodules.

In contrast to the CCZ, Peru Basin sediments are characterized by oxygen penetration down to only 5 - 10 cm depth followed by a strong increase of dissolved Mn^{2+} in the pore water (50 - 150 µmol/l) at this shallow sediment depth (Haeckel et al., 2001). Therefore, a significant amount of Mn from suboxic pore-water currently contributes to the chemical composition of nodules growing in the upper 10 cm of the sediment causing the formation of diagenetic type

2 layers (von Stackelberg, 1997). The formation of suboxic conditions in the sediment pore water is controlled by the flux of organic carbon (Froelich et al., 1979). Sedimentation rates in the CCZ are around 0.35 cm/kyr (Mewes et al., 2014). A similar sedimentation rate is reported from site 2 in the PB (0.4 cm/kyr) with a flux of total organic carbon of 6.65 $\mu mol/cm^{-2}*a^{-1}$ and a distinct suboxic front at about 10 cm sediment depth (Haeckel et al., 2001). The current flux of organic carbon to sediments in the study area (eastern CCZ) is 3 $\mu mol/cm^{-2}*a^{-1}$ (Mewes et al., 2014). The organic carbon flux has to be increased only by factor of ~2 to get similar values as in the PB. It is suggested that this increased flux rate can lead to suboxic conditions close to the sediment surface similar to the current situation in the PB.

These results demonstrate that suboxic conditions may have alternated with oxic conditions during the growth of nodules in the CCZ. This may occur due to fluctuating bioproductivity, which led to changing organic carbon flux as well as changes in ventilation (reduced ventilation) of the deep ocean in the equatorial Pacific surface waters during glacial-interglacial periods (as described by König et al., 2001, for the PB). Both processes may lead to oxygen consumption in the near surface sediments and to the reduction of particulate Mn^{4+} during the ongoing early diagenetic degradation of organic carbon (Froelich et al., 1979; Bradmiller et al., 2010).

2.6.4 The "Cu problem"

One of the major differences between nodules from the CCZ and the PB is the Cu content, which is distinctly lower in PB nodules (Table 2.2; Fig. 2.7). This difference is may be controlled by the different composition of the sediments in both regions. The PB sediments contain a significant amount of carbonate (10.3 ± 8.1 to 21.7 ± 12.9 wt.%; Stummeyer and Marchig, 2001), whereas the sediments from the eastern CCZ are almost devoid of carbonate (0.5 wt.% at the sediment surface and 0.2 wt.% at 50 cm depth; Mewes et al., 2014). Sediments in the eastern CCZ mainly consist of siliceous ooze and pelagic clay. Copper recycling in oxic carbonate-rich sediments is much more efficient with up to 98% of the total primary Cu flux, than in oxic siliceous sediments (83 - 94%; Callender and Bowser, 1980) resulting in a higher loss of Cu into the near-bottom sea water in carbonate-rich sediments. Moreover, Koschinsky (2001) showed that Cu in sediments underneath the current surface layer in the PB is bound to a significant degree to Fe-oxyhydroxides and to residual phases that were not mobilized during suboxic diagenesis. In contrast, Cu in CCZ sediments is almost

completely bound to Mn-oxides which are mobilized during suboxic diagenesis (unpublished BGR data). Sediments in the eastern CCZ mainly consist of siliceous ooze and pelagic clay.

2.6.5 Calculated proportions of the individual end members

There are three distinct chemical end members, which build up the nodules from the CCZ: oxic-hydrogenetic layers, suboxic-diagenetic layers and sediment filling pore space and cracks. The individual proportions of the end members within the nodules were calculate using a simple linear mixing model. Layer type 1 is characteristic for the oxic-hydrogenetic end member, layer type 2 is typical for suboxic diagenesis. No separate oxic-diagenetic end member was used because almost all EMPA data indicate that measured points typical for oxic-diagenetic formation turned out to be mixtures of hydrogenetic- and suboxic-diagenetic material. Because of the high porosity of nodules, there always is sediment in the pore space affecting the results of the chemical analyses of bulk nodules. Therefore we introduced a sediment end member was introduced in the calculations, which represents the average chemical composition of the pelagic sediments (Table 2.8). For the calculation of the proportions of the different end members the median value of the chemical analyses of the individual layers was used (Table 2.8). The results of the calculation show, that the suboxic-diagenetic end member (Mn/Fe 10 - 500, layer types 2) is most abundant (50 - 60%) in the nodules whereas the oxic-hydrogenetic material constitutes about 35 - 40% and the sediment accounts for 5 - 10% (Table 2.8; Fig. 2.10). Since the oxic-hydrogenetic component is to a certain degree overprinted during post-depositional suboxic conditions, the primary oxic-hydrogenetic proportion might have been higher.

TABLE 2.8 Proportion calculations of different genetic end members of nodules. Median of Mn, Fe, Ni, Cu and Zn contents in [wt.%] of bulk nodule 17KG-D, the two individual layer end members (HG; SD), sediment as a third end member and the resulting calculated proportions of the end members

end member layers of nodule 17KG-D	Mn	Fe	Co	Ni	Cu	Zn	R^2
median hydrogenetic (HG)[1]	25.5	14.2	0.29	0.53	0.34	0.08	
median suboxic diagenetic (SD)[2]	44.5	0.62	0.07	2.01	1.81	0.26	
median sediment (S)[3]	0.24	4.25	-	0.01	0.02	-	
bulk nodule 17KG-D (ICP-OES)	34.0	6.32	0.17	1.55	1.15	0.17	
best fits							
17KG-D (40 HG; 55 SD; 5 S)[4]	34.7	6.24	0.15	1.32	1.13	0.18	0.99
11KG-A (40 HG; 50 SD; 10 S)	29.2	6.47	0.14	1.1	1.2	0.22	0.96
27KG-1a (35 HG; 60 SD; 5 S)	35.5	5.70	0.13	1.34	1.29	0.14	0.98
44KG-2a (40 HG; 55 SD; 5 S)	33.3	5.97	0.14	1.28	1.21	0.13	0.97
68KG-C (40 HG; 55 SD; 5 S)	36.0	5.28	0.13	0.91	1.07	0.18	0.91

[1]HG = hydrogenetic end member, [2] SD = suboxic diagenetic end member,
[3]S = pelagic sediment end member,[4] presented in Fig. 2.9
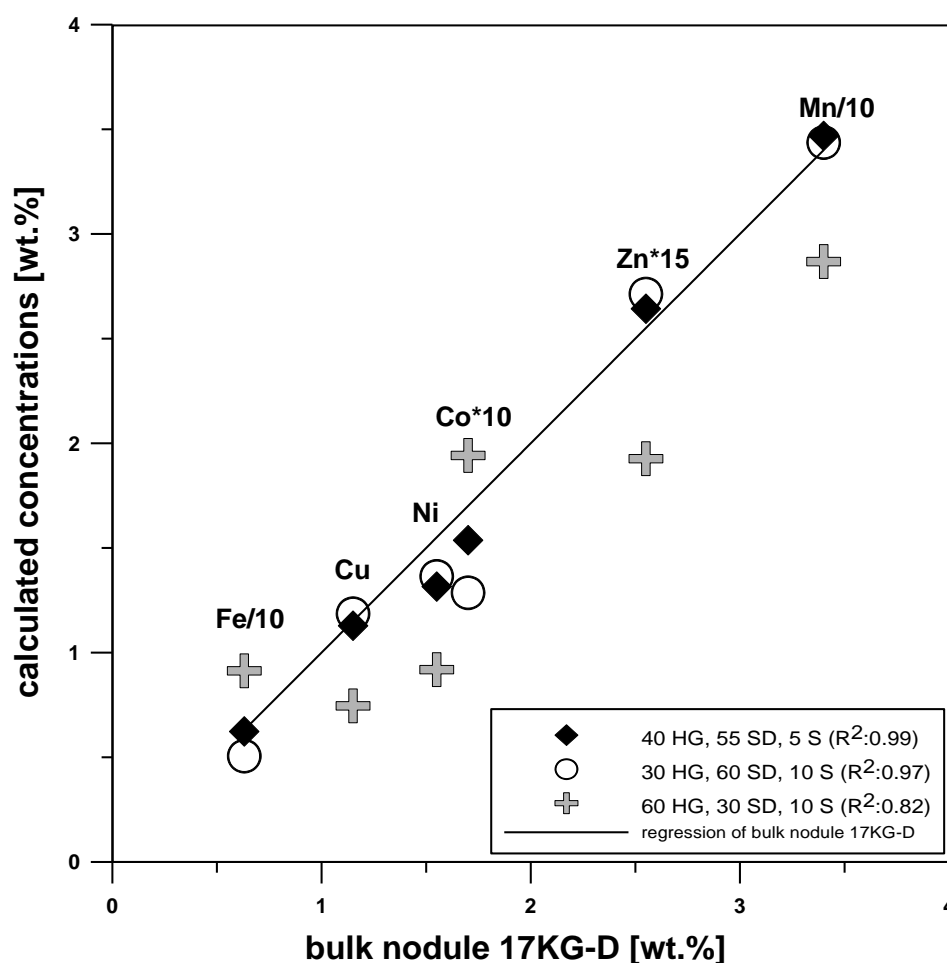
FIGURE 2.10 Diagram displaying element contents from calculation of different mixing proportions of an oxic-hydrogenetic (HG), a suboxic-diagenetic (SD), and a sediment (S) end member of nodule 17KG-D (y-axis) versus element contents from bulk analysis of nodules 17KG-D (x-axis). The end member concentrations were taken from the median of individual layers (Table 2.8). Different calculated proportions are presented, best fit is 40% HG, 55% SD, 5% S.

2.7 Summary and Conclusions

Polymetallic nodules from the Clarion and Clipperton Zone of the central Pacific Ocean which were analyzed in this study represent a heterogeneous chemical and mineralogical system. Individual growth layers of nodules act as an archive for changing environmental conditions during formation of the nodules. Up to now, nodules from the central Pacific were classified as mixed type nodules of hydrogenetic and oxic-diagenetic origin. But the analyses of individual layers indicate that a high proportion of these nodules formed under suboxic conditions. The following conclusions can be drawn:

1) Nanometer- to micrometer -thick individual layers of nodules have a much higher chemical heterogeneity as the bulk nodules. Mn/Fe ratios vary between 0.5 and 826 and the Ni+Cu content range from 0.16 to 6.5 wt.% in individual layers.

2) Highest Ni+Cu concentrations of 6.51 wt.% at a Mn/Fe ratio of 56 show that the incorporation of metals such as Ni^{2+}, Cu^{2+} and other divalent cations is not dependent on the preferential incorporation of Mn^{2+} into the 10 Å manganate lattice at the expense of the metals, as suggested so far (e.g., Halbach et al., 1988).

3) Two genetically different layer types could be distinguished due to their chemical composition and growth structures:

Layer type 1: These layers form from hydrogenetic accretion in the near-bottom sea water as well as in the oxic pore water within the upper few cm of the sediment. The processes of adsorption and complexation of metals on the Mn-Fe oxyhydroxide phases are dominant.

Layer type 2: Those layers are typical for the formation under suboxic-diagenetic conditions with a strong fractionation of Mn and Fe. These layer types build up a large part of the nodules (50 - 60%). Increased bioproductivity in the central Pacific surface waters and/or reduced ventilation of the deep ocean during glacial periods could lead to a pronounced oxygen minimum in the deep sea and rapid oxygen consumption in the near-surface sediments causing suboxic conditions.

4) *Mixed layers type 3* are mixtures between primary hydrogenetic layers which were post-depositionally overprinted by suboxic pore space fillings. They often have typical oxic-diagenetic composition but in most cases, this is just an analytical effect.

5) Mineralogically, the CCZ nodules mainly contain turbostratic 10 Å phyllomanganate with subordinate turbostratic 7 Å phyllomanganate, vernadite (δ-MnO_2) and amorphous FeOOH nanoparticles. Todorokite probably occur in minor amounts and is of secondary formation.

6) Peru Basin nodules exclusively consist of turbostratic 10 Å phyllomanganate and 7 Å phyllomanganate. No todorokite was detected.

Chapter III

Mineralogical characterization of individual growth structures of

Mn-nodules with different Ni+Cu content from the

central Pacific Ocean

This chapter is focused on the characterization of the mineralogical composition of bulk nodules and in detail of investigation of individual genetic different layers. This study should reveal new information about how the mineralogy influences the metal content (e.g., Ni+Cu) of the Mn nodules. Furthermore, analyses of growing structures of different areas within the nodules were investigated to detect epigenetic transformations.

A modified version of this chapter is submitted to American Mineralogist. Mineralogical characterization of individual growth structures of Mn-nodules with different Ni+Cu content from the central Pacific Ocean. Wegorzewski, A. V., Kuhn, T., Dohrmann, R., Wirth, R., Grangeon, S.

3.1 Abstract

X-ray diffraction (XRD) analyses and cation exchange experiments (CEE) were carried out on bulk manganese nodules from the eastern Clarion and Clipperton Zone (CCZ) of the central Pacific Ocean. High-resolution transmission electron microscopy (HRTEM) of individual nm to µm thick growth structures of a nodule provides new information about its mineralogy in context with its metal content.

Bulk nodules of the CCZ as well as their individual diagenetic growth layers contain different turbostratic phyllomanganates: **1)** unstable ~10 Å phyllomanganates collapsing at <100°C, **2)** stable ~10 Å phyllomanganates collapsing at >100°C and **3)** minor amounts of 7 Å phyllomanganates. All three phyllomanganates are of the hexagonal vernadite type. The cation exchange experiments of bulk nodules exhibited a variable but distinct cation exchange capacity and support the occurrence of high amounts of phyllomanganates. Todorokite was neither detected in bulk nodules nor in any of the individual diagenetic growth layers.

A chemical profile through a nodule, using X-ray diffraction analyses, reveal dominating stable turbostratic 10 Å phyllomanganates (not collapsing after heating at 100°C) near the nucleus to dominating unstable turbostratic 10 Å phyllomanganates (collapsing from 10 Å to 7 Å after heating at 100°C) close to the surface. We interpret this succession as an epigenetic transformation from unstable to stable Mn-oxide phases through time due to re-organization and substitution of metals within the interlayer of the crystal structure.

Hydrogenetic layers consist of Fe-bearing vernadite (δ-MnO_2) with inclusions of turbostratic 10 Å and 7 Å phyllomanganates. The latter probably are the product of refilling pores within these layers or post-depositional re-crystallization under suboxic conditions from δ-MnO_2 to a turbostratic 10 Å/7 Å phyllomanganate.

3.2 Introduction

Mn-oxide minerals occur in a wide variety of geological settings. More than 30 different Mn-oxide minerals are known from soils and sediments. They also form nodules at the ocean floor. The most common Mn-oxide minerals in terrestrial deposits and in ocean manganese nodules are 10 Å Mn-phases such as the tectomanganate todorokite and the phyllomanganates such as buserite and birnessite and their turbostratic forms vernadite (10 Å and 7 Å vernadite) (Burns et al., 1977; Burns and Burns, 1978a,b; Usui and Glasby, 1998; Lei and Boström, 1995; Bodeï et al., 2007; Manceau et al., 2007; Peacock and Sherman, 2007a). Furthermore, a Fe-bearing vernadite, which has Mn-rich layers analogous to the synthetic form of δ-MnO$_2$ (McMurdie, 1944) also occur typically in oxic-hydrogenetic precipitates and is epitaxially intergrown with amorphous δ-FeOOH (Burns and Burns, 1975; Halbach et al., 1988; Manceau et al., 1992a; Koschinsky and Hein, 2003).

Ferromanganese precipitates are scavengers of dissolved metals such as Ni, Cu, Zn, Co, and rare earth elements (e.g., Hudson-Edwards, 2000; Hein et al., 2013), which are enriched due to surface adsorption processes and/or incorporation into the crystal structure of Mn-Fe oxy-hydroxides. Phyllomanganates and, to a lesser extent, todorokite can incorporate high amounts of trace metals such as Ni and Cu (Burns and Burns, 1978b; Lei and Böstom, 1995; Bodeï et al., 2007). The phyllomanganates consist of [MnO$_6$] octahedral layers which are stacked with a constant layer-to-layer spacing ranging between ~10 Å and ~7 Å. Turbostratic, nano-sized, phyllomanganates such as vernadite show no three-dimensional (3D) periodicity in $c*$ direction in contrast to birnessite and buserite, which are ordered phyllomanganates (Giovanoli, 1980; Usui and Mita, 1995). Turbostratic layering means the random rotation of the [MnO$_6$] octahedral layers around the crystallographic $c*$-axis or the translation of the [MnO$_6$] layers in the crystallographic ab-plane. This is in contrast to the minerals buserite and birnessite which have a systematic 3D ordering of the [MnO$_6$] octahedral layers along the c-axis (Giovanoli et al., 1975; Drits et al., 1997). X-ray diffraction patterns of turbostratic vernadite have distinct basal reflections at ~7 Å and ~3.5 Å for the 7 Å varieties and ~10 Å and ~5 Å for the 10 Å varieties (Bodeï et al., 2007). Both minerals show at least two asymmetrical hk-bands at higher diffraction angles (2.40 - 2.45 Å and 1.41 - 1.42 Å) and no hkl but 00l reflections (Giovanoli et al., 1975; Drits et al., 1997; Villalobos et al., 2006; Bodeï et al., 2007).

The octahedral layers can have a negative charge deficit because of the isomorphic substitution of Mn^{4+} by Mn^{2+} or Mn^{3+} or of layer vacancies. Their interlayer spacing is

affected by the nature of the hydrated cations which balance the negative charge deficit (typically alkali or alkaline-earth cations in case of isomorphic substitutions by $Mn^{2+/3+}$ or transition metals in the case of layer vacancies; Post and Bish, 1988; Manceau et al., 1997; Bodeï et al., 2007; Peacock and Shelman, 2007a). In contrast to 10 Å phyllomanganates, the 7 Å phyllomanganates contain only a single water layer between two octahedral sheets (Bodeï et al., 2007).

Tectomanganate todorokite forms in contrast to phyllomanganates, tunnel structures consisting of $[MnO_6]$ octahedral chains extending parallel to the b-axis (Post et al., 2003). The octahedral chains can consist of 3 x 3 -octahedra or show a defective structure with 3 x n octahedral layers (n <8; Burns et al., 1983).

Furthermore, Fe-vernadite (Fe-δ-MnO_2) consists of single edge-shared $[MnO_6]$ octahedral layers that are epitaxial intergrown with δ-FeOOH nanoparticles which disrupt parallelism between adjacent layers and, as a consequence, its X-ray diffraction pattern often shows only two asymmetrical *hk*-bands at 2.40 - 2.45 Å and 1.41 - 1.42 Å (Burns and Burns, 1975, Manceau et al., 1992a; Bodeï et al., 2007).

Bulk nodules from the CCZ have Mn/Fe ratios ranging between 4 and 6, and a Ni+Cu content ranging from 2 - 3 wt.% and Co content between 0.12 and 0.17 wt.% (Chapter II). According to Halbach et al., (1981) these nodules are typical for oxic-diagenetic growth. However, individual growth layers within nodules have a broad range of Mn/Fe ratios from <3 (oxic-hydrogenetic precipitates) to >800 (suboxic-diagenetic growth) indicating that the nodules are a mixture of oxic and suboxic processes (Chapter II).

Hydrogenetic layers generally have low Ni+Cu contents but high amounts of Co, and high-field strength elements (HFSE) (Hein et al., 2013 and references therein), whereas diagenetic layers show variable metal contents (e.g., Ni+Cu: $0.8 - 6.5$ wt.%, Ti: < 0.01 - 1.4 wt.%, Co: <0.01 - 0.77 wt.%, Mo: < 0.01 - 0.23 wt.%; Chapter II). According to Bodeï et al. (2007) phyllomanganates can incorporate much higher amounts of metals (~5 wt.%) than the tectomanganate todorokite (~2 wt.%). According to that, layers of diagenetic growth with high Ni+Cu content (>2 wt.%) are probably made of 10 Å phyllomanganate (10 Å vernadite/buserite) and those with lower Ni+Cu contents (<2 wt.%) may be composed of todorokite (Chapter II).

In this work results of drying and cation exchange experiments of bulk nodules from the CCZ are presented to distinguish between different 10 Å manganates such as todorokite or different forms of phyllomanganates (ordered and disordered).

Furthermore, results of nm to μm thick diagenetic and hydrogenetic layers of nodules using high-resolution transmission electron microscopy (HRTEM) in combination with the metal content detected by electron microprobe analysis (EMPA) of the same layers will be presented. These analyses provide information about how the mineralogical composition of Mn oxides control or influence the incorporation of metals, especially Ni and Cu, into the nodules. Furthermore, HRTEM investigations of crystallized inclusions within hydrogenetic growth structures provide insight into post-depositional transformation (overprinting) of Mn oxides due to changing redox conditions (oxic/suboxic).

3.3 Samples and analytical methods

3.3.1 Nodule samples

The nodules that are presented in this work (09KG-B, 26KG, 29KG-C, 32KG-4, 32KG-5, 44KG-2, 62KG-A) were collected in the eastern German license area within the CCZ in the central Pacific Ocean during cruise SO205 in 2010 (R/V SONNE; Rühlemann et al., 2010) and cruise BIONOD 2012 (R/V L`Àtalante; Rühlemann et al., 2012). The exploration area is located between 119°30`W to 115°`W and 13°N to 11°N at a water depth of 4000 - 4500 m (Fig. 3.1, Table 3.1). Detailed information about the origin of the nodules and the environment can be found in Rühlemann et al., 2010.
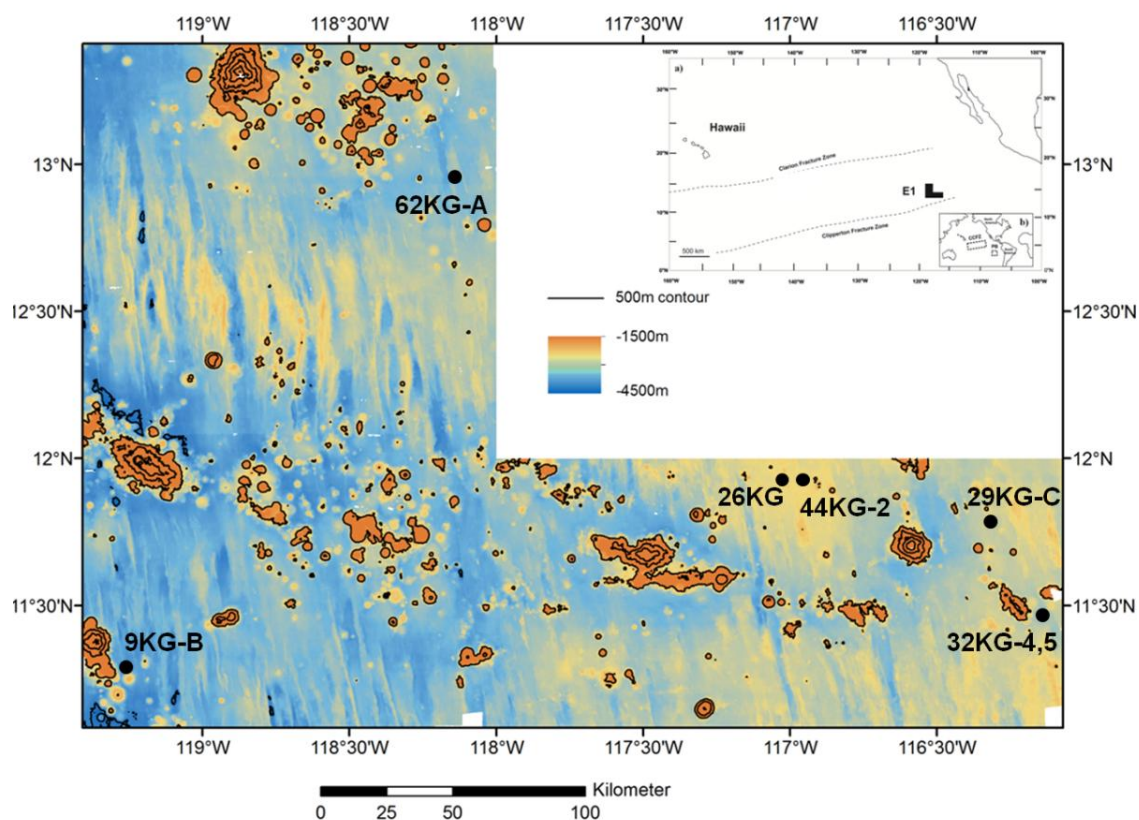
FIGURE 3.1 German eastern license area and the location of nodules which were analyzed in this study (modified after Rühlemann et al., 2010, 2012).

TABLE 3.1 Location of samples analyzed during this study

Study area (SA)	Sample-ID	Position		Water depth [m]	Water depth [m]
		Latitude	Longitude		
1	SO205 09 KG-B	11°18.6 N	119°14.8 W	4303	midsized discoidal nodule wit smooth surface and rough bottom side
3	SO205 29KG-C	11°35.4 N	116°14.1 W	4203	large discoidal nodule, smooth surface and rough bottom side
	SO205 32KG-4	11°28.6 N	116°9.2 W	4240	midsized nodule with smooth surface and rough bottom side
	SO205 32KG-5	11°28.6 N	116°9.2 W	4240	midsized nodule with smooth surface and rough bottom side
5	SO205 44KG-2	11°57.4 N	116°57.2 W	4188	large nodule, botryoidal growth structures on both sides with a smooth surface and rough bottom side
	BIONOD 26KG	11°53.4 N	117°4.4 W	4137	large discoidal nodule
6	SO205 62 KG-A	13°10.5 N	118°6.3 W	4282	midsized nodule

The nodules are ellipsoidal to spherical in shape with approximate diameters between 4 and 8 cm. They have smooth upper sides which were in contact with the near bottom sea water and rough lower sides that were buried within the upper few cm in the sediment. Bigger nodules show botryoidal growth structures on both sides. Figure 3.2 show two typical nodules from the CCZ.

Mineralogical investigations were carried out on several bulk nodules and on individual nm to μm thick growth layers of nodule 32KG-5 as well as of subsamples of a drilled profile through nodule 44KG-2 (Fig. 3.2A).
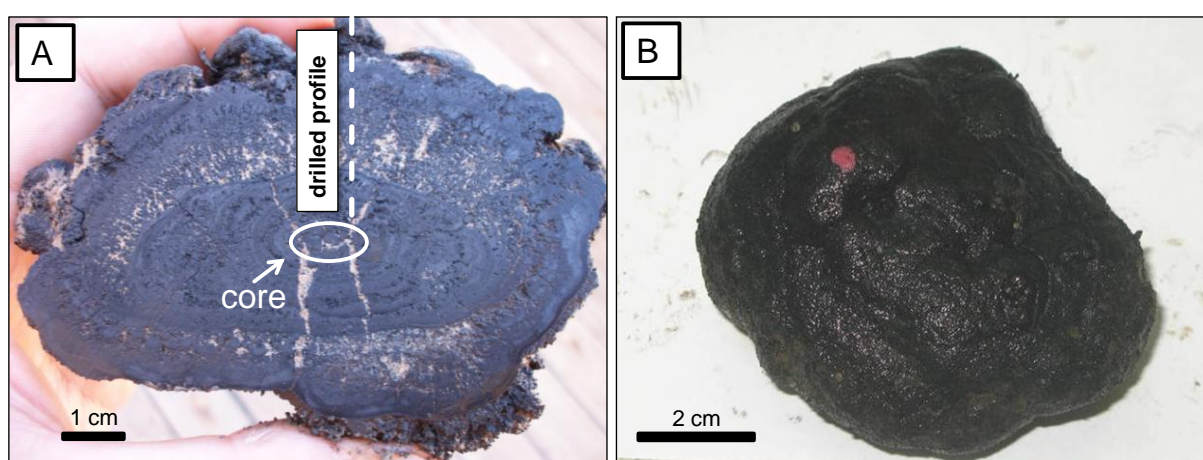
Figure 3.2 A: Typical large ellipsoidal nodule (SO205 44KG-2; 10 x 10 x 6.7 cm) with botryoidal grow structures on all sides of the nodule. **B:** typical nodule of medium size (SO205 32KG-5; 6 x 5 x 2 cm). The top sides of both nodules, which were in contact with the near-bottom water (marked by red dot in B), are smooth and the bottom sides, which were stacking in the upper few cm of the sediment, are rough.

3.3.2 Analytical methods

3.3.2.1 X-ray diffractometry

For the drying experiments two nodules were dried at different temperatures. Nodule 26KG was grinded at room temperature (RT) in a first step, without prior drying and analyzed using X-ray diffractometry (XRD). Further XRD analyses of this nodule were conducted after drying the sample at 40°C, 100°C and 300°C for 24 hours each. Sample 32KG-5 was dried at 40°C, 100°C, 150°C, 200°C and 300°C to get information about the behaviour of the Mn-phases during drying.

This approach allows to distinguish between thermally stable 10 Å manganese phases (e.g., todorokite) and thermally unstable 10 Å Mn phase (phyllomanganates) because both Mn phases have similar reflections at RT at ~10 Å (001) and ~5 Å (002), respectively. The basal reflections of the thermally unstable 10 Å phases collapse upon drying at 100°C whereas those of the thermally stable 10 Å phases do not (Uspenskaya et al., 1987).

Furthermore, several additional nodules (9KG-B; 29KG-C, 32KG-4, 44KG-2, 62KG-A) were analyzed just after drying at 40°C and 100°C to investigate if thermally stable and thermally unstable 10 Å Mn-phases occur.

Additionally, a hydrothermal Mn oxide from South Africa was analyzed at different temperatures (40°C, 100°C, 200°C, 300°C, 400°C, 500°C) to compare the collapsing processes of a hydrothermal Mn-phase with those of nodules from the CCZ. As discussed below, this sample can be used as a reference for todorokite.

X-ray diffractograms of bulk nodules (described above) were recorded using a PANalytical X'Pert PRO MPD Θ-Θ diffractometer (Cu-Kα radiation generated at 40 kV and 30 mA), equipped with a variable divergence slit (20 mm irradiated length), primary and secondary soller, Scientific X´Celerator detector (active length 0.59°), and a sample changer (sample diameter 28 mm). The samples were investigated from 2° to 85° 2Θ with a step size of 0.0167° 2Θ and a measuring time of 10 sec per step. Specimens were prepared using the top loading technique.

In addition to bulk samples, individual samples of a drilled profile through nodule 44KG-2 were analyzed using XRD. We chose this nodule because of its size (10 x 10 x 6.7 cm) that allowed drilling a long profile. The samples were drilled with a high precision planar drill bit (diameter of 6 mm) from nodule surface down to the core (~3 cm). The powder samples were analyzed with a Philips PW-1800 X-ray diffractometer at the University of Hannover. The apparature has a graphite diffracted beam monochromator (Cu-Kα1/2 radiation generated at 40 kV and 40 mA) equipped with an automatic divergence slit. The samples were investigated from 2° to 80° 2Θ with a step size of 0.02° 2Θ and a measuring time of 5 sec per step. All samples were analyzed twice, after drying the sample at 40°C and at 100°C for 24h each.

Simulation of powder X-ray diffraction pattern was performed using the mathematical formalism developed by Drits and Tchoubar (1990), which allows the calculation of patterns from structures affected by various nature and density of layer crystallization defects (e.g. layer vacancies, isomorphic substitutions) and of layer stacking defects (e.g.

interstratification, random stacking faults) (personal comm. S. Grangeon). As this method is based on a trial-and-error procedure, a correlation matrix cannot be extracted, and thus, uncertainties cannot be evaluated from a mathematic procedure. These uncertainties are retrieved from sensitivity tests, which have demonstrated that this method can accurately determine the structure of various layered structures, such as phyllomanganates, phyllosilicates and nanocrystalline calcium silicate hydrates (Grangeon et al., 2010, 2013; Lanson et al., 2008, Manceau et al., 1997; Villalobos et al., 2006). For example, the uncertainty on the density of interlayer species adsorbed above layer vacancies is typically $\pm$ 0.01 per layer octahedron (Manceau et al., 1997) (personal comm. S. Grangeon).

3.3.2.2 Electron microprobe analysis

Chemical composition of individual growth structures within nodule 32KG-5 was investigated using electron microprobe analysis (EMPA; CAMECA SX 100). For the analysis, thick sections (~200 μm thickness of the sample) were prepared. The analyses of genetically different layers were performed using a 15/20 kV accelerating voltage and 40 nA beam current. The bright layers (Mn rich) were measured with a focused (1 - 5 μm) beam and the darker layers (Fe rich) with a defocused (5 - 20 μm) beam. The counting times for the analyzed elements were 10 s for Mn, Fe, Ni, Cu, Na, Mg, Al, Si, K, Ca, Ti, P, S, Cl, 40 s for V, 45 s for Pb, 50 s for Co, 90 s for Zn, 100 s for Ba, Mo and Sr, and 110 s for Ce. Rhodochrosite (Mn), haematite (Fe), cobaltite (Co), synthetic Ni_2Si (Ni), cuprite (Cu), albite (Na), kaersutite (Mg, Al, Si), biotite (K), apatite (Ca, P), rutile (Ti), willemite (Zn), barite (S, Ba), monazite (Ce), molybdenite (Mo), krokoite (Pb), celestine (Sr), vanadium metal (V) and tugtupite (Cl) were used as standards (BGR standards). Furthermore, a PAP matrix correction was done according to Pouchou and Pichoir (1991).

The hydrated, very porous Mn oxides that build up the individual layers of Mn nodules contain a high amount of water (approx. 20%; Hein et al., 2013). Therefore, this material is sensitive to the high beam current causing total analytical sums to be less than 100%. We decided to take total analytical sums of $\geq$ 80% as acceptable, all analyses <80% were omitted from further investigations.

3.3.2.3 Inductively coupled plasma optical emission spectrometry

In order to determine their chemical composition, the samples were dried at 110°C for 24h. Afterwards the samples were dissolved with HCl/HNO$_3$/HF in a ratio of 3:1:1 ml. The solution was diluted to 50 g in 0.5 M HNO$_3$ and 0.05 M HCl. Major and minor elements (Mn, Fe, Ni, Cu, Co, Al, K, Ca etc.) were analyzed with ICP-OES (Spectro Ciros Vision). Analytical precision and accuracy were checked by analyses of certified standard materials such as BGR standard FeMn-1 (Kriete, 2012), Mn nodule standards NOD-P-1 (United States Geologic Survey) and JMn-1 (Geological Survey of Japan). For a detailed description of the methodology, accuracy, and precision as well as interference refer to Alexander (2008).

3.3.2.4 Focused ion beam and high-resolution transmission electron microscopy

For structural analysis of individual layers high-resolution transmission electron microscopy (HRTEM) was used. Electron transparent foils from layers in nodule 32KG-5 were cut using a focused ion beam preparation technique (FIB). Cutting sites from growth structures of interest were selected based on EMPA analysis. The foils (15 x 10 x 0.150 μm) were sputtered from the target material using Ga-ions with energy of 30keV (Wirth, 2009). For TEM analyses, foils were taken out from their excavation sites applying the so-called lift-out technique (Giannuzzi et al., 1997). Detailed description of the FIB techniques is given in Gianuzzi and Stevie (2005) and Wirth (2004, 2009). TEM analyses were carried out with a FEI F20 X-Twin transmission electron microscope with Schottky field emitter as an electron source at the GeoForschungs Zentrum Potsdam (GFZ). The TEM is equipped with a Gatan Imaging Filter (GIF). TEM bright-field and dark-field images as well as high-resolution lattice fringe images were acquired as energy filtered images applying a 20 eV window to the zero-loss peak. Diffraction pattern were calculated from high-resolution lattice fringe images (Fast Fourier Transformations - FFT). High-angle annular dark field images (HAADF) were acquired using a Fishione system. Analytical electron microscopy was performed with an energy dispersive system (EDAX).

3.3.2.5 Cation exchange experiments

For further differentiation between the two "10 Å manganese minerals" todorokite and phyllomanganates, cation exchange experiments (CEE) were carried out on different nodules from the CCZ and one hydrothermal todorokite sample. Powdered samples were filled in centrifuge tubes with 2 ml KCl solution. After centrifugation, the supernatant was decanted and fresh solution was added. This procedure was performed three times. Thereafter, the samples were transferred to porous ceramic tiles and washed three times with deionized water and analyzed via XRD. The same procedure was subsequently carried out on the same samples with 2 ml $MgCl_2$.

3.4 Results

3.4.1 Chemistry of individual layers of nodule 32KG-5

Layer type 1: Dense layers with low Mn/Fe ratio

Layer type 1 is a dense layer of low reflectivity and occurs throughout the whole nodule. For a detailed description see Chapter II. We analyzed layers of type 1 at two locations: near the upper surface of the nodule 32KG-5 (box 1 in Fig. 3.3 and the high resolution image Fig. 3.4A) and on the bottom side of it (box 3 in Fig. 3.3 and 3.5A). Layer type 1 is also recognized in Figures 3.7A and 3.8A. The Mn/Fe ratios show a median of 1.13, the Ni+Cu content as well as the Zn concentrations are also low ranging between 0.38 and 1.0 wt.% (median 0.58 wt.%) and 0.07 - 0.10 wt.% (median 0.09 wt.%), respectively (Table 3.2). In contrast, Co, Ti, and Ce are enriched in layers of type 1 compared to layers of type 2. Alkali and alkaline earth metals show lower contents within layer type 1 compared to layer types 2 (Table 3.2).

Spots and veins of high reflectivity can widely be found within layer type 1 (Figs. 3.4A, 3.7A). The Mn/Fe ratios of the bright material vary from 12 to 26, Ni+Cu and Zn concentrations are 5.4 ± 0.2 wt.% and 0.2 ± 0.01 wt.%, respectively. These metal contents are significantly higher compared to the surrounding material of low reflectivity. The same holds true for the alkali and alkaline earth metals. In contrast, Co, Ti, and Ce concentrations are much lower compared to the surrounding material (Table 3.2).
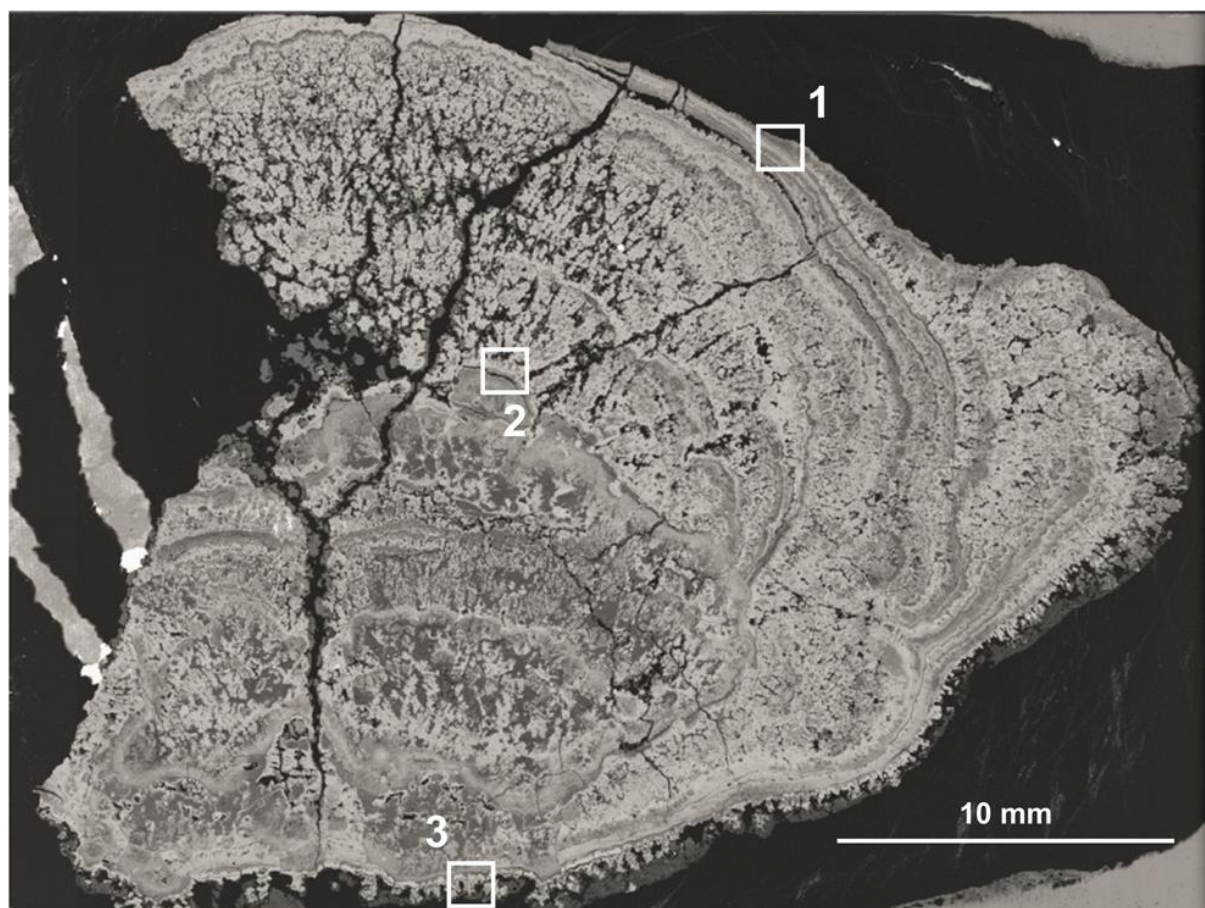
Figure 3.3 Overview of the thick section of nodule SO205-32KG-5 with the areas (white boxes) of high-resolution chemical and mineralogical analyses.
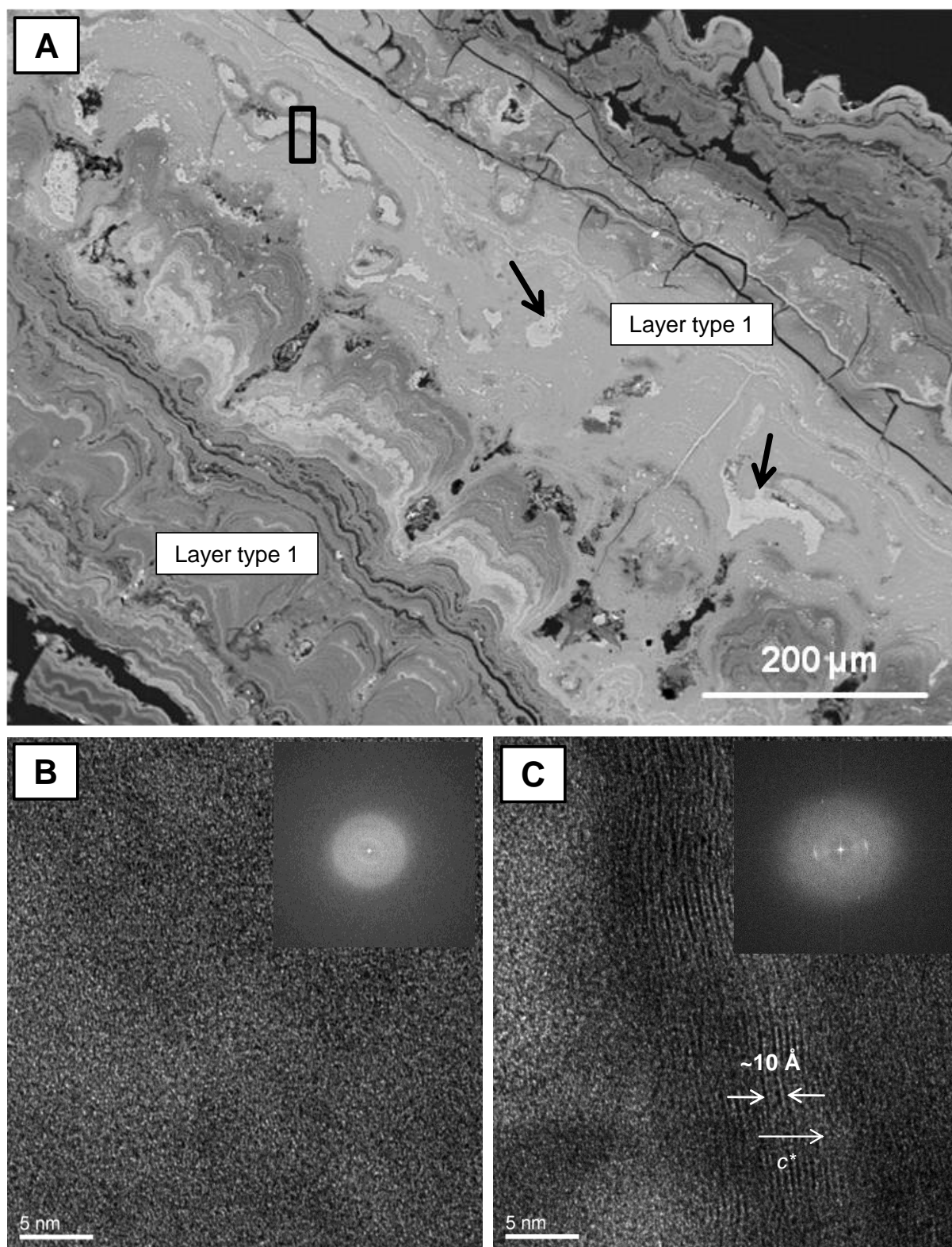
FIGURE 3.4 A: Layer type 1 (hydrogenetic) near the surface of nodule 32KG-5 (marked as area 1 in Fig. 3.3) with spots and veins of high reflectivity (marked by black arrows) and high Mn/Fe ratios (12-26), probably epigenetic overprints. The small black box indicates the zone which was analyzed with HRTEM (Fig. 3.4**B**,**C**) **B:** HRTEM of the material of low reflectivity (layer type 1) no lattice fringes or any reflections within the electron diffraction pattern (insert) are shown. **C:** HRTEM of the bright material of the box shown in Fig. 3.4A. Distinct 10 Å lattice fringes can be distinguished which correspond to 10 Å phyllomanganate and represent the d-spacing between two [MnO_6] octahedral layers; insert the corresponding electron diffraction image.

TABLE 3.2 Average content of major and minor elements of individual layers of type 1 and 2 of nodule 32KG-5 from the CCZ as well as of bright spots/veins within layer type 1 and dark areas of layer type 2 (EMPA data, wt.%)

individual layer	layer description		Mn	Fe	Co	Ni	Cu	Zn	Mn/Fe	Ni+Cu	Na	Al	Ca	Mg	K	Si	Ti	Mo	Ba	Ce	Ni/Mn	Cu/Mn	Co/Mn
layer type 1	dense layer of low reflectivity	AVERAGE (n*1=27)	21.1	17.9	0.44	0.37	0.22	0.09	1.19	0.59	1.52	0.88	2.07	0.98	0.34	4.93	1.30	0.03	0.29	0.149	0.017	0.010	0.02061
		STD.DEV.	1.76	1.37	0.06	0.10	0.05	0.01	0.17	0.14	0.2	0.12	0.15	0.11	0.03	0.62	0.26	0.02	0.03	0.037	0.003	0.002	0.00221
		MEDIAN	20.8	17.6	0.44	0.35	0.21	0.09	1.13	0.58	1.54	0.85	2.11	0.98	0.34	4.94	1.36	0.03	0.29	0.147	0.018	0.010	0.02078
		MIN	18.1	15.4	0.35	0.22	0.15	0.07	0.95	0.38	1.03	0.67	1.73	0.81	0.29	3.76	0.75	b.d.l*2	0.25	0.082	0.012	0.007	0.01543
		MAX	25.2	21.4	0.54	0.62	0.38	0.10	1.51	1.00	1.81	1.16	2.26	1.17	0.39	6.22	1.74	0.06	0.36	0.261	0.025	0.016	0.02422
	spots/veins of high reflectivity in layer type 1	AVERAGE (n*1=2)	42.8	2.54	0.13	3.47	1.90	0.21	19.3	5.37	2.37	1.18	1.60	2.43	0.78	0.75	0.20	0.04	0.12	0.012	0.081	0.044	0.00301
		STD.DEV.	1.47	1.24	0.09	0.03	0.24	0.01	9.96	0.21	0.78	0.25	0.00	0.68	0.41	0.81	0.09	0.01	0.01	0.018	0.003	0.004	0.00222
		MIN	41.8	1.67	0.06	3.45	1.73	0.20	12.2	5.22	1.82	1.00	1.60	1.95	0.49	0.17	0.14	0.03	0.11	b.d.l*2	0.079	0.041	0.00144
		MAX	43.9	3.41	0.19	3.49	2.06	0.22	26.3	5.52	2.92	1.36	1.60	2.90	1.06	1.32	0.27	0.05	0.13	0.025	0.084	0.047	0.00459
layer type 2.1	dendritic structure of high reflectivity,	AVERAGE (n*1=9)	42.1	1.11	0.01	1.31	1.85	0.62	45.8	3.16	3.72	1.02	2.02	1.32	0.71	2.45	0.07	0.13	0.10	0.003	0.031	0.044	0.00041
		STD.DEV.	1.70	0.75	0.01	0.29	0.37	0.12	14.0	0.61	0.32	0.36	0.16	0.22	0.21	0.48	0.06	0.02	0.01	0.008	0.007	0.009	0.00003
		MEDIAN	42.1	0.86	b.d.l*2	1.38	1.96	0.63	48.5	3.32	3.81	0.89	2.06	1.30	0.64	2.36	0.05	0.12	0.10	b.d.l*2	0.033	0.046	0.00041
		MIN	38.8	0.75	b.d.l*2	0.84	1.11	0.42	12.5	1.96	3.18	0.56	1.77	1.09	0.57	1.49	0.04	0.11	0.08	b.d.l*2	0.020	0.026	0.00038
		MAX	44.6	3.10	0.02	1.77	2.29	0.76	56.5	3.81	4.18	1.66	2.23	1.75	1.25	3.04	0.23	0.17	0.12	0.025	0.044	0.054	0.00044
	dark areas of layer type 2.1 (total analyzed sums <60%)	AVERAGE (n*1=3)	18.4	0.80	b.d.l*2	0.98	0.58	0.14	24.3	1.57	1.45	1.04	0.78	0.95	0.49	2.71	0.10	0.07	0.15	b.d.l*2	0.053	0.031	-
		STD.DEV.	1.39	0.22	b.d.l*2	0.28	0.17	0.03	7.90	0.45	0.21	0.43	0.04	0.13	0.15	1.29	0.02	0.01	0.01	b.d.l*2	0.011	0.007	-
		MIN	16.8	0.57	b.d.l*2	0.68	0.40	0.12	19.4	1.08	1.22	0.65	0.75	0.87	0.36	1.54	0.08	0.05	0.14	b.d.l*2	0.041	0.024	-
		MAX	19.4	1.00	b.d.l*2	1.22	0.74	0.17	33.5	1.96	1.62	1.50	0.82	1.11	0.66	4.09	0.12	0.07	0.17	b.d.l*2	0.063	0.038	-
layer type 2.2	dense layer of high reflectivity, low Ni+Cu	AVERAGE (n*1=8)	47.9	0.25	0.01	0.51	0.81	0.64	322	1.32	2.93	0.24	1.94	1.74	0.87	0.69	0.03	0.08	0.11	0.008	0.011	0.017	0.00048
		STD.DEV.	1.64	0.20	0.01	0.29	0.33	0.13	211	0.61	0.33	0.23	0.05	0.10	0.06	0.91	0.01	0.01	0.01	0.011	0.007	0.008	0.00008
		MEDIAN	48.2	0.13	0.01	0.44	0.71	0.68	363	1.14	3.01	0.15	1.94	1.76	0.88	0.29	0.03	0.08	0.11	b.d.l*2	0.009	0.015	0.00047
		MIN	44.7	0.07	b.d.l*2	0.27	0.54	0.41	82.7	0.84	2.28	0.02	1.89	1.55	0.79	0.05	0.02	0.06	0.08	b.d.l*2	0.005	0.011	0.00040
		Max	49.9	0.54	0.03	1.15	1.54	0.78	667	2.69	3.37	0.60	2.05	1.84	0.95	2.71	0.04	0.09	0.13	0.023	0.026	0.035	0.00057
layer type 2.3	dense layer of high reflectivity, high Ni+Cu	AVERAGE (n*1=29)	46.2	0.33	0.02	2.02	2.61	0.38	235	4.63	2.95	0.68	1.8	1.86	0.85	0.93	0.04	0.07	0.15	0.002	0.044	0.056	0.00071
		STD.DEV.	1.28	0.23	0.02	0.32	0.27	0.07	191	0.45	0.21	0.29	0.08	0.13	0.11	0.81	0.02	0.01	0.04	0.006	0.007	0.005	0.00052
		MEDIAN	46.4	0.32	0.02	2.02	2.62	0.37	145	4.61	2.95	0.59	1.82	1.85	0.84	0.89	0.03	0.06	0.16	b.d.l*2	0.044	0.056	0.00054
		MIN	42.9	0.06	b.d.l*2	1.41	1.66	0.22	41.0	3.83	2.6	0.22	1.52	1.64	0.61	0.03	b.d.l*2	0.05	0.09	b.d.l*2	0.030	0.039	0.00039
		MAX	48.0	1.10	0.11	2.61	3.00	0.49	826	5.42	3.48	1.62	1.91	2.23	1.17	3.43	0.12	0.10	0.24	0.02	0.056	0.064	0.00256
layer type 2.4	material of high reflectivity, near core	AVERAGE (n*1=5)	45.6	0.54	0.04	1.58	1.99	0.23	97.9	3.56	1.98	0.72	1.34	2.18	0.89	1.12	0.04	0.06	0.42	0.008	0.035	0.044	0.0010
		STD.DEV.	1.30	0.19	0.01	0.23	0.02	0.01	50.4	0.22	0.10	0.24	0.05	0.2	0.04	0.6	0.01	0.01	0.04	0.005	0.006	0.001	0.0002
		MEDIAN	45.0	0.66	0.04	1.59	1.98	0.23	67.9	3.57	1.94	0.82	1.34	2.19	0.87	1.16	0.04	0.05	0.4	0.006	0.036	0.044	0.0009
		MIN	44.6	0.26	0.03	1.25	1.96	0.22	65.0	3.25	1.92	0.31	1.28	1.97	0.85	0.41	0.02	0.04	0.39	0.003	0.026	0.042	0.0008
		MAX	47.7	0.69	0.06	1.79	2.01	0.24	183	3.79	2.16	0.91	1.40	2.40	0.93	1.98	0.05	0.08	0.49	0.016	0.040	0.044	0.0013

*1n = number of analyses; *2b.d.l = below detection limit

Layer type 2:

Layers of type 2 occur in two different growth structures: as dendritic and dense layers with high Mn/Fe ratios (>10). Since their chemical composition is similar to each other they are both interpreted as suboxic-diagenetic precipitates (cf. Chapter II). For further investigation using HRTEM these layers will be separated in different subtypes:

Dendritic growth structure with high Mn/Fe ratio (Layer type 2.1)

The studied dendritic growth structure of nodule 32KG-5 builds up the layer on the bottom side of the nodule which was buried in the upper few cm of the sediment (box 3 in Fig. 3.3 and its high resolution image in Fig. 3.5A).

High Mn/Fe ratios between 13 and 57 (median 49) and Ni+Cu contents of 2 - 3.8 wt.% (median 3.3 wt.%) are characteristic for this layer (Fig. 3.6). The Ni content is slightly lower than the Cu content (Table 3.2). Zn concentrations are relatively high with 0.4 to 0.8 wt.% (median 0.6 wt.%) but the Co contents are generally low (0.01 ± 0.01 wt.%).

Within the centres of dendritic growth structures dark spots occur (Fig. 3.5A). Those zones have low total analytical sums (< 60%, Table 3.2) in EMPA, which is probably due to the high porosity of the material and/or higher water content. However, they are chemically similar to their surroundings with Mn/Fe ratios between 19 and 34 and Ni+Cu concentrations between 1 and 2 wt.%. Only the elements Al, Si and Ti are enriched in the areas of low reflectivity compared to its surroundings which might indicate that these zones are sediment residues (Table 3.2, Fig. 3.5B).
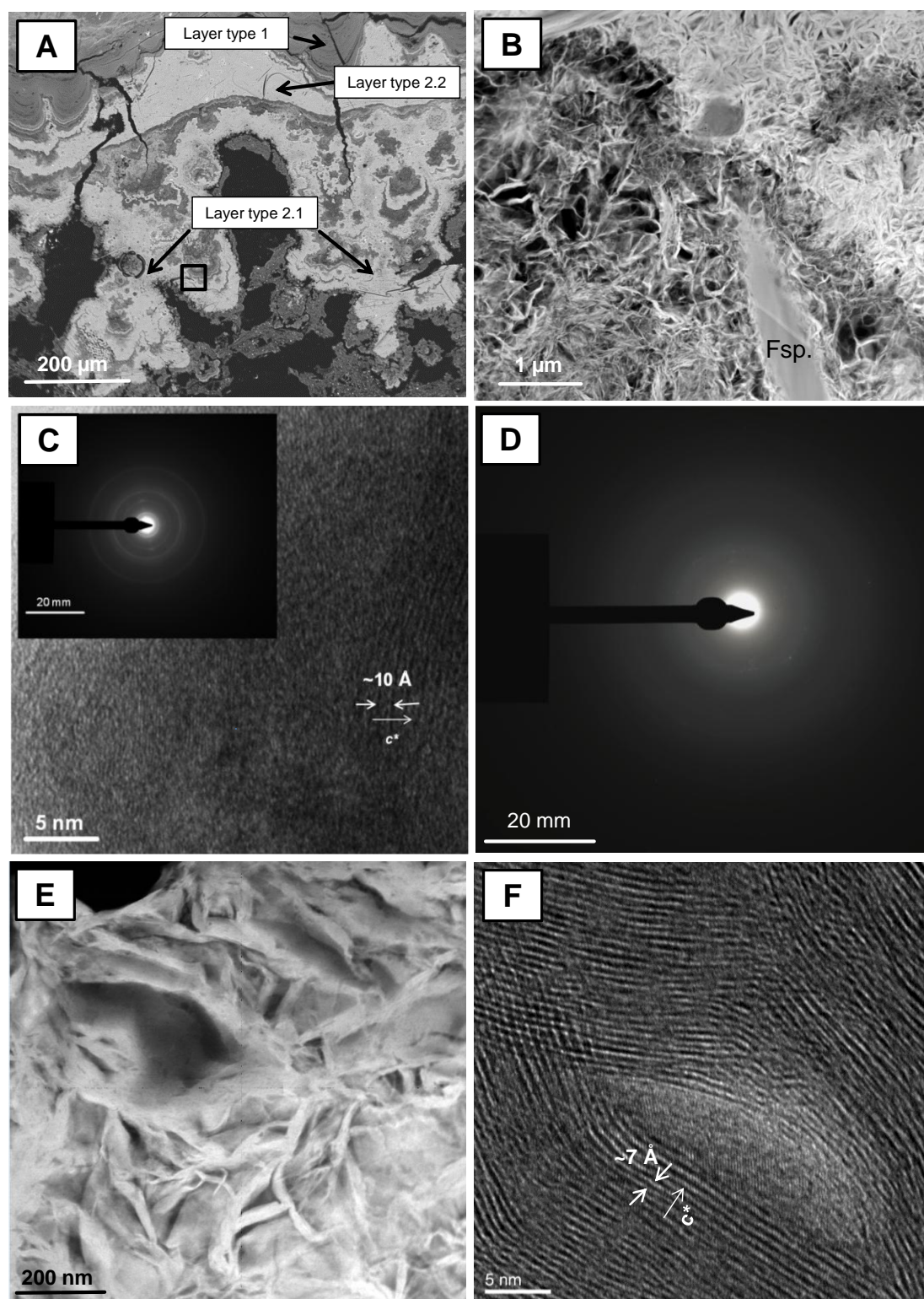
Figure 3.5 A: Three different layer types of the bottom side of nodule SO205-32KG-5 (marked as area 3 in Fig. 3.3). Dendritic growth structures (layer type 2.1) show dark areas within their centers. **B:** High-angle annular dark field images (HAADF) (for location see black rectangle in **A**, showing the internal growth structure of layer type 2.1 with thin needles/ plates growing together to form a network of variable density. Detrital minerals such as feldspar (Fsp.) occur in the more porous (darker) parts of the dendritic growth structures. **C:** HRTEM image and insert the coresponding SAED pattern of the bright dendritic material with diffraction points at ~10 Å, ~5 Å and 3.3 Å as well as ~7 Å, ~3.5 Å, 2.45 Å, 2.2 Å and 1.4 Å corresponding to 10 Å and 7 Å phyllomanganates. **D:** SAED of darker areas within layer type 2.1, indicating diffraction rings ~4.5 Å, ~3.3 Å, 2.5 Å, 2.2 Å. **E:** HAADF of dense layer type 2.2 in **A** show a dense network of needles. **F:** HRTEM image of E with distinct lattice fringes of ~7.

Dense layers with high Mn/Fe ratio (Layer type 2.2 and 2.3)

Two dense layers of high reflectivity were analyzed. Layer type 2.2 occurs at the bottom side of the nodule, directly below the outermost dendritic growth structure (box 3 in Fig. 3.3 and high resolution image in Fig. 3.5A) and has Mn/Fe ratios between 83 and 667. The Ni+Cu content range between 0.8 and 2.7 wt.% (median 1.1 wt.%; Fig. 3.6; Table 3.2). In contrast, the second dense layer 2.3 is located near the nodule top side which was in contact with the bottom ocean water (box 1 in Fig. 3.3 and high resolution image in Fig. 3.7A). The Mn/Fe ratios are high and vary between 41 and 826 (median 145). In contrast to layer type 2.2 this kind of layer shows much higher Ni+Cu contents (3.8 - 5.4 wt.%; median 4.6 wt.%, Fig. 3.6). The Cu content is higher than Ni in both dense layer types. Furthermore, both dense layers show low Co contents and quite similar amounts of alkali and earth alkali metals (Table 3.2).
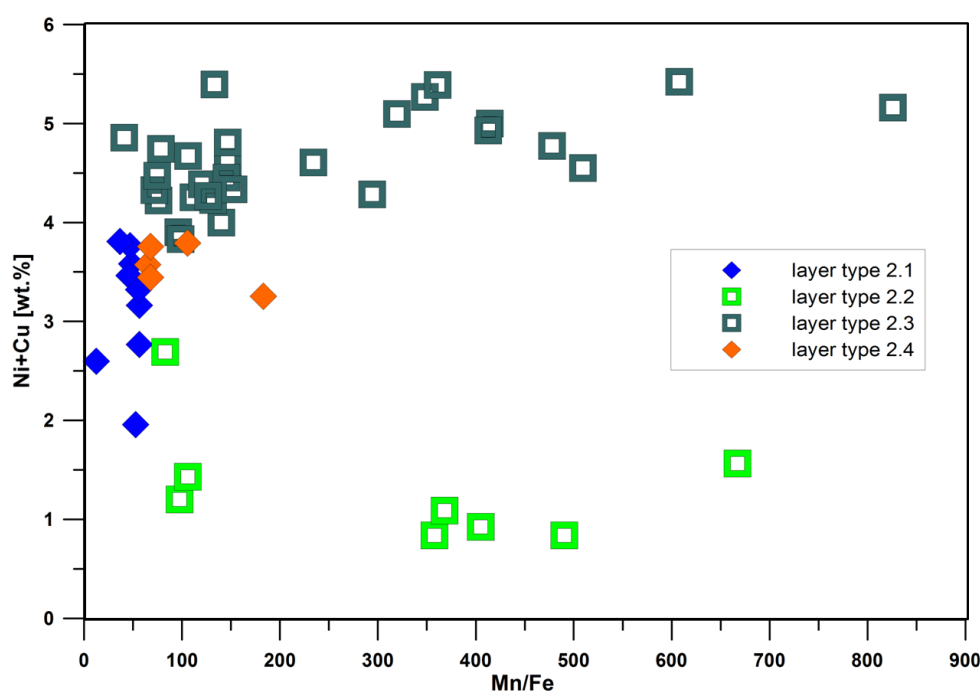
FIGURE 3.6 Mn/Fe versus Ni+Cu content of individual type 2 layers of nodule SO205-32KG-5. All individual layers have high Mn/Fe ratios and show high variation of Ni+Cu.
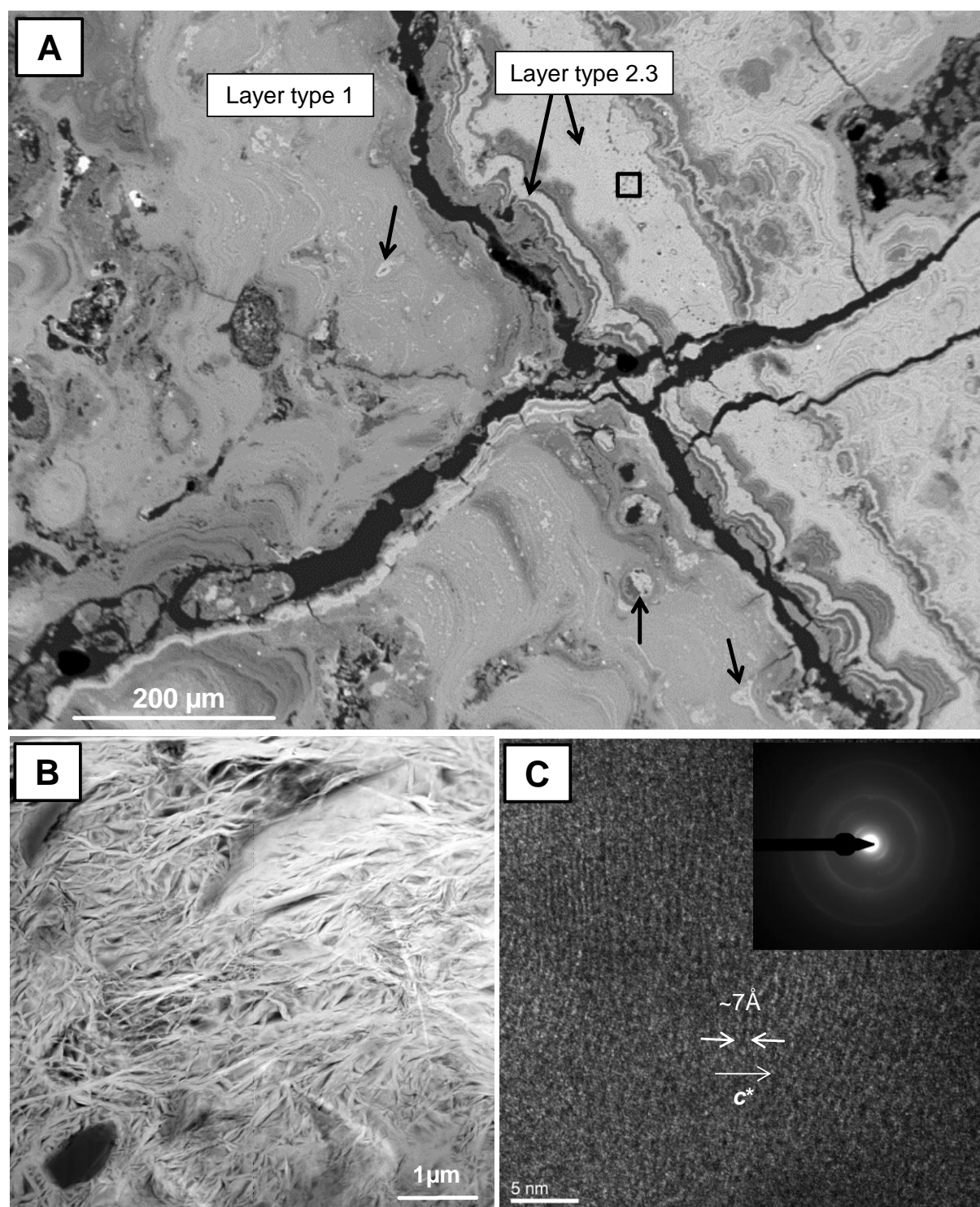
FIGRUE 3.7 A: Layer types 1 and 2.3 near the top of the nodule (marked as area 1 in Fig. 3.3). The black square in layer type 2.3 marks the area of HRTEM analyses **(B)**. **B:** HAADF image of layer type 2.3 showing internal growth structure forming a network of plates and needles. **C:** HREM image of dense layer type 2.3, lattice fringe separation is ~7Å corresponding to turbostratic 7 Å phyllomanganate. Electron diffraction (inset) shows diffuse and weak rings around 7 Å, 3.5 Å, 2.4 Å belonging to the 7 Å Mn-phase. Diffraction rings around 4.5 Å probably indicate the occurrence of 10 Å phyllomanganates.

Layer near the core with high Mn/Fe ratio (Layer 2.4)

Layer 2.4 represents the second layer around the nucleus of the nodule and has similar optical properties as the dense layers (box 2 in Fig. 3.3 and its high resolution image in 3.8A). The Mn/Fe ratios vary between 65 and 183 (median 68), the Ni+Cu contents are rather homogenous (3.3 - 3.8 wt.%, median 3.6 wt.%; Fig. 3.6; Table 3.2) and Zn shows concentrations of 0.23 ± 0.01 wt.%. Similar to layer types 2, the Co contents are low (0.04 ± 0.01 wt.%; Table 3.2). This layer shows slightly higher Mg than Na concentration which is in contrast to the other layers of type 2.
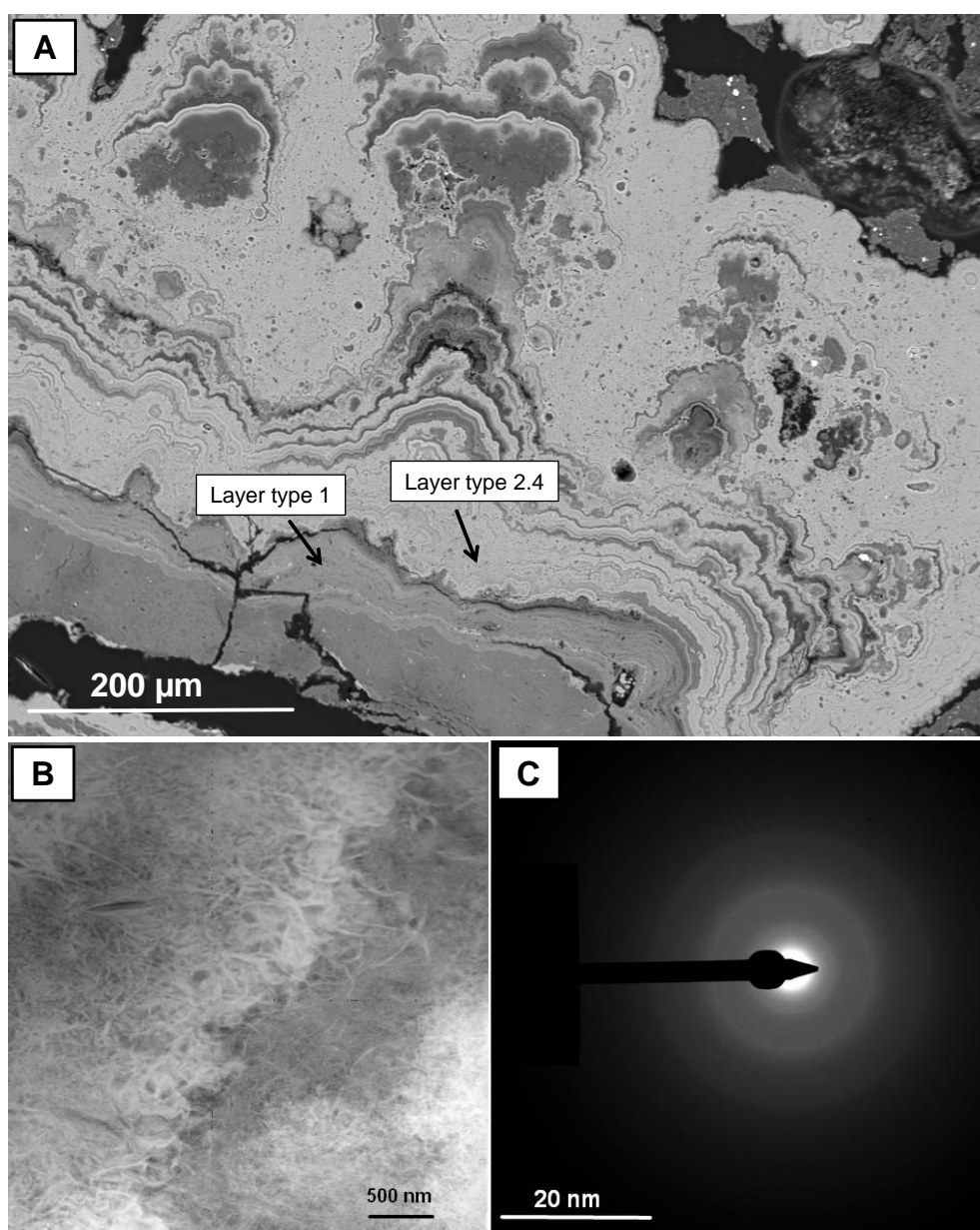
FIGURE 3.8 A: Layer type 2.4 near the core of nodule 32KG-5 (marked as area 2 in Fig. 3.3) also layer type 1 is recognized below layer type 2.4. **B:** HAADF image displaying internal growth structure with very thin needles forming a fluffy network. **C:** SAED pattern of the layer with diffractions at ~5 Å, 2.5 Å and ~1.4 Å indicating 10 Å phyllomanganates.

3.4.2 Chemical investigation of the profile through nodule 44KG-2

Chemical analysis of the profile through nodule 44KG-2 (Fig. 3.2A) reveals slight chemical changes from the outer surface of the nodule to their centre (near core). The Mn/Fe ratio increases from 5.21 ± 0.63 (upper 10 mm) to 10.79 ± 3.62 (down to 32 mm (near core); Table 3.3). The content of Ni+Cu is variable within the whole profile without a distinct trend. In contrast to that alkali (Na, K) and earth alkali metals (Mg, Ca Ba) show distinct changes within the measured profile. An increase of Mg, K and Ba accompanied by a decrease of Na and Ca with depth was observed (Table 3.3, Fig. 3.9).

TABLE 3.3 Chemical composition of the profile trough nodule 44KG-2 (ICP-OES data; wt.%)

distance from the surface to the core		Mn	Fe	Ni	Cu	Co	Zn	Mn/Fe	Ni+Cu	Na	K	Al	Ca	Mg	Ti	Mo	Ce	Ba
surface	0.5-2mm	33.70	7.27	1.27	1.14	0.15	0.17	4.64	2.41	3.66	0.89	2.09	1.73	1.95	0.25	0.05	0.03	0.17
	2-4mm	36.00	6.41	1.54	1.40	0.16	0.14	5.62	2.94	3.09	0.95	2.44	1.74	1.83	0.25	0.05	0.02	0.17
	4-6mm	34.30	5.74	1.68	1.38	0.17	0.14	5.98	3.06	2.65	0.96	2.95	1.74	1.94	0.28	0.05	0.02	0.23
	6-8mm	31.00	5.80	1.42	1.16	0.12	0.12	5.34	2.58	2.44	0.90	2.46	1.71	1.63	0.27	0.06	0.03	0.30
	8-10mm	32.90	7.31	1.22	1.17	0.16	0.11	4.50	2.39	2.27	0.96	2.14	1.55	1.76	0.28	0.06	0.03	0.32
	10-12mm	36.90	4.65	1.18	1.35	0.09	0.13	7.94	2.53	1.89	1.17	1.97	1.28	2.10	0.20	0.05	0.02	0.34
	12-14mm	38.10	5.00	1.41	1.67	0.15	0.15	7.62	3.08	2.25	1.50	3.07	1.30	2.77	0.17	0.04	0.02	0.38
	14-16mm	35.80	3.09	1.33	1.59	0.21	0.14	11.6	2.92	2.02	1.30	3.21	1.21	2.58	0.20	0.04	0.02	0.46
	18-20mm	33.50	2.89	1.11	1.41	0.21	0.12	11.6	2.52	2.06	1.50	3.62	1.12	2.50	0.19	0.04	0.01	0.59
	20-22mm	33.20	2.44	1.03	1.24	0.18	0.11	13.6	2.27	1.95	1.46	3.24	1.02	2.28	0.19	0.05	0.02	0.67
	22-24mm	35.60	2.37	1.07	1.22	0.16	0.10	15.0	2.29	2.03	1.63	3.34	1.09	2.30	0.16	0.05	0.01	0.68
	24-26mm	39.90	2.46	1.14	1.32	0.15	0.12	16.2	2.46	1.95	1.63	2.95	1.18	2.40	0.13	0.05	0.01	0.58
	26-28mm	39.50	3.40	1.46	1.50	0.14	0.14	11.6	2.96	1.87	1.30	2.12	1.26	2.42	0.12	0.05	0.01	0.43
near core	28-30mm	34.10	6.77	1.48	1.27	0.21	0.17	5.04	2.75	2.04	1.04	2.32	1.73	1.98	0.22	0.06	0.02	0.36
	30-32mm	36.00	4.67	1.22	1.30	0.18	0.13	7.71	2.52	1.55	1.35	2.43	1.29	2.31	0.15	0.06	0.02	0.44
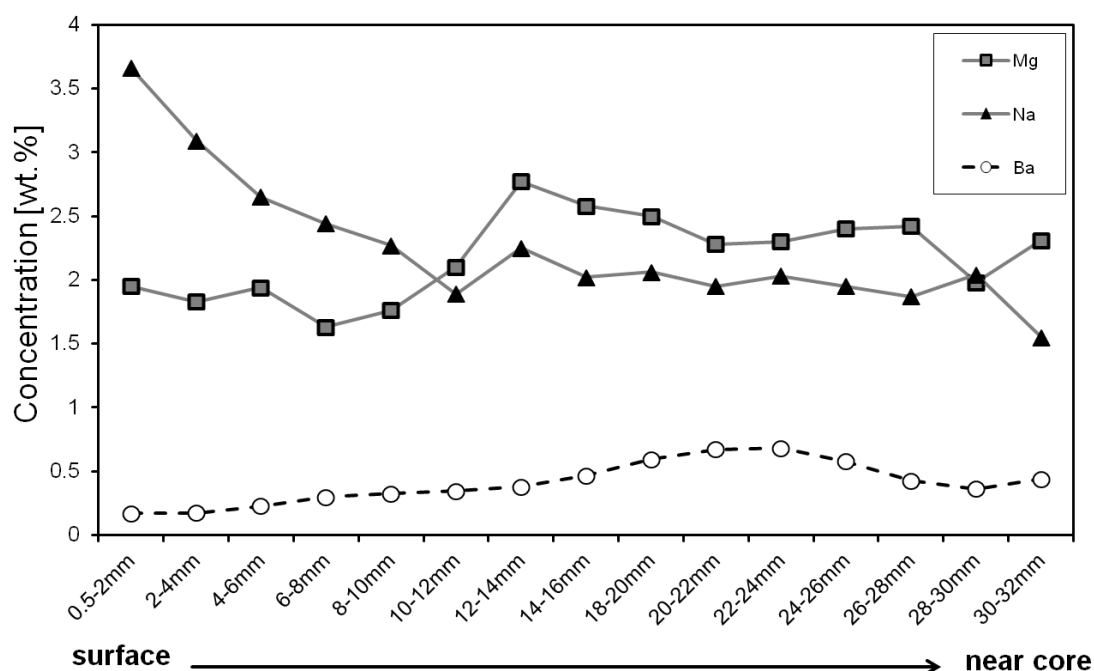
FIGURE 3.9 The distribution of Mg, Na and Ba along a profile through nodule 44KG-2. In the outer layers Na is enriched over Mg and Ba, whereas in the inner layers of the nodule Mg is enriched compared to Na. The content of Ba also increased in the inner layers.

3.4.3 Mineralogy of bulk nodules

3.4.3.1 XRD drying experiments

Figure 3.10 show XRD patterns of a typical CCZ nodule (BIONOD 26KG) after different drying steps (RT – room temperature, 40°C, 100°C, and 300°C). The XRD pattern of the RT sample shows distinct but broad reflections at ≈10 Å (9.9 Å) and ≈5 Å (4.9 Å) which can be attributed to the 001 and 002 basal reflections of a 10 Å phyllomanganate or to the most intense diffraction maximum of todorokite (100 reflection, using the structure model from Post and Bish, 1988). Only a small and weak hump around 7 Å can be recognized, which could represent the 001 basal reflection of minor amounts of a 7 Å phyllomanganate phase. The patterns after drying at 40°C and 100°C indicate a decrease in intensity of the ≈10 Å peak and a simultaneous increase of the ≈7 Å peak, which indicate that the original mineral is a phyllomanganate (and not todorokite). After drying at 300°C the basal reflections at ≈10 Å and ≈5 Å as well as ≈7 Å disappeared. In another sample (32KG-5), which was analyzed after drying at 40°C, 100°C, 150°C, 200°C and 300°C, basal reflections completely disappeared already at 200°C (Table 3.4).

All analyzed nodules display patterns with two *hk*-bands at ≈2.45 Å (100) and ≈1.42 Å (110) which remain constant after each drying step. Additionally, the 2.45 Å peak is asymmetrical indicating that the studied phyllomanganate is a turbostratic vernadite. The calculated d_{100}/d_{110} ratio of the *hk*-bands of every nodule is ~1.73 and therefore, close to √3, which suggests hexagonal layer symmetry of the Mn-phases (Drits et al., 1997; Bodeï et al., 2007; Grangeon et al., 2008). This is confirmed by the almost symmetrical shape of the (110) reflection, which would be split into a double peak in case of triclinic symmetry (Drits et al., 2007). All these information can be quantitatively validated by modelling an X-ray diffraction pattern typical for this kind of nodules (Fig. 3.11, Table 3.5).

X-ray diffraction analyses of different bulk nodules after drying at 40°C and 100°C, reveal considerable intensity changes of the diffraction peaks from distinct ≈10 Å (9.7 - 9.9 Å) and weak broad ≈7 Å (7.1 - 7.4 Å) to very weak and broad diffraction peaks between 9 and 9.7 Å and a more distinct ≈7 Å reflection (7.1 - 7.3 Å; Table 3.4). After drying the (001) reflections of both basal reflections (10 and 7 Å) are broad and difficult to distinguish. Furthermore, all samples show two *hk*-bands at ≈2.45 (asymmetrical) and ≈1.42 Å (Table 3.4). These features are characteristic for the occurrence of turbostratic vernadite. Furthermore, quartz (Qz) and minor amounts of phillipsite (Ph) were detected (Fig. 3.10).
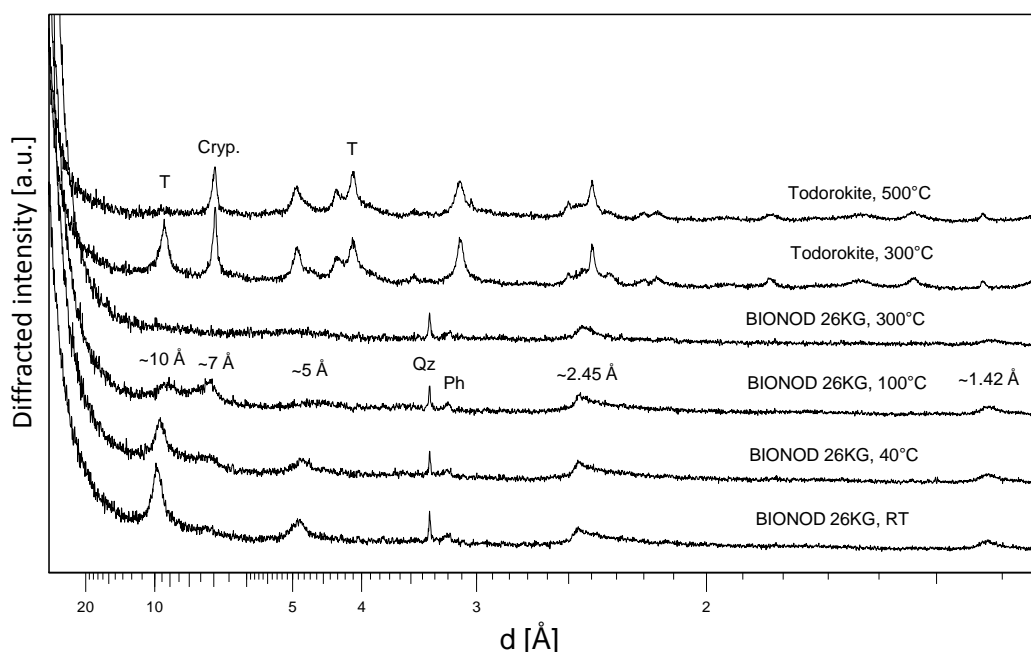
Figure 3.10 XRD patterns of a typical CCZ nodule (26KG) and a hydrothermal todorokite (T) after drying at different temperatures (RT=room temperature). Basal reflections of ≈10 Å and ≈7 Å of nodule 26KG change between all drying steps, an increase of the ≈7 Å and a simultaneous decrease of the ≈10 Å peaks represent different stable and unstable turbostratic phyllomanganates with a hexagonal layer symmetry (*hk*-bands at 2.45 and 1.42 Å; $d_{100/110}$ = ~1.73). The basal reflections of the CCZ nodule completely disappeared upon drying at 300°C whereas the hydrothermal todorokite still shows a distinct 10 Å peak even at 300°C and is completely disappeared at 500°C. Within the hydrothermal sample also cryptomelane (Cryp.) was detected.

TABLE 3.4 Results of XRD analyses of bulk nodules after different heating steps compared with a hydrothermal todorokite. Symbol x indicates the occurrence and the intensity of the diffraction peaks

sample SO205	RT		40°C		100°C		150°C		200°C		300°C		400°C		500°C	
	10 Å	7 Å	10 Å	7 Å	10 Å	7 Å	10 Å	7 Å	10 Å	7 Å	10 Å	7 Å	10 Å	7 Å	10 Å	7 Å
09KG-B	n.a.	n.a.	+++	+	+	++	n.a.	n.a.	n.a.	n.a.	n.a.	n.a.	n.a.	n.a.	n.a.	n.a.
29KG-C	n.a.	n.a.	++	+	hump	++	n.a.	n.a.	n.a.	n.a.	n.a.	n.a.	–	–	–	–
26KG	+++	hump	++	+	+	++	n.a.	n.a.	n.a.	n.a.	–	–	n.a.	n.a.	n.a.	n.a.
32KG-4*1	n.a.	n.a.	++	+	+	+	n.a.	n.a.	n.a.	n.a.	n.a.	n.a.	n.a.	n.a.	n.a.	n.a.
32KG-5	n.a.	n.a.	++	+	+	+	–	–	–	–	–	–	–	–	–	–
44KG-2*1	n.a.	n.a.	+++	+	++	++	n.a.	n.a.	n.a.	n.a.	n.a.	n.a.	–	–	–	–
62KG-A	n.a.	n.a.	++	hump	++	++	n.a.	n.a.	n.a.	n.a.	n.a.	n.a.	–	–	–	–
Todorokite	n.a.	n.a.	++++	Cryp.	++++	Cryp.	n.a.	n.a.	++++	Cryp.	+++	Cryp.	++	Cryp.	–	Cryp.

*1 = analyzed in Capter II, n.a. = not analyzed, - = diffraction peaks disappear; Cryp. = Cryptomelane
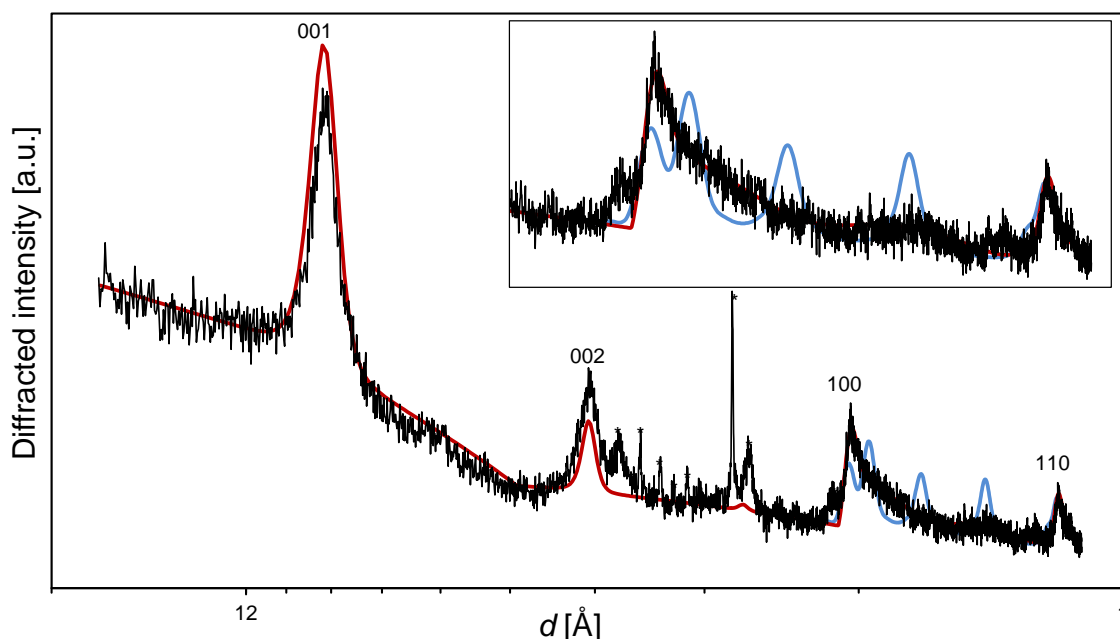
FIGURE 3.11 Experimental X-ray diffraction pattern from a typical nodule from German eastern license area of the CCZ (black solid line) and calculated patterns of a turbostratic vernadite (red solid line) and of a birnessite (blue solid line) have the same structure than the vernadite, but 1H stacking mode (i.e. no random stacking fault). In the birnessite pattern (i.e. ordered variation), *hkl* Bragg peaks are expressed, but not observed in the experimental pattern. In the vernadite (i.e. turbostratic variation) pattern, only 00*l* Bragg reflections and asymmetric *hk* bands are expressed, as in the experimental pattern. The experimental pattern is thus, indexed using the vernadite structure model. Stars indicate impurities. Inset: detailed view of the 3 Å to 1.4 Å region (calculation of the patterns were done by S. Grangeon)

TABLE 3.5 Parameters for the modeling of X-ray diffraction pattern of vernadite typical for nodules of this study

Atom[1]	Atomic coordinates[1]			Site occupancy[2]
	x	*y*	*z*	
Mn	0.000	0	0	0.92
O	0.333	0	0.103	2
Mn	0.000	0	0.221	0.16
O	-0.333	0	0.349	0.48
K	-0.500	0	0.500	0.02
K	-0.250	0.250	0.500	0.02
K	-0.250	-0.250	0.500	0.02
O	0.160	0.000	0.500	0.02
O	-0.080	0.240	0.500	0.02
O	-0.080	-0.240	0.500	0.02

Note: symmetry operations: (x, y, z), $(-x,-y,-z)$, $(x+\frac{1}{2}, y+\frac{1}{2}, z)$, $(-x+\frac{1}{2}, -y+\frac{1}{2}, -z)$. The structure can be drawn in the *C2/m* space group to ease representation, but care must be taken not to generate positions from adjacent layers, as the structure is turbostratic. The refined mean coherent scattering domains are 7 nm in the **a-b** plane and 7.8 nm along **c***.

[1] Debye-Waller factors were set to 0.5 Å² for Mn1, 1 Å² for OMn1 and 2 Å² for all other species.

[1] Atomic coordinates in fraction of a, b and c which are respectively equal to 4.940 Å, 2.852 Å and 9.750 Å. $\gamma = 90°$. The structure is described using $\gamma=90°$ to ease comparison with previously published structure models, but it could also be described using $\gamma=120°$, as layer symmetry is hexagonal.

[2] Expressed per layer octahedron, and as the sum of the equivalent (x, y, z) and (-x, -y, -z) sites. (Parameters for the calculation of the patterns in Fig. 3.11 were summarized by S. Grangeon)

3.4.3.2 Hydrothermal Mn oxide sample

In addition to the CCZ nodules, a hydrothermal Mn oxide was analyzed at 40°C, 100°C, 200°C, 300°C, 400°C and 500°C as a reference sample for todorokite. Characteristic XRD peaks to distinguish todorokite from phyllomanganates are the distinct reflections at ≈10 Å and ≈5 Å that are indicative for the (001) and (002*)* basal reflections of phyllomanganates or of (100) and (200) reflections of todorokite (using the structure model from Post and Bish, 1988). In contrast to those observed in the CCZ nodules, the mineralogy does not change during heating up to 200°C (Fig. 3.10). The ≈10 Å peak decreased slightly after drying at 300°C. All other diffraction peaks remain constant. During the drying experiments up to 500°C the ≈10 Å peak completely disappeared (Table 3.4; Fig. 3.10). The absence of collapsing structure together with thermal stability up to ~500°C (Shen et al., 1993) is typical for todorokite. Furthermore, characteristical peaks of cryptomelane can also be detected which is probably intergrown with todorokite on a fine scale (Fig. 3.10).

3.4.3.3 XRD of profile across nodule 44KG-2

Subsamples from a drilled profile across nodule 44KG-2 (bulk composition described in Chapter II) were investigated using XRD (Fig. 3.12). All subsamples starting at the nodule surface down to ~30 mm (near the core within the nodule) display distinct basal reflections at ≈10 Å and small peaks around ≈7 Å after heating at 40°C (XRD pattern not shown). Furthermore, two *hk*-bands are present at ≈2.45 Å (indexed as a (100) reflection assuming a hexagonal unit cell with γ = 120°*)* and ≈1.42 Å (110).

Upon heating to 100°C, samples from 0 to 5 mm reveal distinct changes in the low angle region, especially around ≈10 Å and ≈7 Å (Fig. 3.12). The intensive broad ≈10 Å-peak (before heating at 100°C, XRD pattern not shown) disappeared and the peak around ≈7 Å increased. Samples from 5.2 to 6.8 mm have peaks at ≈10 Å and ≈7 Å which are almost equal. The reflection around 10 Å moved to lower angle regions (9 - 9.6 Å). In samples from 6.8 to ~30 mm, the ≈10 Å peak changed to slightly lower diffraction angles (9 - 9.5 Å) but is still present upon heating to 100°C but the ≈7 Å peak disappeared (Fig. 3.12). The diffraction patterns are very weak and broad, which is probably due to the small amount and nano size of the sample material. Nevertheless, the different changes within the lower and higher angle region, which are characteristic for the different Mn-phases, (stable and unstable 10 Å manganates) are

distinct and some conclusions about mineralogical changes from the surface of the nodule to the inner layers can be drawn.
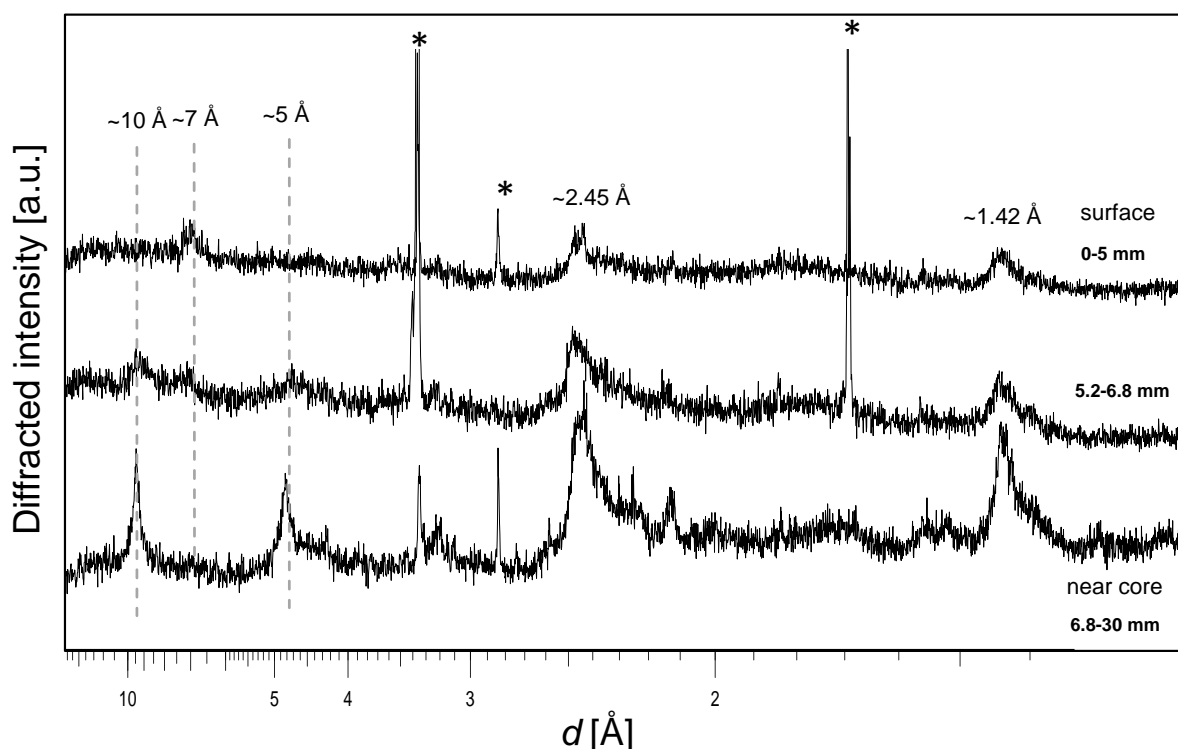
FIGURE 3.12 Three characteristic XRD patterns (after drying at 100°C) of different depth intervals (0 – 30 mm) within nodule SO205 44KG-2. Samples from 0 – 5mm reveal only one basal peak at ≈7 Å, in samples from 5.2 – 6.8mm two peaks at ≈10Å and ≈7Å occur, and in the lower interval only the 10Å peak is present. This shift indicates the presence of only stable 10 Å phyllomanganates in the lower (older) part of the nodule, a transition zone with both stable and unstable 10 Å phyllomanganates and only unstable ones close to the surface (youngest part). Stars indicate impurities. Two *hk*-bands at ≈2.45 Å and ≈1.42 Å can be distinguished.

3.4.3.4 High resolution transmission electron microscopy

High resolution transmission electron microscopy (HRTEM) was performed on foils from individual, chemically different layers of nodule 32KG-5. Figure 3.3 represents a BSE image of nodule 32KG-5 with marked locations (boxes 1 - 3) of TEM foil preparation.

Layers of low Mn/Fe (Layer type 1)

The two type 1 layers investigated during this study consist of very small and thin 50 nm crystals/needles. Energy-dispersive X-ray (EDX) analyses of the nm-structures indicate almost equal amounts of Mn and Fe (Mn/Fe 1 - 3; Figs. 3.13A, B). The Fe content is much higher than in the layer type 2 (similar to results of EMPA, Table 3.2). Metal concentrations of Ni, Cu and Co were below the detection limit of the EDX system. Neither HRTEM images

show any lattice fringes nor electron diffraction patterns show any diffraction spots (Fig. 3.4B) suggesting an amorphous or cryptocrystalline state of the material.

In layers of type 1 bright spots and veins of high reflectivity can be detected (Fig. 3.4A). One of those veins was analyzed using HRTEM (Fig. 3.4C). In contrast to the fine-grained material of low reflectivity, the bright vein shows distinct needles which are well crystallized similar to the growth structures of type 2 layers. EDX analyses of the bright material revealed an enrichment of Mn relative to Fe (Fig. 3.13C), which is in agreement with the results of the EMPA analyses (Fig. 3.13C). Furthermore, Ni, Cu, Na and Mg were also detected in much higher concentrations within the bright vein (see also Table 3.2, EMPA data).

HRTEM images (Fig. 3.4C) of the vein indicate distinct lattice fringes with *d*-spacings of approximately $\approx$10 Å (001) which is characteristic for 10 Å phyllomanganates but also lattice fringes with *d*-spacings of $\approx$6.7 - 7 Å can be detected which is typical for 7 Å phyllomanganates. The selected area electron diffraction (SAED) pattern of the bright vein shows diffraction rings at $\approx$4.6 Å, $\approx$2.5 Å, $\approx$2.4 Å, and $\approx$1.4 Å (Table 3.6). The reflection at $\approx$4.6 Å is indicative for the (002) reflection of the 10 Å phyllomanganate even if the (001) reflection could not be detected in the SAED pattern. The reason is that the high intensity of the primary electron beam overlaps the comparatively weak intensities of the 10 Å reflections. In reciprocal space the 10 Å reflections are very close to the primary electron beam. Only the reflection detected around 5 Å indicates that this is the 002 basal reflection of 10 Å phyllomanganate. The two reflexions at $\approx$2.4 Å (100) and $\approx$1.4 Å (110*)* are probably *hk*-bands from vernadite. This indicates hexagonal layer symmetry ($d_{100/110}$=1.73 similar to $\sqrt{3}$; Drits et al., 1997; Bodeï et al., 2007; Grangeon et al., 2008).

Furthermore, within the hydrogenetic layer, in the surrounding of a bright spot, material enriched in Ti, Si, Fe, Al and Na was detected (Fig. 3.13D).
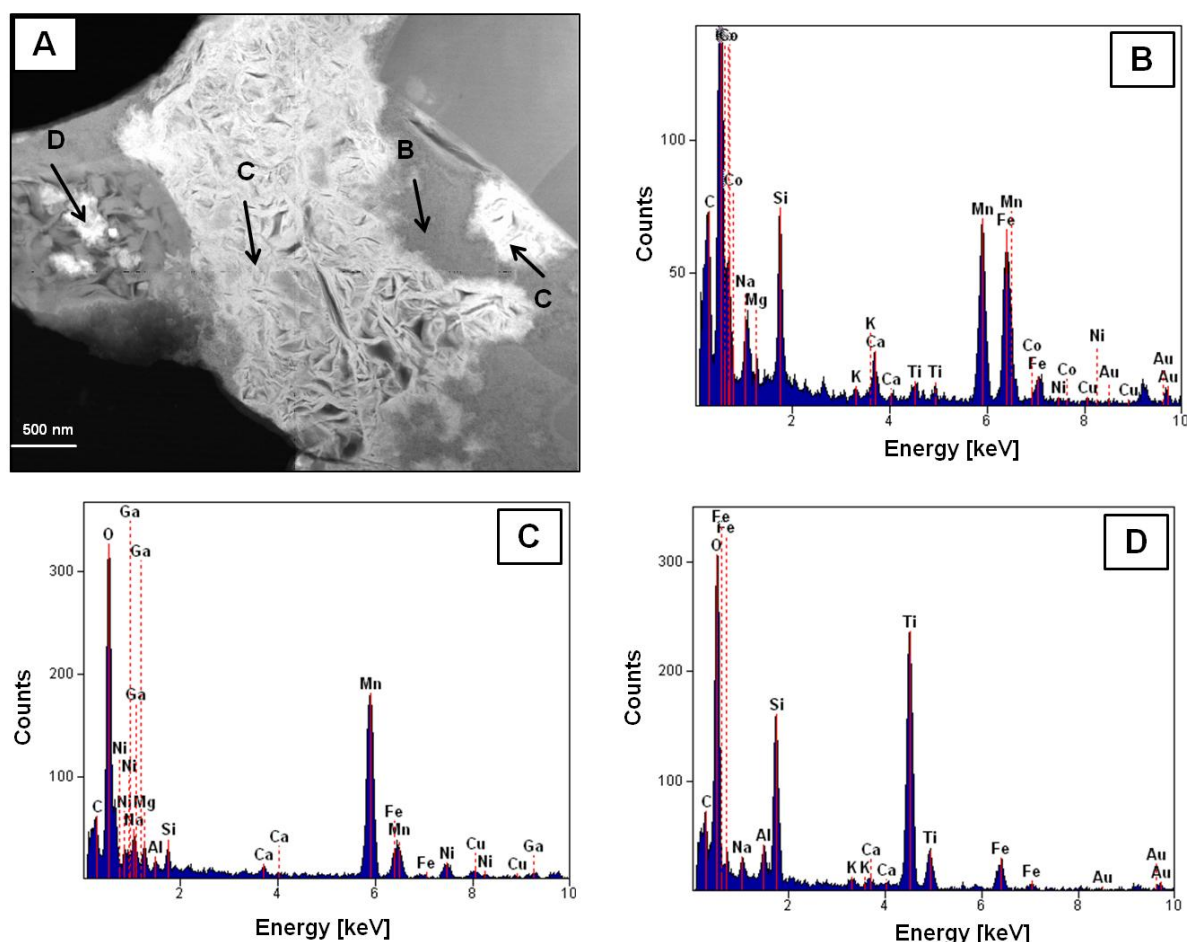
FIGURE 3.13 A: HAADF image of **layer type 1** with spots and veins of high reflectivity and their chemical analyses using EDX (B - D). **B:** EDX analyses of materials of low reflectivity, with similar Mn and Fe contents (hydrogenetic). **C:** EDX analyses of bright spot indicating high amounts of Mn in contrast to Fe. **D:** EDX analyses of Fe-Ti phase within layer type 1.

Layers of high Mn/Fe ratios (Layer type 2)

All layers of type 2 with high Mn/Fe ratios consist of individual, needle-like and platy crystals varying in size and density forming a porous network (Figs. 3.5B, E, 3.7B, 3.8B). EDX analyses of the layers indicate high Mn concentrations, no detectable Fe, the presence of Ni in different amounts as well as Na and Mg as major cations where Na is exceeding Mg (Fig. 3.14A - D).

Darker areas within the dendritic layer type 2 are similar to the surrounding material with high Mn contents and significant enrichment of metals such as Ni (Fig. 3.14B; Table 3.2). In contrast to the bright dendritic material as well as to the other layers, these darker zones consist of very thin needles that are intergrown with each other forming a porous network (Fig. 3.5B). Within darker areas higher amounts of detrital minerals can be detected such as kaolinite, illite, feldspar or quartz (Fig. 3.5B).
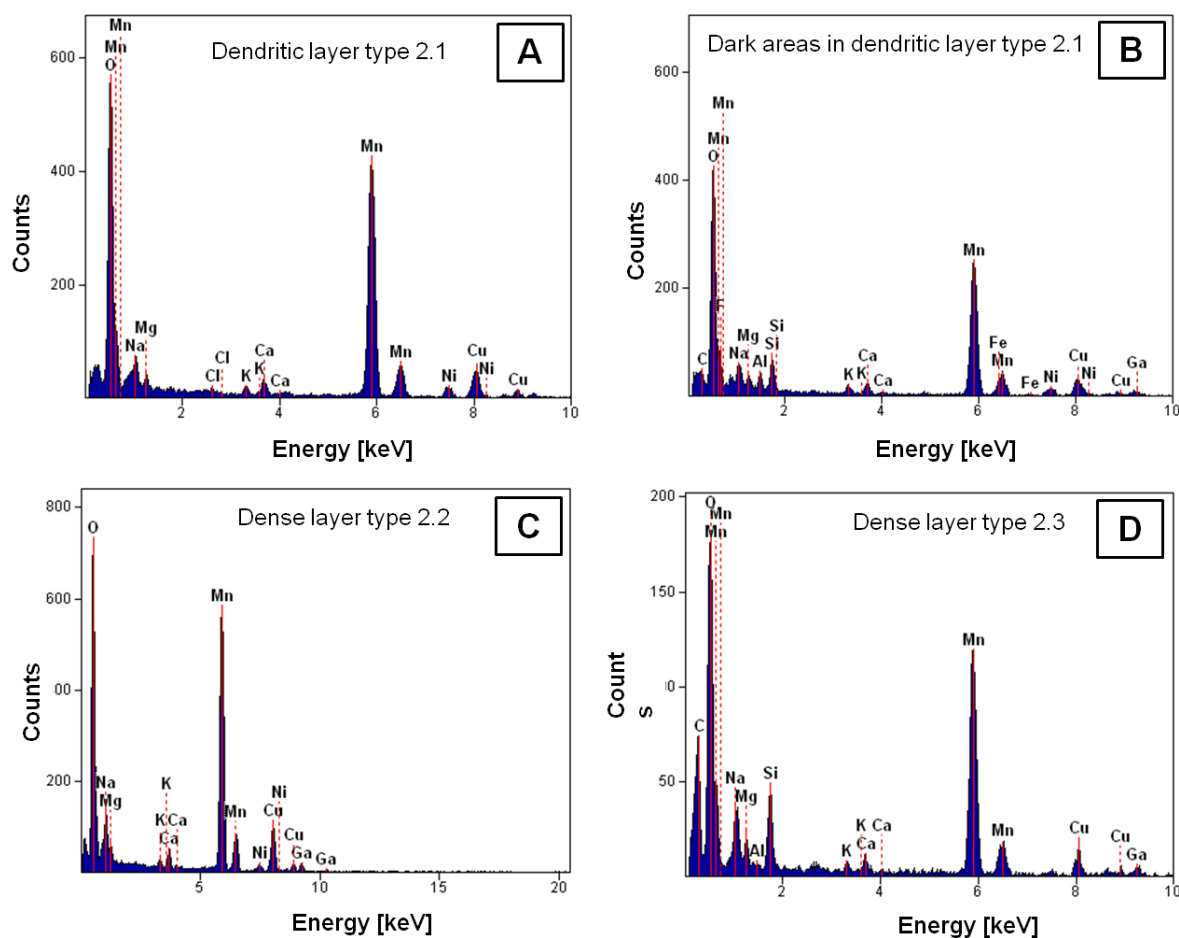
FIGURE 3.14 A: EDX analyses of the dendritic growth structure (layer type 2.1). **B:** EDX analyses of the dark porous areas within the dendritic growth structure. Similar to the bright material high Mn contents can be detected. **C:** EDX spectrum of layer type 2.2 with high Mn concentrations but no Fe. **D:** EDX analyses of layer type 2.3 with high Mn contents and no Fe. Na is enriched over Mg in all samples. Cu is enriched over Ni in all samples caused by the sample holder consisting of Cu.

All layers with high Mn/Fe ratios except of layer type 2.4, show distinct *d*-spacing lattice fringes in HRTEM images of ≈7 Å. The SAED patterns also show distinct diffraction peaks around 7 Å, 3.5 Å, and weak at around 2.5 Å, 2.4 Å, 2.2 Å and 1.4 Å which correspond to a 7 Å phyllomanganate (Fig. 3.7C; Table 3.6).

Additionally, the dendritic growth structure and dense layer with high Ni+Cu content (layer type 2.3) have SAED patterns with diffraction rings around 5 Å which are attributable to the (002) reflection of 10 Å phyllomanganate. Moreover, the dendritic growth structures (layer type 2.1) display 10 Å in the SAED pattern and show HRTEM images with distinct *d*-lattice fringes of ≈10 Å, supporting the presence of 10 Å phyllomanganates (Fig. 3.5C). SAED pattern of dark areas of dendritic growth structure reveal reflections at ≈5 Å, 3.3 Å, 2.5 Å and 2.2 Å.

Dense layers of type 2.2 and 2.3 have additionally lattice fringes with *d*-spacing corresponding to ≈5.5 Å which is characteristic for a completely dehydrated phyllomanganate (Cygan et al., 2012).

The SAED pattern of layer type 2.4 shows only diffraction rings around ≈5 Å (002), and weak pattern ≈2.5 Å and ≈1.4 Å (Fig. 3.8C) indicating a 10 Å phyllomanganate. There is no evidence for the presence of 7 Å phyllomanganate.

All layers reveal weak reflections around 2.4 and 1.4 Å, which are characteristic for *hk* bands of phyllomanganates with hexagonal layer symmetry. The absence of these reflections in some regions of the layers might be explained by the small particle size (nano-range) and the low crystallinity of the material. Table 3.6 summarizes the observed *d*-lattice spacings from HRTEM images and the corresponding electron diffraction pattern of each layer.

In most cases the occurrence of the 10 Å reflections can be detected exclusively within the HRTEM images but not within the SAED pattern from individual layers.

TABLE 3.6 Results of the HRTEM analyses of individual layers of nodule 32KG-5. Symbol x indicates the occurrence of individual lattice fringes and the detectable reflections within selected area electron diffraction pattern of individual layers

individual layers	layer description	10 Å (001) (HRTEM)	10 Å (001) (SAED)	5.5 Å (001) (HRTEM)	5.5 Å (001) (SAED)	5 Å (002) (SAED)	3.3 Å (003) (SAED)	7 Å (001) (HRTEM)	7 Å (001) (SAED)	3.5 Å (002) (SAED)	2.5 Å (SAED)	2.2 Å (SAED)	2.4 Å (SAED)	1.4 Å (SAED)
layer type 1	dense layer of low reflectivity	-	-	-	-	-	-	-	-	-	-	-	-	-
spots/veins of high reflectivity in layer type 1		x	-	-	-	x	-	x	-	-	x	-	x	x
layer type 2.1	dendritic structure of high reflectivity	x	x	-	-	x	x	x	x	x	x	x	x	x
dark areas in layer type 2.1		n.a.	-	-	-	x	x	n.a.	-	-	x	x	-	-
layer type 2.2	dense layer of high reflectivity, low Ni+Cu	-	-	x	x	-	-	x	x	x	x	x	x	x
layer type 2.3	dense layer of high reflectivity, high Ni+Cu	-	-	x	x	x	-	x	x	x	x	x	x	x
layer type 2.4	material of high reflectivity, near core	n.a.	-	-	-	x	-	-	-	-	x	-	-	x

n.a. = not analyzed

77

3.4.3.5 Cation exchange experiments

Cation exchange experiments were carried out in order to investigate if the phyllomanganates have an ability to exchange K^+ and Mg^{2+} ions in their interlayers (Golden et al., 1986). In samples treated with a KCl solution, the peak position of 10 Å phyllomanganate (buserite with 2-water layers) changed from ≈10 Å to lower diffraction angles of ≈7 Å. After treating the same samples with $MgCl_2$ solution, the peak position changed from ≈7 Å back to ≈10 Å. This reaction pathway indicates cation exchange ability typical for phyllomanganates (Fig. 3.15).

The hydrothermal Mn oxide does not show any changes in the diffractogram after treatment with both solutions suggesting that this phase has no K and Mg exchange capability at all.
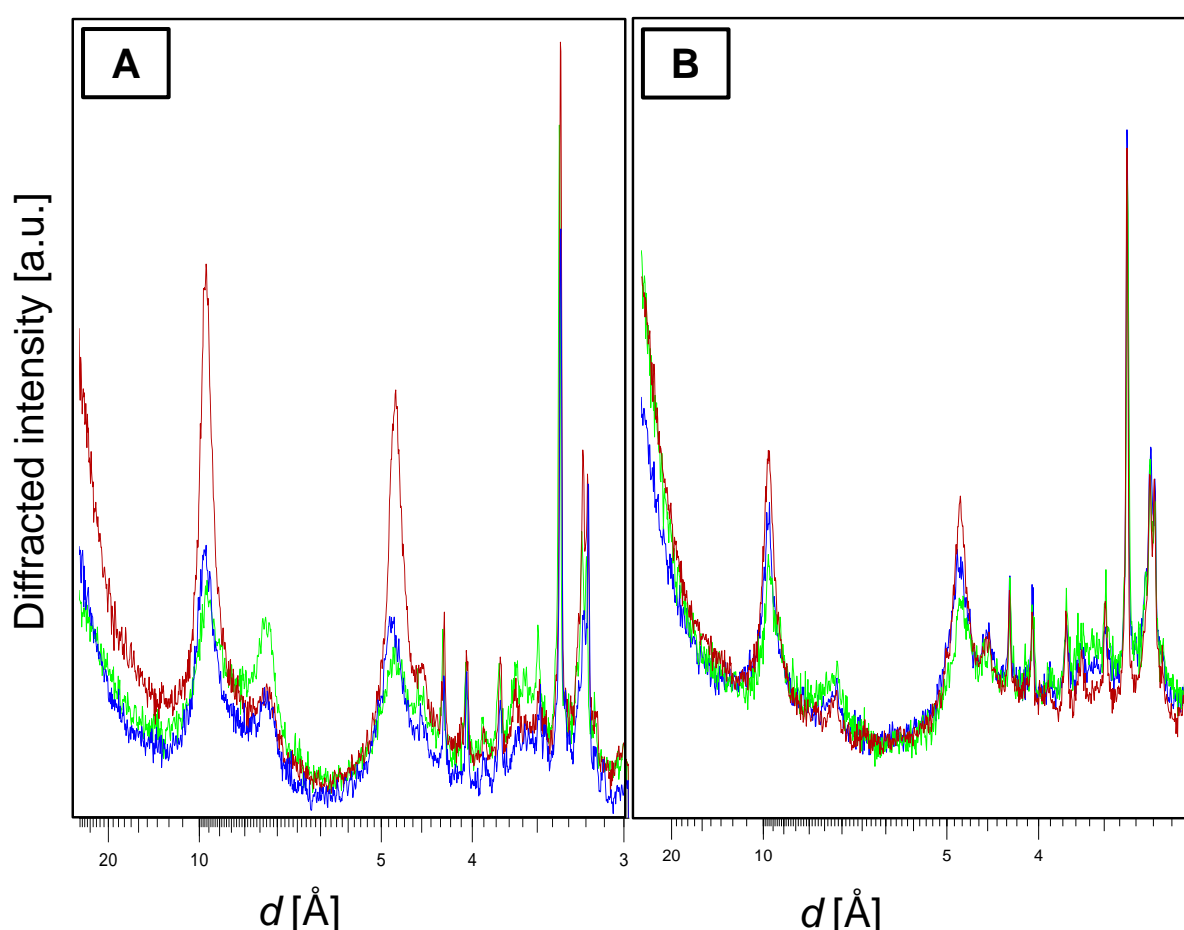
FIGURE 3.15 XRD patterns of (**A**) sample 29KG-C and (**B**) sample 62KG-A after cation exchange experiments with KCl and MgCl. Blue: original sample without treatment; green: after KCl treatment, red: after MgCl treatment. Note the significant changes in (**A**).

3.5 Discussion

In many publications the tectomanganate todorokite has been suggested to be the major 10 Å Mn-mineral of marine ferromanganese nodules, even if it has been known that there is a turbostratic Mn oxide with similar basal X-ray diffraction peaks at ≈10 Å and ≈5 Å (e.g., Calvert and Piper, 1984; Mellin and Lei, 1993; Halbach 1981; Turner et al., 1982). Since the fibrous to platy habitus of both minerals is similar (Giovanoli and Arrhzenius, 1985), special methods and approaches are needed for the differentiation of both minerals. In this study heating and cation exchange experiments as well as HRTEM were used for this task.

3.5.1 Bulk mineralogy

The detection and the characterization of different Mn-minerals within nodules is difficult because of the nano-sized minerals, poor crystallinity and the fact that different Mn-minerals are intergrown with each other on a fine scale.

After drying at room temperature, the XRD pattern of bulk nodules from the CCZ show distinct diffraction peaks around 10 Å and 5 Å that are characteristic for todorokite or 10 Å phyllomanganates (buserite/vernadite). No or only minor amounts of 7 Å phyllomanganate (birnessite/vernadite) can be detected. After drying the nodule samples at 40°C and 100°C, respectively, we recognized a distinct decrease of the ≈10 Å peak and simultaneously an increase of the ≈7 Å peak (Fig. 3.10). Furthermore, the 10 Å peak (after heating at 40°C and 100°C) is broad and changes the position to slightly lower diffraction angles of ≈9 - 9.6 Å. We interpret this as a reduction of the interlayer space due to the release of interlayer water molecules as discussed in the literature (Wadsley, 1950; Shen et al., 1994; Mellin and Lei, 1993). According to Johnson and Post (2006) birnessite-like structures with large interlayer cations with low valence state (e.g., Na^+, K^+) will dehydrate more rapidly during heating than those with small, high-valence interlayer cations (e.g., Ca^{2+}, Mg^{2+}, Ni^{2+}, Cu^{2+}), which were also shown by Mellin and Lei (1993). The hydration heat and the formation of inner-sphere or outer-sphere complexes control the different dehydration behaviour.

The fact that the Bragg peak at ≈10 Å shifts towards lower d-spacing at temperatures compatible with water volatilization (~100°C), but much cooler than the temperature required for dehydroxylation (~400 - 500°C) is characteristic for phyllomanganates.

These observations together with the XRD patterns of a typical todorokite (Fig. 3.10) lead us to the conclusion that todorokite is not a main Mn-phase in nodules of the CCZ.

Furthermore, all pattern (before and after heating steps) show only two *hk*-bands at lower diffraction angles around 2.45 Å and 1.42 Å, whereof the first one is asymmetric. These results indicate that the phyllomanganates are turbostratic such as the 10 Å and 7 Å vernadite, which are the disordered forms of the birnessite-like structures (birnessite, buserite). The $[MnO_6]$ octahedral layers of vernadite are stacked parallel to each other with a constant separation (*d*-spacing), according to the dehydration cations, but the layers are rotated or/and translated to each other and because of that the unit cell periodicity in *c* direction is lost (no 3D order; Giovanoli et al., 1975; Drits et al., 1997; Villalobos et al., 2006; Bodeï et al., 2007). For a better characterization of different Mn-phases, all characteristics of possible Mn-phases are summarized in Table 3.7.

The dehydration experiments revealed that already at RT some of the phyllomanganates dehydrate (Usui et al., 1989; Mellin and Lei, 1993). These results further suggest that the 7 Å peaks after heating (40°C and 100°C) are dehydration products of an unstable turbostratic 10 Å phyllomanganate and do not represent an original 7 Å vernadite as already suggested by Arrhenius and Tsai (1981) as well as Mellin and Lei (1993).

After drying of different nodules at 150°C, 200°C and 300°C the samples show neither the (001) nor (002) basal reflections of a 10 Å or 7 Å Mn-phase that were present at lower temperature (Table 3.4). Still, two *hk*-bands remain (Fig. 3.10) indicating that heating above 100°C induces a loss of coherence between adjacent layers, possibly because of an increased layer bending. In contrast, thermal stability experiments revealed that the Mg-rich todorokite remains intact until 400°C whereas the structures of Co, Ni, Cu-todorokite melt at 300°C (Ching et al., 1999). The todorokite included in this study, however, does melt at temperatures above 300°C indicating that this is a high-temperature todorokite with low amounts of Ni+Cu (<1 wt.%; Fig. 3.10).

Moreover, the investigated CCZ nodules have variable but distinct cation exchange capacities (Fig. 3.15) supporting our interpretation that these nodules are mainly built up by phyllomanganates. The cation exchange capacity of todorokite is generally low compared to phyllomanganates (Bish and Post, 1989; Golden et al., 1986; Cui et al., 2009). Nodules with a higher ability to exchange K^+ and Mg^{2+} ions in their interlayers (sample 29KG-C) seem to contain higher proportions of unstable phyllomanganates compared to nodules with lower

exchange capacity, which contain a higher fraction of stable phyllomanganates (62KG-A). Samples 09KG-B, 29KG-C and 26KG mainly consist of unstable 10 Å vernadite (defined in the present study as collapsing at <100°C), whereas nodules 62KG-A, 32KG-4, 44KG-2; 32KG-5 contain stable (collapsing at >100°C) and unstable 10 Å vernadite in almost equal proportions (Table 3.4).

TABLE 3.7 Characterization of different Mn-minerals in ferromanganese nodules

Group	Mineral name	Position (001)(002)	ability to collapse	order/disorder	layer symmetry	position of main diffraction maxima	Note
Vernadite[1] group / δ-MnO$_2$[2]	7 Å vernadite[3]	~7.2 Å; ~3.6 Å	yes	turbostratic	hexagonal	hk band: ~2.4 and ~1.4 Å	nanocrystals, 2.4 band is asymmetrical, one water layer within two [MnO$_6$]-octahedral layer
					triclinic	hk band: ~2.4 and ~1.52, 1.4 Å	nanocrystals, 2.4 band is asymmetrical, the band at ~1.4 Å is split in two, one water layer within two [MnO$_6$]-octahedral layer
	10 Å vernadite[3,4]	~10 Å; ~5 Å	yes	turbostratic	hexagonal	hk band: ~2.4 and ~1.4 Å	nanocrystals, 2.4 band is asymmetrical, two water layer within two [MnO$_6$]-octahedral layer
					triclinic	hk band: ~2.4 and ~1.52, 1.4 Å	nanocrystals, 2.4 band is asymmetrical, the band at ~1.4 Å is split in two, one water layer within two [MnO$_6$]-octahedral layer
	Fe-vernadite[3]	-	absent	turbostratic	hexagonal	hk band ~2.4 and ~1.4 Å	vernadite is epitaxially intergrown with amorphous δ-FeOOH
Birnessite group	7 Å birnessite[5]	~7.2 Å; ~3.6 Å	yes	ordered	hexagonal	hkl are variable, depending of the layer stacking and the cations	This mineral has three-dimensional order, one water layer
				ordered	triclinic	hkl are variable, depending of the layer stacking and the cations	This mineral has three-dimensional order, one water layer. Mn^{3+} cations arranged in rows parallel to b, one row of Mn^{3+} cation is followed by two rows of Mn^{4+}.
	10 Å buserite[5]	~10 Å; ~5 Å	yes	ordered	triclinic	hkl are variable, depending of the layer stacking and the cations	only triclinic is known to our knowledge, Mn^{3+} and Mn^{4+} in the octahedra layers, no significant amounts of vacancies are expected, but the structure has not been refined yet.
	Asbolane[6]	~10 Å; ~5 Å	yes	turbostratic	hexagonal	two incommensurate hexagonal networks of hk bands at positions comparable to vernadite	Ni(OH)$_2$, CoOOH or Co(OH)$_3$ within interlayer of two [MnO$_6$] octahedral layers
	Chalcophanite[7]	~6.94; ~3.47	yes	ordered	hexagonal	hkl: 2.23; 4.07; 1.59; 3.51	one out of 7 Mn^{4+} is missing and 2 Zn^{2+}O$_6$ octahedra are below and above vacancies (one on each side)
	Lithiophorite[8]	~9.39; 4.69	no (no interlayer water)	ordered	hexagonal	hkl: 2.38; 1.88; 1.46; 1.39; 1.58	lattice parameter are higher than those of hexagonal birnessite. Should be a criterion sufficient for identification in a turbostratic variation.
	Todorokite[9]	no basal reflections but peaks at ~10 Å and ~5 Å (9.7; 4.8 Å)	no (tunnel structure preserved collapsing)	ordered	layer symmetry is not applicable but the (ab) plane can be described as a hexagonal system	hkl: 2.40 (intense and symmetric)	tunnel structure with 3 x 3 octahedra or 3 x n (n <8)

[1] natural mineral; [2] synthetic form of vernadite; [3] Bodeï et al., 2007; [4] Webb et al., 2005; [5] Drits et al., 2007; [6] Manceau et al. 1992a; [7] Post and Appleman, 1988; [8] Post and Appleman, 1994; [9] Burns et al., 1983;

3.5.2 Individual layers

HRTEM analyses of individual layers were carried out to investigate the relation between the mineralogy of individual layers and their chemical composition, determined by EMPA.

Layer type 1 is of hydrogenetic growth by metal precipitation from oxic sea water and oxic pore water. Layers of type 2 are of suboxic-diagenetic growth by metal precipitation from suboxic pore water.

HRTEM analyses of layers of type 2.1 and 2.3 reveal reflections indicative for 7 Å vernadite as the major and 10 Å vernadite as the subordinate Mn-phase. This result seems to be in contrast to the XRD analyses of bulk nodules with 10 Å vernadite being the major Mn phase with minor amounts of 7 Å vernadite. We assume that the high amounts of 7 Å phyllomanganate in the HRTEM analyses of the individual layers may be a product of a primary unstable 10 Å phase which dehydrates and collapses during sample preparation (drying samples at 40°C and grinding; Usui et al., 1989) and/or during analyses under vacuum within EMPA and HRTEM (Turner and Buseck, 1979; Post and Veblen, 1990). Moreover, SAED also revealed 5 Å reflections in these layers, which is interpreted as the (002) diffraction peak of a 10 Å phyllomanganate.

Dense layer type 2.2 (low Ni+Cu contents) indicates only 7 Å phyllomanganates and Mn-phases with d-spacings of around 5.5 Å. The detected 7 Å reflection can be an original Mn-phase or a dehydration product of a prior 10 Å phyllomanganate. SAED reflections around 5.5 Å were interpreted as dehydration product of 7 Å (or 10 Å) phyllomanganates according to Cygan et al., (2012).

In general it can be concluded that layers of type 2 may contain a high proportion of an unstable 10 Å phyllomanganate and lower amounts of a stable 10 Å phyllomanganate. This conclusion is in agreement with the bulk mineralogy of the nodules. No todorokite was detected using HRTEM.

In contrast to these layers, layer type 2.4 is exclusively made up of a stable 10 Å phyllomanganate; there are no indications of 7 Å phyllomanganates. The sum of Mg + Ca within all suboxic layers are similar but layer type 2.4 shows an enrichment of Mg compared to Ca (Table 3.2). The content of K^+ and Na^+ is lower in layer type 2.4 compared to other type 2 layers. This may support the formation of a stable 10 Å vernadite. The stabilization of the structures is not caused by higher amounts of metals such as Ni+Cu, because they can be

located within the interlayers or in the layers. It is rather controlled by elements that can only form inner-sphere complexes above layer vacancies, meaning that they share 3 oxygen atoms from layer vacancies, and they are coordinated to other water molecules and/or hydroxyl groups that point towards the interlayer (e.g. Mg). Such coordination sphere cannot accommodate a strong layer-to-layer decrease when it faces a similar complex located on the other side of the interlayer, because that would lead to too short O-O distances. In contrast, elements forming outer-sphere complexes (K^+, Na^+, Ca^{2+}) can accommodate such decrease by movement of the water molecules towards the center of the interlayer space. This would explain why stable and unstable phyllomanganates are detected.

The absence of todorokite and the occurrence of phyllomanganates irrespective of the metal content of the layers indicate that the mineralogy alone does not control the incorporation of metals into the lattice of the suboxic diagenetic phases. The amount of metals is rather dependent on the availability of such metals in the surrounding pore water which depends on the environmental conditions such as the redox state (oxic/suboxic), the metal flux into the sediment and the early-diagenetic mobilization potential of the sediments.

3.5.3 Post depositional stabilization of crystal structure of phyllomanganates

An XRD profile through nodule 44KG-2 reveals that the older, inner layers are dominated by stable turbostratic 10 Å phyllomanganates. Layers from the middle part of the nodule contain both stable and unstable 10 Å vernadite and near-surface layers are mainly made up of unstable 10 Å vernadites (Fig. 3.12). Similar mineral distribution was already observed by Smetannikova et al., (1991). Moreover, HRTEM investigation from near-core layer type 2.4 similarly revealed that this layer type is made up of stable 10 Å phyllomanganate, only. This layer is further characterized by intermediate and less variable Ni+Cu contents as well as higher average Mg amounts compared to other diagenetic layers of type 2 (Table 3.2). It can be also observed an increase of Mg within the analyzed profile of nodule 44KG-2 and a simultaneous decrease of Na. Magnesium is known to stabilize the 10 Å phyllomanganate structure and prevents it from collapsing, but a high Na content, with the low hydrating energy of Na may lead to the collapse of the structure upon drying (Golden et al., 1986; Mellin and Lei, 1993).

3.5.4 The absence of todorokite

The mineralogical investigations of this study indicate the absence of todorokite as major Mn-phase in CCZ nodules. We attribute this absence to three facts. First, the relatively low Mg contents in the nodules. The Mg concentration of phyllomanganate necessary to form todorokite ranges between 4.1 and 4.9 wt.% (Table 2 in Bodeï et al., 2007). Second, the transition from 10 Å phyllomanganate to todorokite in synthetic samples takes place at increased temperatures (e.g., 160°C, Ching et al., 1999; Bodeï et al., 2007). The CCZ nodules were not influenced by hydrothermal fluids and thus no todorokite has formed. A similar conclusion was drawn by Usui et al. (1989). They interpreted their mineralogical data as two series of manganates: a hydrothermal, todorokite-like series consisting of tunnel structures with low amounts of cations and a buserite-like series consisting of octahedral layers with a high content of stabilizing cations. Third, according to Bodeï et al. (2007), the formation of natural as well as synthetic todorokite starts with a *c*-ordered Mg-rich 10 Å-phyllomanganate rather than with a turbostratic 10 Å phyllomanganate such as vernadite. The product of the transformation from a turbostratic phyllomanganate is a mixture of 7 Å vernadite with jianshuite/Mg-chalcophanite and secondary poorly-crystallized todorokite.

3.5.5 The dependency of the different Mn oxide phases on Eh-pH conditions

The mineralogical variation (10 Å manganates and δ-MnO_2) of Mn-nodules depends on different physico-chemical parameters (Eh, pH, Mn^{2+} content etc.) at the site of their deposition (Cronan and Tooms, 1969; Price and Calvert, 1970; Glasby, 1972; Crerar and Barnes, 1974; Smetannikova et al., 1991). The authors suggest that δ-MnO_2 is characteristic for the formation under oxic conditions (Glasby, 1972; Crerar and Barnes, 1974; Smetannikova et al., 1991) as it is typical for the formation of hydrogenetic crusts. The latter form due to the mixture of upwelling oxygen-rich deep water with water from the oxygen-minimum-zone along the flanks and summit areas of seamounts (Cronan and Tooms, 1969).

The behaviour of individual metals under different Eh-pH conditions may influence the formation of Mn-minerals. Within sea water Fe and Mn show different Eh-pH stability fields (Glasby and Schulz, 1999). Under oxic sea water conditions, as they prevail today (Eh ~0.5 V, pH ~7.5, dissolved Mn ~3 nmol/l) in the CCZ, Mn and Fe behave similar (Froelich et al., 1979), causing the formation of layer type 1 (low Mn/Fe ratios, Table 3.2).

Under such conditions the 10 Å manganate phases as well as δ-MnO$_2$ can thermodynamically be formed if a certain saturation threshold has been reached. But the formation of stacked 10 Å manganate phases is inhibited by the simultaneous formation of amorphous δ-FeOOH phases, destroying the stacking structure through epitaxial intergrowth with the Mn-phase (Burns and Burns, 1975).

Type 2 layers, with high Mn/Fe ratios (>800), consist of 10 Å vernadites with minor amounts of 7 Å vernadites. Such chemical as well as mineralogical composition is typical for growth under suboxic environmental conditions with Mn and Fe being stronger fractionated (Halbach et al., 1988; cf. Chapter II). Under suboxic conditions the solubility of Mn increases (Crerar and Barnes, 1974; Froelich et al., 1979) causing higher mobility of Mn, which is in contrast to the Fe solubility that remains unchanged.

Due to lower ventilation of the Pacific Ocean and/or higher sedimentation rates of organic matter during glacial periods, the near-bottom water becomes oxygen-depleted (Bradmiller et al., 2010; Froelich et al., 1979). The Eh will be lowered (<<0.4 V) causing an increased influx of dissolved Mn^{2+} with subsequent formation of diagenetic Mn oxides (phyllomanagantes) according to equation (3.1):

$$Mn^{4+}O_2 + Mn^{2+} + 2H_2O \rightarrow 2Mn^{4+}O_2 + 4H^+ \qquad (3.1)$$
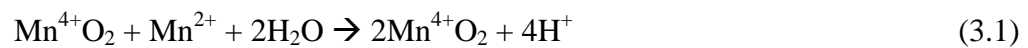
However, the production of hydrogen ions leads to the decrease of the pH value and may limit the Mn oxidation and thus, the formation of phyllomanganates. In order to produce the type 2 layers it is necessary to buffer the H$^+$ ions. The buffering system may be through the dissolution of carbonates according to the equation (3.2):

$$CaCO_3 + H_2O \rightarrow Ca^{2+} + HCO_3^- + OH^- \qquad (3.2)$$

The carbonate compensation depth (CCD) in the eastern CCZ is between 4200 to 4500 m water depth (Cronan, 2000), i.e. the surface sediments of the working area are almost devoid of carbonates. However, carbonate peaks could be found in 19-28 cm depth below seafloor in some sediment cores in the study area which are interpreted as the result of an extended CCD during glacial periods (Widmann et al., 2014). If these periods are also related to an increased

carbonate flux, the pH conditions could be sufficiently high to enable the phyllomanganate formation under low redox conditions, a situation similar to the current Peru Basin.

Bright spots and veins within the hydrogenetic layer type 1 (Fig. 3.4A) consist of turbostratic phyllomanganates similar to the layer type 2. We interpret these inclusions as secondary products for two reasons. Firstly, refilling of pores within hydrogenetic layers takes place during suboxic conditions, as it was already shown in ferromanganese crust by suboxic influence during their grow history (Halbach et al., 2009). Secondly, these phases may form by dissolution and re-precipitation of the prior δ-MnO_2 phases under the influence of an increased Mn^{2+}-flux, according to the reaction path given in equation 3.1. Slightly higher Fe contents of those inclusions (~2.54 wt.%) compared to lower contents in typical type 2 layers (Table 3.2) support this assumption. Moreover, Fe-Ti oxides were found close to these veins and spots with secondary Mn-oxides (Fig. 3.13A, D). We interpret the latter as residual phases left behind by the dissolution of primary hydrogenetic Mn-Fe oxides. Similar re-crystallization processes were already shown for Fe-Mn crusts under suboxic conditions in the phosphate-rich-water of the oxygen minimum zone (Koschinsky et al., 1997).

3.6 Summary and Conclusion

Ferromanganese nodules from the CCZ predominantly consist of the following different types of turbostratic phyllomanganates with a distinct cation exchange capacity:

1) 7 Å phyllomanganate forming a minor component in the nodules, mainly as dehydration product of unstable turbostratic 10 Å phyllomanganates.

2) Unstable 10 Å phyllomanganate (10 Å vernadite) collapsing after drying at 40°C - 100°C.

3) Stable 10 Å phyllomanganate (10 Å vernadite) collapsing upon heating at >100°C.

In older samples, which were taken near the nucleus, stable phyllomanganates dominate, whereas unstable phyllomanganates are the main Mn oxides in young layers near the surface of nodules. This could be explained by a post-depositional transition of the position of trace metals in the crystal lattice of the Mn oxides or the incorporation of stabilizing elements such as Mg^{2+}.

The stabilization of the structures is not caused by higher amounts of metals such as Ni+Cu.

Neither XRD analyses of bulk nodules nor HRTEM analyses of individual layers indicate the major occurrence of todorokite within the nodules from the CCZ.

Hydrogenetic layers were also subject to post-depositional overprinting by pore space fillings of well-crystallized phyllomanganates when the original oxic-hydrogenetic layers of δ-MnO$_2$ were subject to suboxic conditions.

Chapter IV

Porosity distribution and permeability of ferromanganese nodules from the central Pacific Ocean deduced from CT, EMP and XPS analyses

Ferromanganese nodules have been formed at the sea floor over millions of years. Therefore, they could be used as an archive of environmental conditions like climate and/or oceanographic changes. These variations are often associated with changes in organic and inorganic flux rates and connected chemistry have influenced the growth of individual nodule layers causing their chemical, mineralogical and structural heterogeneity (cf. Chapter II).

This chapter is focused on high resolution computer tomography analysis of manganese nodules from the Clarion Clipperton Zone (CCZ) of the Pacific Ocean to determine their porosity, pore size distribution and the connectivity of the pores. These analyses should demonstrate if fluids of the nodule environment (bottom near water or sediment pore water) are able to penetrate through nodules and therefore, influence the prior precipitated Mn-phases post genetically.

The results of the computer tomography analyses are presented in a manuscript, which is submitted to Environmental Science & Technology. "Microbe-mineral interactions in deep-sea manganese nodules" Blöthe, M., Wegorzewski, A.V., Müller, C., Simon, F., Kuhn, T., Schippers, A.

4.1 Abstract

High resolution computer tomography analysis (CT) have been carried out on polymetallic nodules from the Clarion and Clipperton Zone (CCZ) of the equatorial eastern Pacific Ocean in order to determine nodule porosity, pore size and pore size distribution. These analyses should provide a better understanding of the nodule growth structures and the possibility of fluid penetration through the nodules with a simultaneously influence of prior precipitated Mn-phases. Nodules have a high bulk porosity (43 ± 7.5 vol.% on average) with substantial variations within single, genetically different growth layers. The CT analyses show that up to 80% of the pores are interconnected with each other. This enables the fluids, enriched with dissolved metals from the (surrounding) near bottom water and/or pore water, to penetrate through the whole nodule. There, Mn and/or Fe oxides can precipitate and refill the pores and cracks. Furthermore, circulating fluids can interact with existing mineral phases causing a re-arrangement of the Mn-phases, how was already suggested in Chapter II and III. Pore sizes decrease from the surface to the innermost part of the nodules due to refilling of pores with Mn-minerals. The chemistry of pore filling material is similar to that of the outermost growth layers which are oxic-hydrogenetic precipitates (Mn/Fe: 0.61 - 1.22; Ni+Cu: 0.28 - 0.54 wt.%; Co: 0.14 - 0.29 wt.%). The Mn-speciation of the outermost layer and the pore fillings are similar dominating by 67 - 82% Mn^{4+} and 18 - 33% of reduced Mn-species ($Mn^{2+}+Mn^{3+}$).

Furthermore, primary hydrogenetic layers (vernadite (δ-MnO_2); Mn/Fe ratios <3) reveal indications for epigenetic transformations to suboxic diagenetic material (10 Å/7 Å vernadite; Mn/Fe >>10). In addition, pore size and the open pore space provide a habitat for a prokaryotic community consisting of Mn(II)-oxidizing and Mn(IV)-reducing bacteria (Blöthe et al., submitted).

4.2 Introduction

Polymetallic nodules possess high porosities (mean value 58 vol.%; Halbach et al., 1988) which are due to growth conditions and to micro fractures formed by shrinkage and dehydration of the nodules on the seafloor (Halbach et al., 1988). Nodules from the CCZ predominantly consist of hydrogenetic layers (layer type 1), suboxic dendritic and dense growth layers (layer type 2) (cf. Chapter II). The dendritic growth structures build up very large (up to 10 mm) porous areas which cause the high porosity within the nodules. In Chapter II it has been documented that the pores of the dendritic growth type are partly filled with mineral phases of hydrogenetic origin. Furthermore, hydrogenetic layers show small spots and veins of suboxic-diagenetic precipitation. These spots and veins reveal pore fillings and/or re-precipitates of the already precipitated hydrogenetic layer during suboxic events (cf. Chapter III).

This study should show if fluids from the surrounding environment are able to penetrate into the nodules and what kind of epigenetic processes occur within the pore space and whether this epigenetic processes leads to a substantial change of the chemical composition of nodules, how it was already assumed in prior chapters. Therefore, non-destructive high resolution CT analyses were performed to determine the porosity, the distribution of pores within the nodule and the pore connectivity to obtain a better understanding for the possibility of fluids to penetrate through the nodules. Furthermore, results of EMPA and high resolution XPS analyses of nm- and μm-growth structures within nodules were carried out to investigate the products of the interaction between inner nodule surfaces and ambient water from nodule environment (bottom near water and sediment pore water).

4.3 Samples and analytical methods

4.3.1 Samples

For the CT investigations two small ferromanganese nodules (44KG-A (2.2 x 1.8 x 1.6 cm), 49KG-B (2 x 2 x 2.2 cm)) were studied in detail. Figure 4.1 show such typical small nodules. Both nodules were found in the upper few cm of the sediment (2 - 4 cm). They show botryoidal growth structures which are slightly rough on all sides. These nodules were chosen because of their small size, which is better for whole analyses of the nodules using computer tomography.

Furthermore, three nodules deriving from different localities in the eastern German license area and of different sizes (27KG-1, 32KG and 49KG; cf. Chapter II, Table 2.1; Fig. 2.2) were used for further XPS investigations. Detailed chemical and mineralogical composition of several bulk nodules have been reported in Chapter II and III.

FIGURE 4.1 Typical small nodules which were taken for high resolution computer tomography analysis. These nodules show slightly botryoidal rough growth structure on every side.

4.3.2 Analytical methods

4.3.2.1 High-resolution computer tomography

The high-resolution scans were performed on small bulk nodules (44KG-A, 49KG-B) with the Phoenix nanotom s 180 computer tomography (CT) scanner at the Leibniz Institute for Applied Geophysics (LIAG) in Hannover. Scans of the nodule were carried out with a water-cooled nanofocus X-ray tube (180kV/15W). The further visualization of pore space/pore network extraction and 3D imaging were performed with the software program AVIZO Fire. For determination of varying porosity and pore size distribution within the whole nodule, the 3D image of nodule 49KG-B was segmented into eight individual layers in all three directions (X, Y, Z).

4.3.2.2 X-ray photoelectron spectroscopy

X-ray photoelectron spectroscopy (XPS) is a highly surface-sensitive analytical technique quantitatively analyzing the elemental composition allowing the measurement of the (surface) uppermost 10 nm. All analyses were performed on individual subsamples (powder samples) of nodule 27KG-1 from the CCZ at the Leibniz Institute of Polymer Research in Dresden,

Germany. For the subsamples of 27KG-1, a profile through the nodule was drilled using a high precision planar drill bit with a diameter of 6 mm. The powder material was placed on the sampling holder using double-sided adhesive tape. XPS spectra were recorded using an AXIS Ultra photoelectron spectrometer (Kratos Analytical, Manchester, UK). The spectrometer was equipped with a monochromatic Al Kα (h·v = 1486.6 eV) X-ray source of 300 W at 15 kV. The kinetic energy of photoelectrons was determined with a hemispheric analyzer set to pass energy of 160 eV for wide-scan spectra and 20 eV for high-resolution spectra. The pressure in the analysis chamber was not higher than $3\cdot10^{-8}$ mbar. For each sample, an area of ca. 1 mm² was analyzed. During all measurements, electrostatic charging of the sample was avoided by means of a low-energy electron source working in combination with a magnetic immersion lens. Later, all recorded peaks were shifted by the same value that was necessary to set the C 1s peak to 285.00 eV.

Quantitative elemental compositions were determined from peak areas using experimentally determined sensitivity factors and the spectrometer transmission function. Spectrum background was subtracted according to Shirley. The high-resolution spectra were deconvoluted by means of the Kratos spectra deconvolution software. Free parameters of component peaks were their binding energy (BE), height, full width at half maximum and the Gaussian-Lorentzian ratio (personal comm. F. Simon).

4.3.2.3 Electron microprobe analyses

The chemical composition of individual areas (pore space fillings) within the nodules (27KG-1, 44KG-A, 49KG-B) was investigated using electron microprobe analyses (EMPA; CAMECA SX - 100). Thick sections (~200 µm thickness of the sample) of nodules were prepared. Measurements of the material were carried out using a 15/20 kV accelerating voltage and 40 nA beam current. Mn-rich layers were measured with a focused (1 to 5 µm) beam. Fe-rich layers were analysed with a defocused (20 µm) beam, due to their higher sensitivity to the beam because of their poor crystallinity (cf. Chapter II).

4.3.2.4 Density analyses

The material density was measured using the AccuPyc 1330. The samples were placed in the sample chamber which will then be filled with helium gas. The gas molecules filled the pores and cracks of the sample. During the analyses the sample volume is determined. Due to the detected volume and the weight of the sample the material density can be calculated (Micromeriticd, 1996).

Bulk density and porosity were analyzed using the GeoPyc 1360. The displacement measurement technique is based on a quasi-fluid, which is composed of small, rigid spherical particles (Dry Flow) having a high degree of flow-ability. Samples of known weight and volume (previously detected using measurement description above) were placed together with the Dry Flo in a sample chamber. During the following rotation, the Dry Flow particles were arranged around and within all cavities (pores and cracks) of the nodule. After that the displacement data were collected and the bulk density as well as the porosity can be determined (Micromeritics, 2009).

4.3.2.5 Brunauer-Emmett-Teller Method (BET)

Specific inner surface areas (SSA) of three different nodules were obtained by measurement of the gas volume (N_2) which was adsorbed on the surface of a known weight of a manganese nodule for at least 3.31 h under vacuum equilibrium. For these analyses the Quantachrome Autosorb-iQ MP at the Leibniz Institute for Applied Geophysics (LIAG) in Hannover was used.

4.4 Results

4.4.1 Bulk Porosity and BET

Polymetallic nodules which were analyzed during this study have a high internal porosity ranging between 26 and 61 vol.% (Table 4.1). Furthermore, mineral density (2.83 ± 0.26 g/cm^3) and dry density (1.60 ± 0.18 g/cm^3) are presented in Table 4.1. For explanation, the mineral density is the density of the material without pores and the dry bulk density is the density of the material after drying (40°C). The specific surface areas of three different nodules range between 102 and 130 m^2/g. Table 4.1.

TABLE 4.1 Mean values of mineral density, dry bulk density, porosity and surface area of bulk manganese nodules from the CCZ

SO205 nodules	mineral density (g/cm^3)	dry bulk density (g/cm^3)	porosity[1] (vol.%)	surface area[2] [m^2/g]
MEAN	2.83	1.60	43.0	119
STD.DEV.	0.26	0.18	7.52	15
MIN	2.48	1.00	25.9	102
MAX	4.00	1.94	60.6	130

[1] 48 samples, [2] three samples

4.4.2 High resolution X-ray Computer Tomography

CT analyses of two small nodules (44KG-A and 49KG-B) were performed to determine their internal porosity, pore size and the pore size distribution.

Figures 4.2A and 4.2B show two different slices of nodule 49KG-B that exhibit different growth structures. In general, growth structures of ferromanganese nodules are very heterogeneous, as was already shown in Chapter II. The outermost areas of nodule 49KG-B (all sides: top side, rim, bottom side) are predominantly composed of dendritic growth structure associated with high porosities (Fig. 4.2A; Table 4.2). The X-ray CT slice of the inner part of the nodule (Fig. 4.2B) shows alternating dense and porous layers of different reflectivity. The nodule center is predominantly characterized by dendritic growth structures. No other nucleus can be identified.
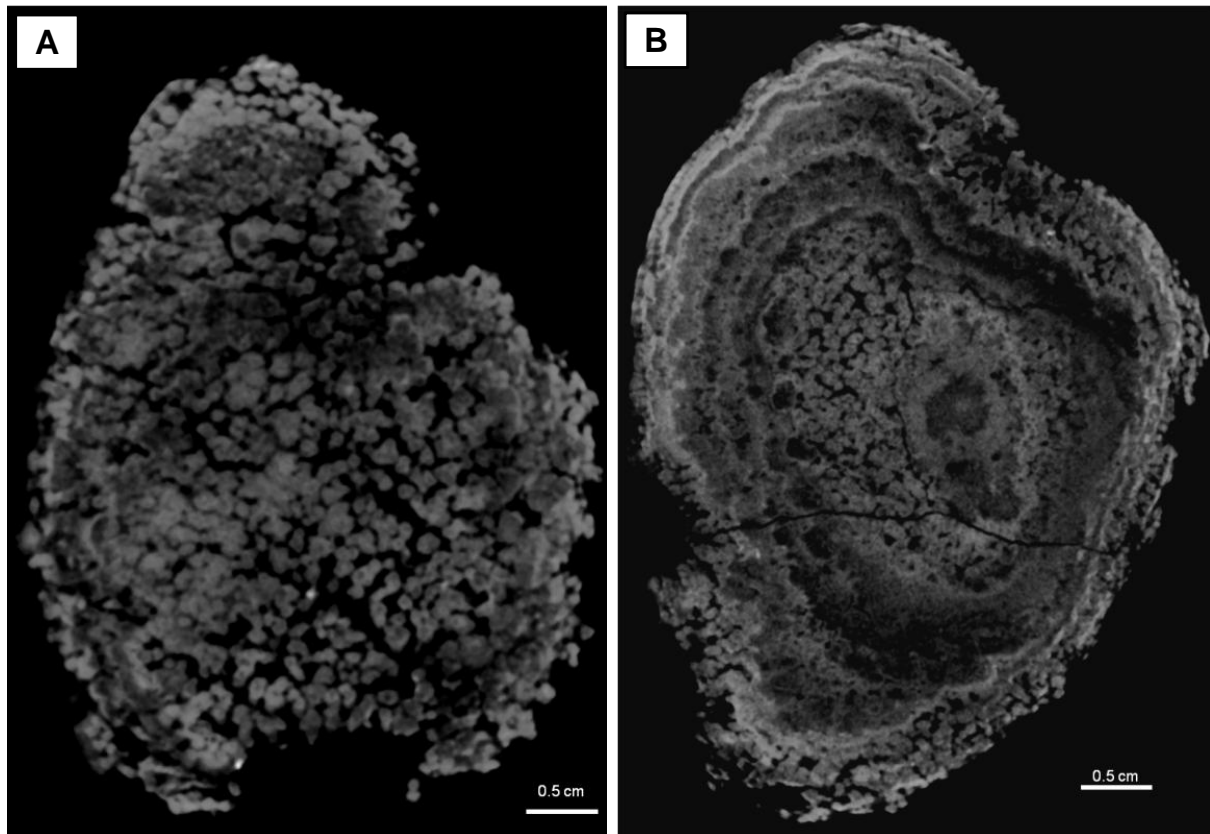
FIGURE 4.2 A: X-ray CT image of dendritic growth structure of the outermost μm of nodule 49KG-B. High amounts of large pores (>0.011 mm^3) can be distinguished. **B:** X-ray image of a slice inside of nodule 49KG-B. The nodule texture is very heterogeneous. Different dense and porous layers can be distinguished, which are disturbed by cracks.

The porosity of nodule 49KG-B has a large variability within all three directions (X, Y, Z; Table 4.2; Fig. 4.3) with highest porosity at the surface in all three directions. The nucleus of the nodule, consisting of dendritic growth structures and sediment, is not directly located in the center of the nodule. Therefore, the lower part of the nodule is slightly denser than the upper outermost layer. One reason for the lower porosity of the bottom side (Table 4.2) can be the refilling of the pores by glue which is necessary to fix the nodule on a stick for the CT analyses.

Table 4.2 Individual slices and their thickness and porosities of nodule 49KG-B

individual slices	thickness of the slices	Porosity [vol.%]		thickness of the slices	Porosity [vol.%]		thickness of the slices	Porosity [vol.%]	
	x [mm]	AVERAGE	STD. DEV.	y [mm]	AVERAGE	STD. DEV.	z [mm]	AVERAGE	STD. DEV.
1	9.30	22.1	10.9	16.2	23.2	7.32	6.22	17.6	11.27
2	13.7	6.02	3.79	21.1	5.66	3.10	2.49	5.68	2.12
3	13.7	4.60	3.47	21.1	3.75	2.95	2.49	4.01	0.47
4	13.7	14.8	9.82	21.1	13	8.26	2.49	14.7	0.38
5	13.7	10.5	7.44	21.1	9.4	5.56	2.49	10.2	0.38
6	13.7	10.7	8.02	21.1	10	5.17	2.49	10.5	1.34
7	13.7	9.42	6.31	21.1	8.86	3.57	2.49	9.75	0.56
8	11.2	6.01	2.68	14.9	7.33	3.48	4.97	8.67	4.04
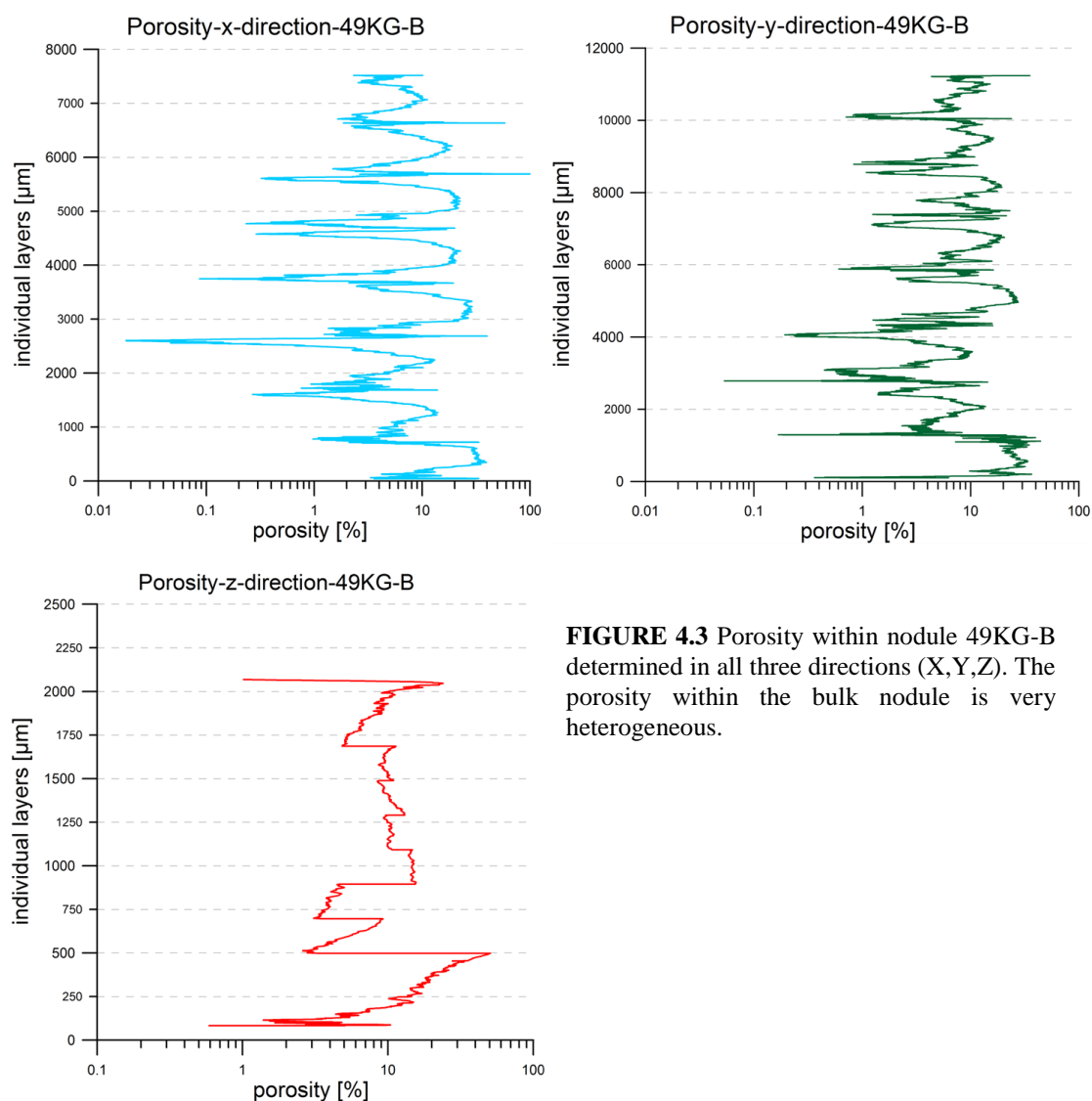
FIGURE 4.3 Porosity within nodule 49KG-B determined in all three directions (X,Y,Z). The porosity within the bulk nodule is very heterogeneous.

The pore size analyses of different areas within nodule 49KG-B revealed that the outermost layers (includes the uppermost ~11 mm of the nodule) contain ~38% small pores (<0.011 mm^3) and ~62% of pores larger than 0.011 mm^3 (Fig. 4.4A). The inner areas show distinct changes in the pore size relation. For example, the number of smaller pores increases up to 59%, whereas the proportion of the larger pores decreases (41%) when moving away from the outermost layer (>11 - 26 mm; Fig. 4.4B). The analysis of nodule 44KG-A also indicates that the outermost areas have larger pores (0.34 to 0.50 mm) than the inner pores (0.16 to 0.08 mm; Fig. 4.5).
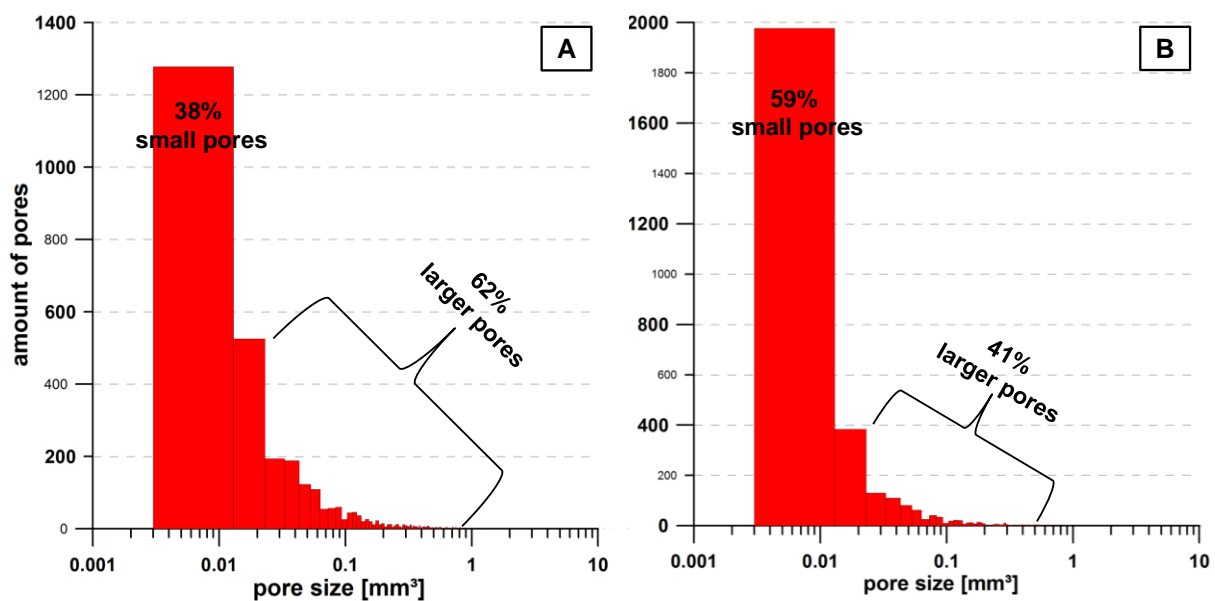
FIGURE 4.4 Pore size distribution within individual slices of nodule 49KG-B **A:** upper 11 mm of nodule 49KG-B with 62% large pores and lower amounts of smaller pores (38%), **B:** areas inside of nodule 49KG-B (>11 - 26 mm) show more small pores (59%) and only 41% larger pores.
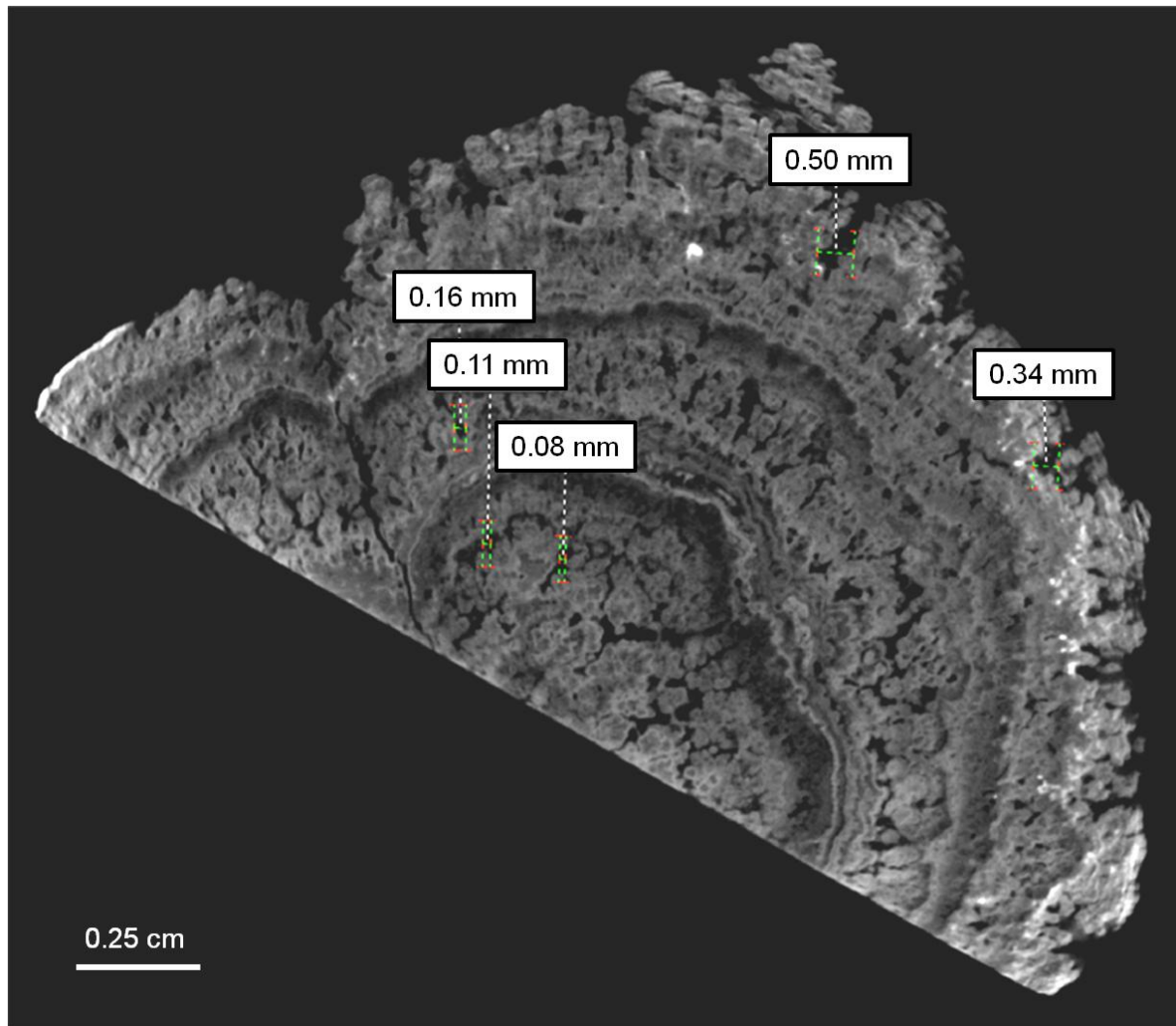
FIGURE 4.5 Pore size within different areas of nodule 44KG-A. Outermost areas of the nodule show larger pores (up to 0.50 mm) than parts inside the nodules (0.08 mm). Pores within the nodules are smaller because they are partly filled with post depositional material during their growth history. Cracks through the nodule connect the environment with the inner laying areas.

The connectivity among individual pores within nodules 44KG-A and 49KG-B is shown in Figure 4.6. In both nodules, up to 80% of the individual pores are connected (300 to 400 mm^3) with each other throughout the whole nodule. Several isolated pore systems can be distinguished within both nodules (Fig. 4.6).

Pores of the outermost areas are connected with pores in the central, older parts of the nodules as well as with the surrounding environment (near bottom water and/or pore water). Furthermore, cracks through the whole nodule can be detected, which connect the surrounding environment with the inner parts of the nodules (Figs. 4.2B and 4.5).
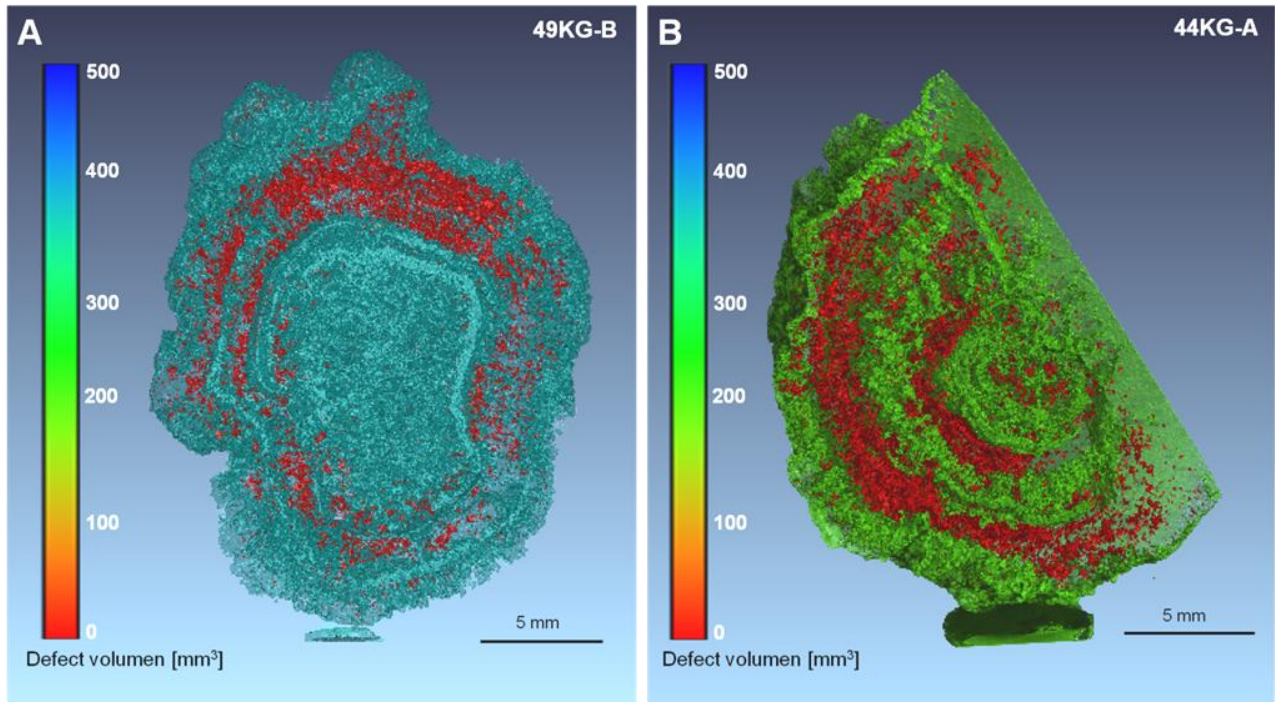
FIGURE 4.6 A: X-ray CT image of pore connectivity of nodule 49KG-B and **B:** of nodule 44KG-A. Each color forms an interconnected pore system. The blue color in **(A)** and the green color in **(B)** mark the same interconnected pore system (350 to 400 mm^3) which represents about 80% of all pores. The red color stands for a second pore system made up of smaller and fewer pores (<40 mm^3).

4.4.3 X-ray Photoelectron Spectroscopy

X-ray photoelectron spectroscopy (XPS) is a method for analyzing the material surface and to distinguish various possible oxidation states of the different elements (Siegbahn et al., 1967; Murray and Dillard, 1979).

4.4.3.1 Chemical characterization of the outermost material via XPS

Six subsamples at different depths within nodule 27KG-1 were analyzed to determine the chemical composition similar to the analyses of the outermost layers of nodules 32KG and 49KG in Chapter II. Figure 4.7 shows a characteristic XPS wide-scan spectrum of the sample 27KG-1, which is (qualitatively) representative for all three nodules.
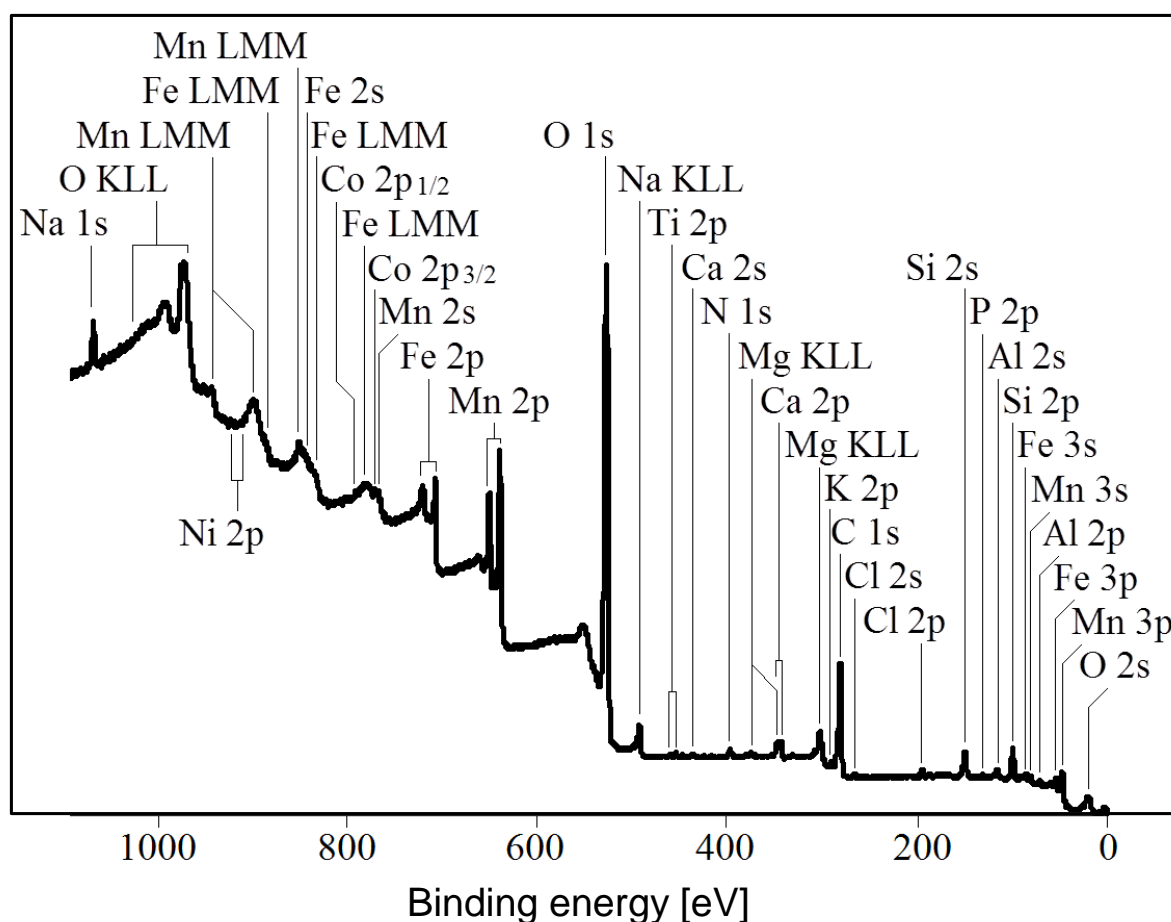
FIGURE 4.7 XPS wide-spectrum of subsample 27KG-1-1 representing the outermost layer of the nodule (intensive photoelectron and Auger peaks of the key elements were labeled).

To characterize the material of the six subsamples (Fig. 4.8; Ss1-6) of nodule 27KG-1 genetically (oxic-hydrogenetic or suboxic-diagenetic; the Mn/Fe, Ni/Co, as well as Ni/Mn, Cu/Mn and Co/Mn ratios were used Table 4.3). The Mn/Fe ratios of most subsamples (Ss1, 3, 4, 6) of nodule 27KG-1 are in the range between 1.36 and 2.78. Two of the subsamples (Ss2 and Ss5), have slightly increased Mn/Fe ratios of 4.26 and 4.59 (Table 4.3). The Co contents were generally higher than the Ni contents in all subsamples. The calculated Ni/Co ratios varied between 0.14 and 1.25. Subsample of the bottom side of the nodule, which was embedded in the upper few cm of the sediment (Ss6) revealed the highest Ni/Co ratio. Included in Table 4.3 are the results of nodules 32KG and 49KG, which were already presented and discussed in Chapter II. The Ni/Co ratios of the outermost layers (surface, rim, bottom side) of nodule 32KG and 49KG varied between 0.59 and 2.13 (Table 4.3). Although the Ni contents of these outermost layers were slightly higher, the Mn/Fe ratios are still low (Mn/Fe ≤3).

In general the chemical composition of the outermost layers of the subsamples of nodule 27KG-1 as well as the outermost layers of 32KG and 49KG nodule are comparable with hydrogenetic

FIGURE 4.8 Back scatter image of nodule thick section (27KG-1). Areas of the subsamples (Ss1-6) of XPS analyses correspond to the depth of the profile samples. White boxes mark areas of analyses using electron microprobe (EMPA).

ferromanganese crust (Table 4.3 vs. Table 2.4; Fig. 4.9) and therefore of hydrogenetic growth, how it was already shown in Chapter II.

TABLE 4.3 Calculated Mn/Fe and Ni/Co ratios of the outermost material of different subsamples of the analyzed nodules from the CCZ. Data represent the proportions of Mn^{2+} + Mn^{3+} and Mn^{4+}, their binding energies and the calculated percentage of the particular Mn-species, (XPS data)

Sample SO205	sample description	Mn/Fe	Ni/Co	Ni/Mn	Cu/Mn	Co/Mn	$Mn^{2+} + Mn^{3+}$ Binding energy (eV)	proportion of $Mn^{2+} + Mn^{3+}$ component A [wt.%]	Mn^{4+} Binding energy (eV)	proportion of Mn^{4+} [wt.%] component B	percentage [%] of $Mn^{2+}Mn^{3+}$	percentage [%] of Mn^{4+}
27KG-1-1	0-1.1mm, outermost surface, which was in contact with near bottom seawater, hydrogenetic material	2.30	0.50	0.005	0.008	0.010	640.86	19	642.05	38	33	67
27KG-1-2	14.2-16.2mm, dendritic growth structure,	4.26	0.19	0.005	0.014	0.024	640.85	17	642.06	39	31	69
27KG-1-3	30.2-35.2mm, middel of the nodule, dendritic growth structure	2.78	0.14	0.005	0.015	0.036	640.74	15	641.98	37	29	71
27KG-1-4	6500-11500µm from the bottom side of the nodule, mainly of dendritic growth structure	1.36	0.16	0.008	0.021	0.050	640.75	14	642.00	39	26	74
27KG-1-5	500-1500µm, near of the bottom side, dendritic and hydrogenetic growth structures	4.59	0.40	0.003	0.011	0.008	640.90	13	642.15	40	25	75
27KG-1-6	0-200µm, outermost bottom side, which was stuck in the sediment	1.70	1.25	0.018	-	0.014	640.93	16	642.15	39	29	71
32 KG-1	surface of the nodule (in contact with near bottom water)	2.76	1.03	0.014	-	0.014	641.29	11	642.5	39	22	78
32 KG-3	bottom side of the nodule (embeddet in the sediment)	2.25	-	-	-	-	640.25	9	641.45	39	18	82
32 KG-5	sample of the rim	1.38	-	-	0.08	0.03	641.10	9	642.33	38	19	81
49 KG-1	surface of the nodule (in contact with near bottom water)	2.33	0.68	0.02	0.01	0.04	640.98	13	642.18	41	24	76
49 KG-2	equatorial rim of the nodule	3.03	2.13	0.03	0.01	0.02	640.91	10	642.14	40	20	80
49 KG-3	bottom side of the nodule (embeddet in the sediment)	3.06	0.59	0.02	0.01	0.03	641.06	11	642.17	37	23	77
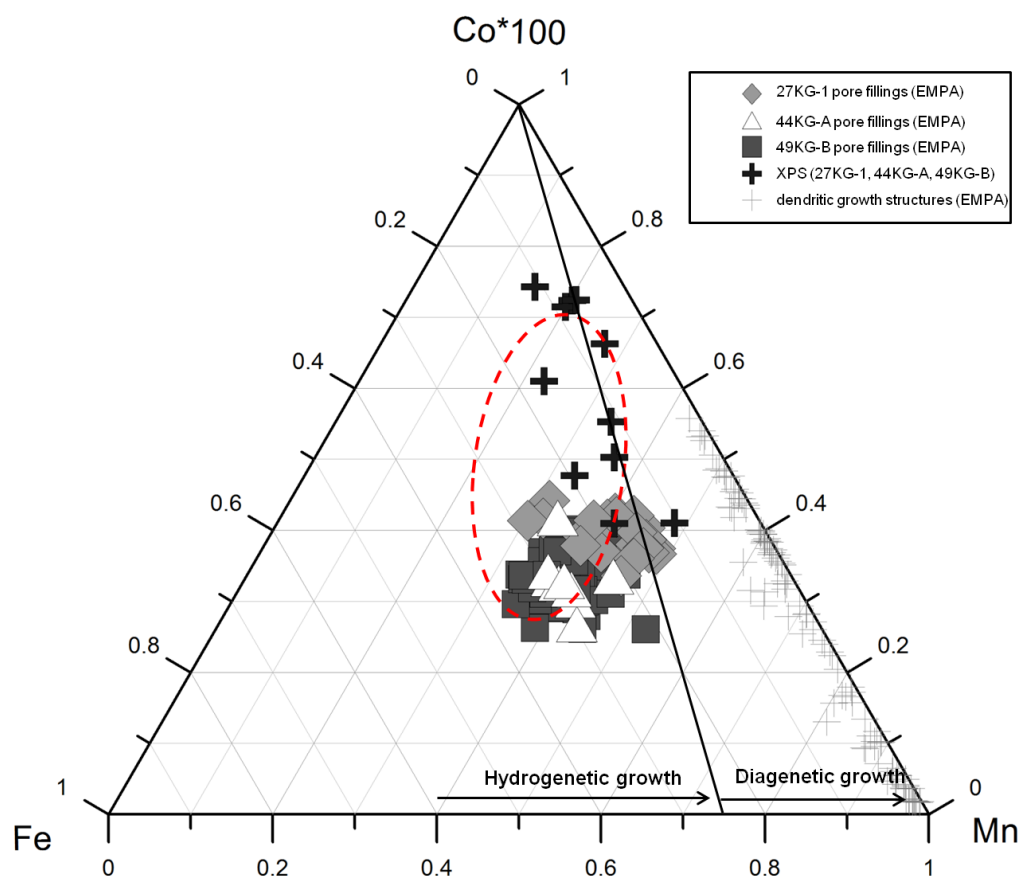
FIGURE 4.9 Three-component diagram Fe-Mn-Co*100 according to Bonatti et al., (1972) showing the chemical relationship of pore fillings of different nodules using electron microprobe analyses (EMPA) compared with X-ray photoelectron spectroscopy (XPS). The red dashed ring marks the area of individual data points of Fe-Mn crust from the CCZ (37KG-3; Chapter II). Furthermore, analyses of dendritic growth structures are plotted, which show high diagenetic influence in contrast to the surrounding and refilling material of the pores between the dendrites.

4.4.3.2 Mn speciation

In addition to the chemical characterization of the subsamples from nodules 27KG-1, 32KG and 49KG, the oxidation states of manganese (Mn^{2+}, Mn^{3+}, Mn^{4+}) were identified using the high-resolution Mn 2p XPS element spectra.

Due to the *j-j* coupling all Mn 2p spectra are composed of the Mn $2p_{3/2}$ and Mn $2p_{1/2}$ peaks. The spectra showed a distinct shoulder at the side of lower binding energy values and a clear tailing on the side of higher binding energy values (Fig. 4.10; personal comm. F. Simon).
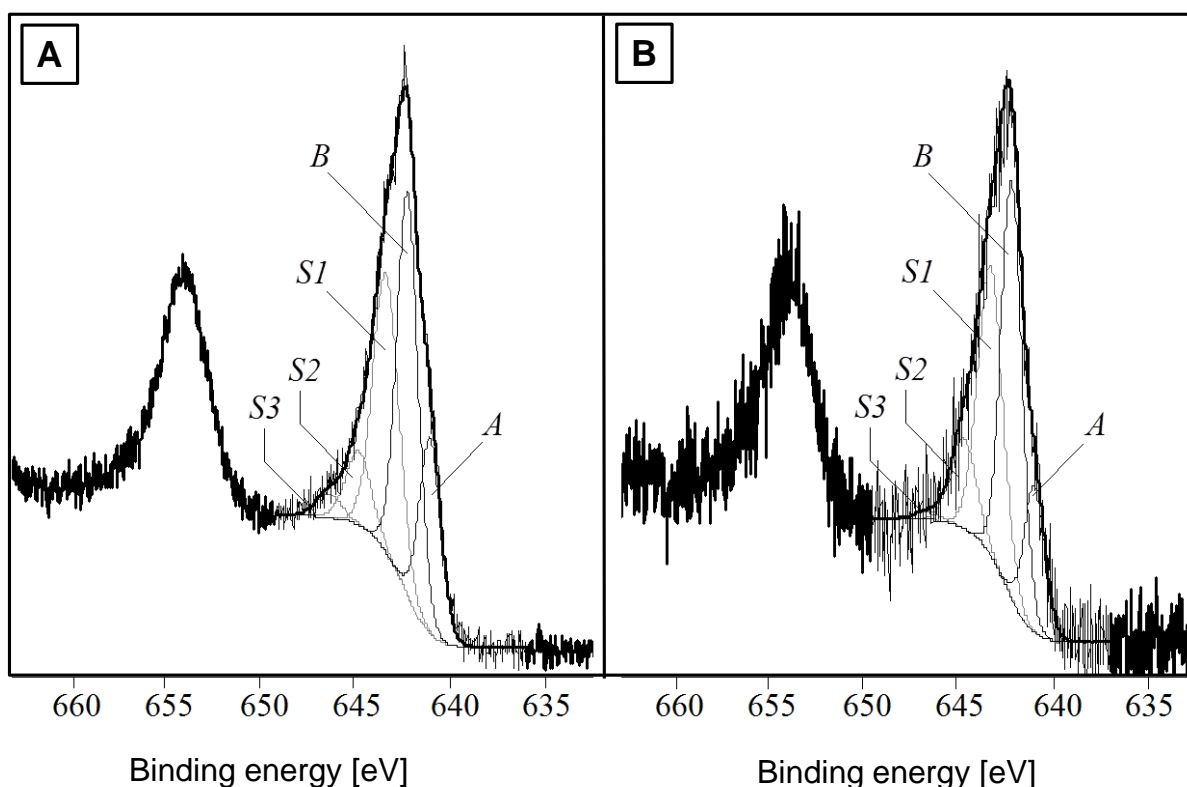
FIGURE 4.10 High-resolution Mn 2p XPS element spectra of **A)** surface subsample of nodule 27KG-1-1, which was in contact with the near-bottom water and **B)** subsample from the inner part of nodule 27KG-1-2.

In order to distinguish between different Mn species, the Mn $2p_{3/2}$ spectra were deconvoluted into five component peaks (Fig 4.10), whereby the two component peaks *A* and *B* are characteristic for the different oxidation states of Mn while the three peaks *S1*, *S2*, and *S3* appear from excited states of the manganese atoms. According to the binding energy, different Mn oxidation components can be found. Component peak *A* (640.73 to 641.10 eV) derived from Mn^{2+} and Mn^{3+}, whereas the more intensive component peak *B* result from Mn^{4+} (641.97 to 642.29 eV) (Di Castro and Polzonetti, 1989). These results are in good agreement with previously reported values for different Mn species in different Mn-phases (Foord et al., 1984; Di Castro and Polzonetti, 1989). Table 4.3 summarizes the experimentally determined binding energy values as well as the intensity ratios calculated from the area of the component peaks showing the reduced Mn species (Mn^{2+} and Mn^{3+}) and the oxidized Mn species (Mn^{4+}). The outermost layers of all three nodules as well as the inner laying Subsamples of nodule 27KG-1 reveal 67 to 81% Mn^{4+} and 19 to 33% $Mn^{2+} + Mn^{3+}$.

4.4.3.3 Carbon components (C1s)

The shape of the recorded C1s spectra indicates the presence of different carbon compounds. Hence, the C1s spectra were separated into six component peaks (*A* to *E*, and *G*; Fig. 4.11). Component peaks *A* to *E* result from organically bound carbon, which are the major carbon compounds. Smaller amounts of inorganically bound CO_3^{2-} and HCO_3^- ions were analyzed as component peak *G* at 289.5 eV (Table 4.4).

Saturated hydrocarbons (component *A* at 285.00 eV) are the most common carbon compounds on the surfaces of the samples. They are more enriched in nodule 27KG-1 than in nodules 32KG and 49KG. The intensities of component peaks *B* at 285.9 eV (C–N bonds of amines and amine-sided carbon atoms of peptides) and *C* at 286.6 eV (C–O bonds of alcohol, phenol and ether groups, and alcohol-sided carbon atoms of carboxylated ester groups) were variable and showed more or less similar composition of the outermost layers as well as in the layers from inside of the nodules (Table 4.4; Fig. 4.11).

The component peaks *D* at 287.7 eV are characteristic for carbonyl carbons of peptide bonds (found only in sample 27KG-1) and *E* at 288.2 eV, which result from carbonyl carbons of carboxylate ester groups are less intensive than the other C 1s component peaks resulting from organically bound carbon species. Compared to the sample taken from the inner part of nodule 27KG-1 (Ss 3, 4), the area of component peak *D* of the sample taken from the outer sphere (Ss 1, 2, 5, 6) seemed to be increased (Table 4.4). In contrast, component peak *E* showed the highest intensity at the outermost parts (surface and bottom side) and was decreased towards the inner parts of nodule 27KG-1 (personal comm. F. Simon).
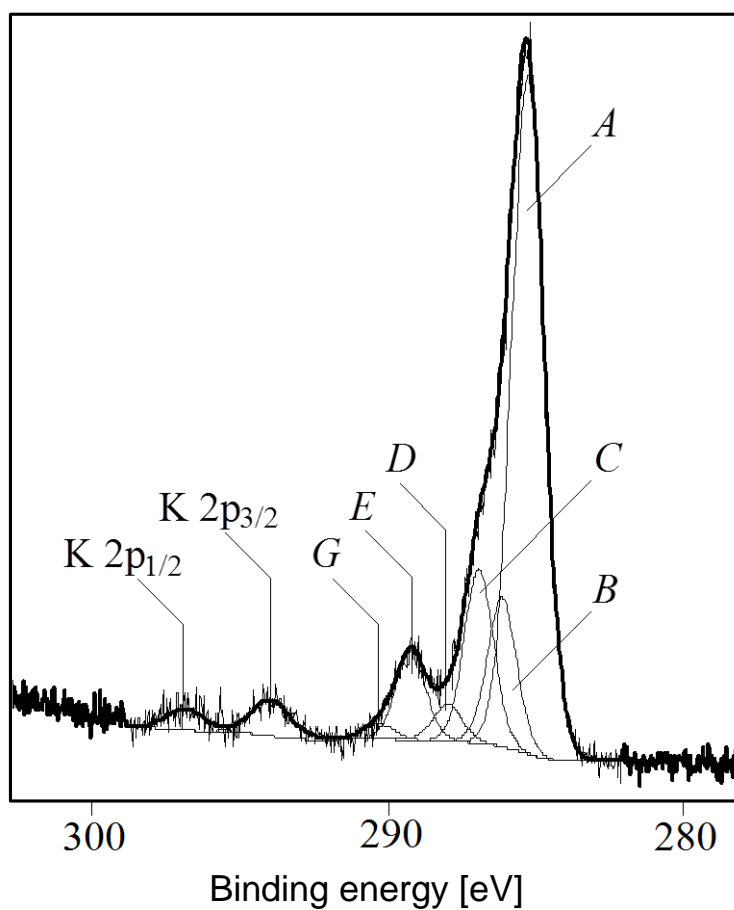
FIGURE 4.11 C 1s XPS high-resolution element spectrum of subsample 27-KG-1-1. The spectrum shows different binding states of carbon atoms, which were explained above. Two element peaks of potassium (K 2p3/2 and K 2p1/2) arose at 292.8 and 295.6 eV.

TABLE 4.4 XPS data of the different C1s compounds detected on different subsamples of CCZ nodules in [wt.%]

Sample SO205	sample description	A	B	C	D	E	G
27KG-1-1	0-1.1mm, surface of nodule (in contact with near bottom seawater)	60.91	12.13	14.05	3.81	7.29	1.81
27KG-1-2	14.2-16.2mm, dendritic growth structure	63.53	9.12	14.77	3.66	3.84	5.07
27KG-1-3	30.2-35.2mm, middle of the nodule, dendritic growth structure	61.29	11.35	12.88	7.13	4.38	2.97
27KG-1-4	6500-11500 μm (dendritic growth structure)	58.13	14.12	12.48	7.68	4.22	3.38
27KG-1-5	500-1500μm (dendritic and hydrogenetic growth structures)	65.67	7.24	14.75	4.00	4.04	4.30
27KG-1-6	0-200μm, outermost bottom side (which was stuck in the sediment)	65.05	9.45	13.45	2.84	5.64	3.56
32 KG-1	surface of nodule (in contact with near bottom water)	54.05	11.75	15.86	-	4.87	13.47
32 KG-3	bottom side of nodule (embedded in the sediment)	41.04	18.48	23.96	-	8.01	13.1
32 KG-5	sample of the rim	36.46	11.61	12.28	-	7.42	11.94
49 KG-1	surface of nodule (in contact with near bottom water)	47.18	16.93	22.00	-	7.46	11.54
49 KG-2	sample of the rim	39.62	9.82	17.58	-	4.73	9.08
49 KG-3	bottom side of nodule (embedded in the sediment)	56.74	15.70	16.76	-	11.37	3.08

108

4.4.6 Electron microprobe analyses

The thick section of nodule 27KG-1 was analyzed to obtain chemical and structural information of this nodule. The sample was analyzed at similar positions where the six drilled subsamples (Ss1-6) which were analyzed using XPS were taken to get more information about the material (Fig. 4.8).

The material of Ss1 of nodule 27KG-1, represent nodule surface, which was recently in contact with the oxic near-bottom water (Fig. 4.12A). This material shows low Mn/Fe ratios ranging from 0.61 - 1.22 and a low Ni+Cu content (0.28 - 0.54 wt.%) but an enrichment of Co (0.14 - 0.29 wt.%). All other subsamples (Ss 2 - 6), predominantly show dendritic growth structures, of high Mn/Fe ratios (15 - 254) and high Ni+Cu contents (1.5 - 5.3 wt.%,), but lower Co contents (0.04 ± 0.03 wt.%; Table 4.5). The dendritic growth structures (4.12B -F) are surrounded by material of low reflectivity and low Mn/Fe ratios (1.08 - 3.27), low Ni+Cu contents (0.46 - 1.42 wt.%) and higher contents of Co (0.13 - 0.29 wt.%; Table 4.5). This material can also refill the entire pore space (pore fillings) within the dendritic growth structures (Figs. 4.12B - F). Chemically, the pore fillings of nodule 27KG-1 differ slightly from that of the surface layer (Fig. 4.9; Table 4.5). The pore fillings have slightly elevated Mn, Ni, Cu, Al, Si, and K concentrations. In contrast to that Fe, Co, Ca, Ti, and Ce are enriched in the outermost layer of the nodule (Table 4.5). However, both, the surface layers as well as the pore fillings have chemical (Mn/Fe <3) and structural characteristics typical for hydrogenetic growth (Halbach et al., 1988). XPS analyses of individual subsamples of the profile through nodule 27KG-1 probably detect those hydrogenetic growth structures.

Electron microprobe analyses of nodules 44KG-A and 49KG-B also reveal dendritic growth structures with high Mn/Fe ratios (10 - 505) and high Ni+Cu contents (Table 4.5; Fig. 4.9). The individual dendrites are surrounded by material of low reflectivity and low Mn/Fe ratios (0.98 - 2.4), which further refill the pore spaces similar to nodule 27KG-1 (Table 4.5; Fig. 4.12B - F).
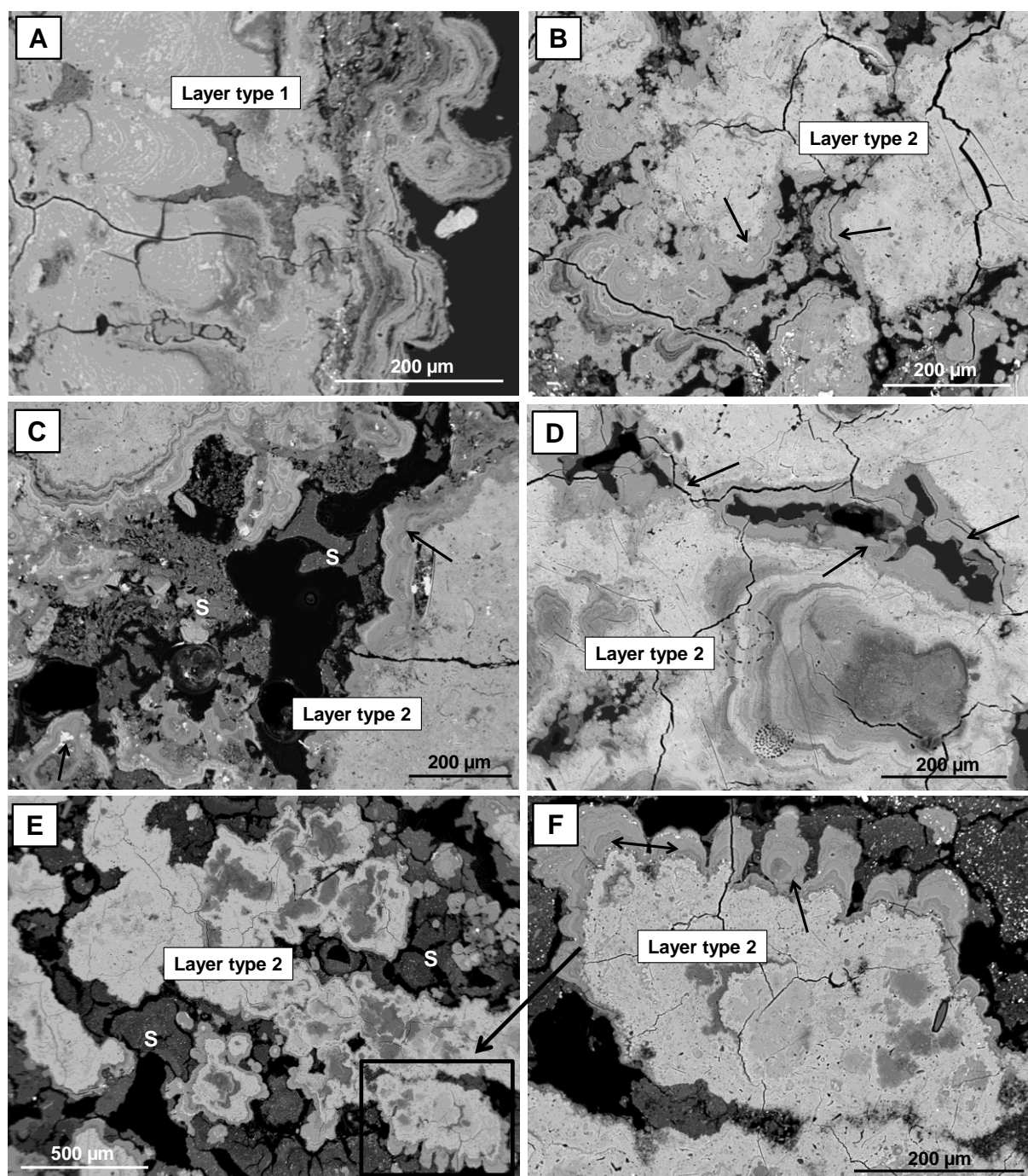
FIGURE 4.12 A: Back scatter electron (BSE) images of the outermost layer of nodule 27KG-1 which correspond to subsample (Ss1). **B-F:** Dendritic, porous growth structures of nodules from the CCZ (27KG-1, 44KG, 49KG). Dendritic growth structures are surrounded by µm thick layers of dense material of low reflectivity (hydrogenetic, marked by black arrows). Pores are filled with material of low reflectivity **(D)**. **F:** Enlargement of dendritic growth structure surrounded by hydrogenetic layer in Figure **E.** S marked ambient sediment in which the nodules have grown.

Table 4.5 Average content of major and minor elements of hydrogenetic layer, pore fillings and the dendritic growth structures (EMPA data, wt.%)

sample SO 205	Mn	Fe	Co	Ni	Cu	Zn	Na	Mg	Al	Si	K	Ca	Ti	Ba	Mo	Ce	Mn/Fe	Ni+Cu	Ni/Co	Ni/Mn	Cu/Mn	Co/Mn
27KG-1 outermost layer																						
AVERAGE (n[1]=14)	17.5	18.1	0.24	0.28	0.15	0.11	1.46	0.88	0.76	4.52	0.38	2.23	0.93	0.19	b.d.l[2]	0.12	0.98	0.43	1.16	0.02	0.01	0.014
STD. DEV.	1.67	1.68	0.04	0.07	0.02	0.01	0.28	0.12	0.18	0.64	0.04	0.15	0.13	0.02	b.d.l[2]	0.04	0.16	0.07	0.16	0.00	0.00	0.002
MEDIAN	17.6	17.7	0.26	0.30	0.14	0.10	1.46	0.89	0.69	4.69	0.39	2.29	0.97	0.19	b.d.l[2]	0.12	1.00	0.44	1.17	0.02	0.01	0.014
MIN	13.2	15.7	0.14	0.14	0.10	0.09	0.90	0.61	0.59	3.70	0.32	1.95	0.67	0.16	b.d.l[2]	0.08	0.61	0.28	0.88	0.01	0.01	0.007
MAX	20.0	21.6	0.29	0.37	0.19	0.14	1.96	1.05	1.07	5.62	0.45	2.43	1.09	0.25	b.d.l[2]	0.21	1.22	0.54	1.40	0.02	0.01	0.017
27KG-1 pore fillings																						
AVERAGE (n[1]=22)	23.2	10.45	0.22	0.55	0.46	0.09	1.48	1.04	2.06	6.34	0.70	1.95	0.71	0.33	0.05	0.06	2.36	1.01	2.56	0.02	0.02	0.010
STD. DEV.	4.15	2.64	0.04	0.18	0.11	0.02	0.47	0.31	0.97	3.01	0.46	0.51	0.12	0.24	0.03	0.02	0.67	0.29	0.88	0.01	0.00	0.002
MEDIAN	24.3	9.63	0.22	0.60	0.48	0.09	1.50	1.00	1.85	4.82	0.51	2.05	0.73	0.26	0.05	0.06	2.46	1.05	2.70	0.02	0.02	0.009
MIN	15.1	5.79	0.13	0.23	0.22	0.04	0.70	0.52	0.94	3.20	0.35	1.21	0.34	0.11	b.d.l[2]	0.04	1.08	0.46	1.02	0.01	0.01	0.007
MAX	28.8	15.16	0.29	0.84	0.59	0.13	2.37	1.73	4.34	14.0	2.26	3.65	0.95	1.35	0.15	0.10	3.27	1.42	3.77	0.03	0.02	0.014
44KG pore fillings																						
AVERAGE (n[1]=9)	20.0	13.8	0.17	0.19	0.30	0.07	2.25	0.71	1.52	6.13	0.33	1.80	0.53	0.20	0.02	0.08	1.46	0.49	1.12	0.01	0.01	0.008
STD. DEV.	3.18	1.41	0.04	0.12	0.11	0.02	0.54	0.12	1.20	2.37	0.15	0.27	0.07	0.03	0.02	0.01	0.24	0.23	0.56	0.00	0.00	0.002
MEDIAN	19.2	13.9	0.17	0.16	0.28	0.06	2.16	0.71	1.03	5.07	0.27	1.67	0.53	0.19	0.03	0.08	1.39	0.45	1.00	0.01	0.01	0.008
MIN	15.6	10.4	0.11	0.11	0.23	0.05	1.65	0.50	0.91	3.77	0.21	1.59	0.38	0.17	b.d.l[2]	0.07	1.24	0.34	0.71	0.01	0.01	0.006
MAX	27.3	15.0	0.24	0.51	0.59	0.10	3.29	0.93	4.58	11.68	0.67	2.45	0.64	0.28	0.05	0.11	2.06	1.11	2.51	0.02	0.02	0.012
49KG pore fillings																						
AVERAGE (n[1]=66)	19.8	13.7	0.17	0.28	0.40	0.06	1.31	0.80	1.66	5.87	0.43	2.01	0.50	0.19	0.02	0.04	1.48	0.67	1.69	0.01	0.02	0.009
STD. DEV.	2.04	1.66	0.03	0.15	0.15	0.01	0.43	0.19	0.67	1.26	0.22	0.29	0.10	0.02	0.02	0.01	0.30	0.29	1.15	0.01	0.01	0.001
MEDIAN	20.0	13.9	0.17	0.23	0.35	0.06	1.32	0.75	1.43	5.72	0.37	1.97	0.51	0.19	0.03	0.04	1.48	0.57	1.27	0.01	0.02	0.008
MIN	15.5	9.26	0.11	0.11	0.22	0.04	0.43	0.56	0.83	3.65	0.20	1.61	0.21	0.14	b.d.l[2]	0.01	0.98	0.37	0.67	0.01	0.01	0.005
MAX	24.4	17.0	0.23	0.89	1.02	0.11	2.50	1.49	4.27	9.67	1.18	3.68	0.68	0.24	0.06	0.06	2.44	1.91	7.89	0.04	0.05	0.011
27KG-1 dendritic growth structure																						
AVERAGE (n[1]=58)	45.7	0.72	0.04	1.58	1.60	0.21	1.99	2.07	1.06	1.96	1.10	1.34	0.06	0.45	0.07	0.01	90.8	3.19	39.73	0.04	0.04	0.0010
STD. DEV.	3.71	0.49	0.03	0.58	0.47	0.06	0.50	0.56	0.54	1.12	0.22	0.39	0.11	0.21	0.03	0.01	55.9	0.90	24.76	0.02	0.01	0.0007
MEDIAN	46.4	0.60	0.04	1.43	1.68	0.19	1.88	2.05	0.96	1.77	1.11	1.15	0.04	0.47	0.06	0.01	78.2	3.01	34.60	0.03	0.04	0.0009
MIN	32.4	0.19	b.d.l[2]	0.72	0.75	0.12	0.97	1.12	0.29	0.38	0.65	0.88	0.00	0.10	0.03	b.d.l[2]	14.7	1.49	10.83	0.01	0.02	0.0000
MAX	50.4	2.93	0.11	2.96	2.37	0.39	3.30	3.44	2.26	6.16	1.63	2.33	0.82	0.92	0.17	0.03	254	5.34	148	0.07	0.06	0.0024
44KG dendritic growth structure																						
AVERAGE (n[1]=14)	43.4	0.75	0.05	0.87	1.34	0.34	3.32	1.63	1.11	2.46	0.85	1.20	0.07	0.12	0.05	b.d.l[2]	72.5	2.21	29.0	0.02	0.03	0.0012
STD. DEV.	2.29	0.32	0.03	0.16	0.19	0.08	0.46	0.39	0.51	1.56	0.17	0.06	0.07	0.04	0.01	b.d.l[2]	42.1	0.31	27.5	0.00	0.00	0.0008
MEDIAN	43.4	0.77	0.05	0.91	1.37	0.34	3.40	1.58	1.20	2.49	0.85	1.21	0.05	0.12	0.05	b.d.l[2]	56.3	2.23	18.4	0.02	0.03	0.0011
MIN	38.8	0.26	0.01	0.62	1.04	0.22	2.64	0.95	0.12	0.11	0.44	1.11	0.02	0.08	0.03	b.d.l[2]	27.3	1.74	8.14	0.01	0.02	0.0002
MAX	46.8	1.52	0.13	1.09	1.62	0.49	3.99	2.39	1.81	5.79	1.11	1.29	0.30	0.19	0.07	0.03	179	2.59	91.4	0.03	0.04	0.0029
49KG dendritic growth structure																						
AVERAGE (n[1]=37)	44.0	0.91	0.06	2.62	1.97	0.25	2.53	2.12	1.19	1.68	0.94	1.42	0.06	0.21	0.06	b.d.l[2]	102	4.59	63.8	0.06	0.04	0.0014
STD. DEV.	3.76	0.91	0.06	0.50	0.24	0.04	0.71	0.60	0.76	1.37	0.18	0.24	0.05	0.06	0.02	b.d.l[2]	97.8	0.63	45.7	0.01	0.00	0.0017
MEDIAN	44.7	0.54	0.03	2.65	2.02	0.25	2.74	2.00	1.08	1.33	1.00	1.36	0.04	0.20	0.05	b.d.l[2]	80.7	4.62	45.8	0.06	0.04	0.0007
MIN	34.6	0.09	b.d.l[2]	1.66	1.23	0.18	0.53	1.51	0.10	0.03	0.52	1.03	0.00	0.12	0.04	b.d.l[2]	10.5	2.94	9.77	0.04	0.04	0.0000
MAX	51.1	3.31	0.23	3.59	2.33	0.37	3.31	4.18	3.42	7.21	1.21	2.10	0.22	0.39	0.12	b.d.l[2]	505	5.90	137	0.09	0.06	0.0060

[1] n = number of analyses; [2] b.d.l = below detection limit

Heterogeneous growth structures

The growth structures of ferromanganese nodules are very heterogeneous. Not only the individual layers differ from each other, but also the individual layers show high structural and chemical heterogeneities (cf. Chapter II).

Figure 4.13 shows a layer of low reflectivity (layer type 1 of nodule 27KG-1) containing nm- to µm-thick spots and veins of high reflectivity (black arrows). A profile across layer type 1, including white spots and veins, was analyzed. The material of low reflectivity (zone I and zone V) has Mn/Fe ratios between 0.55 and 2.5. The content of Ni+Cu are between 0.48 and 2.04 wt.% and Co concentrations are between 0.18 and 0.63 wt.%, respectively. Zone II, a vein of high reflectivity, has high Mn/Fe ratios (16.46 - 59.07) and high Ni+Cu contents (4.42 - 5.36 wt.%) but lower Co concentrations (0.29 ± 0.07 wt.%) than the areas I and V.
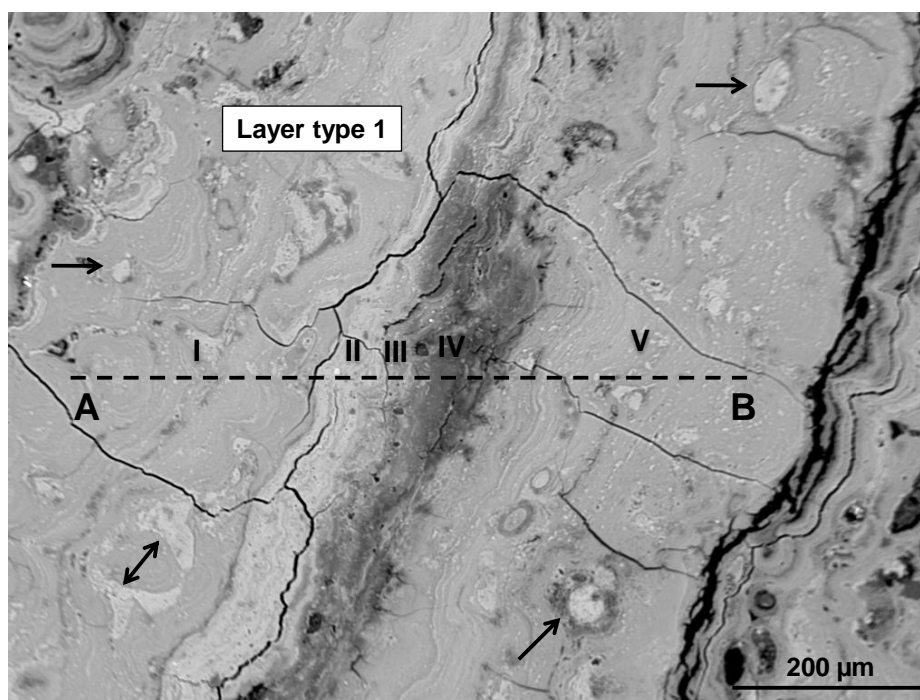
FIGURE 4.13 Hydrogenetic layer (layer type 1) of nodule 27KG-1with nm to µm thick spots and veins of high reflectivity (marked with black arrows).

Between the zones of high reflectivity (II) and the surrounded material of low reflectivity (V) transition zones (III and IV) occur. Zone III shows intermediate Mn/Fe ratios (5.81 - 8.92) and Ni+Cu contents (2.12 - 3.92 wt.%). Zone IV is much darker, the total analytical sums of detectable compounds is lower than 60 wt.% and was therefore, omitted from further discussion (Table 4.6).

TABLE 4.6 Average composition of major and minor elements of the profile through layer type 1 in nodule 27KG-1. Four different parts can be distinguished chemically (I – V; EMPA data, wt.%)

Profile sample	Mn	Fe	Co	Ni	Cu	Zn	Mn/Fe	Ni+Cu	Na	Mg	Al	Si	K	Ca	Ti	Mo	Ba	Ce
Zone (I) hydrogenetic																		
AVERAGE (n*¹=19)	26.2	16.7	0.47	0.63	0.44	0.08	1.64	1.07	1.97	1.15	1.06	4.71	0.44	2.27	1.13	0.05	0.32	0.12
STD. DEV.	4.10	2.56	0.08	0.22	0.10	0.01	0.46	0.32	0.22	0.17	0.24	1.83	0.05	0.26	0.12	0.03	0.05	0.03
MEDIAN	26.6	16.3	0.48	0.61	0.44	0.08	1.64	1.05	2.01	1.09	1.01	4.21	0.46	2.29	1.14	0.05	0.32	0.11
MIN	14.6	13.0	0.25	0.30	0.28	0.07	0.76	0.58	1.28	0.93	0.84	3.21	0.34	1.48	0.86	0.00	0.19	0.08
MAX	31.2	22.4	0.63	1.03	0.60	0.11	2.39	1.63	2.24	1.51	1.88	11.7	0.52	2.66	1.30	0.08	0.39	0.18
Zone (II) suboxic-diagenetic																		
AVERAGE (n*¹=8)	41.2	1.36	0.29	3.42	1.48	0.20	36.02	4.90	2.00	2.80	1.87	2.28	0.63	1.59	0.21	0.05	0.18	0.01
STD. DEV.	2.15	0.58	0.07	0.24	0.13	0.02	15.75	0.33	0.41	0.37	0.63	1.65	0.12	0.24	0.02	0.01	0.03	0.01
MEDIAN	41.8	1.26	0.29	3.50	1.46	0.20	33.58	4.90	1.84	2.70	1.72	1.54	0.64	1.50	0.22	0.05	0.17	b.d.l*²
MIN	37.7	0.74	0.19	3.05	1.32	0.15	16.46	4.42	1.71	2.40	1.23	0.37	0.37	1.35	0.17	0.03	0.15	b.d.l*²
MAX	43.5	2.33	0.43	3.70	1.66	0.22	59.07	5.36	2.86	3.29	3.14	4.86	0.80	2.08	0.23	0.06	0.25	0.03
Zone (III) oxic-diagenetic																		
AVERAGE (n*¹=3)	35.5	4.99	0.34	1.75	1.05	0.13	7.25	2.80	1.19	2.50	1.42	3.01	0.62	1.55	0.40	0.08	0.29	0.03
STD. DEV.	3.50	0.61	0.06	0.78	0.20	0.02	1.57	0.98	0.37	0.39	0.29	1.34	0.10	0.21	0.05	0.01	0.06	0.00
MEDIAN	36.6	5.22	0.34	1.39	0.96	0.13	7.01	2.36	1.22	2.34	1.27	2.55	0.64	1.63	0.40	0.08	0.27	0.03
MIN	31.6	4.30	0.29	1.22	0.90	0.11	5.81	2.12	0.81	2.21	1.23	1.96	0.52	1.32	0.34	0.08	0.24	0.03
MAX	38.4	5.44	0.40	2.64	1.28	0.14	8.92	3.92	1.54	2.94	1.76	4.51	0.71	1.71	0.45	0.09	0.36	0.03
Zone (IV) analyses tot sums < 60%																		
AVERAGE (n*¹=4)	18.3	7.27	0.31	0.74	0.42	0.07	3.10	1.16	0.81	1.32	1.21	4.39	0.44	1.06	0.43	0.05	0.18	0.03
STD. DEV.	2.35	4.23	0.06	0.14	0.07	0.01	1.40	0.21	0.36	0.16	0.38	1.11	0.05	0.15	0.22	0.01	0.04	0.01
MEDIAN	18.3	5.40	0.31	0.80	0.44	0.07	3.41	1.24	0.89	1.34	1.13	4.35	0.45	1.04	0.34	0.05	0.18	0.03
MIN	15.4	4.71	0.24	0.53	0.33	0.06	1.14	0.86	0.33	1.11	0.83	3.16	0.37	0.90	0.28	0.03	0.14	0.02
MAX	20.9	13.6	0.37	0.84	0.47	0.08	4.44	1.31	1.13	1.49	1.73	5.70	0.48	1.26	0.74	0.07	0.23	0.04
Zone (V) hydrogenetic																		
AVERAGE (n*¹=20)	23.2	16.5	0.42	0.62	0.35	0.08	1.50	0.96	1.38	1.08	1.25	6.54	0.53	2.08	1.06	0.05	0.29	0.14
STD. DEV.	5.88	4.23	0.12	0.31	0.13	0.02	0.53	0.44	0.24	0.28	0.69	5.39	0.38	0.43	0.23	0.02	0.05	0.05
MEDIAN	25.0	16.3	0.47	0.56	0.31	0.08	1.59	0.86	1.40	1.05	0.94	5.02	0.37	2.18	1.13	0.05	0.31	0.14
MIN	12.5	6.75	0.18	0.25	0.18	0.06	0.55	0.48	0.60	0.48	0.75	3.16	0.30	1.25	0.68	0.00	0.18	0.06
MAX	30.1	26.2	0.56	1.36	0.69	0.12	2.49	2.04	1.70	1.72	3.03	22.5	1.93	2.56	1.43	0.09	0.36	0.24

*¹ n = number of analyses; *² b.d.l = below detection limit

Figure 4.14 demonstrate the behavior of Ni, Cu, Co through the profile. Furthermore, the concentrations of Si, Ti, Ba, P, S, V, Pb and Ce are lower within the bright material than in the surrounding material of low reflectivity. Aluminum increased slightly within the bright veins and spots. Potassium and Mo possess similar concentrations in both zones (Table 4.6). Figure 4.15 shows the distribution of Mg and Ca within the two different zones. Calcium is compared to Mg more enriched in zones of low reflectivity (I and IV). In contrast to that, the material of high reflectivity (II) shows an increase in the Mg contents and a decrease of the Ca concentrations (Table 4.6; Fig. 4.15).
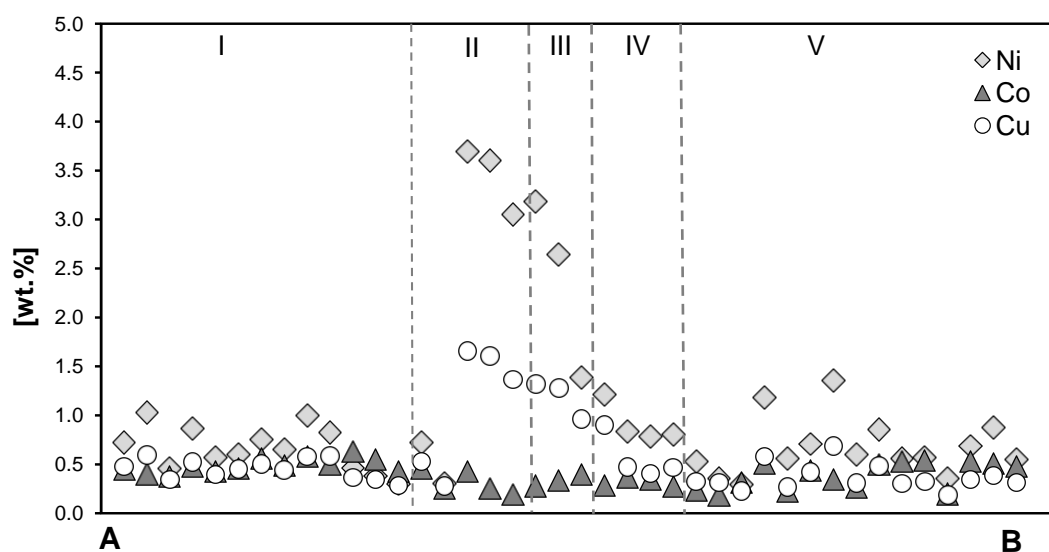
FIGURE 4.14 Ni, Cu, Co profiles through a heterogeneous layer type 1. Ni and Cu contents increase within the material of high reflectivity (zone II) and Co decreases. Cu is enriched to a lower degree than Ni in this zone.
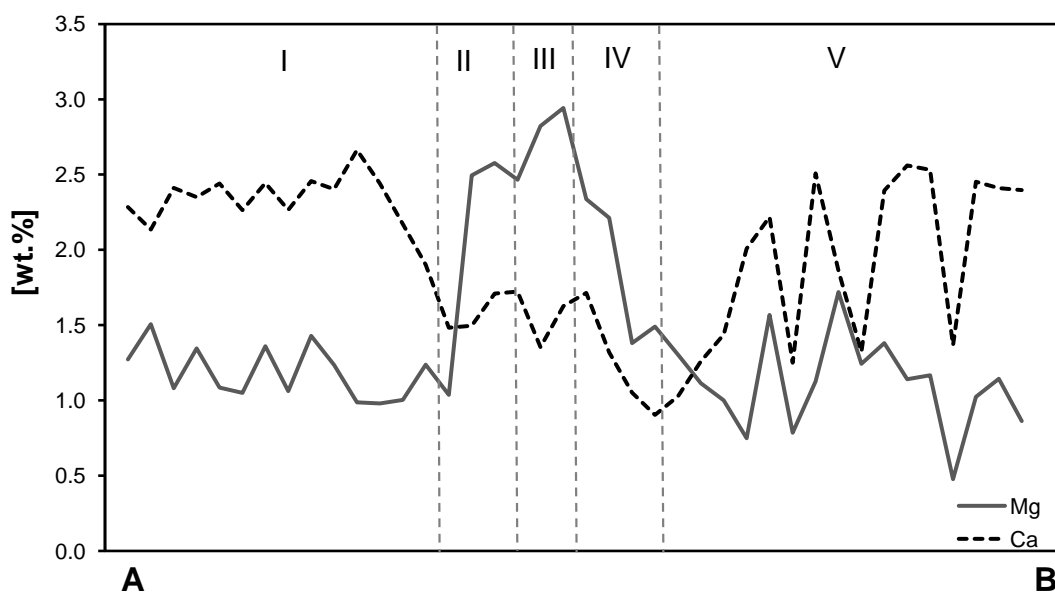
FIGURE 4.15 Profiles of Mg and Ca through the layer type 1 with enclaves of high reflectivity. In the layer of low reflectivity Ca is enriched in contrast to Mg which is enriched in the bright layer. Ca decreased in the bright layer.

114

4.5 Discussion

4.5.1 Pore size and the porosity of ferromanganese nodules

Polymetallic nodules from the CCZ analyzed in this study show a high porosity up to 61%, depending on their different genetic growth structures. On one hand, there are layers of low reflectivity displaying low Mn/Fe ratios and Ni+Cu contents but higher concentrations of Co, representing layer type 1 (Table 4.5, Fig. 4.12A, also cf. Chapter II). According to different authors (e.g., Halbach et al., 1988), these layers are of hydrogenetic origin and were formed under oxic conditions by metal precipitation out of the water column but also out of the oxic pore water within the upper few cm of the sediment as shown in (cf. Chapter II). This accretion process is very slowly, but continuously within the water column (<6 mm/Ma; Halbach et al., (1988)). Such quiescent conditions probably result in layers without high amounts of pores (Nath, 2007) in contrast to the dendritic growth structures.

On the other hand, zones of dendritic growth (layer type 2) with very high Mn/Fe ratios and varying metal contents (Table 4.5) are of suboxic-diagenetic origin (cf. Chapter II). Dendritic growth structures are indicative for a high growth rate (>10 mm/Ma) within the sediment (Halbach et al., 1988) causing cauliflower growth structures, forming areas of high porosity within the nodules. Bigger nodules show larger areas of dendritic growth structures and probably for that reason exhibit higher porosity (up to 61 vol.%).

Due to the high porosity and the pore connectivity of nodules from CCZ, fluids with dissolved metals from the near bottom water as well as from the sediment pore water are able to penetrate the whole nodules. Mn-Fe hydroxides as well as other metals can precipitate out of the fluids and re-fill the pores. The refilling can explain the pore sizes distribution within the nodules. The innermost pores have been longer exposed to the fluids and are therefore more refilled with secondary material and therefore smaller than outermost laying pores.

4.5.2 Pore fillings and epigenetic products

XPS analyses of the recent outermost layers around the nodules (surface, rim, bottom side) as well as XPS and EMP analyses of the pore fillings within the nodules point out that this material is of oxic-hydrogenetic growth with low Mn/Fe ratios and low Ni+Cu contents. This is typical for recent oxic conditions within the environment, as already discussed in Chapter II. Due to the large nodule surface area of ~102 - 130 m^2/g high amounts of trace metals will be adsorbed from the fluids (Koschinsky and Halbach, 1995). These analyses demonstrate that nodules do not only grow on their outsides but also inside by secondary refilling of the pores.

However, the pore fillings within the dendritic growth structures show slightly higher Mn/Fe ratios and higher Ni+Cu contents than the outermost hydrogenetic surface layer. Slight differences are probably due to: **1)** different conditions during the different accumulation periods of the material. The redox conditions of the nodule environment vary because of changes in sedimentation rates, organic content of the sediments and sediment type which influence the behavior of metals causing different chemical composition (Glasby, 1982). **2)** The chemistry of the fluids within nodules can be slightly changed due to reaction with the already precipitated nodule material during nodule penetration. **3)** The Eh and pH conditions vary probably within the micro-milieu due to organic matter relicts within the pores, during the process of sedimentation. This organic matter will be degraded by oxygen, causing more reduced conditions within the pores than within the near bottom or pore water. This results in a higher Mn enrichment due to the dissolution of prior precipitated Mn-phases such as δ-MnO_2, which is less stable under reduced conditions than under oxic. Simultaneously associated elements will be mobilized, which can also be incorporated into the new forming Mn-phases (Koschinsky et. al., 1997). **4)** XPS and EMPA analyses are at different resolution levels (nm vs. µm).

In the last Chapters (II and III) it was demonstrated that nodules had to grow under suboxic conditions. This means, that also the inner parts of the nodules were influenced by suboxic fluids due to the high pore connectivity. Hydrogenetic layers show suboxic precipitations which can be pore fillings as well as re-crystallization effects of primary Mn-phases. Thus, mainly Mn^{4+} of the primary Mn-phases such as δ-MnO_2 can partly be reduced and released to the surrounding fluids. The combination of higher Mn^{2+} flux and the partial dissolution of the hydrogenetic phases lead to re-crystallization of the Mn-minerals, as it was already discussed in Chapter III. Figures 4.13 represent such typical hydrogenetic layer with inclusions of suboxic material. Between the hydrogenetic and the suboxic-diagenetic zones of the nodules

an area of intermediate chemical composition (zone III in Fig. 4.13) can be identified, which probably represent a transition zone. The chemical composition indicates oxic diagenetic growth. But this area is not a distinct individual layer and will be rather interpreted as a reaction margin during dissolution of the hydrogenetic material and re-crystallization of δ-MnO_2 to 10 Å/7 Å vernadite. If the suboxic inclusions were only due to pore refilling within the layer, the transition zone has to be much sharper.

4.5.3 Mn speciation

The oxidation state of manganese in synthetic Mn-oxides, natural Mn-oxides of bulk nodules and of individual areas of nodules (top, bottom) has been studied by various authors (e.g. Murray and Dillard, 1979; Dillard et al., 1982; 1984; Kalhorn and Emerson, 1984; Murray et al., 1984, Piper et al., 1984). The authors suggest, that Mn occurs predominantly as Mn^{4+} in nodules of the Pacific Ocean and only ~1% of the total Mn is presented as Mn^{2+}. In contrast, there are some studies, which report the detection of reduced Mn species in those Mn-phases (e.g., Dymond et al., 1984; Drits et al., 2007). Mn^{2+} has been detected in marine and freshwater nodules (e.g. Wakeham and Carpenter, 1974; Pattan and Mudholkar, 1990) but the occurrence of Mn^{2+} in deep-ocean deposits in comparison with Mn^{4+} is weak or even negligible (Piper et al., 1984).

However, the amount of reduced Mn species ($Mn^{2+}+Mn^{3+} \leq 33\%$) of the analyzed outermost hydrogenetic layer consisting mineralogically of Fe-vernadite (δ-MnO_2) is higher than those given in other studies.

The outermost layer of CCZ nodules is characteristic for hydrogenetic growth and therefore, of an enrichment of Co. Cobalt is adsorbed as Co^{2+} at the negative MnO_2 surface where it can be oxidized (Murray and Dillard, 1979) and subsequently incorporated into the crystal structure of the Mn-phases. Burns (1976) suggests that the oxidation of the adsorbed Co^{2+} to Co^{3+} at the MnO_2 surface is caused by Mn^{4+}. According to this, Mn^{4+} would then be reduced to Mn^{2+}. Dillard et al. (1982) suggested that only a small fraction of Mn^{4+} would be reduced by Co-oxidation after adsorption. Such small abundances of reduced manganese in the presence of Mn^{4+} could probably not be detected in the XPS measurements, according to the authors.

Furthermore, Hem (1978) proposed that Co oxidation is coupled to the disproportionation of hausmannite, which would subsequently lead to higher amounts of Mn^{3+} in the samples. In

mineralogical analyses of nodules by different authors (e.g., Burns and Burns, 1977) and in the study presented here, hausmannite was not identified (cf. Chapter II, Chapter III).

However, Mn^{3+} is thermodynamically unstable relative to Mn^{2+} and Mn^{4+} and will disproportionate (Boughriet et al., 1996) according to equation (4.1; Murray et al., 1984):

$$2\ Mn^{3+}OOH + 2H^+ \rightarrow Mn^{4+}O_2{}^{2-} + Mn^{2+} + 2H_2O \qquad (4.1)$$
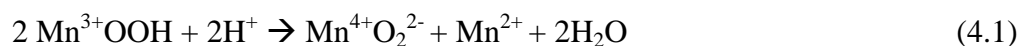
After that the Mn^{2+} will be reoxidized to MnOOH (e.g., Hem and Lind, 1983). It can be assumed that the higher proportion of reduced Mn which were detected in the hydrogenetic layers and pore fillings are due to the adsorbed Mn^{2+} ions on the nodule surface, which is still in the process of oxidation and incorporation into the already solid $Mn^{4+}O_2$ phases.

Furthermore, XPS analyses of the outermost layers of the different nodule subsamples show different C-compounds, which can be an indication for the activity of microorganisms on nodules surface (Blöthe et al., submitted). Due to that the Mn^{2+} could be also a reduction product of bacteria.

4.5.4 Pore space as habitat for bacteria

Several authors suggest that Mn-Fe encrustations are not only of abiotic formation (mineralization) but are also influenced by biologically driven processes due to the activity of microorganisms (bacteria, biomineralization; Ehrlich, 1963; Schweissfurth, 1971; Rosson and Nealson, 1982; Wang et al., 2012).

Ehrlich et al. (1972) determined three types of bacteria within nodules: Mn^{2+}-oxidizers, Mn^{4+}-reducers and bacteria which neither oxidize (Mn^{2+}) nor reduce (Mn^4). Mn^{4+}-reducers are the most abundant bacteria found in the nodules (Ehrlich et al., 1972). Manganese oxides generally have a high capacity to scavenge cations such as Mn^{2+} and other ions (Koschinsky and Halbach, 1995). This Mn^{2+} can serve as an energy source for Mn^{2+}-oxidizing bacteria, which are living on/in nodules (Ehrlich and Newman, 2009) and thus, can contribute to the nodule growth.

Blöthe et al. (submitted) have found a diverse prokaryotic community dominated by nodule-specific Mn^{4+}-reducing and Mn^{2+}-oxidizing bacteria (*Shewanella* and *Colwellia*) within nodules from the eastern license area within the CCZ. The detected pore space provides a habitat for bacteria. Furthermore, due to the connected pore system the fluids of the near

bottom water and the sediment pore water are able to penetrate trough the whole nodules. In addition to dissolved metals, the fluids contain nutrients and molecular oxygen which are necessary for bacteria growth and Mn^{2+} oxidation activity (Blöthe et al., submitted). The occurrence of Mn-cycling bacteria that can be found only in the nodules and not in the surrounding sediment, suggest a contribution in nodule formation and degradation (Blöthe et al. submitted). Up to now, it is not clear if those bacteria are involved in the manganese nodule growth or not. XPS analyses of the outermost surface layers as well as of the inner laying parts revealed different carbonate compounds. At this state it is not clear if the different carbon compounds are indicative for microorganisms only or serve as energy source for bacteria and their processes. However, since Mn^{4+}-reducers probably dominate in nodules (Ehrlich et al., 1972) they may support the dissolution of the MnO_2-oxides/ nodules rather than their growth. The slightly higher amount of Mn^{2+} in some of the outermost nodule layers can probably indicate reduction processes by the detected bacteria. However, within the growth structures no evidence for dissolution can be recognized. If microbial mediated processes would dominate in the Mn nodule growth, biogenic structures (bacteria and/or biofilms) should be found much more often in the nodules (Ehrlich et al., 1972). Until now, biogenic structures were not found in nodules analyzed in this study. Webb et al. (2005) suggested the formation of a Ca pseudo-orthogonal birnessite with a triclinic symmetry as the end product of biogenic Mn oxidation in seawater. However, bulk XRD analyses (cf. Chapter II and III) indicate turbostratic phyllomanganates of hexagonal layer symmetry, which is not in accordance with the findings of Webb et al. (2005). Reichert (2012) conducted a high-resolution study on the growth rate of one nodule from the study area 5 in the German eastern license area (Fig. 2.2 in Chapter II). The results of that study reveal growth rates of 1.8 to 45 mm/Ma. These values are typical for abiotic processes during hydrogenetic precipitation and early diagenesis which are rather more related to climatic control than to biogenic processes (Bollhöfer et al., 1996; Han et al., 2003). Therefore, it can be suggest that the biogenic Mn oxidation/reduction may occur during nodule formation/destruction but it is not the dominate process during nodule formation.

4.6 Summary and Conclusion

The high-resolution computer tomography (CT) analyses of polymetallic nodules from the central equatorial Pacific Ocean within the CCZ reveal a heterogeneous porosity within nodules (<61%) which is due to the different growth structures (dense layers and dendritic growth structures).

The pore size decreases from the surface towards the inner parts of the nodules. The outermost areas are dominated by larger pores (62% >0.011 mm^3) whereas the inner growth structures consist to a large extent of smaller pores.

Pores of nodules are interconnected with each other as well as with the surrounding environment (near bottom as well as pore water). Due to the connectivity between the pores and the surrounding environment, seawater or porewater are able to penetrate through the nodules. They can precipitate metals within the pores and form ferromanganese oxides similar to hydrogenetic precipitates as they are found on the nodule surface and bottom side under recent oxic conditions.

The main Mn-speciation here is Mn^{4+} (67 - 82%) with minor amounts of reduced Mn (Mn^{2+} + Mn^{3+} = 18 - 33%). Their distribution is similar in the whole nodule indicating analogous growth processes.

The pore space within nodules provides a potential habitat for bacteria. Until now, little is known about the microbial community in Mn-nodules and their role in nodule formation.

During suboxic conditions suboxic pore water penetrates the nodules through the open pore system and fill pore space or reacts with the primary Mn-oxide phases causing in mineralogical and chemical re-arrangement.

These results demonstrate that polymetallic nodules, which remain for millions of years on the seafloor, are an active open system growing not only on the outermost surface but also within the inner pores.

Chapter V

Pre-edge analysis of Mn *K*-edge XANES spectra of different genetic layers in polymetallic nodules from the Clarion and Clipperton Zone

In this chapter, results of X-ray absorption near-edge structure (XANES) spectroscopy on individual µm-sized growth structures of ferromanganese nodules from the Clarion Clipperton Zone are presented in order to determine the oxidation state of manganese in these nodules. Tectomanganates and phyllomanganates have the potential to incorporate various metals, to replace Mn^{3+}/Mn^{2+} within the $[MnO_6]$ octahedral layers or are located above vacancies in the MnO_6 octahedral layers. This study should show how the manganese oxidation state varied between genetically different (oxic-hydrogenetic and suboxic-diagenetic) layers as well as between genetically similar (suboxic-diagenetic) layers but with different Ni+Cu content.

5.1 Abstract

The Mn oxidation state in individual growth layers of polymetallic nodules from the eastern Clarion and Clipperton Zone (CCZ) was determined at the μm-scale by Mn K-edge X-ray absorption near edge structure (XANES) spectroscopy.

Suboxic diagenetic layers (layer type 2) of nodules from the CCZ and the Peru Basin (PB) consisting of turbostratic 10 Å and 7 Å phyllomanganates (vernadites) with high Mn/Fe ratios (>>10) and varying metal contents (e.g., Ni+Cu <1 - 6.51 wt.%) showed predominantly Mn oxidation states between 3.3 and 3.8. Hydrogenetic layers of nodules and crust consisting of Fe-bearing vernadite and amorphous δ-FeOOH with low Mn/Fe ratios and low Ni+Cu contents showed predominantly Mn oxidation state around 2.9 ± 0.4. The Mn oxidation state measured in the hydrogenetic layers and crust at the μm-scale was not consistent with the manganese oxidation state measured in the powdered Fe-bearing vernadite (δ-MnO$_2$; ~3.8) that served as a reference for Fe-Mn crust. Moreover, it did not fit at all with literature data. In contrast to the reference powder, nodules and crust samples of this study were analyzed as thin sections which were impregnated with a two component resin (Araldite®; contains organic carbon). The discrepancy between Mn oxidation states in hydrogenetic material in thin sections and in powder form is a potential indication of Mn reduction under the micro-beam during XANES spectra acquisition in the thin sections.

The diagenetic layers which showed no or only low reduction of Mn during XANES measurements have a much lower Fe content than the hydrogenetic phases. It is hypothesized that under the presence of organic carbon the high energy micro-beam induced the reduction of Fe present in high quantity in the hydrogenetic layers. The reduced iron (Fe^{2+}) subsequently reacts with Mn^{4+} in a redox reaction which leads to the oxidation of Fe (to Fe^{3+}) and the equivalent reduction of Mn (to Mn^{2+}) in these layers. The oxidation of organic carbon might also have induced a reduction of the Mn phases in diagenetic layers but to a significantly lower degree compared to the hydrogenetic layers.

5.2 Introduction

Polymetallic nodules of this study consist of turbostratic phyllomanganates (vernadites). Suboxic diagenetic layers (layer type 2) consist of 10 Å vernadite with minor amounts of 7 Å vernadite. Hydrogenetic layers (layer type 1) and ferromanganese crusts consist of Fe-bearing vernadite (δ-MnO_2) which is epitaxially intergrown with an amorphous δ-FeOOH phase.

These Mn minerals consist of [MnO_6] octahedral layers, which are stacked vertically in the c^* direction and separated by hydrated cations. Manganese can be incorporated in different oxidation states (Mn^{2+}, Mn^{3+} and Mn^{4+}) within the octahedra causing a negative layer charge deficit (Bodeï et al., 2007; Manceau et al., 2012). Furthermore, vacancies within the octahedral layers lead also to negative charge deficits (Bodeï et al., 2007; Manceau et al., 2012). This negative charge deficit can be balanced by the incorporation of different cations (alkali and alkaline earth metal ions) as well as hydrolysable cations (e.g., Ni, Zn, Pb; Manceau et al., 2012). The incorporation mechanism of different metals such as Co, Ni, Zn, and Cu has been discussed by different authors (Manceau et al., 2007; Silvester et al., 1997; Peacock and Sherman, 2007a,b; Peacock, 2009).

The study of the oxidation state of Mn is very important for a better understanding of Mn-minerals and their incorporation mechanism of economically interesting metals (e.g., Ni, Cu).

For the determination of the valence states of manganese, Mn K-edge XANES spectroscopy can be used (Manceau et al., 1992b; 2012; Ross et al., 2001; Chalmin et al., 2009). Due to the incorporation of a Mn mixture of up to three valences (Mn^{2+}, Mn^{3+}, Mn^{4+}) in Mn minerals, the determination of the Mn species is not straightforward. Furthermore, the poorly crystalline nano-sized phyllomanganates (biogenic/abiotic) are highly sensitive to X-ray electron damage (Garvie and Craven, 1994; Bargar et al., 2005). During analyses Mn^{4+} can be reduced to $Mn^{3+}$and/or Mn^{2+} (Ross et al., 2001; Manceau et al., 2012).

The XANES spectrum is separated into two parts: the pre-edge and the main-edge region (Brown et al., 1988). The pre-edge is located to the lower energy side of the steeply rising adsorption edge and corresponds to transition of bound state orbitals (1s $\rightarrow$ 3d type electronic transitions; Dräger et al., 1988; Manceau et al., 1992b; Ross et al., 2001). The main-edge is located above the pre-edge at higher energies and corresponds to the electron binding strength (Ross et al., 2001). The Mn K-edge spectra shift towards higher energy with increasing oxidation state (Apte and Mande, 1982; Belli et al., 1980).

5.3 Samples and analytical methods

5.3.1 Mn-mineral standards and reference materials

For this study selected areas of three different nodules sampled during the expedition SO205 (32KG-5, 44KG-2, 49KG-4) and of a ferromanganese crust (37KG-3) from the CCZ, as well as of a nodule from the Peru Basin (PB, SO79 176-3, see Chapter II), were analyzed. Detailed information on the origin of the samples and their chemical and mineralogical composition were presented and discussed in Chapter II and III.

Thin sections (1 x 1 x 0.2 cm, thickness of the material ~200 µm) of different nodules and of one crust were prepared to determine individual genetic growth structures. Powders of Mn-bearing minerals such as rhodocrosite ($Mn^{2+}CO_3$), Mn-diaspore ($Mn^{3+}OOH$) and pyrolusite ($Mn^{4+}O_2$) were used as standards for Mn^{2+}, Mn^{3+} and Mn^{4+}, respectively. Furthermore, powders of a hydrothermal todorokite, of a nodule from the Peru Basin and of a ferromanganese crust (37KG-3) of known chemistry and mineralogy (Chapter III) were chosen as reference materials for comparison with different genetic layers of nodules and crust. The hydrothermal todorokite is a 10 Å tectomanganate, the nodule from the PB consist of turbostratic 10 Å vernadite and the Fe-Mn crust consists of cryptocrystalline Fe-bearing vernadite which is epitaxially intergrown with amorphous δ-FeOOH particles (cf. Chapter II, Chapter III).

5.3.2 XANES spectroscopy at the Mn K-edge

The micro-XANES measurements were performed on the beamline ID21 at the European Synchrotron Radiation Facility (ESRF, Grenoble, France). Manganese reference compounds were prepared as a powder and spread over a sulfur-free tape. Thin sections (1 x 1 x 0.2 cm) of nodule samples were put between two ultralene foils. The distribution of Mn in the nodule thin sections was imaged using the scanning X-ray microscope at ID21 beamline (Susini et al., 2002). Samples were scanned in the microscope chamber under vacuum with a monochromatic beam focused by a Fresnel zone plate at a spot size of 0.25 µm x 0.75 µm (VxH, FWHM). The microprobe intensity was 9x 10^9 ph s^{-1} with a storage ring current of 200 mA. The Mn Kα fluorescence line was excited with energy of 6.7 keV and its intensity was recorded using a photodiode. The integration time per pixel was 100 ms. Maps of several hundreds of µm were recorded. Mn K-edge XANES spectra were recorded from 6.52 to 6.70

keV in 485 points with 0.3 s counting time using a fixed exit double-crystal Si111 monochromator of energy resolution 0.75 eV at 6.60 keV. Reference spectra were measured on reference powders with a large beam (100 µm) in transmission mode with a photodiode. Due to the fragility of the samples, the thin sections of the nodules could not be prepared thin enough to perform measurements in the transmission mode. Micro-XANES measurements at the Mn K-edge were performed in the fluorescence mode on the thin sections of the nodule samples on selected spots covering a large range of Mn abundances. The four detected spectra at each measure point were measured at one spot and averaged. Only the first spectrum was evaluated in the case of potential Mn reduction during the measurements. The incident beam energy was calibrated using a foil of elemental Mn(0). Furthermore, micro-XRF analyses were performed to get qualitative information about the distribution of Mn within individual samples (Mn-maps).

5.3.3 Data analysis

The XANES spectra were post-processed (base line correction and normalization) using the ALS 10.3.2 beamline software (Marcus et al., 2004). The pre-edge region was extracted from the normalized XANES spectra and fitted with a series of Gaussian functions using the software Origin. The pre-edge centroids were calculated for each sample from the average position of the Gaussian functions, weighted by their integrated areas (sum of individual integrated areas) as described in Chalmin et al. (2009).

5.4 Results

### 5.4.1 Mn-mineral standards and reference materials

Mn K-edge XANES spectra of the three Mn-bearing reference compounds are presented in Figure 5.1. We observed a shift of the Mn K-edge spectra (pre-edge; Fig. 5.2) and main-edge (Fig. 5.1) towards higher energies with increasing valence from rhodocrosite (Mn^{2+}) over Mn-diaspore (Mn^{3+}) to pyrolusite (Mn^{4+}). The rhodochrosite and diaspore standards are comparable with Mn^{2+} and Mn^{3+} -bearing Mn-minerals of the literature. The pyrolusite standard show higher pre-edge position than Mn^{4+} bearing Mn-minerals of the literature (Chalmin et al., 2009).

The hydrothermal todorokite, the hydrogenetic vernadite (Fe-Mn crust) as well as the PB nodule reference materials show slightly lower centroid positions of the pre-edge as well as slightly higher of the main-edges than the Mn^{4+} standard pyrolusite (Fig. 5.1). However, the three Mn-reference materials show lower pre-edge centroid positions than pyrolusite and are interpreted containing Mn predominantly as Mn^{4+} with minor amounts of Mn^{3+}.The shape of the whole Mn K-edge spectra as well as of the pre-edge of todorokite, vernadite, and PB nodule reference materials are in good agreement with results of Manceau et al. (1992b; 2012). Slight differences in energy positions in comparison to the literature come from measurements performed at different instruments thus leading to instrumental offsets. Table 5.1 summarizes the calculated pre-edge centroid positions, the main-edge positions as well as the Mn oxidation states of the analyzed standards.
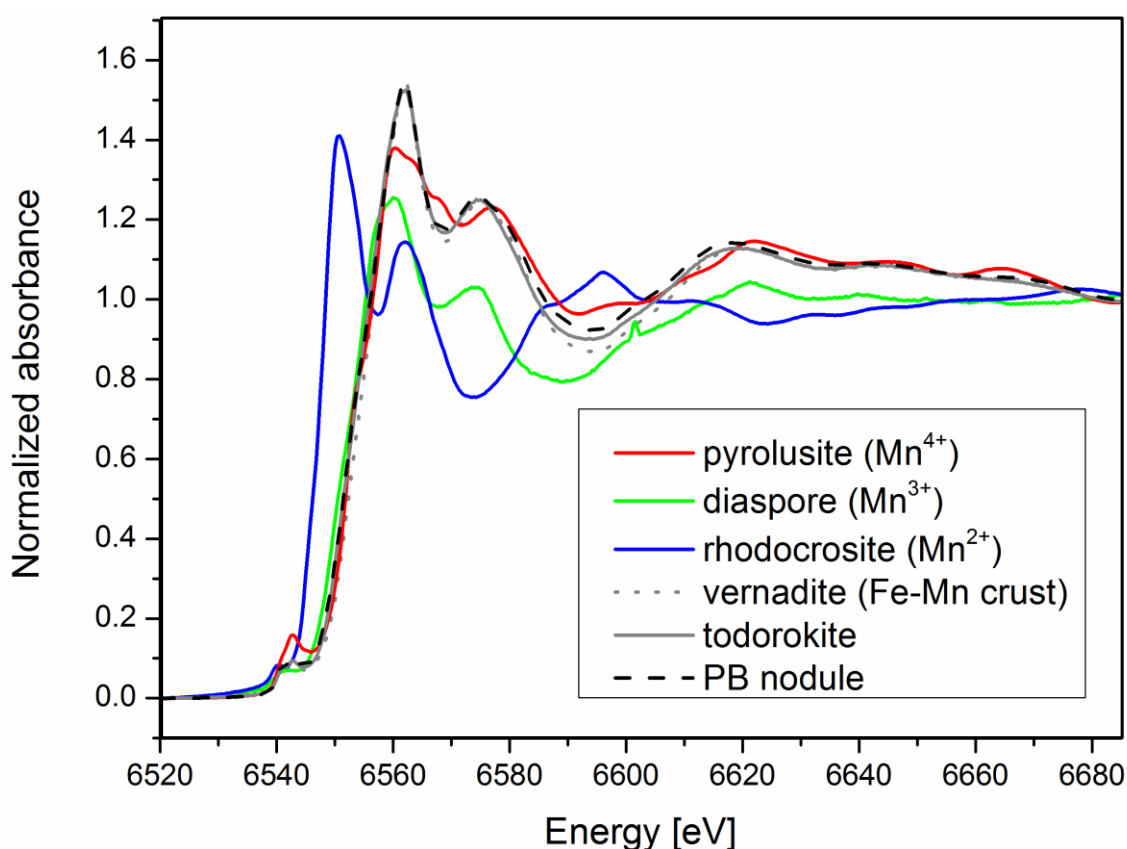
FIGURE 5.1 XANES Mn K-edge spectra of the standards Mn minerals rhodochrosite (Mn^{2+}), Mn-diaspore (Mn^{3+}), pyrolusite (Mn^{4+}), and the reference materials hydrothermal todorokite, vernadite (Fe-Mn crust) and PB nodule. A shift of the spectra from higher to lower energies is typical of a decrease in Mn oxidation state. All samples were analyzed as powders of bulk samples.
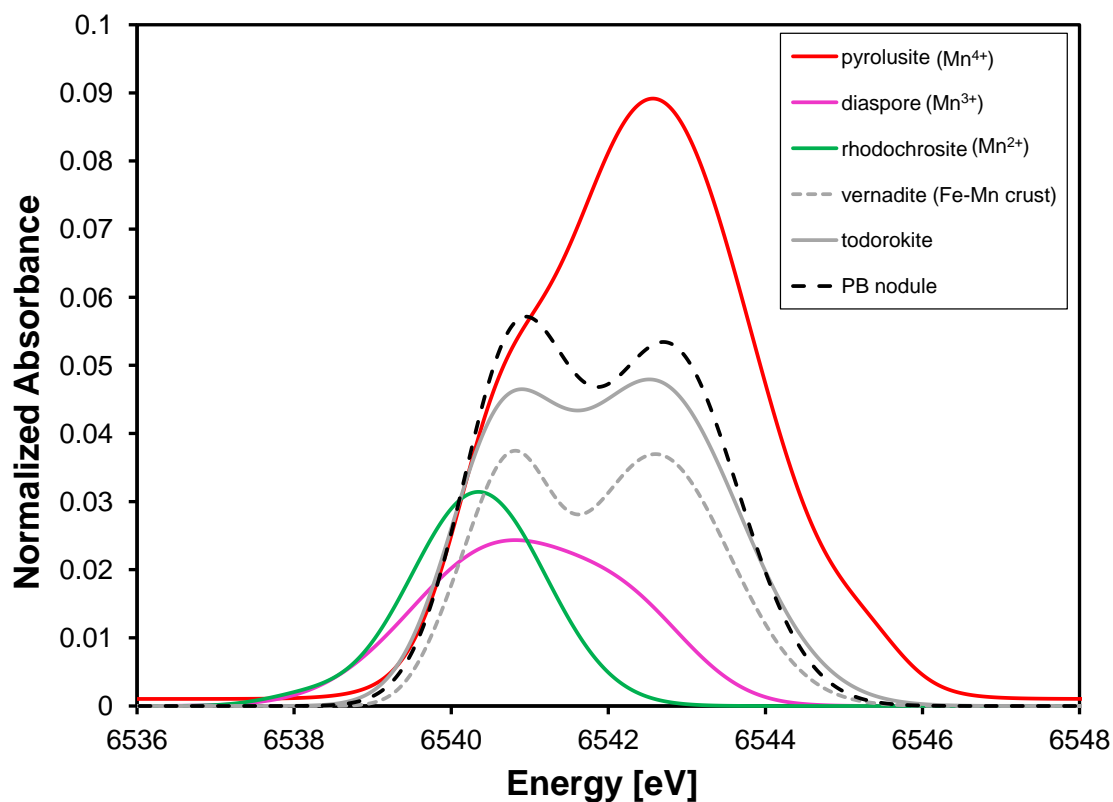
FIGURE 5.2 Pre-edges of the Mn *K*-edge spectra of the standards rhodocrosite (Mn^{2+}), diaspore (Mn^{3+}) and pyrolusite (Mn^{4+}) in comparison with hydrothermal todorokite, vernadite (Fe-Mn crust) and PB nodule reference materials.

TABLE 5.1 Summary of the oxidation states and of the pre-edge and main-edge values of reference minerals used in this study.

Reference compound	Mn-oxidation state	Pre-edge centroid [eV]	Main-edge [eV]
Rhodochrosite	2+	6540.29	6551.16
Mn-Diaspore	3+	6540.91	6560.23
Pyrolusite	4+	6542.42	6560.52
Vernadite (Fe-Mn crust)	~3.8	6541.92	6561.98
Todorokite	~3.9	6541.95	6561.89
Peru Basin (nodules)	~3.8	6541.92	6561.92

Figure 5.3 represent the first derivatives of Mn *K*-edge spectra of vernadite, PB nodule and todorokite. All three spectra are similar and have their absorption edge located around 6562 eV. According to Manceau et al. (2012) the first derivative of the spectrum shows the spectroscopic structure more clearly than the absorption spectrum. Furthermore, the shape of the derivative is not affected by small errors in the post-edge normalization.
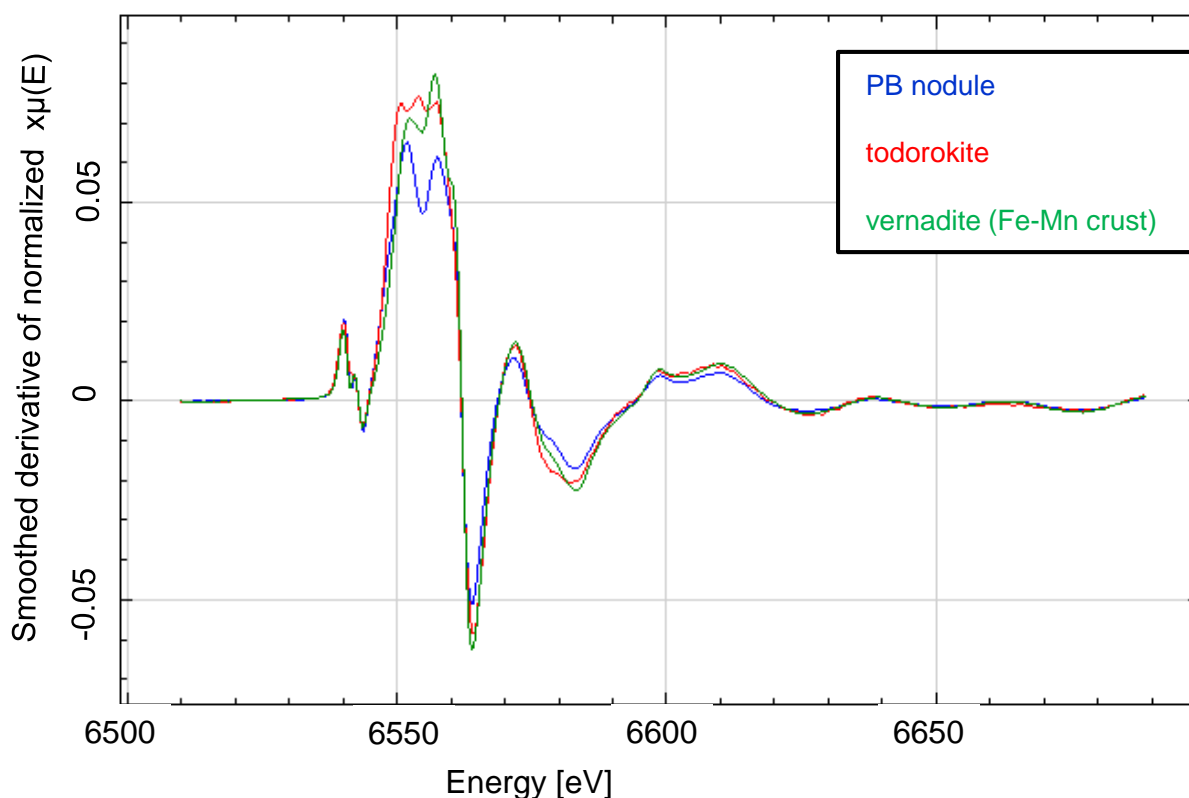

FIGURE 5.3 Comparison of the first derivatives of the spectra of vernadite (Fe-Mn crust), PB nodule and hydrothermal todorokite. All three Mn-phases show similar absorption edges at ~6562 eV.

5.4.2 Individual layers of nodules

1. Dendritic growth structures *(layer type 2)*

The bottom sides of all nodules showed dendritic growth structures of bright material (called layer type 2) with darker areas in their centers. Figure 5.4 represents µ-XRF Mn maps of such dendritic growth structures, where brighter areas are of higher Mn content than darker ones. The darker areas within bright dendritic growth structures show a higher porosity but chemically and mineralogically both structures are similar. Mineralogical investigations by HRTEM of both materials (bright and dark areas) reveal 7 Å/10 Å phyllomanganates (cf. Chapter III). Electron microprobe analyses of bright material reveal that the Mn content (~42 wt.%) is half the content of the darker areas (17 - 19 wt.%). This could be explained by the higher porosity observed in the dark areas (cf. Chapter III, Table 3.2). Both structures show low Fe contents ranging between <0.1 and 4 wt.%. The pre-edge centroid positions of the dendritic growth structures, which have high reflectivity (Fig. 5.4) show slightly higher centroid positions (MP1: 6541.70 ± 0.19 eV) than areas of low reflectivity (MP3: 6541.44 ± 0.14 eV; in Fig. 5.5; Table 5.2). Analyses of medium reflectivity (MP2) show pre- edge centroid positions between 6541.67 and 6541.88 eV). The energy positions of the main-edge show a similar trend from slightly higher energies (6561.41 ± 0.74 eV) in bright material (MP1) to slightly lower energies (6561.32 ± 0.4 eV) in material of lower reflectivity (MP2-MP3). The results of individual measurement points are presented in Table 5.2. The position of the spectra measured in the dark material shifts to slightly lower energies and the pre-edge become more asymmetric and less intense (Fig. 5.5).

The spectra of the dendritic growth structures had a similar shape and comparable pre-edge and main-edge positions to the spectrum of the PB reference material, which is mainly composed of 10 Å and 7 Å vernadites. These results indicate that dendritic growth structures contain of high amounts of Mn^{4+} with minor amounts of reduced Mn-species (Mn^{2+} or Mn^{3+}). Table 5.2 summarizes calculated pre-edge centroids, main edge positions and the resulting oxidation states (calculated from the pre-edge centroids) of dendritic growth structures.
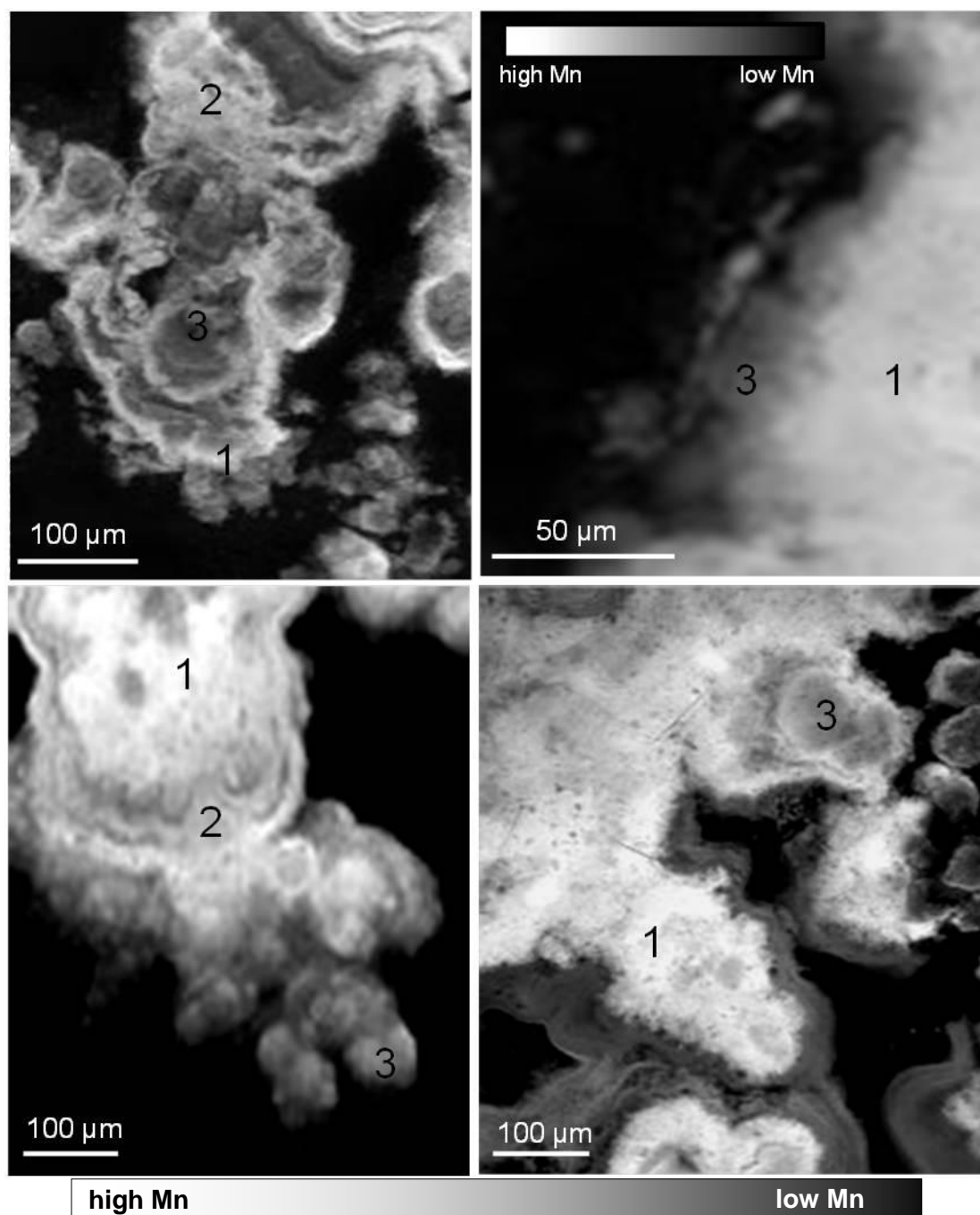
FIGURE 5.4: Dendritic growth structures (layer type 2) of the bottom side of different nodules from the CCZ. The brighter material the higher the Mn content (MP1 - 3).
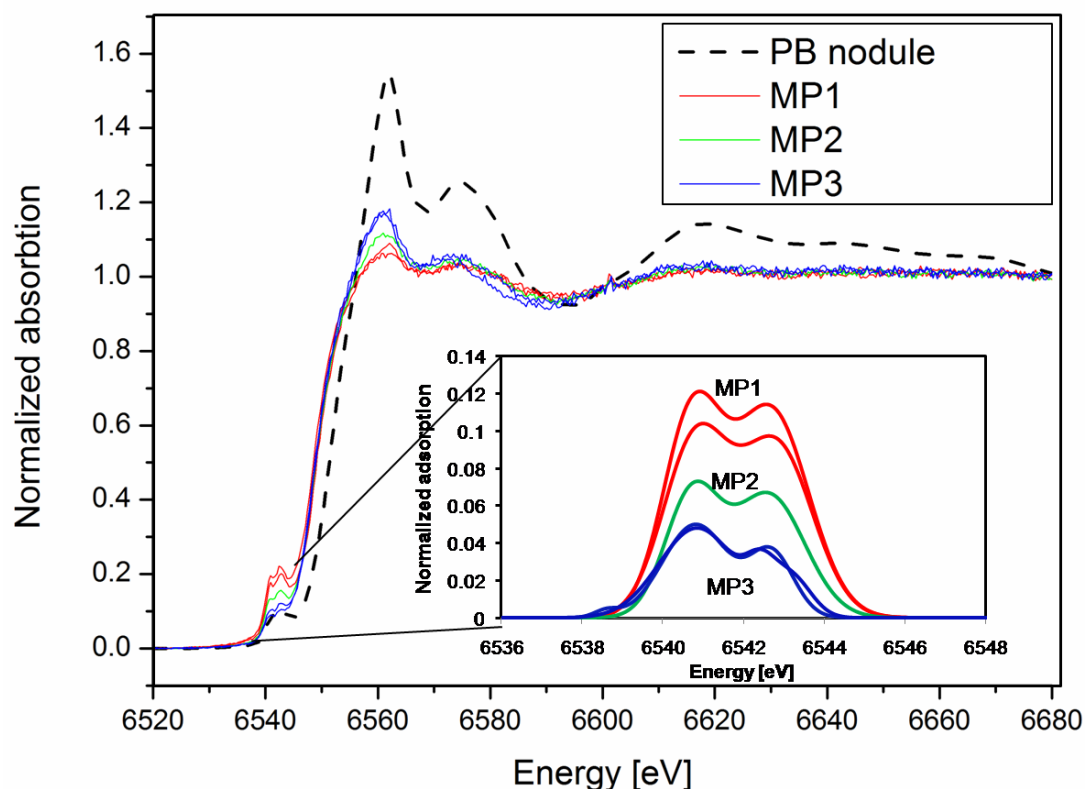
FIGURE 5.5 Mn *K*-edge spectra of different areas within dendritic growth structures (measurements in thin sections) compared with PB nodule reference material (measured as powder). Insert is the Mn *K* pre-edge of different areas within dendritic growth structures. The brighter the material is the more symmetric and intense the pre-edges spectra are. Red spectra are of bright material and therefore of higher Mn content (MP1) than green (medium grey (MP2)) and blue spectrum (dark grey areas (MP3)).
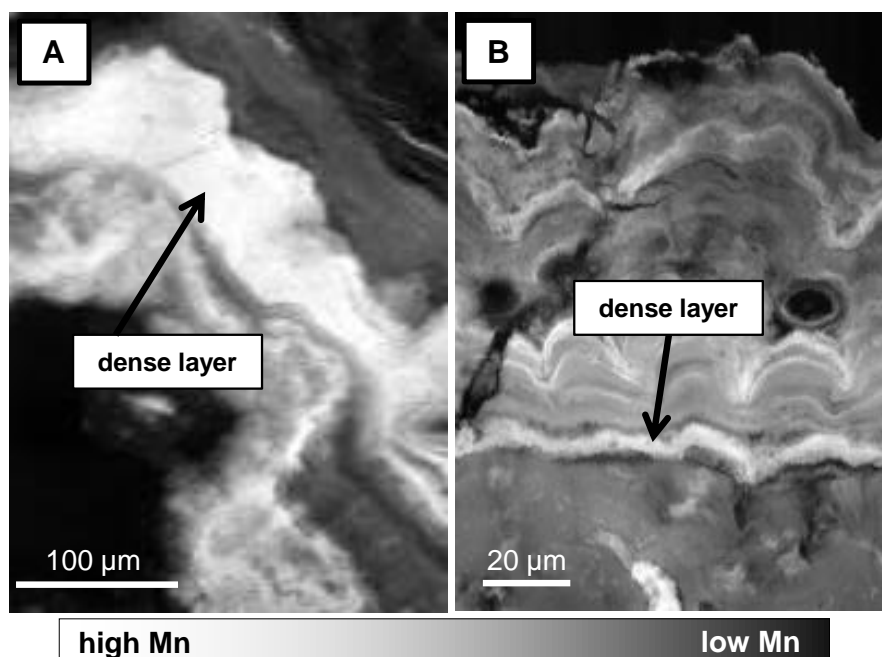
2. Dense layers of high reflectivity *(layer type 2)*

Two dense layers of high reflectivity (layers type 2) of nodule 32KG-5 were analyzed (Fig. 5.6). Both layers show high Mn/Fe ratios (41 - 826) but different Ni+Cu contents. Dense layers from the surface of the nodule (layer type 2.3) contained up to 5.4 wt.% Ni+Cu whereas dense layers from the bottom side contained only up to ~3 wt.% (layer type 2.2; cf. Chapter III, Table 3.2). However, both types of layers are of suboxic diagenetic growth (Halbach et al., 1988) and consist of 7 Å and/or 10 Å vernadites (cf. Chapter III).

The pre-edge centroid of the dense layers ranges from 6541.69 eV to 6541.80 eV and the main-edge is located at 6561.7 ± 0.1 eV (Fig. 5.7; Table 5.2). The shape and positions of the Mn *K*-edge spectra are in good agreement with PB nodule reference material measured in this study.

Although a slight shift in energy is observed between the results of this study and the literature, the shape of the pre-edge of these analyses corresponds to those of Mn-minerals (todorokite, birnessite) in the literature Manceau et al. (1992b). Given the comparison of

samples with standards of this study, the dense suboxic layers have a high content of Mn^{4+} and only minor amounts of Mn^{3+} (Table 5.2).

FIGURE 5.6 Micro XRF Mn-maps of individual areas of nodules that contain two dense layers of high reflectivity (high Mn content (<50 wt.%). **A:** Dense layer type 2.2 with high Mn/Fe ratios and low Ni+Cu contents (<3 wt.%). **B:** Layer type 2.3 with high Mn/Fe ratios and high Ni+Cu contents (3 - 5.4 wt.%) (cf. Chapter III).
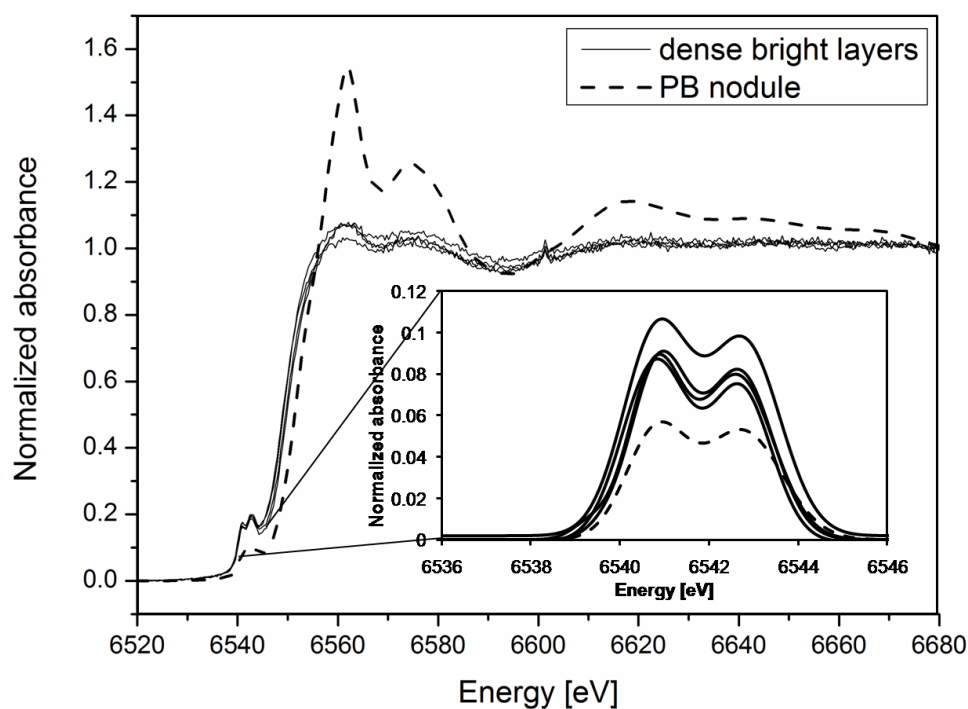

FIGURE 5.7 Mn K-edge spectra of the dense layers (Fig. 5.6). Insert is the Mn K pre-edge of dense layers compared with the PB nodule reference material. All four analysis points show a similar spectrum.

3. Layers of low reflectivity *(layer type 1)*

Figure 5.8 shows areas of nodules with low reflectivity, which is due to a lower content of Mn than within the high-reflectivity dense and dendritic layers. Electron microprobe analyses of those layers reveal low Mn/Fe ratios (<4) with Mn content of 7 - 37 wt.% and Fe is up to 23 wt.% (cf. Chapter II-IV). These layers are of hydrogenetic growth (Halbach et al., 1988) and were called layer type 1. Furthermore, this material fills up the pores between the dendritic growths structures (cf. Chapter IV). Mineralogically these layers are of Fe-bearing vernadite which is epitaxially intergrown with amorphous δ-FeOOH phases (cf. Chapter III).

All material of low reflectivity (except the dark areas within layer type 2) studied in this work have pre-edge centroids ranging between 6540.32 and 6541.35 eV with two individual measurements at slightly higher energies (6541.51; 6541.78 eV; Table 5.2). The slightly higher values are probably because of intergrown suboxic-diagenetic material of a very fine scale with the hydrogenetic material, how it was shown in the Chapters before. The low reflectivity material is expected to be similar to the vernadite standard (Fe-Mn crust). There is therefore a discrepancy between the XANES measurements performed on the thin sections with a micro-beam and the XANES spectra acquired with a macro-beam on the powder reference samples. The Mn *K*-edge spectra of the layer type 1 do not show high evidence of Mn^{4+}. Not only the position of the spectra differs from the vernadite standard but also the shape of the pre-edge is different (Fig. 5.9). The lower the reflectivity of the material is the more asymmetric the pre-edge is, showing only one shoulder instead of two like in the Mn-standards (vernadite, todorokite, PB nodule). Figure 5.10 compares the first derivatives of the two different genetic materials (hydrogenetic and suboxic-diagenetic dense layer), which definitely show a shift from higher energies in the diagenetic layer to lower energies in hydrogenetic material and therefore different Mn oxidation states.
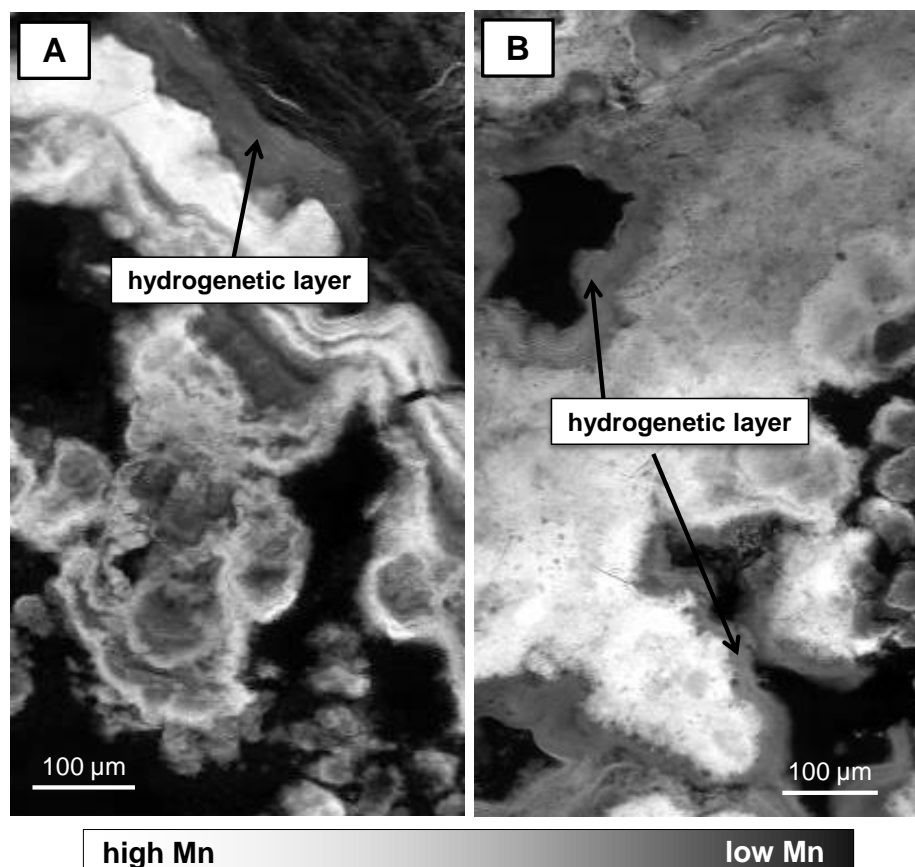
FIGURE 5.8 µ-XRF Mn maps of material of low reflectivity (hydrogenetic) as layers **(A)** and pore fillings **(B)**.
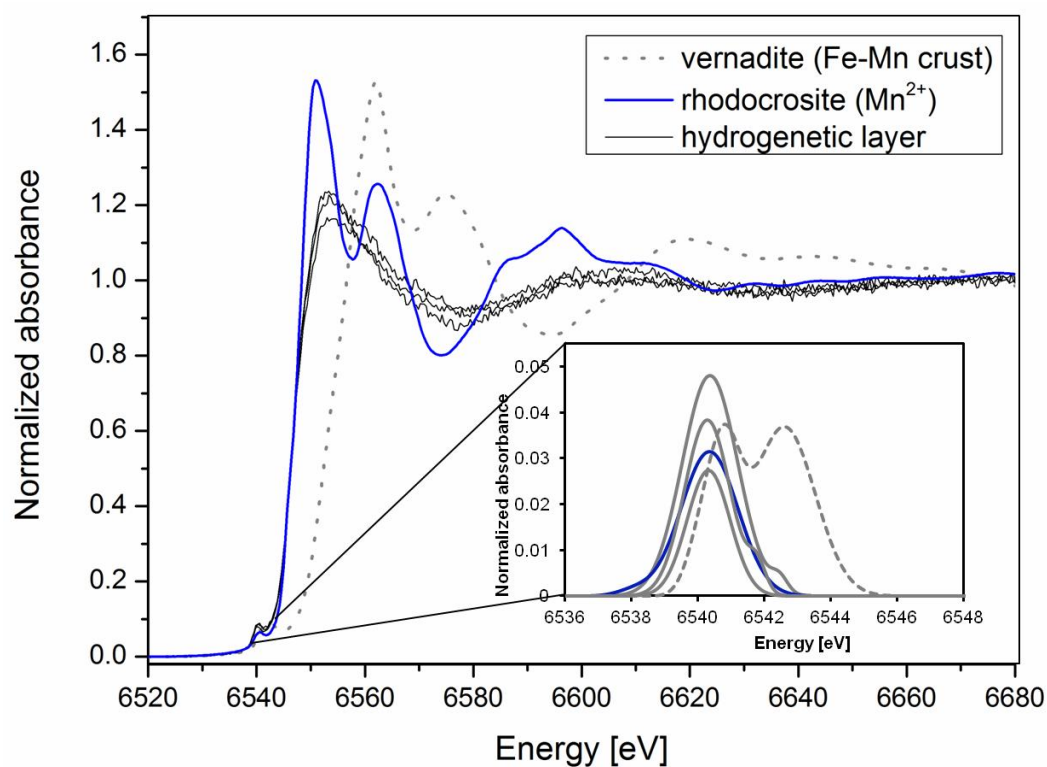
FIGURE 5.9 Mn *K*-edge spectra of hydrogenetic material as shown in Fig. 5.8 in comparison to rhodocrosite (Mn^{2+}) and vernadite (Fe-Mn-crust) reference material. The spectra of the hydrogenetic low-reflectivity material are shifted to lower energies which is indicative of reduced Mn (Mn^{2+}/Mn^{3+}). Insert Mn *K* pre-edge of different material of low reflectivity in comparison with rhodocrosite (Mn^{2+}) and vernadite (Fe-Mn crust).

134
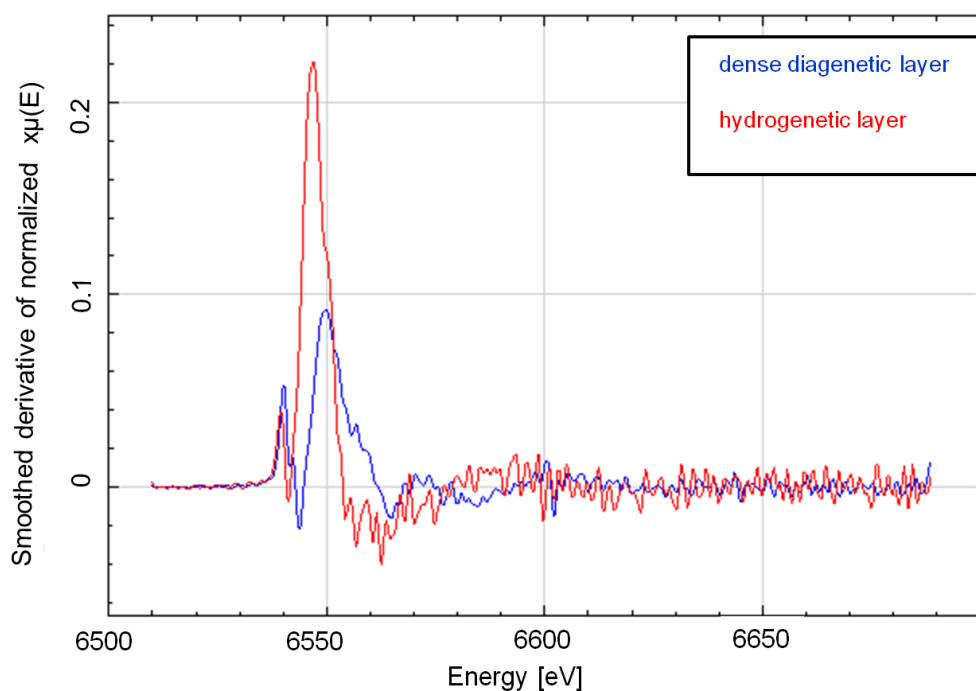
FIGURE 5.10 First derivatives of spectra from a dense suboxic diagenetic layer of high reflectivity (suboxic-diagenetic, layer type 2; Fig.5.6) and of a hydrogenetic layer of low reflectivity (layer type 1; Fig. 5.8).

Noticeably is that to decrease noise in the spectra four different spectra were acquired and summed for each measurement point. To rule out the possibility that Mn became reduced under the micro-beam during acquisition, the first spectra of each measurement point was extracted and analyzed in this study.

Figure 5.11 represents the four individual spectra (MP1-4) acquired at one point of analysis in hydrogenetic material. The first spectrum shows already a shift to lower energies in contrast to the spectra of the dense bright layer type 2 and of the vernadite standard. When comparing the four individual spectra of one measurement point slight changes in the Mn K-edge spectra can be observed. The first spectrum is slightly broader than the second spectrum. The main-edge position changes from 6554.12 eV to 6553.15 eV. This indicates high amounts of Mn^{2+} with minor amounts of Mn^{3+} and a further change to higher amounts of Mn^{2+}.
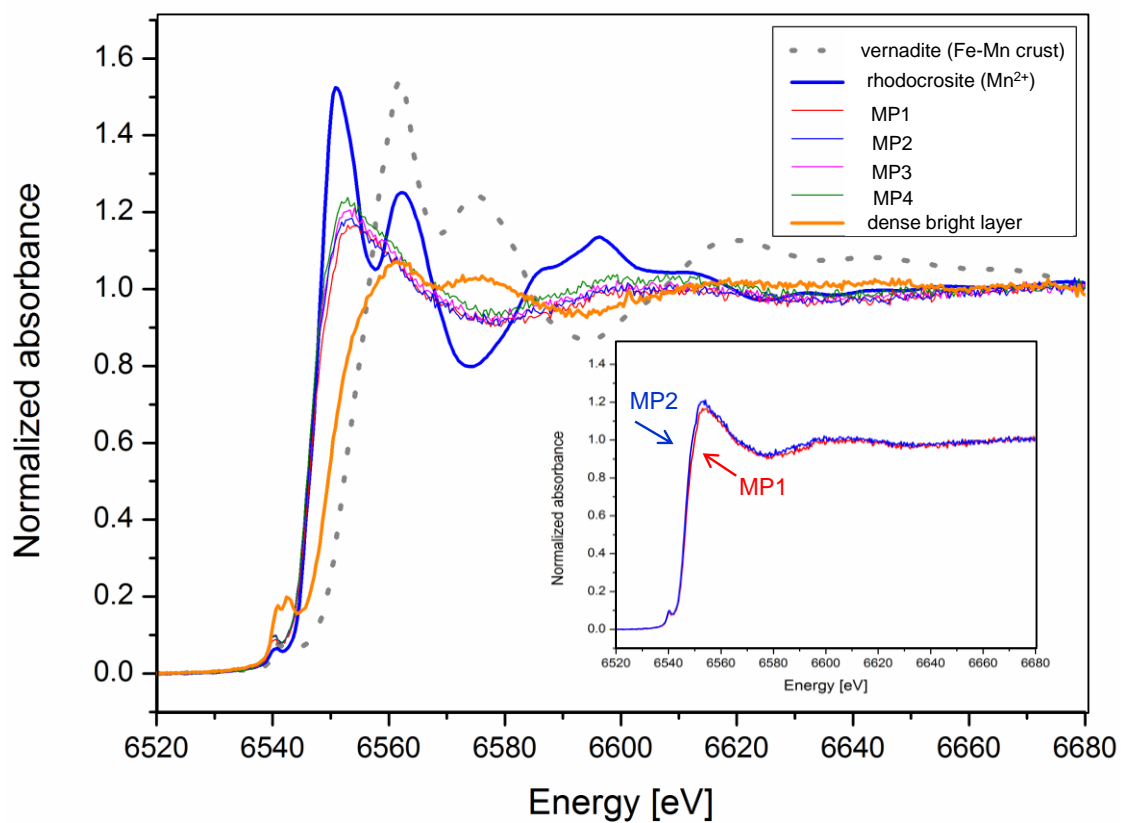
FIGURE 5.11 Mn *K*-edge spectra of a hydrogenetic layer acquired at the same measurement point over time (MP1-4) compared with spectra of rhodocrosite (Mn^{2+}) and vernadite (Fe-Mn crust). Insert: Mn *K*-edge spectra of MP1 and MP2 of the same analyze point. A slight shift can be observed through the analyses with the most important change between the first and second scan acquisition.

TABLE 5.2 Main-edge and pre-edge centroid positions of individual measurement points of nodules from the CCZ with calculated oxidation states (calculated from the pre-edge centroids). The colors in the table correspond to the reflectivity of the measured material (MP1, MP2, MP3 in the figures) and therefore to their Mn content (the brighter the material (MP1) the higher is the Mn content)

| dendritic growth structures (high and low reflectivity)	pre-edge centroid [eV]	main-edge [eV]	Mn oxidation state	dense layers of high reflectivity	pre-edge centroid [eV]	main-edge [eV]	Mn oxidation state	areas of low reflectivity (layer type 1)	pre-edge centroid [eV]	main-edge [eV]	Mn oxidation state
32KG-5c-2, pt4	6541.68	6561.06	3.6	32KG-5b-1, pt7	6541.79	6561.80	3.7	49KG-4b pt1	6540.75	6557.11	2.8
32KG-5c-2, pt3	6541.62	6561.29	3.6	32KG-5b-1, pt8	6541.69	6561.72	3.6	49KG-4b pt5	6541.04	6560.81	3.0
49KG-4c pt8	6541.85	6562.07	3.8	32KG-5c-2, pt13	6541.75	6561.79	3.7	49KG-4b pt6	6540.43	6556.94	2.5
49KG-4c pt9	6541.84	6562.14	3.8	32KG-5c-2, pt14	6541.80	6561.52	3.7	49KG-4b pt9	6541.10	6560.61	3.1
49KG-4b pt13	6541.28	6560.82	3.3	AVERAGE	6541.76	6561.71	3.7	49KG-4b pt11	6540.73	6561.21	2.8
49KG-4b pt15	6541.32	6559.41	3.3	STD.DEV:	0.05	0.13	0.04	32KG-5b-1, pt13	6540.81	6560.27	2.8
44KG-2a-2 pt3	6541.88	6561.90	3.8	MEDIAN	6541.77	6561.76	3.7	44KG-2a-1 pt10	6540.41	6560.81	2.5
44KG-2a-2 pt4	6541.86	6562.09	3.8	MIN	6541.69	6561.52	3.6	44KG-2a-1 pt4	6541.32	6560.76	3.3
44KG-2a-2 pt5	6541.81	6561.47	3.7	MAX	6541.80	6561.80	3.7	32KG-5b-1, pt12	6541.51	6561.23	3.5
44KG-2a-1 pt16	6541.75	6561.70	3.7					32KG-5b-1, pt2	6541.78	6561.46	3.7
32KG-5b-2, pt5	6541.76	6561.41	3.7					32KG-5b-1, pt4	6541.21	6560.77	3.2
32KG-5b-2, pt8	6541.68	6561.02	3.6					32KG-5b-1, pt6	6541.35	6560.77	3.3
32KG-5b-2, pt9	6541.72	6561.92	3.7					44KG-2a-1 pt12	6541.27	6561.06	3.3
49KG-4c pt7	6541.80	6561.08	3.7					44KG-2a-1 pt20	6540.38	6554.16	2.5
44KG-2a-1 pt14	6541.67	6561.35	3.6					44KG-2a-1 pt24	6540.32	6559.86	2.4
32KG-5c-2, pt8	6541.88	6561.94	3.8					32KG-5b-1, pt10	6540.37	6556.50	2.5
32KG-5b-2, pt11	6541.38	6561.50	3.3					32KG-5c-2, pt15	6540.36	6554.12	2.4
44KG-2a-1 pt17	6541.45	6560.92	3.4					32KG-5c-2, pt16	6540.39	6553.66	2.5
32KG-5b-2, pt1	6541.40	6560.62	3.4					AVERAGE	6540.86	6559.01	2.9
32KG-5b-2, pt2	6541.45	6561.65	3.4					STD. DEV.	0.47	2.77	0.4
32KG-5c-2, pt1	6541.38	6561.36	3.3					MEDIAN	6540.78	6560.69	2.8
49KG-4c pt2	6541.35	6561.64	3.3					MIN	6540.32	6553.66	2.4
49KG-4c pt4	6541.73	6561.31	3.7					MAX	6541.78	6561.46	3.7
44KG-2a-2 pt1	6541.27	6561.59	3.3								
32KG-5c-2, pt7	6541.57	6560.89	3.5								
AVERAGE	6541.62	6561.37	3.6								
STD. DEV.	0.21	0.59	0.19								
MEDIAN	6541.68	6561.41	3.6								
MIN	6541.27	6559.41	3.3								
MAX	6541.88	6562.14	3.8								

5.4.3 Ferromanganese crust

Analyses of a polished thin section of the ferromanganese crust (Fig.5.12) demonstrated pre-edge positions ranging between 6540.60 and 6541.41 eV. The main-edge of the spectra ranged between 6556.92 and 6560.74 eV (Table 5.3).

The pre-edge centroid positions of individual points shifted from higher energies (6541.41 eV; only one analyze point) in high reflectivity material (MP1 in Fig. 5.12; Fig. 5.13) to lower energies (6540.71 ± 0.14eV) within material of low reflectivity (e.g., MP2 and MP3 in Fig. 5.12; Fig. 5.13). Similarly to what was observed in the nodules, the position of the pre- and main-edges changed as well as the shape of the spectra. The pre-edge and main-edge became asymmetric with shifts to lower energies (Fig. 5.13). The results of the darker areas fall between the rhodocrosite (Mn^{2+}) and diaspore (Mn^{3+}) standard.

Electron microprobe analyses of the crust material revealed that areas of higher reflectivity have higher amounts of Mn, Ni, Cu and less Fe, Co, Si than the areas of low reflectivity (cf. Chapter II). The brighter material show much higher oxidation states ($Mn^{3+} + Mn^{4+}$)
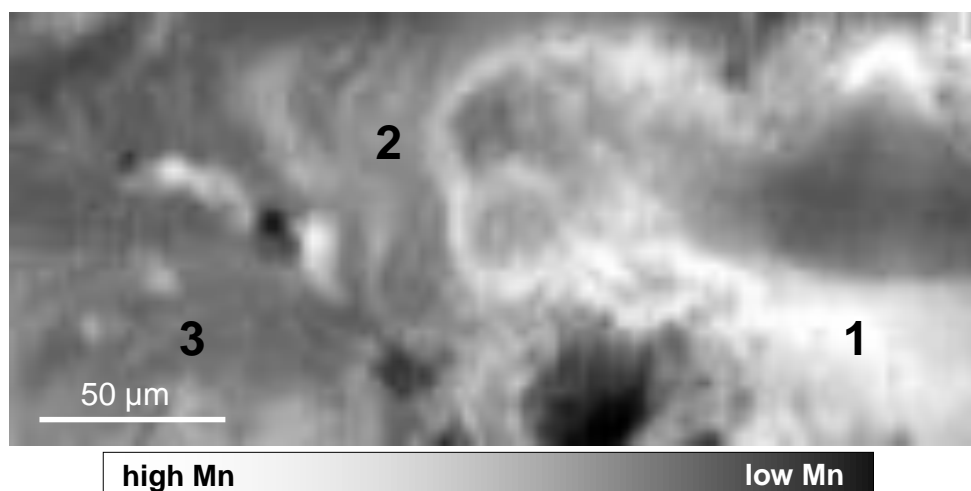

FIGURE 5.12 Micro XRF Mn map of growth structures of a Fe-Mn crust from the CCZ. The brighter the material is (MP1) the higher the Mn, Ni and Cu concentrations are and the lower the Fe and Co content. Individual analyses of the three different areas (MP1-3) were conducted (Fig. 5.13).
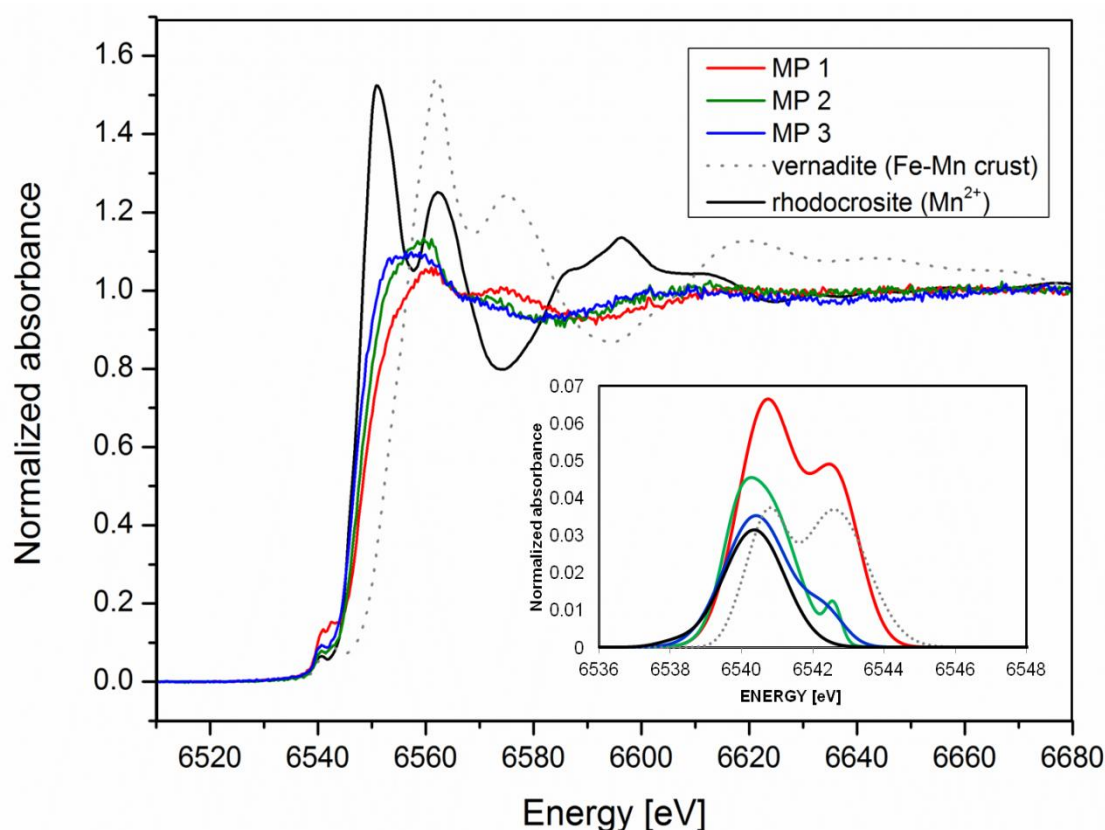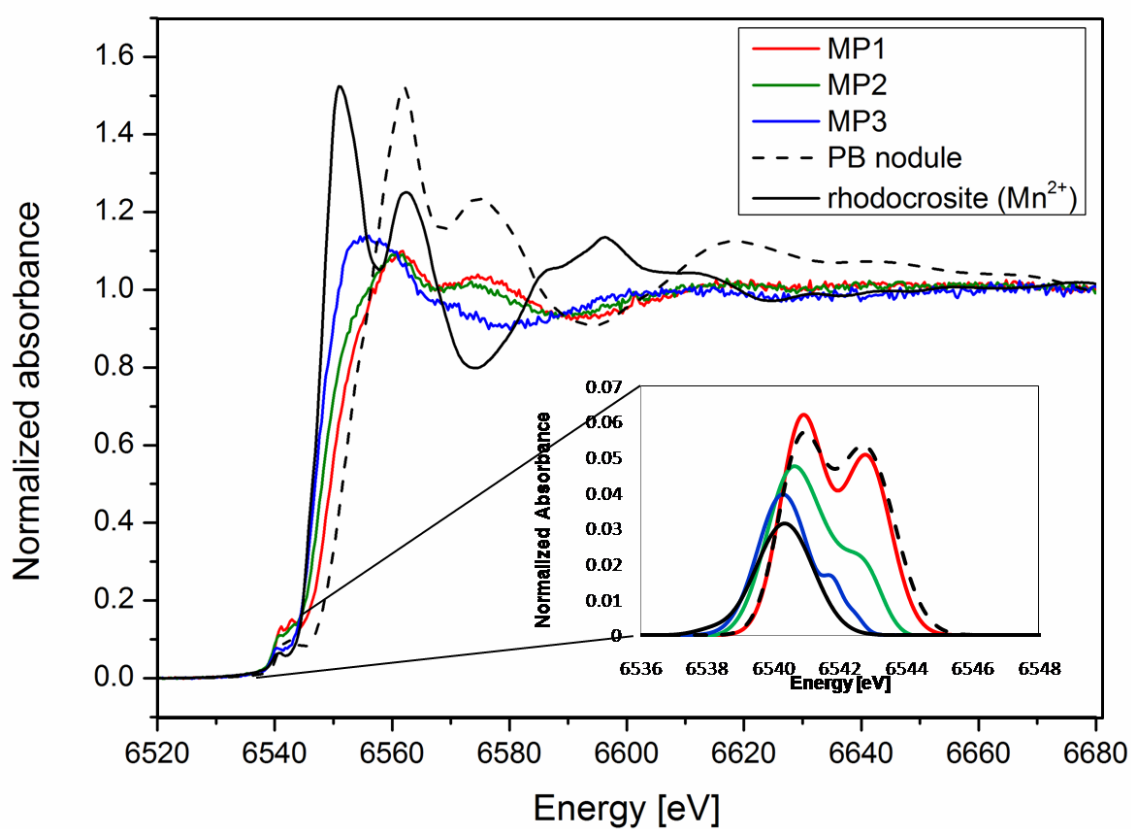
FIGURE 5.13 Mn *K*-edge spectra of individual measurement points of a Fe-Mn crust sample (see Fig. 5.12) compared with rhodocrosite (Mn^{2+}) and vernadite reference material. Insert are Mn *K* pre-edge spectra of individual measurement points of a crust (MP1-3). Bright areas (MP1) show higher centroid energy of the pre-edge as well as of the main-edge than areas of low reflectivity (MP2 - 3).

5.4.4 Peru Basin nodule

The internal growth structure of the nodule from the Peru Basin (PB) shows areas of high and low reflectivity, which are linked to different Mn concentrations similarly to nodules from the CCZ (Fig. 5.14). Mn *K*-edge spectra show within their pre-edge and their main-edge an energy shift from higher energies in bright materials (Fig. 5.14; MP1: 6541.75 ± 0.02 eV) to lower energies in darker areas (Fig.5.14; MP2: 6541.26 ± 0.31 eV and MP3: 6540.47 ± 0.04 eV). Comparing the analyses with the PB nodule reference material, it can be recognized that only MP1 matches more or less the energy position of the pre- and main-edge (Fig. 5.15) indicating high amounts of Mn^{4+} and minor amounts of Mn^{3+}. The darker areas show higher energy shifts of the spectra to lower energies as well as the pre-edges are more asymmetric than of brighter areas (Fig. 5.15). Table 5.3 summarized the main-edge and pre-edge centroid positions of individual areas of the PB nodule.
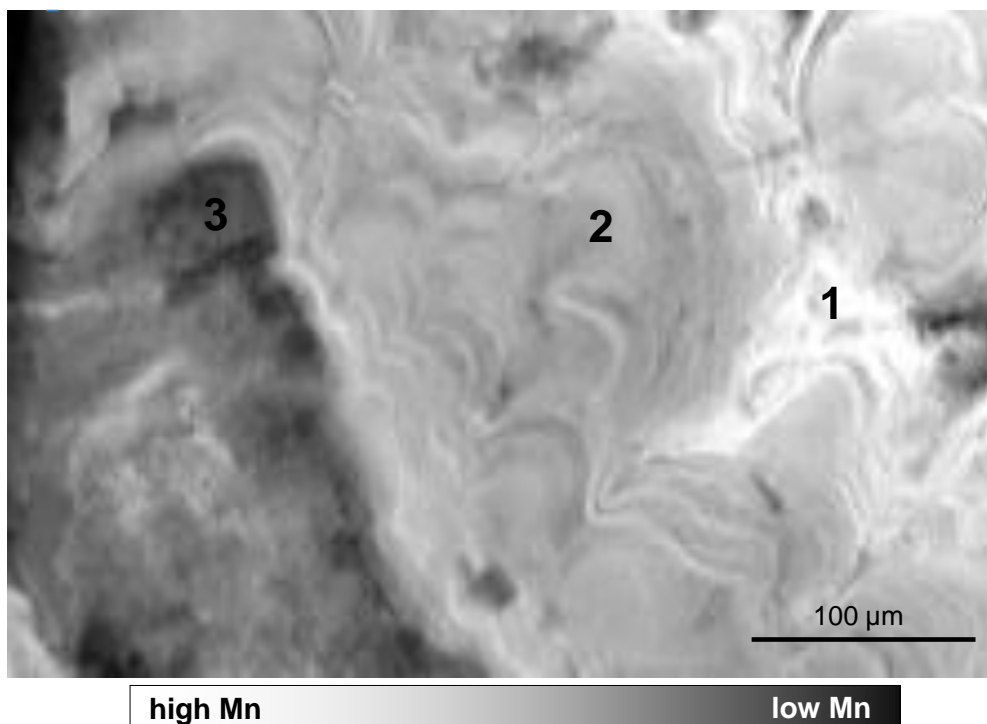
FIGURE 5.14 Micro-XRF Mn map of a Peru Basin nodule with analyze points of three different areas (MP1 - MP3).

FIGURE 5.15 Mn *K*-edge spectra measured at discrete points in a Peru Basin nodule in comparison with those of rhodocrosite (Mn^{2+}) and PB nodule reference material. The insert shows the pre-edge of individual measurement points. MP1 (bright area in Fig. 4.13) pre-edge has a similar shape to the pre-edge of the PB nodule reference material. MP2 and MP3 become more asymmetric and lower in intensity.

TABLE 5.3 Main-edge and pre-edge centroid positions of individual measurement points of Fe-Mn crust from the CCZ and of nodule from the PB with calculated oxidation states (calculated from the pre-edge centroids). The colors in the table correspond to the reflectivity of the measured material (MP1, MP2, MP3) and therefore to their Mn content (the brighter the material (MP1) the higher is the Mn content up to 50 wt.%)

| Fe-Mn crust	pre-edge centroid [eV]	main-edge [eV]	Mn oxidation state	PB nodule	pre-edge centroid [eV]	main-edge [eV]	Mn oxidation state
crust pt1	6540.60	6557.56	2.7	PB pt1	6541.77	6561.55	3.7
crust pt2	6540.65	6556.92	2.7	PB pt3	6541.75	6561.43	3.7
crust pt4	6540.66	6559.95	2.7	PB pt4	6541.74	6561.41	3.7
crust pt5	6540.92	6559.75	2.9	PB pt5	6540.92	6560.89	2.9
crust pt7	6541.41	6560.74	3.4	PB pt9	6541.11	6560.51	3.1
AVERAGE	6540.85	6559.00	2.9	PBpt8	6541.61	6561.34	3.6
STD. DEV.	0.34	1.65	0.3	PB pt7	6541.41	6561.32	3.4
MEDIAN	6540.66	6559.75	2.7	PB pt10	6540.42	6556.12	2.5
MIN	6540.60	6556.92	2.7	PB pt11	6540.50	6555.72	2.6
MAX	6541.41	6560.74	3.4	PB pt14	6540.48	6558.10	2.6
				AVERAGE	6541.17	6559.84	3.2
				STD. DEV.	0.56	2.30	0.5
				MEDIAN	6541.26	6561.11	3.2
				MIN	6540.42	6555.72	2.5
				MAX	6541.77	6561.55	3.7

5.4.5 Calculation of the Mn oxidation state at individual measurement points

Figure 5.16 presents the pre-edge centroid positions of three different Mn standards (Mn^{2+}, Mn^{3+}, Mn^{4+}) and the analyzed samples versus their Mn average oxidation state. The oxidation state of the samples was calculated from the linear relationship of the pre-edge centroid position of the standards (Table 5.1).

The crust layers show predominantly low oxidation states around 2.9 ± 0.3, whereas area of high reflectivity and therefore of higher Mn content show higher oxidation state (~3.4). Materials of low reflectivity within nodules also have lower oxidation states of 2.9± 0.4 (Table 5.2; Table 5.3).

In contrast, dendritic (3.6 ± 0.2) and dense layers (3.7 ± 0.04) of high reflectivity and therefore of high Mn content show high oxidation states with slightly lower oxidation states (3.3 - 3.8) in darker areas in the dendritic growth structures (Table 5.2).

The PB nodule also indicates the same trend, with high Mn oxidation states in bright areas (~3.7) and lower Mn oxidation states (2.5 - 3.6) in darker materials (Table 5.3).
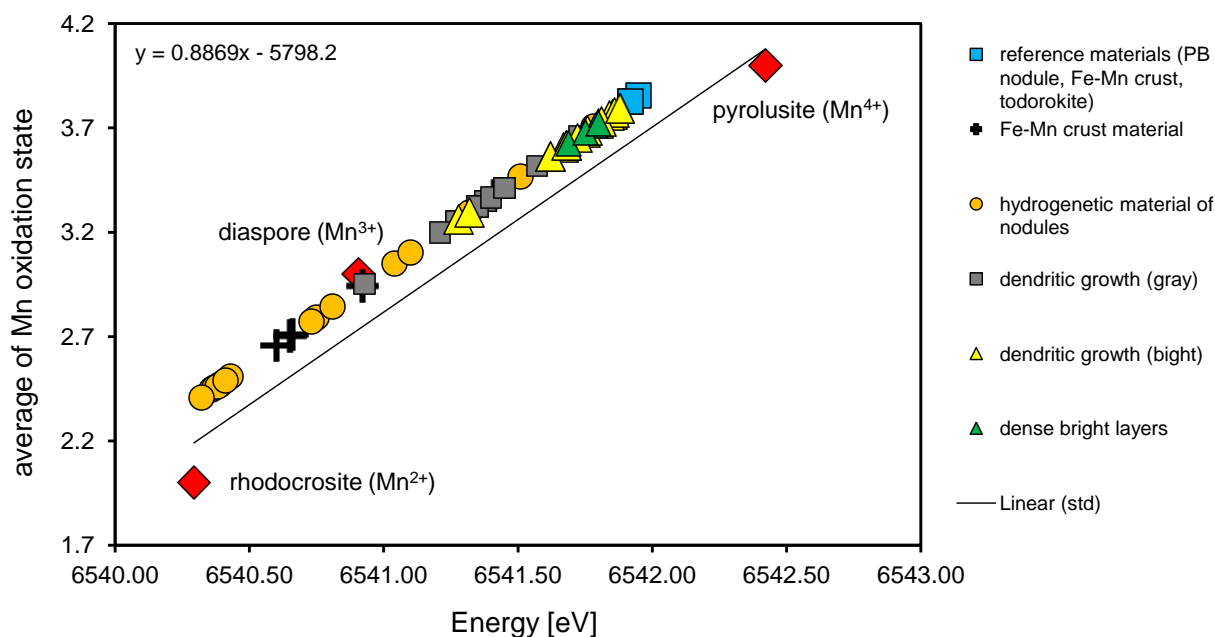
FIGURE 5.16 Pre-edge centroid positions vs. oxidation state of three different standards (Mn^{2+}, Mn^{3+}, Mn^{4+}) (red symbols). The average oxidation state of different CCZ nodules growth structures were calculated from the linear relationship. Hydrogenetic materials of CCZ nodules and crust sample show lower Mn oxidation states than the dendritic and dense growth structures (suboxic-diagenetic). The three reference materials (blue symbols) already indicate a certain amount of reduced Mn-species (Mn^{2+}/Mn^{3+}).

5.5 Discussion and Conclusion

XANES spectroscopy was performed on individual genetic layers of polymetallic nodules and of a ferromanganese crust to determine their Mn oxidation state. The three Mn-reference materials (todorokite, Fe-Mn crust: vernadite, PB nodule: 7 Å/10 Å vernadite) , which are Mn-phases commonly found in marine nodules and crusts, show Mn K-edge spectra which are between the Mn^{4+} and Mn^{3+} standards, with higher Mn^{4+} component.

Dendritic and dense growth structures (layer type 2) of high reflectivity are more or less consistent with the three analyzed Mn reference materials according to their pre-edge shape and energy position. The layers of type 2 show predominantly Mn^{4+} with minor amounts of a reduced Mn-species (Mn^{3+} or Mn^{2+}). The energy difference of the pre-edge centroid between the three Mn-reference materials of this work and the bright diagenetic material (layer type 2) is ~0.2 eV. A slightly larger energy difference of ~0.4 eV is found between darker areas of dendritic growth structures and the Mn-reference materials. Mineralogically as well as chemically both materials are similar but dark areas show a higher porosity than the bright material.

A distinct energy shift from higher (pre- and main-edge) energies in suboxic-diagenetic growth structures (layer type 2) to lower energies in oxic-hydrogenetic layers (layer type 1) was observed.

The oxic-hydrogenetic layers (layer type 1) and the crust are expected to be similar to the Fe-vernadite (δ-MnO$_2$) standard. However, the XANES analysis shows different results. The hydrogenetic layer type 1 material shows Mn K pre- and main-edges positions corresponding to high amounts of Mn^{2+} and Mn^{3+} (Table 5.2; Table 5.3). An energy shift of up to ~1.6 eV was observed between the spectra of the hydrogenetic layers and the spectra of the vernadite reference material. This corresponds to the observed energy shift of about 1.5 eV between Mn^{2+} and Mn^{4+} phases in the literature (Manceau et al., 1992).

The Mn K-edge spectra of oxidized Mn-phases (Mn^{4+}) generally are at higher energies than the reduced Mn-phases (Mn^{2+} and Mn^{3+}). The pre-edges of the spectra measured in brighter areas are more symmetrical than those of darker areas. The intensities of the pre-edges of hydrogenetic material are less than those of the suboxic material. All together these results indicate a change in the Mn oxidation state between the two genetic materials.

This is in contrast to previous XRD studies (Post et al., 1982; Giovanoli, 1985; Post and Bish, 1988) as well as XPS (Murray and Dillard, 1979; Dillard et al., 1982) and titration studies (Murray et al., 1984) of Mn-oxides and especially of Mn-nodules which indicated that Mn occurs completely as Mn^{4+}.

According to Manceau et al. (1992) Mn minerals associated with Fe-oxyhydroxides in the oxidized zone of the seafloor are exclusively composed of Mn^{4+} ions. Furthermore, the absence of low valence Mn ions is in good agreement with nearly all tectomanganates and phyllomanganates having similar unit-cell parameters in the plane of the octahedral chains (Manceau et al., 1992). High amounts of divalent or trivalent Mn atoms would lead to a significant variation in the unit-cell parameters (Manceau et al., 1992). Tectomanganate and phyllomanganates were shown to contain only low amounts of Mn^{3+} and less than ~15% of Mn^{2+} in their octahedral layers (Manceau et al., 1992). According to Drits et al. (1997) birnessite may contain about 20% Mn^{3+}.

Two questions arose from these observations:

1) Why do a high amount of reduced Mn (Mn^{2+}, Mn^{3+}) in certain hydrogenetic layers of the nodule and crust samples can be observed while the macro-analysis of the Mn-reference materials (vernadite /Fe-Mn crust, todorokite, PB nodule) indicates only minor amounts of reduce Mn-species?

2) Why do darker areas (hydrogenetic material, low Mn content) undergo higher reduction while bright areas (diagenetic material, high Mn content) do not or less?

It is known from the literature (Manceau et al., 2012; Ross et al., 2001) that poorly crystallized phyllomanganates (biogenetic and abiotic) are sensitive to electron and X-ray radiations (Garvie and Craven, 1994; Ross et al., 2001; Bargar et al., 2005). During these analyses photo-reduction or reduction of manganese may occur (Manceau et al., 2012).

Manceau et al. (2012) showed that the reduction process of manganese in biogenic δ-MnO_2 occurred in two steps from Mn^{4+} over Mn^{3+} to Mn^{2+} by one electron transfer at a time and this reduction is more intense under the influence of an increasing X-ray flux rate. They also observed a shift of the spectra to lower energies at an increasing flux rate but also a change in the shape of the spectra with one distinct peak becoming asymmetric with a shoulder at the Mn^{2+}-like maximum. According to this, it can be assumed that Mn reduction occurred during the XANES measurements on thin sections of our nodule and crust samples, but only in the hydrogenetic material. Several hypotheses to explain this observation are developed below. It must be stressed again, that the Mn reduction was exclusively detectable in material of the thin sections while it did not occur in similar material measured as powders. It should be noted that reference material was measured as powders using a macro X-ray beam while samples were measured as thin sections using a micro X-ray beam.

Thin sections were used for the XANES analyses to preserve the structure and spatial distribution of layers in the nodules. The thin sections of this study were prepared with Araldite®, a carbon-containing epoxy resin that maintains the structure of samples during polishing. As mentioned above thin sections were analyzed with a micro-beam that focused photons on a very small surface (0.25 x 0.75 μm^2) while powders were measured with a larger beam (100 μm) and were free of araldite. The high beam energy on a small area and the presence of the organic matrix probably lead to a reduction of the Mn within the layers of the thin sections.

The reduction of Mn in Mn-minerals under the X-ray beam was also described in other studies investigating the Mn oxidation state in soils (Ross et al., 2001). The presence of high amounts of organic carbon at the surface of soil Mn-oxides was responsible for the reduction of Mn-oxides under the beam (Ross et al., 2001).

However, suboxic-diagenetic layers, which consist of 7 Å and 10 Å vernadite do not show such intensive reduction. In contrast to hydrogenetic layers, only minor amounts of Fe (<4 wt.%) occur within suboxic-diagenetic structures. The much higher Fe content (up to 23 wt.%) within hydrogenetic layers probably promotes the reduction of Mn. Iron which occurs as Fe^{3+} will be reduced to Fe^{2+} by the organic carbon present in the resin. The re-oxidation of Fe^{2+} to Fe^{3+} will be accompanied by the reduction of Mn^{4+}. Similar reactions are common in anaerobic systems where bacteria are able to catalyze the reduction of Fe^{3+} to Fe^{2+} (Du Plessis et al., 2011). The authors suggest that the solubilisation of manganese oxides (e.g., $Mn_3O_3(HO)_6$) happens through the coupled reduction of Mn^{4+} and oxidation of Fe^{2+}. The reaction can be described as follow (Du Plessis et al., 2011; (5.1)).

$$Mn_3O_3(OH)_6 + 6\ Fe^{2+} + 12\ H^+ \rightarrow 3\ Mn^{2+} + 6\ Fe^{3+} + 9\ H_2O \qquad (5.1)$$
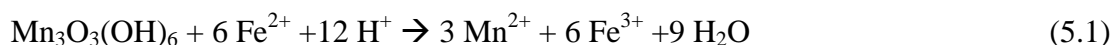
The high amount of Fe in hydrogenetic layers in comparison to diagenetic layers is probably the trigger of the higher reduction of Mn under the XANES beam. At this point it is not clear if the presence of the small amount of reduced Mn-phases in dendritic growth structures is original or is due to the same Mn reduction under the beam, as observed in hydrogenetic layers.

To conclude, the Mn-reference materials show already small amounts of reduced Mn-species (Mn^{2+}/Mn^{3+}) which is in good agreement with X-ray photospectroscopical analyses of this material. These results indicate that the Mn-minerals (vernadite) have some Mn^{3+} and/or Mn^{2+} in their structures.

The dense suboxic diagenetic layers (layer type 2.1 and 2.2) contain predominantly Mn^{4+} and minor amounts of reduced Mn-species independent of their Ni+Cu content (0.84 - 5.4 wt.%; Chapter III). No correlation of the oxidation state of Mn and Ni+Cu content can be drawn.

These results show that the metals such as Ni and Cu can be incorporated by substitution of lower Mn-species, adsorbed over/below vacancy sites within the octahedral or were

incorporated into the vacancy sites and become structurally incorporated, as already described in Peacock (2009).

For future studies, the stability of vernadite and other standards should be tested under the micro-beam before performing measurements on natural samples. Furthermore, the effects of beam size and intensity should be investigated on samples in different forms (powder vs. thin section with Araldite). Reducing the photon flux in the micro-beam is another option to perform measurements in the thin sections. Alternatively, other sample preparations, that do not involve a C-bearing resin, should be tried in order to perform µ-XANES without X-ray beam-induced reduction of Mn-mineral phases. Furthermore, X-ray absorption spectroscopy measurements should be run at liquid helium temperature (17 to 20 K) to prevent sample damage and reduction of Mn (Powers, 1982)

Finally further studies are required to determine exactly the valence of Mn in manganates in individual layers of nodules and crust samples, especially in hydrogenetic ones. To provide valuable information on incorporated metals within the crystal structure of the vernadites, spectroscopic methods should be performed which are sensitive to the local structure of the minerals such as Extended X-ray Absorption Fine Structure (EXAFS) similarly to the work of Peacock and Sherman (2007a,b) and Peacock (2009) who were able to show Ni^{2+} incorporation mechanism within Mn-minerals.

Chapter VI

Summary and Conclusions

This PhD thesis provides new and innovative results of nm-µm thick growth structures of nodules from the eastern German license area in the Clarion and Clipperton Zone (CCZ) of the central Pacific Ocean. The results contribute to a better understanding of nodule growth history and to their mineralogical composition.

1) Bulk nodules vs. individual layers

Geochemical investigations of bulk nodules of this study show relative uniform Mn/Fe ratios of 4 - 6 with a Ni+Cu content of maximal 3 wt.%, which is typical for mixed type nodules of hydrogenetic and oxic-diagenetic growth from the CCZ (Halbach et al., 1981). Detailed investigations of the micro growth structures of individual layers however, reveal much higher chemical heterogeneity with Mn/Fe ratios ranging from 0.53 to 826 as well as variable Ni+Cu contents ranging from 0.2 up to 6.51 wt.%. These findings clearly indicate that the chemical analyses of bulk nodules do not reflect the individual growth processes of the layers. Bulk nodules do only represent an average mixture of two genetically different end members which are oxic-hydrogenetic (*layer type 1*) and suboxic-diagenetic (*layer type 2*).

Layer type 1 displays low Mn/Fe ratios, low Ni+Cu contents and an enrichment of Co. This chemical composition is typical for hydrogenetic growth under oxic conditions. Important and new are the findings that those layers do not only occur on the nodule surface, which is in contact with recent oxic near bottom water, but are also growing as outermost layers on the nodule rim, which is the interface of the near-bottom water and the sediment pore water. This layer type also occurs on the bottom side of nodules, which is buried in the upper few cm of the sediment column and therefore in contact with the pore water.

Layer type 2 forms the second end member with high Mn contents (up to 50 wt.%) and high Mn/Fe ratios (>800), which is typical for suboxic-diagenetic growth. This layer type occurs as dense layers and as dendritic growth structures with variable Ni+Cu contents (0.9 - 6.51 wt.%) and make up about 60% of the CCZ nodules.

The determination of these genetically different layers indicates changes in the physico-chemical parameters (Eh, pH, Mn^{2+} mobilization etc.) from oxic to suboxic within the environment during nodule growth. Under current oxic conditions within the near-bottom sea water and the sediment pore water without detectable dissolved Mn^{2+} (Mewes et al., 2014) only hydrogenetic layers can form. In contrast to that, the high Mn/Fe ratios of *layer type 2* indicate a high fractionation of Mn from Fe, which can only occur under suboxic conditions.

This is in clear contrast to the previous opinion. Authors from the 1980ies and 1990ies stated that nodules from the CCZ completely grow under oxic conditions. The findings of this thesis clearly proved that this is not the case but that suboxic conditions prevailed at or close to the seafloor during certain periods. Recent work on the sediments and the pore water support our interpretation (Mewes et al., 2014; Widmann et al., 2014).

The changes within the CCZ are probably climatically induced due to interglacial-glacial periods. Increased bioproductivity in the central Pacific surface waters and/or reduced ventilation of the deep ocean during glacial periods may have led to a pronounced oxygen minimum in the deep sea and rapid oxygen consumption in the near-surface sediments causing suboxic conditions similar to the Peru Basin (König et al., 2001; Froelich et al., 1979; Bradmiller et al., 2010).

2) Post depositional transformation

This study shows that nodules layers which were interpreted as oxic-diagenetic so far are, indeed, intimate mixtures of hydrogenetic and suboxic growth structures or are the product of secondary diagenetic transformation of primary hydrogenetic layers during suboxic periods.

Computer tomography (CT) investigations reveal high porosity of the nodules, with most of the pores and cracks being connected to individual pore systems. These pore systems are connected with the surrounding environment (near bottom and sediment pore water) and enables fluids to penetrate through the whole nodules and re-fill their pores belated. Chemical analyses of pore fillings reveal a hydrogenetic origin similar to the recent outermost layer. During periods of suboxic conditions, fluids also penetrate and re-filled pores leading to the formation of bright spots and veins of typical suboxic-diagenetic character within hydrogenetic layers. Furthermore, during suboxic conditions the primary Mn-phases (δ-MnO_2) can be dissolved and were replaced by 10 Å/7 Å phyllomanganates, which are more stable under suboxic conditions.

3) Mineralogical composition

Mineralogical investigations of bulk nodules from the CCZ as well as of their individual nm-thick layers show that nodules consist of different, thermally stabile turbostratic phyllomanganates (vernadites), which are disordered phyllomanganate forms of birnessite-like Mn-phases. Todorokite was not detected in the nodules from the CCZ.

The geochemical behavior of Fe and Mn is similar under oxic conditions within the near-bottom water and pore water causing a simultaneous formation of a Mn-phase such as vernadite and amorphous δ-FeOOH phase in layer type 1. Due to the epitaxial intergrowth of δ-FeOOH with vernadite the formation of 10 Å and 7 Å vernadites was inhibited (Burns and Burns, 1975). Therefore, δ-MnO_2 can act as a good indicator for oxic conditions.

Suboxic layers (layer type 2) consist, independent of their Ni+Cu content (0.8 - 6.51 wt.%) of 10 Å and 7 Å vernadites, whereby the 7 Å form predominantly is a dehydration product of 10 Å vernadite. Within nodules a stabilization of the 10 Å vernadites from the outer younger layers into older inner layers can be recognized with a simultaneous increase of Mg^{2+}, which is responsible for the stabilization.

4) Phyllomanganates

Phyllomanganates in general have a high potential to incorporate metals such as Ni and Cu. These minerals show a high negative layer charge generally resulting from the presence of isomorphic substitutions of layer Mn^{4+} by cations of lower valence (e.g. Mn^{3+} or Ni^{2+}) or due to vacancies within the octahedral layers. This charge deficit can be balanced by sorption of divalent cations through inner-sphere surface complexation above/below Mn octahedral vacancies (e.g. Mn^{3+}, Ni^{2+}, Cu^{2+}, Mg^{2+}; Bodeï et al, 2007, Manceau et al., 2007; Peacock and Shermann, 2007a) or by sorption through outer-sphere complexion in the interlayer mid-plane (e.g. Na^+, Ca^{2+}). X-ray absorption near edge spectroscopy and XPS reveal that both the suboxic-diagenetic and the oxic-hydrogenetic layers contain a certain amount of reduced Mn-species (Mn^{2+}/Mn^{3+}).

At this point we cannot say where the metals (e.g., Ni+Cu) are located within the phyllomanganates of the individual growth layers of nodules from the CCZ. However, the mineralogical investigations of this study show that the chemical composition, especially the metal (e.g., Ni+Cu) content, does not depend on the presence of certain Mn-minerals such as

149

tectomanganate todorokite or turbostratic phyllomanganate. In contrast, the diagenetic layers exclusively consist of 10 Å/7 Å phyllomanganates with a variable metal content. The enrichment of metals such as Cu and Ni seems to be related to environment conditions (Eh, pH), their supply from distorting particles as well as the local negative layer charge of the different phyllomanganates. Furthermore, the phyllomanganates have distinct cation exchange capacities and dehydration behaviour, which may be used during future metallurgical treatment.

Further detailed investigations using among other methods extended X-ray absorption fine structure (EXAFS) are needed to determine the structural incorporation of Ni and Cu as well as other economically important metals (Mo, Li, etc.).

References

Alexander, B.W. (2008). Trace element analyses in geological materials using low resolution inductively coupled plasma mass spectrometry (ICPMS). Jacobs University Technical Report 18, 73p.

Antoine, D., André J.M. and Morel, A. (1996). Oceanic primary production 2. Estimation at global scale from satellite (castal zone color scanner) chlorophyll. Global Biogeochemical Cycles 10, 57-69.

Apte, M.Y. and Mande, C. (1982). Chemical effects on the main peak in the K absorption spectrum of manganese in some compounds. Journal of Physics C: Solid State Physics, 15.3, 607-613.

Arrhenius, G. and Tsai, A. (1981). Structure, phase transformation and prepiotic catalysis in marine manganates. Scripps institution of Oceanography Reference Series 81, 1-19.

Bargar, J.R., Tebo, B.M., Bergmann, U., Webb, S.M., Glatzel, P., Chiu, V.Q. and Villalobos, M. (2005). Biotic and abiotic products of Mn(II) oxidation by spores of the marine Bacillus sp. strain SG-1. American Mineralogist, 90, 143-154.

Belli, M., Scafati, A., Bianconi, A., Mobilio, S., Palladino, L., Reale, A. and Burattini, E. (1980). X-ray absorption near edge structures (XANES) in simple and complex Mn compounds. Solid State Communications, 35, 355-361.

Bish, D. L. and Post, J. E. (1989). Thermal behaviour of complex, tunnel-structure manganese oxides. American Mineralogist, 74, 177-186.

Bischoff J.L., Piper D.Z. and Leong K. (1981). The aluminosilicate fraction of North Pacific manganese nodules. Geochemica et Cosmochimica Acta 45, 2047-2063.

Blöthe, M., Wegorzewski, A.V., Müller, C., Simon, F., Kuhn, T. and Schippers, A. (submitted). Microbe-mineral interactions in deep-sea manganese nodules. Nature Communications.

Bodeï, S., Manceau, A., Geoffroy, N., Baronnet, A. and Buatier, M. (2007). Formation of todorokite from vernadite in Ni-rich hemipelagic sediments. Geochimica et Cosmochimica Acta 71, 5698-5716.

Bollhöfer, A., Eisenhauer, A., Frank, N., Pech, D. and Mangini, A. (1996). Thorium and uranium isotopes in a manganese nodule from the Peru basin determined by alpha spectrometry and thermal ionization mass spectrometry (TIMS): Are manganese supply and growth related to climate? Geologische Rundschau 85, 577-585.

Bonatti, E., Kraemer, T. and Rydell, H. (1972). Classification and genesis of submarine iron-manganese deposits. In: Horn, D.R. (Ed.), Ferromanganese deposits on the ocean floor. NSF, Washington D.C., pp. 149-166.

Boughriet, A., Ouddane, B., Wartel, M., Lalou, C., Cordier, C., Gengembres, L. and Sanchez, J.P. (1996). On the oxidation states of Mn and Fe in polymetallic oxide/oxyhydroxide crusts from the Atlantic Ocean. Deep-Sea Research I 43, 321-343.

Bradmiller, L.I., Anderson R.F., Sachs, J.P. and Fleisher, M.Q. (2010). A deep respired carbon pool in the glacial equatorial Pacific Ocean. Earth and Planetary Science Letters 299, 417-425.

Brown, G.E., Jr., Calas, G., Waychunas, G.A. and Petiau, J. (1988). X-ray absorption spectroscopy; applications in mineralogy and geochemistry. Reviews in Mineralogy and Geochemistry 18, 431-512.

Burns, R.G. (1976). The uptake of cobalt into ferromanganese nodules, soils, and synthetic manganese (IV) oxides. Geochimica et Cosmochimica Acta 40, 95-102.

Burns R.G. and Burns, V.M. (1975). Mechanism for nucleation and growth of manganese nodules. Nature, 255, 130-131.

Burns, R.G. and Burns, V.M. (1977). Mineralogy of ferromanganese nodules. In: Glasby, G.P. (Ed.), Marine Manganese Deposits Elsevier, pp. 185-248.

Burns R.G., Burns, V.M. and Easton A.J. (1977). The mineralogy and crystal chemistry of deep sea manganese nodules, a polymetallic resource of the twenty-first century. Philosophical Transactions of the Royal Society A 286, 283-301.

Burns, R.G., Burns, V.M. and Stockman, H.W. (1983). A review of the todorokite-buserite problem: implications to the mineralogy of marine manganaese nodules. American Mineralogist 68, 972-980.

Burns V.M. and Burns R.G. (1978a). Authigenic todorokite and phillipsite inside deep-sea manganese nodules. American Mineralogist 63, 827-831.

Burns V.M. and Burns R.G. (1978b). Post-depositional metal enrichment processes inside manganese nodules from the north equatorial Pacific. Earth and Planetary Science Letters 39, 341-348.

Callender, E. and Bowser, C.J. (1980). Manganese and copper geochemistry of interstitial fluids from manganese nodule-rich pelagic sediments of the northeastern equatorial Pacific Ocean. American Journal of Science 280, 1063-1096.

Calvert, S.E. and Piper, D.Z. (1984). Geochemistry of ferromanganese nodules from DOMES Site A, Northern Equatorial Pacific: Multiple diagenetic metal sources in the deep sea. Geochimica et Cosmochimica Acta 48, 1913-1928.

Chalmin, E., Farges, F. and Brown Jr, G.E. (2009). A pre-edge analysis of Mn K-edge XANES spectra to help determine the speciation of manganese in minerals and glasses. Contribution to Mineralogy and Petrology 157, 111-126.

Chester, R. and Jickells, T. (2012). Marine Geochemistry, 3rd Edition, Wiley-Blackwell, Oxford, 411 p.

Ching, S., Krukowska, K.S. and Suib, S.L. (1999). A new synthetic route to todorokite-type manganese oxides. Inorganica Chimica Acta 294, 123-132.

Chukhrov, F.V., Gorshkov, A.I., Beresovskaya, V.V. and Sivtsov, A.V. (1979). Contributions to the Mineralogy of Authigenic Manganese Phases from Marine Manganese Deposits. Mineralium Deposita 14.3, 249-261.

Crerar, D.A. and Barnes, H.L. (1974). Deposition of deep-sea manganese nodules. Geochimica et Cosmochimica Acta 38, 279-300.

Cronan, D.S. (2000). Handbook of marine mineral deposits. CRC Marine Science Series 17, CRC Press, Boca Roton, 237 p.

Cronan, D.S. and Tooms, J.S. (1969). Sub-surfac concentrations of manganese nodules in Pacific sediments. Deep-Sea Research 14, 117-119.

Cui, H., Qiu, G., Feng, X., Tan, W. and Liu, F. (2009). Birnessites with different average manganese oxidation states synthesized, characterized, and transformed to todorokite at atmospheric pressure. Clays and Clay Minerals 57, 715-724.

Cygan, R.T., Post, J.E, Heaney, P.J. and Kubicki, J.D. (2012). Molecular models of birnessite and related hydrated layered minerals, American Mineralogist 97, 1505-1514.

De Lange, G.J., van Os, B. and Poorter, R. (1992). Geochemical composition and inferred accretion rates of sediments and manganese nodules from a submarine hill in the Madeira Abyssal Plain, eastern North Atlantic. Marine Geology 109, 171-194.

Di Castro, V. and Polzonetti, G. (1989). XPS study of MnO oxidation. Journal of Electron Spectroscopy and Related Phenomena 48, 117-123.

Dillard, J.G., Crowther, D.L. and Murray, J.W. (1982). The oxidation states of cobalt and selected metals in Pacific ferromanganese nodules. Geochimica et Cosmochimica Acta 46, 755-759.

Dillard, J.G., Crowther, D.L. and Calvert, S.E. (1984). X-ray photoelectron spectroscopic study of ferromanganese nodules: Chemical speciation for selected transition metals. Geochimica et Cosmochimica Acta 48, 1565-1569.

Dräger, G., Frahm, R., Materlik, G. and Brümmer, O. (1988). On the multipole character of the X-ray transitions in the pre-edge structure of Fe K absorption spectra. Physica Status Solidi B 146, 287-294.

Drits, V.A. and Tchoubar, C. (1990). X-ray diffraction by disordered lamellar structures: theory and applications to microdivided silicates and carbons. Springer-Verlag: Berlin, p 371.

Drits, V.A., Silvester, E., Gorshov, A.I. and Manceau, A. (1997). Structure of synthetic monoclinic Na-rich birnessite and hexagonal birnessite: I. Results from X-ray diffraction and selected-area electron diffraction. American Mineralogist 82, 946-961.

Drits, V.A., Lanson, B. and Gaillot, A.C. (2007). Birnessite polytype systematics and identification by powder X-ray diffraction. American Mineralogist 92, 771-788.

Du Plessis, C.A., Slabbert, W., Hallberg, K.B. and Johnson, D.B. (2011). Ferredox: A biohydrometallurgical processing concept for limonitic nickel laterites. Hydrometallurgy 109, 221-229.

Dymond, J., Lyle, M., Finney, B., Piper, D.Z., Murphy, K., Conard, R. and Pisoas, N. (1984). Ferromanganese nodules from the MANOP Sites H, S, and R-Control of mineralogical and chemical composition by multiple accretionary processes. Geochemica et Cosmochimica Acta 48, 931-949.

Ehrlich, H.L. (1963). Bacteriology of manganese nodules. I. Bacterial action on manganese in nodules enrichments. Applied microbiology 11, 15-19.

Ehrlich, H.L. (1972). Response of some activities of ferromanganese nodule bacteria to hydrostatic pressure. In: Cilwell, R.R. and Morita, R.Y. (Eds.), Effect of the Ocean Environment on Microbial Activities. University Park Press, Baltimore, MD, pp. 208-211.

Ehrlich, H.L. and Newman, D.K. (2009). Geomicrobiology, 5th ed. CRC Press, Taylor & Francis Group, Boca Raton, 606 p.

Elderfield, H., Hawkesworth, C.J., Greaves, M.J. and Calvert, S.E. (1981). Rare earth element geochemistry of oceanic ferromanganese nodules and associated sediments. Geochimica et Cosmochimica Acta 45, 513-528.

Foord, J.S., Jackman, R.B. and Allen, G.C. (1984). An X-ray photoelectron spectroscopic investigation of the oxidation of manganese. Philosophical Magazine A 49, 657-663.

Friedrich, G., Kunzendorf, H. and Plüger, W.L. (1973). Geochemical investigations of deep-sea manganese nodules from the Pacific on board RV „Valdivia". In: Morgenstein, M. (Ed.), Papers on the origin and distribution of manganese nodules in the Pacific and prospects for their exploration. Valdivia manganese Exploration Group, University of Hawaii and IDOE-NSF, pp. 32-43.

Friedrich, G., Kunzendorf, H. and Plüger, W.L. (1974). Ship-borne geochemical investigations of deep-sea manganese-nodule deposits in the Pacific using a radio-isotope energy-dispersive x-ray system. Journal of Geochemical exploration 3, 303-317.

Froelich, P.N., Klinkhammer, G.P., Bender, M.L., Luedtke, N.A., Cullen, D. and Dauphin, P. (1979). Early oxidation of organic matter in pelagic sediments of the eastern equatorial Atlantic: suboxic diagenesis. Geochemica et Cosmochimica Acta 43, 1075-1090.

Frondel, C., Marvin, U.B. and Ito, J. (1960). New occurrences of todorokite. American Mineralogist 45, 1167-1173.

Garvie, L.A.J. and Craven, A.J. (1994). Electron-beam-induced reduction of Mn^{4+} in manganese oxides as revealed by parallel EELS. Ultramicroscopy 54, 83-92.

Giannuzzi, L.A. and Stevie, F.A. (2005). Introductin to Focused Ion Beams: Instrumentation, Theory, Techniques and Practice, Springer, New York, 339 p.

Giannuzzi, L.A., Drown, J.L., Brown, S.R., Irwin, R.B. and Stevie, F.A. (1997). Focused ion beam milling and micromanipulation lift-out for site-specific cross-section TEM specimen preparation. In: Anderson, R., Walck, S. (Eds.), Proceedings of the Materials Research Society: Workshop on Specimen Preparation for TEM of Materials IV, vol. 480. Materials Research Society, Pittsburgh, PA, pp.19-27.

Giovanoli, R. (1980) On natural synthetic manganese nodules. In: Varentsov I.M. and G. Grassellg (Eds.), Geology and Geochemistry of Manganese. Vol. I, E. Schweizerbart`sche Verlagsbuchhandlung, Stuttgart, pp. 159-202.

Giovanoli, R. (1985). A review of the todorokite-buserite problem: Implications to the mineralogy of marine manganese nodules: Discussion. American Mineralogist 70, 202-204.

Giovanoli, R. and Arrhzenius, G. (1985). Structural chemistry of marine manganese and iron minerals and synthetic model compounds. In: Halbach, P., Friedrich, G., and von Stackelberg, U. (1988) The Manganese Nodule Belt of the Pacific Ocean. Geological Environment, Nodule Formation, and Mining Aspects. Ferdinand Enke Verlag, Stuttgart, pp. 20-31.

Giovanoli, R. and Bürki, P. (1975). Comparison of X-ray evidence of marine manganese nodules and non-marine manganese ore deposits. Chimia 29, 266-269.

Giovanoli, R., Bürki, P., Giuffredi, M. and Stumm, W. (1975). Layer structured manganese oxide-hydroxides. IV. The buserite group: structure stabilisation by transition elements. Chimia 29, 517-520.

Glasby, G.P. (1972). The mineralogy of manganese nodules from a range of marine environments. Marine Geology 13, 57-72.

Glasby, G.P. (1973). Mechanisms of enrichment of the rare earth elements in marine manganese nodules. Marine Chemistry 1, 105-125.

Glasby, G.P. and Schulz, H.D. (1999). E_H, pH Diagrams for Mn, Fe, Co, Ni, Cu and As under Seawater Conditions: Application of Two New Types of E_H, pH Diagrams to the Study of Specific Problems in Marine Geochemistry. Aquatic Geochemistry 5, 227-248.

Glasby, G.P., Stoffers, P., Sioulas, A., Thijssen, T. and Friedrich, G. (1982). Manganese nodules formation in the Pacific Ocean: a general theory. Geo-marine Letters 2, 47-53.

Golden, D.C., Dixon, J.B. and Chen, C.C. (1986). Ion exchange, thermal transformations, and oxidizing properties of birnessite. Clays and Clay Minerals 34, 511-520.

Grangeon, S., Lanson, B., Lanson, M. and Manceau, A. (2008). Crystal structure of Ni-sorbed synthetic vernadite: a powder X-ray diffraction study. Mineralogical Magazine 72, 1279-1291.

Grangeon, S., Lanson, B., Miyata, N., Tani, Y. and Manceau, A. (2010). Structure of nanocrystalline phyllomanganates produced by freshwater fungi. American Mineralogist 95, 1608-1616.

Grangeon, S., Claret, F., Lerouge, C., Warmont, F., Sato, T., Anraku, S., Numako, C., Linard, Y. and Lanson, B. (2013). On the nature of structural disorder in calcium silicate hydrates with a calcium/silicon ratio similar to tobermorite. Cement and Concrete Research 52, 31-37.

Haeckel, M., König, I., Riech, V., Weber, M.E. and Suess, E. (2001). Pore water profiles and numeriacal modeling of biogeochemical processes in Peru Basin deep-sea sediments. Deep-Sea Research II 48, 3713-3736.

Halbach, P. and Özkara, M. (1979). Morphological and geochemical classification of deep-sea ferromanganese nodules and its genetical interpretation. Colloques Internationaux du CNRS 289, 77-88.

Halbach, P., Scherhag, C., Hebisch, U. and Marchig, V. (1981). Geochemical and mineralogical control of different genetic types of deep-sea nodules from the Pacific Ocean. Mineral Deposita 16, 59-84.

Halbach, P., Giovanoli, R. and von Borstel D. (1982). Geochemical processes controlling the relationship between Co, Mn, and Fe in early diagenetic deep-sea nodules. Earth and Planetary Science Letter 60, 226-236.

Halbach, P., Friedrich, G. and von Stackelberg, U. (1988). The Manganese Nodule Belt of the Pacific Ocean. Geological Environment, Nodule Formation, and Mining Aspects. Ferdinand Enke, Stuttgart, 254 p.

Halbach, P., Jahn, A. and Lucka, M. (2009). Geochemical - mineralogical investigations about the distribution, the interelement relationships and the bonding processes of economically important minor and trace metals in marine ferromanganese crusts (Marine Ferromanganese Crusts II). BGR-Projekt No.: 207-4500051248. Berlin, 64 p.

Han, X., Jin, X., Yang, S., Fietzke, J. and Eisenhauer, A. (2003). Rhythic growth of Pacific ferromanganese nodules and their Milankovitch climattic origin. Earth and Planetary Science Letters 211, 143-157.

Hein, J.R. and Koschinsky, A. (2014). Deep-Ocean Ferromanganese Crust and Nodules. In: Holland, H. and Turekian, K. (Eds.), Earth Systems and Environmental Sciences, Treatise on Geochemistry 2nd Edition, Elsevier, Amsterdam, pp. 273-291.

Hein, J.R., Koschinsky, Halbach, P., Manheim, F.T., Bau, M., Kang, J-K. and Lubick, N. (1997). Iron and manganese oxide mineralization in the Pacific. In: Nicholson, K., Hein, J.R., Bühn, B. and Dasgupta, S. (Eds.), Manganese Mineralization: Geochemistry and mineralogy of terrestrial and marine deposits. (Eds. Geological Society, Special Publication 119, 123-138.

Hein, J.R., Koschinsky, A., Bau, M., Manheim, F.T., Kang, J.K. and Roberts, K. (2000). Cobalt-rich ferromanganese crusts in the Pacific, In: Cronan, D. (Ed.), Handbook of Marine Mineral Deposits. CRC Press, Boca Raton, FL, pp. 239-279.

Hein, J.R, Mizell, K., Koschinsky, A. and Conrad, T.A. (2013). Deep-ocean mineral deposits as a source of critical metals for high- and green-technology applications: Comparison with land-based resources. Ore Geology Reviews 51, 1-14.

Hem, J.D. (1978). Redox processes at surfaces of manganese oxide and their effects on aqueous metal ions. Chemical Geology 21, 199-218.

Hem, J.D. (1981). Rates of manganese oxidation in aqueous systems. Geochimica et Cosmochimica Acta 45,1369-1374.

Hem, J.D. and Lind, C.J. (1983). Nonequilibrium models for predicting forms of precipitated manganese oxides. Geochimica et Cosmochimica Acta, 47, 2037-2046.

Hudson-Edwards, K.A. (2000). Heavy metal-bearing Mn oxides in river channel and floodplain sediments. In: Cotter-Howells, J.D.;Campbell, L.S.;Valsami-Jones, E.and Batchelder, M. (Eds.), Environmental mineralogy: microbial interactions, anthropogenic influences, contaminated land and waste management. Mineralogical Society, London, pp. 207–226.

International Seabed Authority (2010). Development of geological models for the Clarion-Clipperton Zone polymetallic nodule deposits. ISA technical study: No. 6. Kingston, Jamaica, 75 p.

International Seabed Authority (2013). http://www.isa.org.jm/files/images/maps/CCZ-Sep2012-Official.jpg.

Jauhari, P. and Pattan, J.N. (2000). Ferromanganesen odules from the central Indian Ocean Basin. In: Cronan D.S. (Ed.), Handbook of Marine Mineral Deposits CRC Press, Boca Raton, Florida, pp. 171-195.

Johnson, E.A. and Post, J. (2006). Water in the interlayer region of birnessite: Importance in cation exchange and structural stability, American Mineralogist 91, 609-618.

Jones, L. H. P. and Milne, A. A. (1956). Birnessite, a new manganese oxide mineral from Aberdeenshire, Scotland. Mineralogical Magazine 31, 283-288.

Kalhorn, S. and Emerson, S. (1984). The oxidation state of manganese in surface sediments of the Pacific Ocean. Geochimica et Cosmochimica Acta 48, 897-902.

Koschinsky, A. (2001). Heavy metal distributions in Peru Basin surface sediments in relation to historic, present and disturbed redox environments. Deep-sea research Part II, 48, 3757-3777.

Koschinsky, A. and Halbach, P. (1995). Sequential leaching of marine ferromanganese precipitates: Genetic implications 59, 5113-5132.

Koschinsky, A. and Hein, J.R. (2003). Uptake of elements from seawater by ferromanganese crusts: solid-phase associations and seawater speciation. Marine Geology 198, 331-351.

Koschinsky, A., Stascheit, A., Bau, M. and Halbach, P. (1997). Effects of phosphatization on the geochemical and mineralogical composition of marine ferromanganese crusts. Geochemica et Cosmochimica Acta 61, 4079-4094.

Koschinsky, A., Bau, M., Marbler, H. and Schmidt, K. (2010a). Rare valuable metals in marine ferromanganese nodules – contents and accumulation processes. Zeitschrift für angewandte Geologie 51, 33-39.

Koschinsky, A., Hein, J.R., Schmidt, K., Alexander, B. and Bau, M. (2010b). Rare and valuable metals for high-tech applications found in marine ferromanganese nodules and crusts: relationship to genetic endmembers. In: Cherkashev, G. (Ed.), Toward the sustainable development of Marine Minerals: Geological, Technological, and Economic Aspects. Underwater Mining Institute, Gelendzhik, Russia.

König, I., Haeckel, M., Lougear, A., Suess, E. and Trautwein, A.X. (2001). Deep-Sea Research II 48, 3737-3756.

Kriete, C. (2012). An Evaluation of the Inter-Method Discrepancies in Ferromanganese Nodule Proficiency Test GeoPT 23A. Geostandards and Geoanalytical research 35, 319-340.

Kuhn, T., Rühlemann, C., Wiedicke-Hombach, M., Barckhausen, U., Schwarz-Schampera, U., Rutkowski, J. and Lehmann, S. (2010). New insights of Mn nodule exploration from the German license area in the Pacific Manganese Nodule Belt, In: Cherkashev, G. (Ed.), Toward the sustainable development of marine minerals: geological, technological, and economic aspects. The Underwater Mining Institute, Gelendzhik, Russia, K 1-12.

Kuhn, T., Rühlemann, C. and Wiedicke-Hombach, M. (2012). Developing a Strategy for the Exploration of Vast Seafloor Areas for Prospective Manganese Nodule Fields, In: Zhou, H. Morgan, C.L. (Eds.), Marine Minerals: Finding the Right Balance of Sustainable Development and Environmental Protection. The Underwater Mining Institute, Shanghai, K1-9.

Lanson, B., Marcus, M.A., Fakra, S., Panfili, F., Geoffroy, N. and Manceau, A. (2008). Formation of Zn-Ca phyllomanganate nanoparticles in grass roots. Geochimica et Cosmochimica Acta 72, 2478-2490.

Lei, G. and Boström, K. (1995). Mineralogical control on transition metal distributions in marine manganese nodules. Marine Geology 123, 253-261.

Lyle, M. (1978). The formation and growth of ferromanganese oxides on the Nazca Plate Ph.D. Thesis Oregon State University, Corvallis, 172 p.

Lyle, M., Dymond, J. and Heath, G.R. (1977). Copper-nickel-enrichmend ferromanganese nodules and assoziated crusts from the Bauer Basin, northwest Nasca Plate. Earth and Planetary Science Letters 35, 55-64.

Lyle, M., Heath, G.R. and Robbins, J.M. (1984). Transport and release of transition elements during early diagenesis: sequential leaching of sediments from MANOP sites M and H, Part I. pH5 acetic acid leach. Geochemica et Cosmochimica Acta 48, 1705-1715.

Manceau, A., Gorshkov, A.I. and Drits, V.A. (1992a). Structural chemistry of Mn, Fe, Co, and Ni in manganese hydrous oxides: Part II. Infromation from EXAFS spectroscopy and electron and X-ray diffraction. American Mineralogist 77, 1144-1157.

Manceau, A., Gorshkov, A.I. and Drits, V.A. (1992b). Structural chemistry of Mn, Fe, Co, and Ni in manganese hydrous oxides: Part I. Information from XANES spectroscopy. American Mineralogist 77, 113-1143.

Manceau, A., Drits, V. A., Silvester, E., Bartoli, C. and Lanson, B. (1997). Structural mechanism of Co^{2+} oxidation by the phyllomanganate buserite. *American Mineralogist* 82, (11-12), 1150-1175.

Manceau, A., Lanson, M. and Geoffroy, N. (2007). Natural speciation of Ni, Zn, Ba, and As in ferromanganese coatings on quartz using X-ray fluorescence, absorption, and diffraction. Geochimica et Cosmochimica Acta 71, 95-128.

Manceau, A., Marcus, M.A. and Grangeon, S. (2012). Determination of Mn valence states in mixed-valent manganates by XANES spectroscopy. American Mineralogist 97, 816-827.

Marcus, M.A., MacDowell, A., Celestre, R., Manceau, A., Miller, T., Padmore, H.A. and Sublett, R.E. (2004). Beamline 10.3.2 at ALS: a hard X-ray microprobe for environmental and materials sciences, Journal of Synchrotron Radiation 11, 239-247.

Mc Murdie, H.F. (1944). Microscopic and diffraction studies on dry cells and their raw materials. Transactions of the Electrochemical Society 89, 313-326.

Mellin, T. A. and Lei, G. (1993). Stabilization of 10Å-manganates by interlayer cations and hydrothermal treatment: Implications for the mineralogy of marine manganese concretions. Marine Geology 115, 67-83.

Mero, J.L. (1965). The mineral resources of the sea Vol 1. Elsevier, Amsterdam, 312 pp.

Mewes, K., Picard, A., Mogollón, J.M., Rühlemann, C., Kuhn, T, Nöthen, K. Eisenhauer, A. and Kasten, S. (2014). The impact of depositional and biogeochemical processes on small scale variations in nodule abundance in the Clarion-Clipperton Fracture Zone. Deep Sea Research Part I: Oceanographic Research Papers 91, 125-141

Micromeritics (1996). Users manual for AccuPyc 1330, Micromeritics GmbH, Mönchengladbach, 19 p.

Micromeritics (2009). Preinstallation Instructions and Checklist, GeoPyc 1360 Pycnometer, 1362 p.

Morgan, C.L. (2000). Resource estimates of the Clarion-Clipperton manganese nodule deposits. In: Cronan, D.S. (Ed.), Handbook of Marine Mineral Deposits, CRC Press, Boca Raton, pp. 145-170.

Murray, J. (1876). Preliminary report on specimens of the sea bottom. Proceedings of the Royal Society, London, 24, 471-532.

Murray, J. and Renard, A.F. (1891). Deep-sea deposits. Report on the scientific results of the voyage of the H.M.S. "Challenger" during the years 1873-1876. First reprinting 1965. New York (Johnson Reprint Corp.), 525 p.

Murray, J.W. and Dillard, J.G. (1979). The oxidation of cobalt(II) adsorbed on manganese dioxide. Geochimica et Cosmochimica Acta 43, 781-787.

Murray, J.W., Balistrieri, L.S. and Paul, B. (1984). The oxidation state of manganese in marine sediments and ferromanganese nodules. Geochimica et Cosmochimica Acta 48, 1237-1247.

Müller, P.J., Hartmann, M. and Suess, E. (1988). The chemical environment of pelagic sediments. Ferdinand Enke, Stuttgart, pp. 70-90.

Nath, B.N. (2007). Processes of formation of ferromanganese manganese nodules and crust. Refresher course on marine geology and geophysics (22 nd October to 2 nd November 2007). Lecture notes 63-69.

Pattan, J.N. and Mudholkar, A.V. (1990). The oxidation state of manganese in ferromanganese nodules and deep-sea sediments from the Central Indian Ocean. Chemical Geology 85, 171-181.

Peacock, C.L. (2009). Physiochemical controls on the crystal-chemistry of Ni in birnessite: Genetic implications for ferromanganese precipitates. Geochimica et Cosmochimica Acta 73, 3568-3578.

Peacock C.L., and Sherman D.M. (2007a). Crystal-chemistry of Ni in marine ferromanganese crusts and nodules. American Mineralogist 92, 1087-1092.

Peacock, C.L. and Sherman, D.M. (2007b). Sorption of Ni by birnessite: Equilibrium controls on Ni in seawater. Chemical Geology 238, 94-106.

Piper, D.Z., Basler, J.R. and Bischoff, J.L. (1984). Oxidation state of marine manganese nodules. Geochimica et Cosmochimica Acta 48, 2347-2355.

Post, J.E. and Appleman, D.E. (1988). Chalcophanite, $ZnMn_3O_7$ H_2O: New crystal-structure determinations. American Mineralogist 73, 1401-1404.

Post, J.E. and Appleman, D.E. (1994). Crystal structure refinement of lithiophorite. American Mineralogist 79, 370-374.

Post, J.E. and Bish, D.L. (1988). Rietveld refinement of the todorokite structure. American Mineralogist 73, 861-869.

Post, J.E. and Veblen, D.R. (1990). Crystal structure determinations of synthetic sodium, magnesium, and potassium birnessite using TEM and the Rietveld method. American Mineralogist 75, 477-489.

Post, J.E., Dreele, R.B. and Buseck, P.R. (1982). Symmetry and cation displacements in hollandites: Structure refinements of hollandite, cryptomelane and priderite. Acta Crystallographica B38, 1056-1065.

Post J.E., Heaney P.J. and Hanson J. (2003). Synchrotron X-ray diffraction of the structure and dehydration behavior of todorokite. American Mineralogist 88, 142-150.

Pouchou, J.L. and Pichoir, F. (1991). Quantitative analysis of homogeneous or stratified microvolumes applying the model "PAP"; In: Heinrich, K.F.J. and Newbury, D.E. (Eds.), Electron probe quantification. Plenum Press, New York, pp. 31-75

Powers, L. (1982). X-ray absorption spectroscopy. Application to biological molecules. Biochimica et Biophysica Acta 683, 1-38.

Price, N.B. and Calvert, S.E. (1970). Compositional variation in Pacific Ocean manganese nodules and its relationship to sediment accumulation rates. Marine Geology 9, 145-171.

Raab, W. (1972). Physical and chemical features of Pacific deep-sea manganese nodules and their implications to the genesis of nodules. In: Horn, D.R. (Ed.),

Ferromanganese Deposits on the Ocean Floor. National Science Foundation, Washington, D.C., pp. 31-49.

Reichert, P. (2012). Geochronology and Geochemistry of the ferromanganese nodules 56KG2 from German license area. Diploma Thesis, Christian-Albrecht-University, Kiel, Germany, 74 p.

Reyss, J.L., Lemaitre, N., KU, T.L., Marchig, V., Southon, J.R., Nelson, D.E. and Vogel, J.S. (1985). Growth of a manganese nodule from Peru basin: A radiochemical anatomy. Geochemica et Cosmochimica Acta 49, 2401-2408.

Ross, D.S., Hales, H.C., Shea-McCarthy, G.C. and Lanzirotti, A. (2001). Sensitivity of Soil Manganese Oxides: XANES Spectroscopy May Cause Reduction. Soil Science Society of American Journal 65, 744-752.

Rosson, R.A. and Nealson, K.H. (1982). Manganese bacteria and the marine manganese cycle. In: Ernst, W.G., Morin, J.G., (Eds.), The environment of the deep sea. Englewood Cliff (Prentice Hall Inc.), pp. 206-216.

Rühlemann, C. and shipboard scientific party (2010) Cruise Report "MANGAN", Microbiology, Paleoceanography and Biodiversity in the Manganese Nodule Belt of the Equatorial NE Pacific. Bundesanstalt für Geowissenschaften und Rohstoffe (BGR), Sonne Cruise, 248 p.

Rühlemann, C., Kuhn, T., Wiedicke, M., Kasten, S., Mewes, K. and Picard, A. (2011). Current status of manganese nodule exploration in the German license area, Proc. Ninth (2011) ISOPE Ocean Mining Symposium. International Society of Offshore and Polar Engineers (ISOPE), Maui, pp. 168-173.

Rühlemann, C. and shipboard scientific party (2012). Cruise Report "BIONOD", Biodiversity, Geology and Geochemistry of the German and French Licence Areas for the Exploration of Polymetallic Nodules in the Equatorial NE Pacific. Federal Institute for Geosciences and Natural Resources (BGR), 302 p.

Schriever, G., Koschinsky, A. and Bluhm, H. (1996). Cruise Report "ATESEPP", Auswirkungen technischer Eingriffe in das Ökosystem der Tiefsee im Sued-Ost-Pazifik vor Peru, (Impacts of potential technical interventions on the deep-sea ecosystem of the southeast Pacific off Peru). Bericht aus dem Zentrum für Meeres- und Klimaforschung Reihe E, 195 p.

Schweissfurth, R. (1971). Manganknollen im Meer. Naturwissenschaften 58, 344-347.

Shen, Y.F., Zerger, R.P., DeGuzman, R.N., Suib, S.L., McCurdy, L., Potter, D.I. and O`Young, C.L. (1993). Manganese oxide octahedral molecular sieves: preparation, characterization, and applications. Science 260, 511-515.

Shen, Y.F., Suib, S.L. and O´Young, C.L. (1994). Effects of Inorganic Cation Templates on Octahedral Molecular Sieves of Manganese Oxide. American Chemical Society 116, 11020-11029.

Siegbahn, K., Nordling, C.N., Fahlman, A., Nordberg, R., Hamin, K., Nedman, J., Johnsson, G., Bermark, T., Karlson, S.E. and Lindberg, B. (1967). ESCA (Electron Spectroscopy for Chemical Analysis): Atomic, Molecular and Solid State Structure Studied by Means of Electron Spectroscopy Almquist and Wiksells (1967).

Silvester, E., Manceau, A. and Drits, V.A. (1997). Structure of synthetic monoclinic Na-rich birnessite and hexagonal birnessite: II. Results from chemical studies and EXAFS spectroscopy. American Mineralogist 82, 962-978.

Smetannikova, O.G., Nndreyev, S.I., Anikeyeva, L.I., Frank-Kamenetsky, V.A. and Suchkov, I.A. (1991). Genetic control of the mineral composition and structure of oceanic-floor ferromanganese deposites. International Geology Review 33, 1124-1135.

Stumm, W. and Morgan, J.J. (1981). Aquatic chemistry: An Introduction Emphasizing Chemical Equilibria in Natural Waters. 2nd Edition, John Wiley & Sons, New York, 1981, 780 p.

Stummeyer, J. and Marchig, V. (2001). Mobility of metals over the redox boundary in Peru Basin sediments. Deep-Sea Research II 48, 3549-3567.

Susini, J., Salomé, M., Fayard, B., Ortega, R. and Kaulich, B. (2002). The scanning X-ray microprobe at the X-ray microscopy beamline at the ESRF, Surface Science, Review Letters 9, 203-211.

Turner, S. and Buseck, P.R. (1979). Manganese oxide tunnel structures and their intergrowths. Science 203, 456-458.

Turner, S., Siegel, M. D. and Buseck, P. R. (1982). Structural features of todorokite intergrowths in manganese nodules. Nature 296, 841-842.

Uspenskaya, T.Y., Gorshkov, A.I. and Sivtsov, A.V. (1987). Mineralogy and internal structure of Fe-Mn nodules from the Clarion-Clipperton fracture zone. International Geology Review 29, 363-371.

Usui, A. (1979). Minerals, Metal Contents, and Mechanism of Formation of Manganese Nodules from the Central Pacific Basin. Marine Geology and Oceanography of the Pacific Manganese Nodule Province. Marine Science 9, 651-679.

Usui, A. and Glasby, G.P. (1998). Submarine hydrothermal manganese deposits in the Izu-Bonin-Mariana arc: an overview. Island Arc 7, 422-431.

Usui, A. and Mita, N. (1995). Geochemistry and mineralogy of a modern buserite deposit from a hot spring in Hokkaido, Japan. Clays and Clay Minerals 43, 116-127.

Usui, A., Mellin, T. A., Nohara, M. and Yuasa, M. (1989). Structural stability of marine 10 Å manganates from the Ogasawara (Bonin) Arc: Implication for low-temperature hydrothermal activity. Marine Geology 86, 41-56.

Villalobos M., Lanson B., Manceau A., Toner B. and Sposito, G. (2006). Structural model for the biogenic Mn oxide produced by Pseudomonas putida. American Mineralogist 91, 489-502.

Von Stackelberg, U. (1997). Growth history of manganese nodules and crusts of the Peru Basin. In: Nicholson, K., Hein, J.R., Bühn, B. and Dasgupta, (Eds.), Manganese Mineralization: Geochemistry and Mineralogy of Terrestrial and Marine Deposits. Special Publication Geological Society of London, London 119, pp. 153-176.

Von Stackelberg, U. and Beiersdorf, H. (1991). The formation of manganese nodules between the Clarion and Clipperton fracture zones southeast of Hawaii. Marine Geology 98, 411-423.

Von Stackelberg, U. and shipboard scientific party (1993). Cruise Report „SEDIPERU", Untersuchung der Sedimentationsgeschichte des Peru-Beckens als Beitrag zum Tiefsee-Umweltschutz, Bundesanstalt für Geowissenschaften und Rohstoffe (BGR), Sonne Cruise, 239 p.

Wadsley, A.D. (1950). A hydrous manganese oxide with exchange properties. Journal of the American Chemical Society 72, 1782-1784.

Wakeham, S. and Carpenter, R. (1974). Electron spin resonance spectra of marine and fresh-water manganese nodules. Chemical Geology 13, 39-47.

Wang, X.H., Schloßmacher, U., Wang, S.F., Schröder, H.C., Wiens, M., Batel, R., Müller, W.E.G. (2012). From nanoparticles via microtemplates and milliparticles to deep-sea nodules: biogenically driven mineral formation. Frontiers of Materials Science 6, 97-115.

Webb, S.M., Tebo, B.M. and Bargar, J.R. (2005). Structural characterization of biogenic Mn oxides produced in seawater by the marine bacillus sp. strain SG-1. American Mineralogist 90, 1342-1357.

Wiedicke-Hombach, M. and Weber, M. (1996). Small-scale variability of seafloor features in the northern Peru Beasin: results from acoustic survey methods. Marine Geophysical Researches 18, 507-526.

Wiedicke-Hombach, M. and shipboard scientific party (2009). Cruise Report „MANGAN 2008", RV Kilo Moana, 13. Oct.-22 Nov. 2008, Bundesanstalt für Geowissenschaften und Rohstoffe (BGR), Hannover, Report, 85 p.

Wiedicke-Hombach, M. and shipboard scientific party (2010). Cruise Report „MANGAN 2009",RV Kilo Moana, 20. Oct. – 27. Nov. 2009, Bundesanstalt für Geowissenschaften und Rohstoffe (BGR), Hannover, Report, 64 p.

Widmann, P., Kuhn, T. and Schulz, H. (2014). Enrichment of mobilizable manganese in deep sea sediments in relation to Mn nodules abundance. Geophysical Research Abstracts, 16, EGU 2014-3875-1.

Wirth, R. (2004). Focused Ion Beam (FIB): a novel technology for advanced application of micro-and nanoanalysis in geosciences and applied mineralogy. European Journal Mineralogy 16, 863-876.

Wirth, R. (2009). Focused Ion Beam (FIB) combined with SEM and TEM: Advanced analytical tools for studies of chemical composition, microstructure and crystal structure in geomaterials on a nanometre scale. Chemical Geology 261, 217-229.

Curriculum Vitae

Personal details

Name:	Anna V. Wegorzewski
Date of birth:	24.06.1983
Place of birth:	Schweidnitz (Poland)
Nationality:	German

Education

since 06/2010	PhD student at the Leibniz University of Hannover (Germany)
	Title of the PhD thesis: „Geochemical and mineralogical investigations of fine growth structures of ferromanganese nodules from the Clarion and Clipperton Zone, Pacific Ocean"
04/2009 - 10/2009:	Diploma Geosciences; Institute of Mineralogy at the Leibniz University Hannover „Crystallization of $FeTa_2O_6$-$MnTa_2O_6$ in pegmatitic melt at 2 kbar"
10/2003 - 10/2009:	Diploma student of Geosciences at the Leibniz University Hannover, Germany
07/2000 - 06/2003:	Secondary-school, Gymnasium Herschelschule in Hannover, Germany

Work experience and internships

06/2010 - 12/2013	Research assistant at the department of marine deposits exploration at the Federal Institute for Geosciences and Natural Resources (BGR) in Hannover, Germany
10/2004 - 05/2010:	Student research assistant at the Lebniz University of Hannover/Institute for Mineralogy, Germany

04/2008:	Internship at the Federal Institute for Geosciences and Natural Resources (BGR) in Hannover, Germany
07 - 08/2007:	Internship at the Department of Earth and Environmental Sciences, University of Waterloo, Canada
02/2005:	Internship at the „Norddeutschen Zentrum für Materialkunde von Kulturgut (ZMK)" in Hannover, Germany

Scientific expeditions

09/2011 - 11/2011	Indian Ocean Exploration, For Seafloor Massive Sulfides (INDEX 2011), R/V SONNE
03/2012 - 05/2012	Biology and Nodules in the NE Pacific (BIONOD 12), R/V L'Átalante
03/2013 - 05/2013	Manganese nodules in the NE-Pazific 2013 (MANGAN 2013), R/V Kilo Moana

Language

German:	native
Polish:	native
English:	very good
French:	some

Additional skills:

- Analytical methods: electron microprobe (EMP), Scanning electron microscope (SEM), X-ray diffraction (XRD)
  Basic knowledge in XANES, HRTEM,
- Computing: Microsoft Office, Grapher 7, Basic Knowledge: Corel DRAW
- Safety training for Offshore-Wind farm-Personal, Hamburg
- Radiation protection course (R2)

References

Dr. Thomas Kuhn, Federal Institute for Geosciences and Natural Resources (BGR), Hannover, Thomas.Kuhn@bgr.de, telephone: 0049 (0)511643 3780

Prof. Dr. Josef-Christian Buhl, Leibniz University of Hannover – Institute for Crystallography, j.buhl@mineralogie.uni-hannover.de, telephone: 0049 (0)511 762 3583

List of publications

Paper

Wegorzewski, A.V. and Kuhn, T. (2014). The influence of suboxic diagenesis on the formation of Manganese nodules in the Clarion Clipperton nodule belt of the Pacific Ocean, Marine Geology

Wegorzewski, A.V., Kuhn, T., Dohrmann, R., Wirth R. and Grangeon, S. (submitted). Mineralogical characterization of individual growth structures of Mn-nodules with different Ni+Cu contents from the central Pacific Ocean, American Mineralogist

Blöthe, M., **Wegorzewski, A.V.**, Kuhn, T., Schippers, A., Müller, C. and Simon, F. (submitted). Microbe-mineral interactions in deep-sea manganese nodules, Environmental Science & Technology.

Abstracts

Wegorzewski, A.V. and Kuhn, T. „Die Genese polymetallischer Knollen und die Interpretation der verantwortlichen Anreicherungsprozesse der Metalle", SONNE-Statusseminar 09. - 10.02.2011, Poster

Wegorzewski, A.V. and Kuhn, T. „Mineralogy of ferromanganese nodules and the metal association", GEO Hannover 01. - 03.10.2012, Talk

Wegorzewski, A.V. and Kuhn, T. „Is the enrichment of metals in ferromanganese nodules from the central Pacific correlated with glacial-interglacial stages: new answers to old questions!", San Francisco, 03. - 07.12.2012, AGU, Poster

Wegorzewski, A.V. and Kuhn, T. „Charakterisierung der mineralogischen Zusammensetzung von Manganknollen und deren Metallassoziation", SONNE-Statusseminar 14. - 15.02.2013, Poster